Activity and Kinematics of Cool and Ultracool Dwarfs

Sarah Jane Schmidt

A dissertation submitted in partial fulfillment
of the requirements for the degree of

Doctor of Philosophy

University of Washington

2012

Suzanne L. Hawley, Chair

Andrew C. Becker

Adam J. Burgasser

Erika M. Harnett

Victoria S. Meadows

Program Authorized to Offer Degree:
Astronomy

University of Washington

Abstract

Activity and Kinematics of Cool and Ultracool Dwarfs

Sarah Jane Schmidt

Chair of the Supervisory Committee:
Professor Suzanne L. Hawley
Astronomy Department

The ages of cool and ultracool dwarfs are particularly important. For cool M dwarfs, accurate ages combined with their ubiquity in the stellar disk could lead to a new level of precision in age dating the Galaxy. A better understanding of the chromospheres of M dwarfs could provide important clues about the relationship between activity and age in these low mass stars. Ultracool (late-M and L) dwarfs have the distinction of including both warm, young brown dwarfs and stars with mean ages more representative of the stellar disk. Kinematics are a source of mean ages and could provide or confirm discriminating features between stars and brown dwarfs. This thesis is composed of several different projects, each investigating the activity or kinematics of cool or ultracool dwarfs.

First, a sample of nearly 500 L dwarfs selected from SDSS DR7 photometry and spectroscopy is examined; we discovered 200 new L dwarfs and found evidence of a bias towards red $J - K_S$ colors in the entire population of previously known L dwarfs. Using the three-dimensional kinematics of 300 SDSS DR7 L dwarfs, we find that their kinematics are consistent with those of the stellar disk and include a previously undetected thick disk component. We also confirmed a relationship between age and $J - K_S$ color (due to our large sample of UVW motions and unbiased $J - K_S$ colors), with blue L dwarfs having hotter kinematics (consistent with older ages) and redder L dwarfs having colder, younger kinematics.

The DR7 L dwarf sample showed no distinct kinematic difference between young brown

dwarfs and disk-age stars, perhaps due to a bias towards early spectral types. In order to probe the kinematic distribution of L dwarfs in a volume-limited sample, we began a survey of radial velocities of nearby (d<20pc) L dwarfs using the TripleSpec instrument on the ARC 3.5-m telescope at APO. While several reduction packages were tested on the TripleSpec data, none were found to provide reductions of sufficient quality for the measurement of radial velocities.

Another avenue for kinematic investigation was identified: the assembly of a large sample of late-M and L dwarfs using a combination of SDSS DR7 and BOSS photometry and spectroscopy, supplemented by photometry from 2MASS and WISE. In agreement with previous work, we find that colors based on a combination of SDSS and 2MASS photometry are well correlated with spectral type for early-L dwarfs, while infrared colors (from 2MASS and WISE alone) are well correlated with spectral type for the latest L dwarfs. Using the kinematics of this sample, we confirm that there is no relationship between velocity dispersions and spectral type, indicating that young brown dwarfs are not a significant component of early-L dwarfs in the field. The velocity dispersions of active and inactive dwarfs are also suggestive of an age activity relation for late-M and L dwarfs.

The BOSS Ultracool Dwarf sample has also proven ideal for investigating the activity properties of M and L dwarfs using the presence and strength of Hα emission. We show that the fraction of objects which show Hα emission increases from early-M dwarfs through the L1 spectral type. Additionally, we use the NLTE radiative transfer code RH to investigate the ranges of temperature structure and filling factors of M and L dwarf chromospheres by generating the observed levels of Hα emission. To produce the observed levels of emission, the typically strongly emitting early-M dwarfs need hot chromospheres covering over 1% of their surfaces, while L dwarfs, which emit Hα at much weaker levels, need much less extended and/or cooler chromospheres.

Hα can be difficult to detect in L dwarfs due to their faint optical luminosities, but they are relatively bright in the infrared. To begin a search for chromospheric indicators in the infrared, we began a monitoring program designed to detect infrared emission lines from M

dwarf flares. We present the first reported detection of infrared emission lines during an M dwarf flare. Based on 50 hours of monitoring in the infrared, we estimate that M dwarfs spend $\sim$3% of the time showing infrared emission lines. Using RH, we show that a very hot chromosphere (T$\sim$30,000K) is required to produce the line flux rations observed in optical and infrared spectra of our strongest flare.

TABLE OF CONTENTS

Page

LIST OF FIGURES

LIST OF TABLES

ACKNOWLEDGMENTS

This thesis would not exist without the help of many friends, mentors, and collaborators. Oliver Fraser is my first acknowledgement because he was of enormous help during my first year at UW. My graduate class also deserves special thanks, particularly Chelsea McLeod and Sarah Loebman. Without them, I would have had a much harder time with the qualifying exam and I would have missed out on a lot of fun. My past and present officemates, Ferah Munshi, Vaishali Bhardwaj, and Yumi Choi have provided much needed support and many study breaks.

Sarah Garner has been a friend, mentor, and excellent resource for all things UW and most things teaching. I would also like to particularly thank John Wisniewski for his help and support during job application season. His assistance made it slightly less stressful and more successful than it otherwise would have been.

The Red Army was essential to all of my research endeavors. Andrew West and John Bochanski have been great collaborators and mentors. Eric Hilton was always ready with a story or a new research question to mull over, and Jim Davenport has always been willing to solve problems with me and share his various IDL codes. Combined with Adam Kowalski, Kevin Covey, John Wisniewski and Lucianne Walkowicz, the Red Army has provided support, assistance, and fun throughout my graduate career.

I would particularly like to thank my committee for their support. Erika Harnett was kind enough to be my GSR on rather short notice. Andy Becker read my thesis even though he didn't have to, and has been an excellent resource on statistics and uncertainties. Adam Burgasser gave this dissertation an extremely thorough reading and produced many thoughtful comments which have greatly improved the final product. Vikki Meadows is largely responsible for coaching me over the finish line

as I struggled to get my revisions done in time.

Last, and most importantly, I would like to acknowledge the continued support and friendship of my advisor, Suzanne Hawley. She has been a source of funding, guidance, paper comments, and ideas for the past six years. Her scientific insight, political guidance, and extensive knowledge of jigsaw puzzles and crisps have been essential to my completion of this dissertation and PhD!

DEDICATION

To David, who is always there for me.

Chapter 1

INTRODUCTION

In this dissertation, I characterize the kinematic and chromospheric properties of cool (M) and ultracool (late-M and L) dwarfs to better understand their ages and magnetic field strengths. An improved understanding of these two properties will ultimately elucidate the differences between stars and brown dwarfs and our understanding of how magnetic fields interact with the atmospheres of these extremely cool and low-mass objects.

The M and L spectral classes include both the end of the stellar main sequence (stars much cooler and less massive than our Sun) and the warmest brown dwarfs (objects formed like stars that are not massive enough for sustained core hydrogen burning). M dwarfs have the distinction of being the most common stars in the galaxy, and as such they are currently drawing attention due to their potential as habitable planet hosts (Scalo et al. 2007; Tarter et al. 2007). The L spectral class holds particular interest because it bridges the gap between stars and brown dwarfs; the coolest stars have L spectral types, and brown dwarfs (with the same effective temperatures and luminosities as L stars) can be found throughout the L spectral sequence depending on their mass and age (Chabrier & Baraffe 2000).

Kinematics, or the velocities of stars, have long been a useful statistical tracer of age (Wielen 1977). Stars are formed in molecular clouds, which typically have nearly circular Galactic orbits. These stellar orbits become increasingly eccentric and inclined as the star ages due to gravitational interactions between the star and molecular clouds in the Galactic plane. Age is particularly important to distinguish between the stellar and sub-stellar (brown dwarf) members of the ultracool dwarf population. Brown dwarfs that have not yet cooled past the L spectral sequence have relatively young ages, while L stars have ages similar to those of the rest of the stellar population (e.g., Burrows et al. 2001).

Activity is a blanket term that refers to any emission tracer of magnetic fields on the surface of stars. M dwarfs are known for their strong magnetic fields (e.g., Donati & Land-

street 2009) that result in strong quiescent activity and flares. Some L dwarfs show evidence of equally strong magnetic fields (e.g., Audard et al. 2007; Hallinan et al. 2008), but tracers of magnetic activity are either present at weaker levels or entirely absent in part due to their cooler, more neutral atmospheres.

I have two main goals in this dissertation. The first is to use the kinematics of cool and ultracool dwarfs to determine the ages of these objects and ultimately provide a mechanism to differentiate between stars and brown dwarfs within the L spectral class. Kinematics provide an essential calibration for additional properties that may depend primarily on age (e.g., color, activity). If ages can be determined well enough to provide a clear separation between these two classes of objects, it will be possible to determine of the mass function at the stellar/sub-stellar boundary.

The second goal is to use emission lines to explore the chromospheric structures of M and L dwarfs. Magnetic fields are ubiquitous on low mass stars and brown dwarfs, and a detailed understanding of chromospheric emission lines indicates how strongly magnetic fields interact with the atmospheres of cool and ultracool dwarfs. I apply the same atmospheric modeling code to detailed observations of a single flare and to observations of Hα emission on thousands of stars to examine both flaring and quiescent chromospheres.

As an introduction, I will review the discovery and characteristics of cool and ultracool dwarfs, discuss magnetic fields and observational tracers of quiescent and flaring magnetic activity, and explain the usefulness of kinematics in examining the ages of ultracool dwarfs. I will also describe the observational resources that were essential to the completion of this dissertation and outline the rest of the chapters.

1.1 Overview of Cool and Ultracool Dwarfs [1]

[1] In general, the term "cool dwarfs" refers to stars the temperature of the Sun and cooler. In this thesis, "cool dwarfs" refers exclusively to M dwarfs and includes no G or K stars. "Ultracool dwarfs" is a term coined by Kirkpatrick et al. (1997) that refers to dwarfs of spectral type M7 and later; in this thesis it will typically refer to spectral types M7-L8.

1.1.1 Discovery and Classification of M and L dwarfs

The classification of stars using spectral features is one of the oldest topics in the science of astronomy. To provide a context for more recent work, I will briefly review the history of classification (which includes M dwarfs, but only in small numbers) before summarizing the discovery and classification of M and L dwarfs.

The Beginnings of Stellar Classification

The first stellar spectrum dates back to Sir Isaac Newton; he used a prism to examine the light of the Sun, but his early attempt did not have sufficient resolution to detect absorption lines in the solar spectrum (Newton 1672). The field of astronomical spectroscopy essentially lay dormant for over a century, until 1802. In the same year, Young (1802) established "wavelength" as a numerical measurement of color and Wollaston (1802) observed the solar spectrum with sufficient resolution to detect absorption lines.

These solar absorption lines were observed in greater detail by Fraunhofer (1823, 1824), who labeled the strongest 10 lines with letters, some of which are still used today (e.g., Ca II H and Na II D). Fraunhofer also examined the spectra of six of the brightest stars and was one of the first to note that they did not all contain the same absorption lines as the Sun, which laid a foundation for spectroscopic classification of stars other than the Sun.

The first stellar classification schemes were published four decades later (Donati 1863; Rutherfurd 1863) based on samples of 10-20 stars. These first attempts typically organized stars into three or four groups based on their colors and spectral features, separating solar-type and cooler stars, white stars with strong absorption lines (likely A and F stars) and white stars with weak or no absorption lines (OB stars). Classification efforts then commenced in earnest, with the largest contemporary catalog containing over 400 stars (Secchi 1867). Secchi was also the first to further subdivide his classification scheme; his types were assigned letters A through M based on the strength of their hydrogen absorption features.

The Henry Draper Memorial stellar catalog, assembled between 1890 and 1930, adapted Secchi's letters, re-arranged into their present configuration (OBAFGKM) to represent a temperature sequence (which had long been suspected, but was proved by Wilsing &

Scheiner 1909). These types were widely adopted, in part because the final catalog included over 200,000 stars (Cannon & Pickering 1924), a number that far surpassed the number of stars classified on any other system.

The last crucial step in designing the modern spectral sequence was the separation of dwarf and giant stars. While dwarfs and giants do have distinct spectral features due to drastically different surface gravity, these were largely unrecognized in early classification efforts. The invention of the Hertzspring-Russell Diagram, which organized stars by both their temperature and luminosity, finally separated M dwarfs from M giants (Hertzsprung 1907; Russell 1913). At the time, very few M dwarfs were known, due to their faint absolute magnitudes ($M_V \geq 6$).

These advancements in classification were all integrated into a single scheme by Morgan et al. (1943, known as the MKK system) that is still in use today. The MKK classification scheme did not include the latest M dwarfs or the (not yet discovered) L dwarfs; those developments are discussed below. More recent additions to spectral classification (which are not discussed in detail) include the definition of the even cooler "T" spectral class (Burgasser et al. 2002b; Geballe et al. 2002; Burgasser et al. 2006) based on near-infrared (9000-25000Å) data, and the current development of a classification scheme for the newly discovered "Y" spectral class (Cushing et al. 2011).

An M Dwarf Spectral Sequence

The MKK system continued to exclude later M dwarfs for nearly 30 years, but in the 1970's a few different classification schemes were proposed. The two most popular schemes were designed by Wing (1973) and Boeshaar (1976) using similar classification philosophies, but differed in the specific relationships between band strength and spectral subtype. For early-M dwarfs, the classifications were based on the strength of a number of TiO bands, and for later M dwarfs the main features used were TiO, VO (at 5736 and 5759Å) and CaOH at 5530-60Å (see Figure 1.1).

These classifications were difficult to use for the latest M dwarfs, where the majority of the spectral flux is at wavelengths redder than 6000Å. The two classification systems

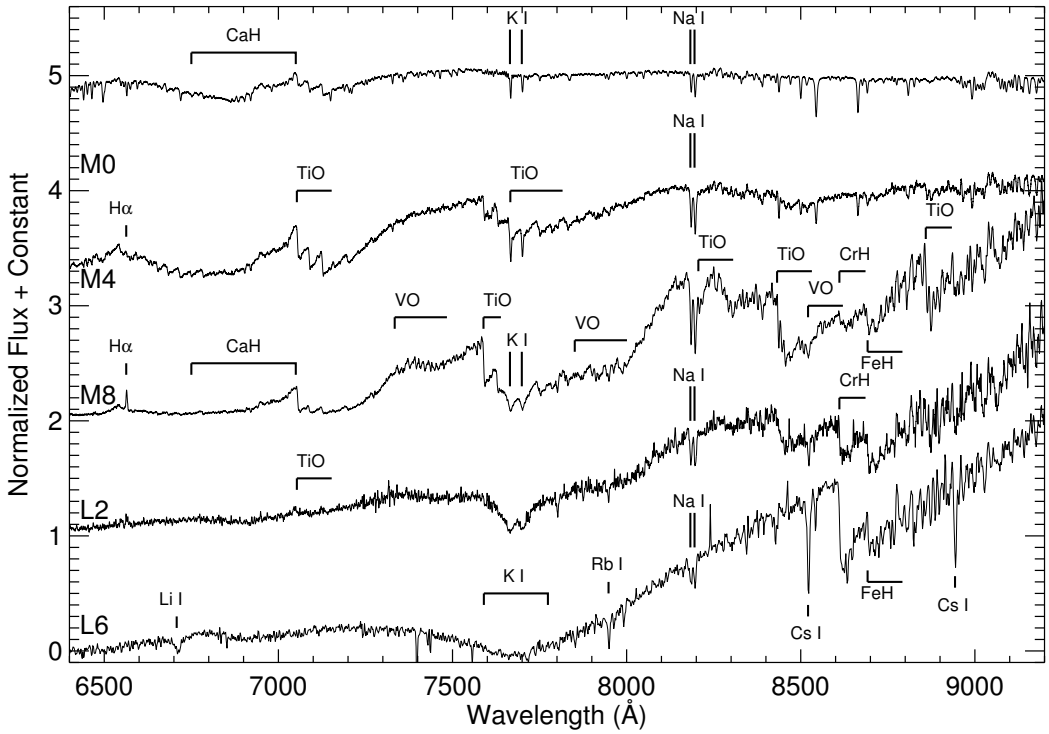

Figure 1.1 Spectra of M0, M4, M8, L2, and L6 dwarfs. The M dwarf spectra are templates from Bochanski et al. (2007b), and the L dwarfs are spectral standards from Kirkpatrick et al. (1999), made available at http://www.stsci.edu/∼inr/ultracool.html. Atomic lines and molecular bands are labeled using the lists provided in Kirkpatrick et al. (1991, 1999).

were adapted to use redder wavelengths (6600-10000Å) by Kirkpatrick et al. (1991) and Bessell (1991) (for the Boeshaar and Wing systems respectively). In subsequent years, the Kirkpatrick et al. (1991) system was more widely adopted (e.g., Reid et al. 1995; Cruz et al. 2003; West et al. 2011) so that system is described here.

The Kirkpatrick et al. (1991) system relies on an overall match to spectral templates, which incorporates both the strength of molecular bands in addition to the overall spectral slope. Both of these features change dramatically over the M spectral sequence (as shown in Figure 1.1). The main features that define the M dwarf sequence are:

- An increasingly red spectral slope
- The increasing strength of the TiO absorption bands (7053Å, 7589Å, 7666Å, etc.)
- The appearance of the VO absorption bands (7334Å, 7851Å, and 8251Å)
- The appearance of the 8692Å FeH band and the 8611Å CrH band

Discovery and Classification of L dwarfs

The first L dwarf, GD 165B, was discovered as the common proper motion companion to a nearby white dwarf (Becklin & Zuckerman 1988), but its peculiar spectrum (now typed as an L4) was not at the time widely recognized as a >M9 object. Due to their intrinsic faintness in optical bands, the discovery of objects which are now identified as L dwarfs were next reported in 1997. In that year, six different L dwarfs were reported (Delfosse et al. 1997; Kirkpatrick et al. 1997; Ruiz et al. 1997; Tinney et al. 1997).

The majority of these L dwarfs were discovered in new infrared surveys - most notably the Deep Near Infrared Survey (DENIS; Epchtein et al. 1994) and the Two Micron All Sky Survey (2MASS; Skrutskie et al. 2006). These surveys had long been impossible due to the insensitivity of classic CCD technology to infrared light, but infrared detectors were developed in the 1990's. With the new detector technology available, surveys of the sky in the J, H, and K bands were not only possible, but essential for the discovery of L dwarfs, which are brightest in infrared colors.

As 2MASS and DENIS expanded their survey coverage, sufficient L dwarfs were discovered to outline a classification scheme based on their red optical spectra. Two classification

schemes were developed concurrently, both based on a temperature scheme but differing primarily in the estimated end of the L spectral sequence. Both schemes were designed so that the onset of the 2.2μm methane band (observed in the spectrum of the coolest known dwarf, Gl 229B; Nakajima et al. 1995; Oppenheimer et al. 1995) would be the defining feature of the next coolest spectral type. Martín et al. (1999) claimed that would happen at T_{eff}=1200K, while the coolest known L dwarf had a temperature of T_{eff}=1600K (based on a calibration by Basri et al. 2000) so they defined a sequence that arranged all known L dwarfs from L0 to L6, expecting that cooler L dwarfs would soon be discovered. Kirkpatrick et al. (1999) argued that methane would appear in objects only slightly cooler than those known, so they defined the latest known dwarf as an L8.

In part because subsequent observations found that methane *was* present in slightly cooler dwarfs (e.g., Geballe et al. 2002), and in part because the Kirkpatrick et al. (1999) classifications were immediately more widely used (e.g., Fan et al. 2000; Kirkpatrick et al. 2000; Gizis et al. 2000), the Kirkpatrick et al. (1999) classifications are more widely adopted, and are used in this thesis as well. The main features used to classify L dwarfs in the red optical (which are shown in Figure 1.1) are:

- The weakening and disappearance of the TiO and VO bands
- The appearance of the Rb I lines at 7948Å and the Cs I lines at 8521Å and 8943Å
- The strengthening and broadening of the 7665/7665Å K I doublet
- The strengthening of the 8611Å CrH band compared to the 8692Å FeH band

1.1.2 Physical Properties of M and L Dwarfs

Concurrently with the definition of the M and L dwarf spectral sequences, a combination of models and observations were used to measure and calculate the physical properties of these low mass objects. Dwarfs in the spectral class M have bolometric luminosities of 5×10^{-2} to 5×10^{-4} $L_{\odot}$ and effective temperatures ranging from 3800 to 2300K (Leggett et al. 2001; Casagrande et al. 2008), masses ranging from 0.6 to 0.08 $M_{\odot}$ and radii of 0.6 to 0.08 $R_{\odot}$ (e.g, López-Morales 2007; Kraus et al. 2011, and references therein). In addition to being small and faint, M dwarfs are predicted to have long lives ($\sim10^{12}$ years) due to the slow

rate of fusion in their cores. L dwarfs have measured bolometric luminosities of 5×10^{-4} to 3×10^{-5} $L_{\odot}$ and effective temperatures of 2200K to 1200K (Golimowski et al. 2004; Cushing et al. 2006), masses smaller than 0.08 $M_{\odot}$ and radii smaller than 0.08 $M_{\odot}$. There is no firm lower limit on masses and radii of L dwarfs because the L spectral class contains both stars (massive enough to sustain core hydrogen burning; $M \geq 0.077M_{\odot}$) and brown dwarfs (lower mass objects with no sustained fusion; $M \leq 0.076M_{\odot}$).

While stellar L dwarfs achieve a constant $T_{\rm eff}$ and luminosity once they initiate core hydrogen fusion, brown dwarfs both cool (decrease in $T_{\rm eff}$) and dim (lose luminosity) as they age (shown in Figure 1.2; Burrows et al. 1993, 1997). Brown dwarfs that are still warm enough to be classified as L dwarfs are still relatively young, while stellar L dwarfs should have ages more representative of disk stars. For example, an L2 dwarf could be an M = 0.078 $M_{\odot}$ star between 4 and 10 Gyr old, or an M = 0.060 $M_{\odot}$ brown dwarf with an age of $\sim$2 Gyr. The radii of brown dwarfs also contract as they age, creating another minor degeneracy between mass, radius, and age. To fully understand the physical properties of L dwarfs, it is important to derive their ages.

1.1.3 Dust Clouds in Ultracool Dwarfs

At the low temperatures of ultracool dwarf atmospheres, molecules begin to condense onto dust grains (e.g., Tsuji et al. 1996a,b). In L dwarfs, the most abundant of these grains are of perovskite and corundum (which begin to form in late-M dwarf atmospheres) and Mg-Silicates (Lodders & Fegley 2006). These grains are a major source of opacity throughout the near- and mid-infrared, and the condensation of perovskite ($CaTiO_3$) is the main avenue for depleting the TiO, leading to the disappearance of the TiO bands from the optical spectrum (Allard 1998; Allard et al. 2001). Due to the relative strengths of dust and H_2 opacity (which mainly absorbs in the K_S band, thicker clouds cause redder $J-K$ colors (strong dust opacity in the J-band), while thin or patchy clouds result in bluer infrared colors (weaker dust opacity in the J-band; Allard 1998; Burrows et al. 2006; Helling et al. 2008; Allard et al. 2011; Marley et al. 2010). Observations relating to the properties of these dust clouds are often split between those focusing on dwarfs either with particularly red or

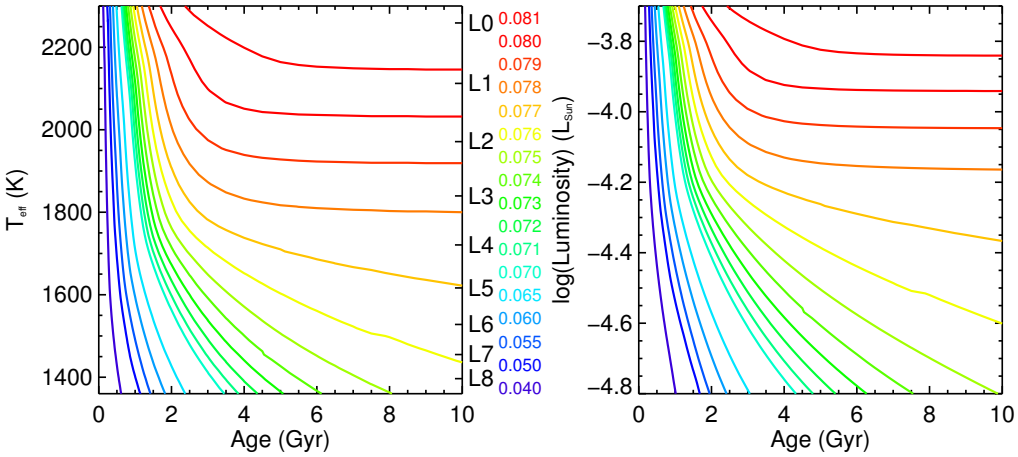

Figure 1.2 T_{eff} (left) and luminosity (right) as a function of age for stars ($M \geq 0.077 M_{\odot}$) and brown dwarfs ($M \leq 0.076 M_{\odot}$) from Burrows et al. (1993, 1997). Brown dwarfs cool and dim as they age, while stars settle at a constant T_{eff} and luminosity. Each color represents a different mass, which are given in terms of $M_{\odot}$ between the two panels. The conversion from temperature to spectral type (shown along the right axis of the left panel) is from Stephens et al. (2009).

blue $J - K_S$ colors, corresponding to thicker and thinner clouds.

Red L dwarfs are particularly easy to select from near-infrared surveys (e.g., 2MASS) because their colors are distinct from those of brighter, slightly bluer late-M dwarfs. These L dwarfs have spectroscopic features consistent with youth, including the presence of lithium absorption and a substantially weakened K I doublet (which typically has pressure-broadened wings; Kirkpatrick et al. 2008; Cruz et al. 2009). Similar features and red $J - K_S$ colors have been found in L dwarfs from young moving groups (Allers et al. 2007; Bannister & Jameson 2007; Jameson et al. 2008b), providing further evidence that these red L dwarfs are young, and measurements of linear polarization confirm their dusty nature (e.g. Zapatero Osorio et al. 2005).

Concurrently with the classification of red L dwarfs, a subclass of blue L dwarfs was also identified in 2MASS and SDSS (e.g., Cruz et al. 2003; Knapp et al. 2004; Chiu et al. 2006; Cruz et al. 2007; Bowler et al. 2010; Schmidt et al. 2010a). These blue L dwarfs have reduced absorption in the J band, which is likely due to a reduction of condensate clouds (Knapp et al. 2004; Burgasser et al. 2008; Bowler et al. 2010; Cushing et al. 2010). The

lack of confirmed Li I detections in any of these blue L dwarfs provides further evidence that they are likely old (Burgasser et al. 2008) and their high tangential velocities indicate they are are part of a kinematically hotter (older) population (Faherty et al. 2009). The blue colors and old ages of these L dwarfs may be a link between blue L dwarfs and low metallicity subdwarfs, which exhibit many of the same spectral features (e.g., weakened alkali absorption Burgasser et al. 2003b; Burgasser 2004; Burgasser et al. 2009; Cushing et al. 2009).

1.2 Magnetic Activity in M and L Dwarfs

Stars and brown dwarfs can host strong magnetic fields, which often result in star spots (located in the photosphere) and non-thermal emission in the chromospheres and coronae of these objects. Chapters 5 and 6 of this thesis focus on observations of chromospheric emission through atomic emission lines. Here, I review some key observational and theoretical results which led to our current understanding of M and L dwarf activity, in addition to specific results relating to quiescent and flaring emission lines originating in the chromosphere.

1.2.1 Background: Magnetic Fields

Early Observations of Magnetic Activity

The first stellar magnetic field was detected on the Sun, using observations of the Zeeman effect (Zeeman 1897) in sunspot spectra taken in the early twentieth century (Hale 1908). These spots were often spatially associated with regions showing the Hα line in emission (Hale 1909) which occasionally were involved in solar events (coronal mass ejections) which caused "magnetic storms" (or aurorae) on the Earth (Lodge 1909). The connections between solar activity and possible activity on other stars were not made until decades later (Kron 1950).

The connection between activity on the Sun and M dwarfs became apparent with additional observational results. Several observers reported flares, typically observed as dramatic increases in stellar brightness, on M dwarf stars (e.g., Luyten 1949; Gordon & Kron 1949;

Lippincott 1952; Shapley 1954). In 1954, a catalog of emission line stars included 67 M dwarfs showing Hα emission (Bidelman 1954). While these observations were noted as being similar to solar phenomena, there were no direct observations of the stellar magnetic fields which were the suspected cause of the stellar activity.

Magnetic Dynamos

Stellar magnetic fields are generated and sustained due to turbulent motions in their interiors (referred to as a "dynamo"). In solar-type stars, this is thought to be the classical $\alpha\Omega$ dynamo, which relies on differential rotation between the inner radiative zone and the outer convective zone (Parker 1955). For fully convective stars ($<0.03 M_\odot$; Chabrier & Baraffe 1997), the dynamo shifts to an α^2 dynamo, which relies mainly on the turbulent convective motions of the plasma (Küker & Rüdiger 1999; Chabrier & Küker 2006).

The strength of field generated by the solar-type dynamo shows a strong dependence on the rotational velocity of the star, which gives rise to a relationship between age and activity, first noted by Skumanich (1972). The interaction of the magnetic field with the outer atmosphere of the star generates a magnetic wind, which dissipates angular momentum (Mestel 1968). The rotation slows as the star ages, which results in a weaker magnetic field.

The relationship between age, rotation, and activity seems to hold over the boundary between solar-type and fully convective stars (Mohanty & Basri 2003; Reiners & Basri 2007; Reiners et al. 2012), which is consistent with dynamo models of fully convective stars (Browning 2008). The rotational rate of M dwarfs seems to increase with spectral type, indicating an increasingly inefficient rotational breaking mechanism in late-M and L dwarfs (Kiraga & Stepien 2007; Reiners & Basri 2008; McLean et al. 2012) which may be the primary reason for the lack of a clear activity/rotation relation for ultracool dwarfs (West & Basri 2009; Reiners & Basri 2010).

Observations of Cool Dwarf Magnetic Fields

Observations of magnetic fields on stars other than the Sun were not possible for many decades; a resolution of R>100,000 is needed to directly detect Zeeman splitting. In 1980,

Robinson suggested a method of comparing the widths of magnetically sensitive lines with the widths of magnetically insensitive lines to detect magnetic fields. These methods were adapted and successfully applied to a few of the most active M dwarfs (Saar & Linsky 1985; Saar 1988), detecting strong (3-4 kG) magnetic fields.

These efforts were continued by Johns-Krull & Valenti (1996) and Valenti & Johns-Krull (2001), who detected fields of 2-4kG for active M0-M5 dwarfs by measuring the Zeeman wings in high resolution (R$\sim$120,000) spectra. More recently, this method was adapted to magnetically sensitive iron hydride bands to measure magnetic fields across the M spectral class. A mix of active and inactive dwarfs showed field strengths of 0-4kG, with active dwarfs (those showing Hα emission) typically grouped amongst those with strong magnetic fields (Reiners & Basri 2007).

In addition to detecting large scale magnetic fields, recent work using Zeeman Doppler Imaging has shed light on the topologies of magnetic fields of M dwarfs (Donati et al. 2006, 2008; Morin et al. 2008, 2010). The technique tracks the change in polarization of Zeeman broadened lines as magnetically active regions (where these lines are generated) rotate past the observer. These magnetic maps of M dwarfs show that their fields are typically less homogeneous than those of solar-type stars, providing important constraints for dynamo models (e.g. Browning 2008).

1.2.2 Chromospheres on Quiescent and Flaring M dwarfs

While it is not yet possible to resolve surface features on M dwarfs, if their magnetic activity is analogous to solar activity, small scale surface magnetic fields interact with ionized material high in the photosphere, causing small active regions. While the M dwarf is in quiescence, an quasi-equilibrium is reached between magnetic heating of the chromosphere and cooling of the chromosphere though atomic emission. Occasionally, magnetic fields experience dramatic reconnection events which result in strong flares, characterized by emission over a wide range of wavelengths.

Quiescent M dwarf Activity

The prevalence of Hα emission on M dwarfs has been known since early spectroscopic observations of M dwarfs (Bidelman 1954; Petit 1961) and has since been an active topic of investigation. For mean activity trends, I will focus on results from the Palomar/MSU Nearby Star Spectroscopic Survey (Gizis et al. 2002; Hawley et al. 1996; Reid et al. 1995) and, more recently, from M dwarfs in SDSS (West et al. 2004, 2008, 2011) due to their larger sample sizes than other contemporary surveys.

The mean strength of activity, often characterized by $\log(L_{H\alpha}/L_{bol})$, is relatively constant for active M0-M4 dwarfs, then declines with later spectral type through M9. The fraction of M dwarfs which show Hα emission increases with spectral type, consistently from M0 to M9 dwarfs (Gizis et al. 2002; West et al. 2011). Activity strength does not show a strong relationship with Galactic height, which may be expected if M dwarfs followed the Skumanich law. However, active M dwarfs have narrower velocity dispersions (younger kinematics) than inactive M dwarfs (Gizis et al. 2002) and the fraction of active M dwarfs declines with galactic height, supporting a relationship between activity, age, and rotation that does not exactly mimic the solar-type relationship (West et al. 2006, 2008).

While Hα is sufficient to detect the presence of activity in M dwarf chromospheres, the combination of Hα emission with additional emission lines is necessary to constrain the shape of the chromosphere. Ca II traces a lower temperature, higher density portion of the chromosphere than Hα, and in weakly active dwarfs it is often in emission when Hα is in absorption (Robinson et al. 1990; Walkowicz & Hawley 2009). Together, the strengths of Hα and Ca II can be used to place strong constraints on chromospheric temperatures, (e.g., Cram & Giampapa 1987; Houdebine & Stempels 1997). Typically, a one-dimensional model is used to generate the relative strengths of these two emission lines, which are compared to the data. For M6 and later dwarfs, it is difficult to observe the relatively blue Ca II lines, and chromosphere models have not been attempted.

M dwarf Flares

A complete understanding of M dwarf flares contains many different components. The first is an understanding of the magnetic field generation in the M dwarf interior and the topology of that magnetic field at the surface, which is discussed above. We infer, based on observations of the Sun, that flare events are caused by electrons accelerated in a magnetic reconnection event. That event must depend on the complex magnetic structures on the stellar surface (e.g., Lin & Hudson 1976). The interaction of these electrons with the M dwarf photosphere is difficult to model and not particularly well understood (e.g., Allred et al. 2006), but the resulting temperature structure can be modeled based on the radio, optical, UV, and X-ray radiation observed during flares.

The chromospheric heating, which is the particular focus of this thesis, can be traced through the relative strengths of atomic emission lines during the flare. Similar to simulations used for quiescent chromospheres, the common method (first attempted by Cram & Woods 1982) is to use a one-dimensional atmosphere to simulate the expected emission lines, and select the best match based on line flux. Most attempts at modeling the flaring chromosphere have been limited to a single time step, often at or near the peak flux of the flare emission. To simplify a very complicated chromosphere, the heated chromosphere is most often modeled as a linear rise in temperature as a function of the logarithm of column mass (Hawley & Fisher 1992; Christian et al. 2003; Fuhrmeister et al. 2010).

One of the last components of understanding M dwarf flares is determination of a flare frequency distribution (which describes the number of flares per energy) as a function of spectral type and activity rate. Early work by Lacy et al. (1976) measured the flare frequency distribution for the most active M dwarfs, and subsequent work continued to focus on the most active M dwarfs (e.g., Mavridis & Avgoloupis 1987; Ishida et al. 1991). Only in recent years have flare frequency distributions been investigated as a function of quiescent activity level and spectral type (Hilton 2011; Kowalski et al. 2009), confirming that active, early M dwarfs flare more frequently than inactive dwarfs, and active mid- to late-M dwarfs. A full understanding of the distribution of flares on all M dwarfs could be used as an additional constraint for dynamo models on a range of M dwarfs.

1.2.3 Magnetically Active L dwarfs

But how does magnetic activity change with the transition from ionized to dusty atmospheres? The magnetic fields generated by M dwarfs show no decline with spectral type (Reiners & Basri 2007), so it is reasonable to assume that L dwarfs (at least the early ones) have similarly strong magnetic fields. Indeed, strong and persistent radio emission detected from a handful of nearby L dwarfs indicate the presence of 1-4 kG fields (Hallinan et al. 2008; Berger et al. 2009). But in an increasingly neutral atmosphere, magnetic resistivity should prevent strong coupling between the magnetic fields and material at the surface, which should prevent heating of a chromosphere (Mohanty et al. 2002).

Yet Hα emission has been detected in $\sim$50 early- to mid- L dwarfs (Gizis et al. 2000; Kirkpatrick et al. 2000; Hall 2002; Mohanty & Basri 2003; Liebert et al. 2003; Schmidt et al. 2007; Reiners & Basri 2008), indicating chromospheres are present in at least some of these ultracool dwarfs[2]. X-ray emission has also been detected in the Kelu-1 system, indicating that L dwarfs can heat a corona (Audard et al. 2007). The answer to this may lie in the dust clouds that are persistent in many L dwarfs. Temporary separation of electrons from dust grains may lead to an electron avalanche that could allow the magnetic field to temporary couple with the atmosphere (Helling et al. 2011a,b). While these electron avalanches may not be common, they could explain the persistence of chromospheres at cooler T_{eff} then had been thought possible.

While blue and UV photometric observations are ideal for flares on M dwarfs, the same observations are very difficult for L dwarfs because they are much fainter at blue/UV wavelengths. A few serendipitous spectroscopic observations of L dwarf flares show strong, variable Hα emission persisting on $\sim$hour timescales (Liebert et al. 2003; Schmidt et al. 2007). It is not known if these flares have the same multi-wavelength signatures as M dwarf flares; a variety of additional observations are needed to truly characterize L dwarf flares.

---

[2]The fraction of L dwarfs showing Hα emission is somewhat undetermined. Each non-detection produces an upper limit for that L dwarf. Some upper limits are higher than the mean activity strength for that spectral type and others are very low. In the absence of uniform spectra, it is reasonable to assume that some of these non-detections are indicative of a true absence of Hα emission while others are simply the result of noisy spectra.

1.3 Kinematics

Kinematics have recently become essential to the study of cool and ultracool dwarfs, through separating out members of moving groups and young associations (e.g., Seifahrt et al. 2005), picking out likely members of the halo to select possible low metallicity objects (e.g., Lépine et al. 2007), and assessing the mean age of the disk population (e.g. Faherty et al. 2009).

1.3.1 Background

When considering the kinematics of stars, the most important process is the diffusion of stellar orbits, first described by Wielen (1977). Previously, stars had been considered as orbiting a smooth Galactic potential, but it had become increasingly apparent that local interactions with a non-smooth potential were having a significant effect on stellar orbits. Wielen (1977) used solar-type stars with known ages(according to the Skumanich law) to derive a basic relation between velocity dispersion and age, inferring that molecular clouds (originally suggested as a kinematic perturber by Spitzer & Schwarzschild 1951) as the main mechanism for the scattering of stellar orbits.

This diffusion process was mainly intended to describe the orbits of stars in the galactic disk. A group of low metallicity, fast moving nearby stars had already been identified as a portion of the galactic halo (e.g. Eggen et al. 1962; Weistrop 1975). As kinematics in the solar neighborhood were more thoroughly investigated, it became apparent that there was a hotter kinematic component (Reid et al. 2002, e.g.,) identifiable with local members the observed "thick disk" of stars (Gilmore & Reid 1983). These three components can be generally distinguished by different sets of velocity means and dispersions (Leggett 1992, e.g.,).

As the study of kinematics progresses, both in models and observations, new mechanisms for stellar diffusion are begin suggested (e.g., migration between different Galactic radii Sellwood & Binney 2002; Loebman et al. 2011) and kinematics have become a sensitive probe of the ages of stars in the solar neighborhood (Aumer & Binney 2009).

1.3.2 M Dwarf Kinematics

While there were early measurements of the radial velocities and proper motions of M dwarfs, Gliese (1958) was the first to examine the kinematics of M dwarfs as a group, examining the sample for differences between active and inactive M dwarfs, finding that the active dwarfs had narrower velocity dispersions than the inactive dwarfs. Further studies of M dwarf kinematics revealed a "low velocity problem," or a detected excess of M dwarfs with small space motions compared to the Sun (Pesch 1972; Staller 1975). This excess of young M dwarfs was thought to be the first evidence of brown dwarfs, but it has since been refuted using larger, unbiased samples (Dawson 1981).

Over the next decade, the numbers of M dwarfs detectable with the current technology grew, enabling studies of different kinematic populations of M dwarfs (Upgren 1978) and continuing work on the activity and kinematics correlations that had previously been observed (Johnson 1983; Stauffer & Hartmann 1986). Before the turn of the century, large samples of M dwarfs began to be useful for understanding the structure of the galaxy; M dwarfs were used to derive the mean solar motion and constants of galactic motion (Cuddeford & Binney 1994; Ratnatunga & Upgren 1997).

In PMSUI, Reid et al. (1995) examined the kinematics of volume-complete sample of 514 stellar systems in the northern hemisphere selected from the Gliese & Jahreiß (1991) catalog. They again confirmed that active M dwarfs show younger kinematics than inactive dwarfs, and found evidence of a high velocity component, perhaps representative of a thick disk. PMSUII (Hawley et al. 1996) continues the kinematic analysis of active and inactive stars, first noting that active early-M dwarfs show younger kinematics than active late-M dwarfs. In the last installment of the PMSU series, Reid et al. (2002) uses the kinematics of M dwarfs to detect a hotter, older kinematic component mixed with the thin disk stars.

The study of M dwarf kinematics was then continued using the large samples of M dwarf detected in SDSS data. While SDSS does not assemble volume complete M dwarf samples, it is a source of tens of thousands of M dwarf spectra, selected without an obvious proper motion or magnitude bias. Bochanski et al. (2007a) used $\sim$7000 M dwarfs from a single line of sight to examine the kinematic structure of the thin and thick disk, providing a test for

galactic kinematic models. SDSS continues to be an excellent source of M dwarf kinematics, and future work should provide additional constraints on Galactic kinematics (e.g., Pineda 2012, in prep.).

1.3.3 L Dwarf Kinematics

Kinematics are especially valuable for L dwarfs as a tool to break the degeneracy between mass and luminosity, enabling the separation of stellar and substellar L dwarfs, so the velocities of L dwarfs have been well studied in the decade since the definition of the spectral class. As a population, L dwarfs could show a rough trend towards younger kinematics due to the inclusion of young brown dwarfs in the mostly stellar spectral class. This trend has been the target of many proper motion and radial velocity surveys of L dwarfs.

The first dynamical study of a handful of L dwarfs showed that they had a slightly larger tangential velocity dispersion than a similar sample of late-M dwarfs, indicating an older age (Gizis et al. 2000). As proper motions were measured for a larger sample of L dwarfs, it became clear that their distribution of tangential velocities generally agreed with those of the nearby galactic disk (Dahn et al. 2002; Vrba et al. 2004; Kendall et al. 2004), a result confirmed using the tangential velocities of a volume limited 20pc sample of L dwarfs (Schmidt et al. 2007; Faherty et al. 2009).

While tangential velocities can provide estimates of the kinematic properties of a sample, they include only two thirds of the information contained in full UVW velocities. Radial velocities are necessary to fully probe the dynamical properties of L dwarfs. The first UVW motions of a six of L dwarfs showed they had velocities consistent with young ages (Zapatero Osorio et al. 2007), but samples consisting of tens of L dwarfs showed faster, older kinematics (Blake et al. 2010; Seifahrt et al. 2010). Chapter 2 describes the conclusions drawn from the largest sample of L dwarfs with complete space motions; L dwarfs are dynamically indistinguishable from the stellar disk.

While the kinematics of the entire L dwarf population show they are similar to stars, the velocities of small numbers or single objects can distinguish younger and older L dwarfs. Velocities have been an essential ingredient in confirming substellar members of young moving

groups (Seifahrt et al. 2005; Bihain et al. 2006; Bannister & Jameson 2007) in conjunction with other youth-associated features. Dynamical arguments have also been useful for distinguishing a class of ultracool subdwarfs from normal metallicity dwarfs (Burgasser et al. 2003b; Burgasser 2004; Reiners & Basri 2006; Burgasser et al. 2009; Sivarani et al. 2009).

1.4 Resources from the Astrophysical Research Consortium

Another unifying theme of this dissertation is the use of the Astrophysical Research Consortium (ARC) telescopes located at Apache Point Observatory (APO). The instruments, observing time, and survey data that are made available through the University of Washington membership in ARC have have allowed the in-depth investigation of kinematics and activity of cool and ultracool dwarfs described in this dissertation.

1.4.1 TripleSpec on the ARC 3.5-m

TripleSpec is an infrared spectrograph that covers the wavelength range from 0.95μm to 2.45μm with a resolution R$\sim$3500. It received first light at APO on March 19, 2008, and the first test data related to this dissertation were taken on March 22, with regular observations commencing later in the year. TripleSpec has an advantage over many infrared spectrographs due to its combination of medium (rather than low) resolution and wavelength coverage over the entirety of the J, H, and K bands, achieved through cross-dispersion of the light into 5 different orders (Wilson et al. 2004). Due to the brightness of cool and ultracool dwarfs at near-infrared wavelengths, this instrument was used for observations of L dwarf radial velocities (Chapter 3) and an investigation of near infrared variability during flares (Chapter 6).

Triplespec data, however, present reduction challenges that become more problematic for faint targets. The individual spectral orders are both curved (meaning variations in the spatial direction) and tilted (indicating variations in wavelength across the order). The subtraction of telluric OH emission lines depend on these orders being fit precisely. Calibration of TripleSpec data are the focus of Chapter 3.

1.4.2 ARCSAT 0.5-m and NMSU 1-m

These small telescopes were both essential to simultaneous photometric and spectroscopic observations of flare stars that are discussed in Chapter 6. The Astrophysical Research Consortium Small Aperture Telescope (ARCSAT) 0.5-m was, until recently, the photometric calibrator telescope for the SDSS-I and -II (Tucker et al. 2006). As SDSS operations transitioned to the entirely spectroscopic components of SDSS-III, the ARCSAT 0.5-m became an excellent resource for simultaneous photometry with ARC 3.5-m observations.

This capacity was improved upon by the addition of Flare-cam as an instrument for the ARCSAT 0.5-m. As part of an NSF grant to determine flare rates in the Galaxy, E. Hilton and S. Hawley purchased a camera with excellent blue response and short read-out time, ideal for observing flares (Hilton 2011). Flare-cam was adapted for remote operation and is often used on ARCSAT in conjunction with the ARC 3.5-m.

The New Mexico State University (NMSU) 1-m telescope was adapted for robotic observing by J. Holtzman in 2005, and NMSU makes some telescope time available to the ARC community. While the camera is not as well suited to flare observing (longer readout and lower blue response), the size of the telescope and its ease of operation make it an ideal supplemental telescope for photometric monitoring.

1.4.3 Sloan Digital Sky Survey

The Sloan Digital Sky Survey (York et al. 2000) yielded a large area, deep photometric and spectroscopic survey of the northern galactic cap. The survey was designed with the main goal of examining the large scale structure of the universe through the identification and spectroscopic follow-up of a large number of distant galaxies and quasars. SDSS-I and -II, which were in operation from 2000 to 2008, include a photometric component in addition to a spectroscopic component. The photometric data were obtained by scanning large strips of the sky nearly simultaneously in *ugriz* filters. The completed photometric data cover 14,555 deg^2 (over a third of the celestial sphere) and contain nearly 500 million unique point sources (as of the eighth data release; Aihara et al. 2011). Photometric searches for ultracool dwarfs based on SDSS colors have yielded hundreds of late-M and L dwarfs (Fan

et al. 2000; Hawley et al. 2002; Chiu et al. 2006; Metchev et al. 2008; Sheppard & Cushing 2009; Zhang et al. 2009; Bowler et al. 2010).

The photometry was essential in selecting targets for spectroscopy using the multi-object SDSS spectrograph, covering the range 3800-9200Å at a resolution of R$\sim$2000 (Abazajian et al. 2003). Each spectroscopic observation consisted of 600 fibers, positioned using survey plates drilled for unique positions on the sky. The total survey conducted by SDSS-I and -II included over 1.6 million spectra within 9380 deg^2 (included in the seventh data release Abazajian et al. 2009). Serendipitously, M dwarfs within 1 kpc have similar colors and magnitudes to distant red galaxies, and L dwarfs often have similar colors to distant quasars, so spectra of $\sim$ 70,000 of these cool and ultracool dwarfs were obtained as part of SDSS observations through DR7 (Chapter 2; West et al. 2011).

Spectroscopic observations are continuing as part of SDSS-III in the form of the Baryon Oscillation Sky Survey (BOSS; Ross et al. 2011). An improved spectrograph provides slightly larger wavelength coverage (3600Å to 10000Å), better CCD response, and an increase to 1000 fibers per observation (Eisenstein et al. 2011). The main survey goal for BOSS is a more precise measure of large scale structure to detect traces of baryon acoustic oscillation in the early universe, but the survey also devotes $\sim$ 10% of its fibers to ancillary programs. I am the PI of an accepted ancillary program to obtain spectra of late-M and L dwarf candidates selected on a combination of SDSS and 2MASS colors.

Spectra from SDSS and BOSS (which are used in Chapters 2, 4, and 5) are ideal for selection and analysis of M and L dwarfs. The automatic targeting system and large numbers of spectra obtained allow a broader selection criteria than would be feasible for a single observer. Additionally, the data are processed in a consistent manner and include a precise telluric correction and wavelength calibration. These spectra are essential for classifying ultracool dwarfs and examining their kinematics and activity.

1.5 Description of the Thesis

The ages and magnetic activity of cool and ultracool dwarfs are two of the most interesting mysteries in the Solar neighborhood. Using kinematics to determine the ages of ultracool dwarfs will allow us to distinguish stars from brown dwarfs and understand other observable

differences between the two populations, while understanding the chromospheric structure of the quiescent and flaring dwarfs will paint a more complete picture of magnetic activity on these dwarfs.

Chapter 2 is chronologically the earliest work from the thesis. I examined a sample of ∼500 L dwarfs selected from SDSS DR7 photometry and spectroscopy. This chapter is notable in part because it marks the discovery of 200 new L dwarfs that increased the sample of known L dwarfs by 30%. Using the colors of the L dwarf sample, I uncovered a bias in the $J - K_S$ colors of the previously known sample of L dwarfs, often selected based on those colors in 2MASS. Using kinematics I also determined that $J - K_S$ color is correlated to L dwarf age, meaning that previously known L dwarf were subjected to an age bias as well.

Upon the completion of the SDSS L dwarf chapter, I identified two primary avenues of investigation that would use kinematics to investigate the ages of L dwarfs. The SDSS sample was heavily biased towards early-L dwarfs; they are more common than late-L dwarfs in magnitude-limited survey data due to their intrinsically brighter luminosities. As part of the Brown Dwarf Kinematics Project (BDKP; led by J. Faherty; Faherty et al. 2009, 2010, 2012), I began work to obtain radial velocities for a volume-limited sample of L dwarfs with TripleSpec on the ARC 3.5-m that was intended to supplement the existing proper motion survey (Faherty et al. 2009) and additional radial velocity surveys for M and T dwarfs in progress by the BDKP collaboration.

In Chapter 3 I describe the results of the four year BDKP observing campaign on TripleSpec. Soon after I began taking data, I realized that the TripleSpec reduction software (based on the Spextool code) did not produce results of sufficient quality for the measurement of radial velocities. Over the next three years, I tried many different reduction methods, the best of which is still not sufficient for the measurement of radial velocities. While the future may hold a new reduction method or additional observations to complete the project, it is not within the scope of this dissertation.

The other avenue for investigation was the assembly of a large sample of late-M and L dwarfs with kinematics using a combination of SDSS DR7 and BOSS data, supplemented by 2MASS and WISE. Chapter 4 contains the colors and kinematics of the large sample

of ultracool dwarfs from SDSS. The colors of these ultracool dwarfs span the gap between current work on WISE colors for earlier main sequence stars (Davenport 2012, in prep.) and the coolest brown dwarfs (Kirkpatrick et al. 2011).

The spectroscopic sample assembled from BOSS and DR7 has also proven useful to investigate activity in late-M and early-L dwarfs, which is presented in Chapter 5. Using a larger sample of high S/N spectra, I show that the fraction of active L dwarfs continues to rise as long as we can observe Hα emission against the declining continuum flux. I use the RH spectral synthesis code to investigate the area coverage and temperature structures needed to produce Hα emission on late-M and L dwarfs.

The difficulty of examining L dwarf activity at the relatively blue (for L dwarfs) wavelengths of the Hα emission lines was one of the inspirations for Chapter 6, which presents the first reported detection of infrared emission lines during an M dwarf flare. A strong emission line in the infrared would be easily detectable on late-M and L dwarfs due to their brightness at those wavelengths. However, my models show that a very hot chromosphere (T$\sim$30,000K) is required to produce the observed infrared emission, so it is not likely to be a useful wavelength range for quiescent activity studies of L dwarfs. The lack of any observed Paschen emission in the spectra examined in Chapter 3 indicates that those emission lines are either not present or very uncommon in L dwarf spectra.

Chapter 7 contains a summary of each chapter, conclusions based on the results of several chapters, and some questions either raised or left unanswered by the work presented in this dissertation.

Chapter 2

COLORS AND KINEMATICS OF L DWARFS FROM THE SLOAN DIGITAL SKY SURVEY

Kinematic indicators of age are typically based on the motions of large populations, but prior to the publication of this Chapter in 2010, there were very small numbers of L dwarfs with radial velocities (∼30). Using these small numbers of velocities, previous results had shown that the L dwarf population was younger than the stellar disk and thus likely composed mostly of brown dwarfs (Zapatero Osorio et al. 2007). But the entire population of L dwarfs as biased towards objects with redder 2MASS $J - K_S$ colors and these red L dwarfs had shown evidence of youth (Faherty et al. 2009; Cruz et al. 2009).

In order to examine ages for disk L dwarfs without a bias towards younger objects, we needed a large sample of dwarfs with complete space motions selected without reference to $J - K_S$ colors. The selection of this sample (in the SDSS photometric and spectroscopic databases) and its analysis is presented in this chapter.

This chapter was originally published in collaboration with Andrew A. West, Suzanne L. Hawley, and J. Sebastian Pineda in the May 2010 edition of the Astronomical Journal (Schmidt et al. 2010b, AJ, Vol. 139, pp. 1808-1821;

2.1 Introduction

The Sloan Digital Sky Survey (York et al. 2000, SDSS) is a valuable tool for discovering nearby L dwarfs. Initial work typically employed optical and near-infrared selection criteria combined with follow-up spectroscopy of candidate objects on other telescopes (Fan et al. 2000; Schneider et al. 2002; Geballe et al. 2002). Hawley et al. (2002, hereafter H02) was the first study that included SDSS spectroscopy for a large sample. West et al. (2004, 2008) included L dwarfs in their investigations of magnetic activity, but West et al. (2004) used a strict quality cut on the spectra and West et al. (2008) restricted their analysis to

L0 and earlier dwarfs. Other work relied on the SDSS photometric database for target selection, but used infrared spectroscopy from other facilities to confirm candidate dwarfs (Knapp et al. 2004; Chiu et al. 2006). Recently, the search for additional SDSS dwarfs has focused on cross-matches of SDSS and 2MASS for candidate selection, either taking advantage of additional colors or using proper motion as a selection tool (Metchev et al. 2008; Scholz et al. 2009; Sheppard & Cushing 2009; Zhang et al. 2009). Since H02, there has been no comprehensive search of the SDSS spectroscopic database to select and confirm L dwarfs. During that time, the SDSS spectroscopic database has grown by roughly an order of magnitude, from ∼180,000 sources (DR1; Abazajian et al. 2003) to ∼1.6 million sources (DR7; Abazajian et al. 2009).

The reliance of many of the past searches on color and proper motion selection criteria may have introduced significant biases into the sample of presently known L dwarfs. The recent discovery of a new L dwarf within 10 pc (SDSS 1416+13; Schmidt et al. 2010b; Bowler et al. 2010) points to a need to use a different set of criteria in order to investigate a representative sample of L dwarfs that spans the entire range of colors and kinematic properties. Selecting objects based on their SDSS spectra allows us to relax the color criteria in order to mitigate the possible biases in the L dwarf sample.

The use of SDSS spectra also allows us to measure radial velocities for a large number of L dwarfs. Previous work has found that the L dwarf population is kinematically younger than most thin disk stars but was limited either by small numbers (Zapatero Osorio et al. 2007) or by a lack of radial velocities, restricting kinematic analysis to two dimensions (Schmidt et al. 2007; Faherty et al. 2009). A larger sample with both proper motions and radial velocities is needed to confirm these results and to allow an investigation into the ages of L dwarfs.

While many of the L dwarfs in the SDSS spectroscopic database have relatively low signal to noise ratios (SNR), most have sufficient flux to assign a spectral type and determine the radial velocity. We combine these data with photometric and proper motion information from SDSS and 2MASS to investigate the colors and kinematics of SDSS L dwarfs. In Section 2.2, we introduce our spectroscopic sample, including a brief discussion of Hα emission, and describe our photometric sample which includes both new and known

L and T dwarfs. We present colors and derive photometric distance relations in Section 2.3. Section 2.4 describes our kinematic measurements and the resulting velocity distributions.

2.2 Sample

2.2.1 Spectroscopic Sample

The SDSS (York et al. 2000; Stoughton et al. 2002; Pier et al. 2003; Ivezić et al. 2004) is a multicolor (*ugriz* Fukugita et al. 1996; Gunn et al. 1998; Hogg et al. 2001; Smith et al. 2002; Tucker et al. 2006) photometric and spectroscopic survey centered on the northern Galactic cap. The most recent data release (Abazajian et al. 2009, DR7) comprises 11000 deg^2 of imaging, yielding photometry of ∼357 million unique objects. SDSS also has twin fiber-fed spectrographs which simultaneously obtain 640 medium-resolution (R ∼1800), flux-calibrated, optical (3800-9200Å) spectra per 3° plate (Abazajian et al. 2004). While the SDSS primarily targets extragalactic objects, of the ∼1.6 million spectra in DR7, ∼84,000 are from M or later type stars (Abazajian et al. 2009).

Our initial sample of 13,874 spectra was selected from the SDSS photometric and spectroscopic databases by requiring $i-z > 1.4$. This large number of spectra and loose selection criteria were used to produce the most complete sample possible. While previous work has shown that L0 dwarfs have a median color of $i - z = 1.84$ (West et al. 2008), we used a bluer color to ensure that any spread of L0 colors was included while mid-M dwarfs were excluded. We did not restrict the $r-i$ color because the r-band photometry of these dwarfs is faint and often unreliable. We then used the Hammer spectral typing facility (Covey et al. 2007) to analyze each spectrum and assign a spectral type. The Hammer first calculates an initial spectral type based on several molecular and atomic indices, then allows direct comparison of the spectrum to standard templates. We reviewed each spectrum by eye to confirm spectral types and to exclude objects with insufficient SNR for classification, allowing us to construct the most complete sample possible from the SDSS spectroscopic database.

Of the initial 13,874 objects, we were unable to classify ∼9000 objects due to low SNR, ∼4000 were late-M dwarfs, and 484 were L dwarfs. Our selection criteria did not yield any

T dwarfs. This sample of 484 L dwarfs represents an order of magnitude increase from H02, which uncovered 42 L dwarfs from SDSS DR1 spectra. We refer to the 484 L dwarfs selected from SDSS spectra as the spectroscopic sample. Their spectral types (typically good to ±1 subtype) are given in Table 2.1 and their spectral type distribution is shown in the top panel of Figure 2.1. The spectroscopic sample is heavily skewed towards early-L dwarfs (compared to the L dwarf luminosity function; Cruz et al. 2007) because they are both more numerous and intrinsically brighter than later-L dwarfs. Of the 484 L dwarfs in our spectroscopic sample, 210 are newly discovered, which represents a ∼25% increase in the number of known L dwarfs. Of the previously known dwarfs, agreement with previous spectral types is generally good (within 0-2 types) but ∼60 objects that we visually classified as L0 dwarfs were classified by West et al. (2008) as M9 dwarfs. Our visual inspection is more certain than the automated algorithm used in West et al. (2008), but was not practical given the size of the West et al. (2008) sample. This discrepancy is within the published uncertainties of the Hammer automatic algorithm (±1 spectral type; Covey et al. 2007)

There are five known L dwarfs with SDSS spectra and that were included in our initial 13,874 objects but were not identified as L dwarfs during spectral typing. Three of them were typed as M9 dwarfs instead of L0 dwarfs so they were excluded from this analysis by our spectral type cut. Another two had SDSS spectra with very low SNR and we were not able to assign a spectral type. These low SNR objects are included in the photometric sample (see Section 2.2.3), but not the spectroscopic sample.

2.2.2 Activity

The presence and strength of Hα emission is used as an indicator of chromospheric activity in low mass stars and brown dwarfs (e.g., Gizis et al. 2000; West et al. 2004; Schmidt et al. 2007). The low SNR of our spectra in the region surrounding Hα prevented us from a detailed study of activity in the SDSS L dwarf sample. Out of 484 L dwarfs in the spectroscopic sample, only 32 have SNR > 3 in the Hα region. In Table 2.2, we list measured Hα equivalent widths (EW) and activity classifications for those dwarfs.

Hα EW were measured using trapezoidal integration to calculate the flux in both the

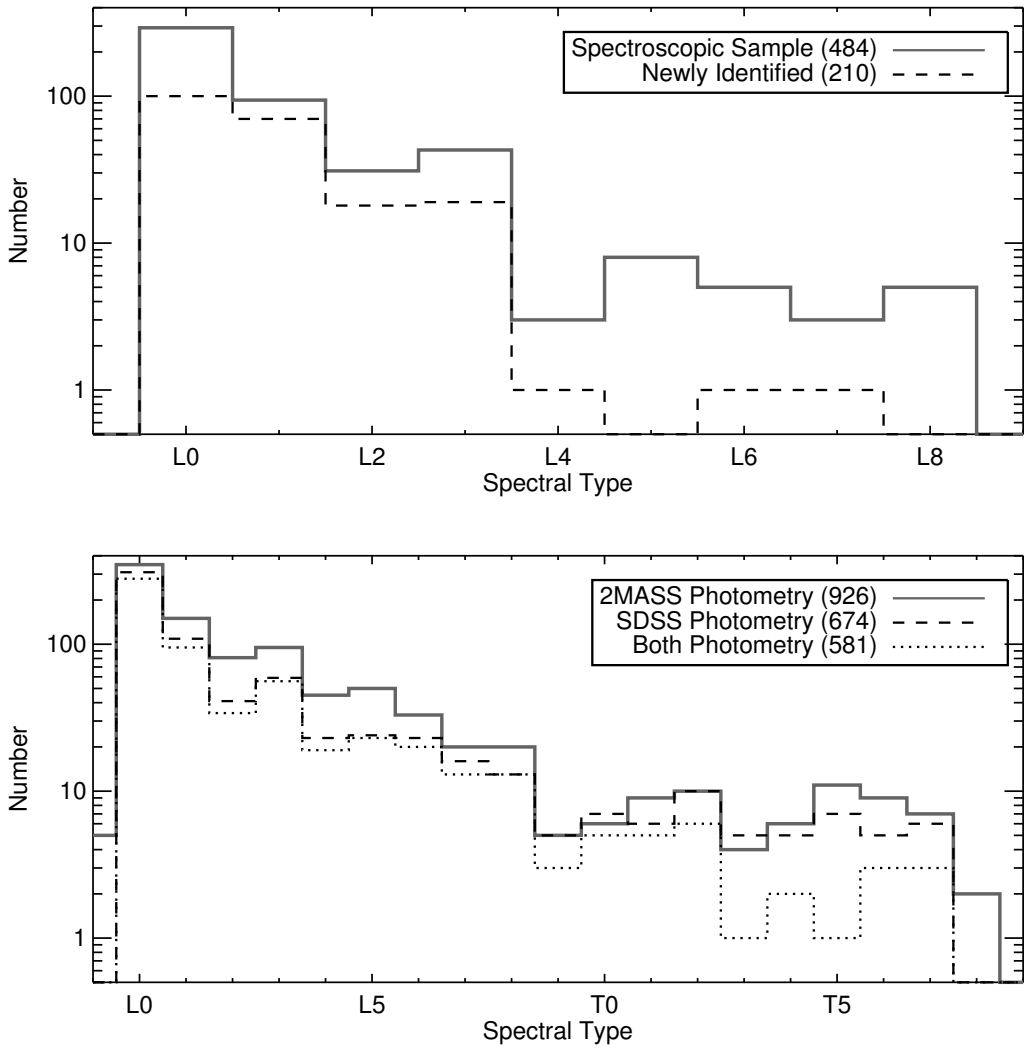

Figure 2.1 Top: number of objects per spectral type for the spectroscopic sample. The entire sample (grey solid line) and the new dwarfs (black dashed line) are shown. Bottom: number of objects per spectral type bin for the photometric sample. The dwarfs with 2MASS photometry (grey solid line), SDSS photometry (black dashed line), and with both SDSS and 2MASS photometry (black dotted line) are shown.

line and continuum regions. Following West et al. (2004), stars that we classified as active must have a measured Hα EW greater than 1Å and meet three quality control criteria: (1) a measured EW greater than its uncertainty; (2) an Hα EW greater than the EW of the comparison regions; and (3) a measured height of the line three times larger than the noise at line center. Objects with Hα EW greater than 1Å but only meeting some of the quality control criteria were classified as maybe active. Of the 32 L dwarfs, 23 were classified as active, 6 as maybe active, and 3 as inactive. This fraction of active objects ($\sim$70%) is consistent with results for early-L dwarfs (West et al. 2004; Schmidt et al. 2007) and reflects a decline from the nearly 100% active fraction observed in nearby late-M dwarfs (West et al. 2008).

None of our L dwarfs have notably large Hα EW, but we report Hα detections for some objects previously observed to have emission (noted in Table 2.2). 2MASS J0746425+200032 has been observed in a multi-wavelength campaign by Berger et al. (2009) to have periodically variable Hα emission with strength of 2.4-3.3Å. Our measurement of 2.4$\pm$0.2Å is consistent with the previous detections. LHS 2924, a well known active M9 dwarf (e. g., Fleming et al. 1993; Reiners et al. 2007), was classified as an L0 dwarf during the spectral typing of our sample, which is within our $\pm$1 subtype uncertainty. The Hα EW of 4.5$\pm$0.3Å measured from its SDSS spectrum is consistent with previous quiescent values.

2.2.3 Photometric Sample

SDSS iz and 2MASS JHK_S photometry for the spectroscopic sample is given in Table 2.1. Every object in the sample had SDSS photometry, but we excluded photometry for nine objects with SATURATED, BAD_COUNTS_ERROR, INTERP_CENTER, PSF_FLUX_INTERP, or NO_DEBLEND flags set in the i or z band (Stoughton et al. 2002). Photometry from 2MASS was obtained via a cross-match to the 2MASS point source catalog with a search radius of 5″; no objects in the spectroscopic sample had more than one match in the 2MASS database. A total of 471 L dwarfs matched 2MASS sources, but we excluded 2MASS photometry for 35 objects with ph_qual or cc_flg flags set in the J, H, or K_S bands (Cutri et al. 2003).

To perform a more complete analysis of L dwarf colors and examine color trends into the T dwarf regime, we augmented the spectroscopic sample with known L and T dwarfs from the Dwarf Archives[1] as of October 2009 to construct the photometric sample. For these additional objects, we used previously assigned spectral types (we preferred optical spectral types and rounded half types to earlier whole types) and excluded subdwarfs. Using the same flag cuts as for the spectroscopic sample, we obtained iz magnitudes from SDSS for 148 L and 51 T dwarfs. 2MASS photometry was available for 396 L and 63 T dwarfs, with totals of 48 L and 23 T dwarfs having both SDSS and 2MASS photometry. In four cases ($\sim$1%), the cross-match between Dwarf Archives and 2MASS returned more than one match. For those objects, we selected the closest source to the input position. We found no obvious color outliers in the sample that would signal a mismatch between objects. The spectral type distribution of photometric sample, including those in our spectroscopic sample, is shown in the bottom panel of Figure 2.1.

2.3 Colors

2.3.1 Color-Spectral Type Relations

In order to examine the colors of the L and T dwarfs in our photometric sample, we made additional cuts for good quality photometry (photometric uncertainties less than 0.08, 0.06, 0.12, 0.12, and 0.16 for i, z, J, H, and K_S respectively) in each band. These uncertainty limits are similar to limiting magnitudes – the majority of the photometry that is rejected is at or past the limiting magnitudes of SDSS and 2MASS. This cut could preferentially reject objects that are redder in $i - z$ color, because the average SDSS magnitude limits in the i- and z- band (21.3 and 20.5 respectively) may exclude dwarfs with redder $i - z$ colors. Comprehensive follow up of the redder sources is needed to confirm median colors, especially for the later-L dwarfs.

Examining the relationship of broadband colors to spectral type is useful both to provide insight into mean L dwarf properties and to assist future searches for L dwarfs. Table 2.3 lists median colors as a function of spectral type for a variety of SDSS and 2MASS colors.

[1]Available at `http://dwarfarchives.org`.

For each spectral type, we give the number of objects in the photometric sample with good photometry that contribute to each color, the median color with associated uncertainty, and the standard deviation (σ). The uncertainties in the median were calculated using the standard deviation divided by the the square root of the total number of stars in the sample. While the uncertainty reflects how well we know the median color of each spectral type bin, the standard deviation reflects the intrinsic scatter in each color. Figure 2.2 shows color as a function of spectral type for the same SDSS and 2MASS colors. The median colors with standard deviation are shown for types L0-L8.

As has been noted by previous studies (H02; Knapp et al. 2004; Chiu et al. 2006), the $i-z$ color gets redder at increasing spectral type – rising slowly from L0-L3 and then rapidly with later spectral type through mid-T dwarfs. This is because the i-band is centered near the K I doublet (7665, 7699Å), which broadens with decreasing temperature and suppresses proportionally more flux in the i-band than the z-band. The $i-J$ color also becomes redder with later spectral type, but changes more linearly than $i-z$ (H02; Sheppard & Cushing 2009). Both $i-z$ and $i-J$ are relatively good predictors of spectral type.

The $z-J$ color becomes redder from early- to mid-L, stays constant from mid- to late-L types, and reddens slightly from late-L to late-T. This is consistent with both the SDSS/MKO $z-J$ (Knapp et al. 2004; Chiu et al. 2006) colors and SDSS/2MASS $z-J$ colors than found in H02. Because of this behavior, $z-J$ color is a less reliable predictor of spectral type than $i-z$ and $i-J$ throughout the L spectral sequence.

Both the $z-K_S$ and $J-K_S$ color redden until mid-L types, then turn over and become more blue into the late-T (H02; Knapp et al. 2004; Chiu et al. 2006; Faherty et al. 2009). This behavior is likely due to the decrease in K_S-band flux due to increasingly strong absorption in water and methane bands (Marley et al. 2002; Knapp et al. 2004).

2.3.2 Red Bias in $J-K_S$ in Previous Samples

The median colors for L0 dwarfs in the spectroscopic sample are consistent with those given by West et al. (2008), and the SDSS/2MASS colors for the rest of the dwarfs are similar to those in previous work (H02; Knapp et al. 2004; Chiu et al. 2006), but the $J-K_S$ colors

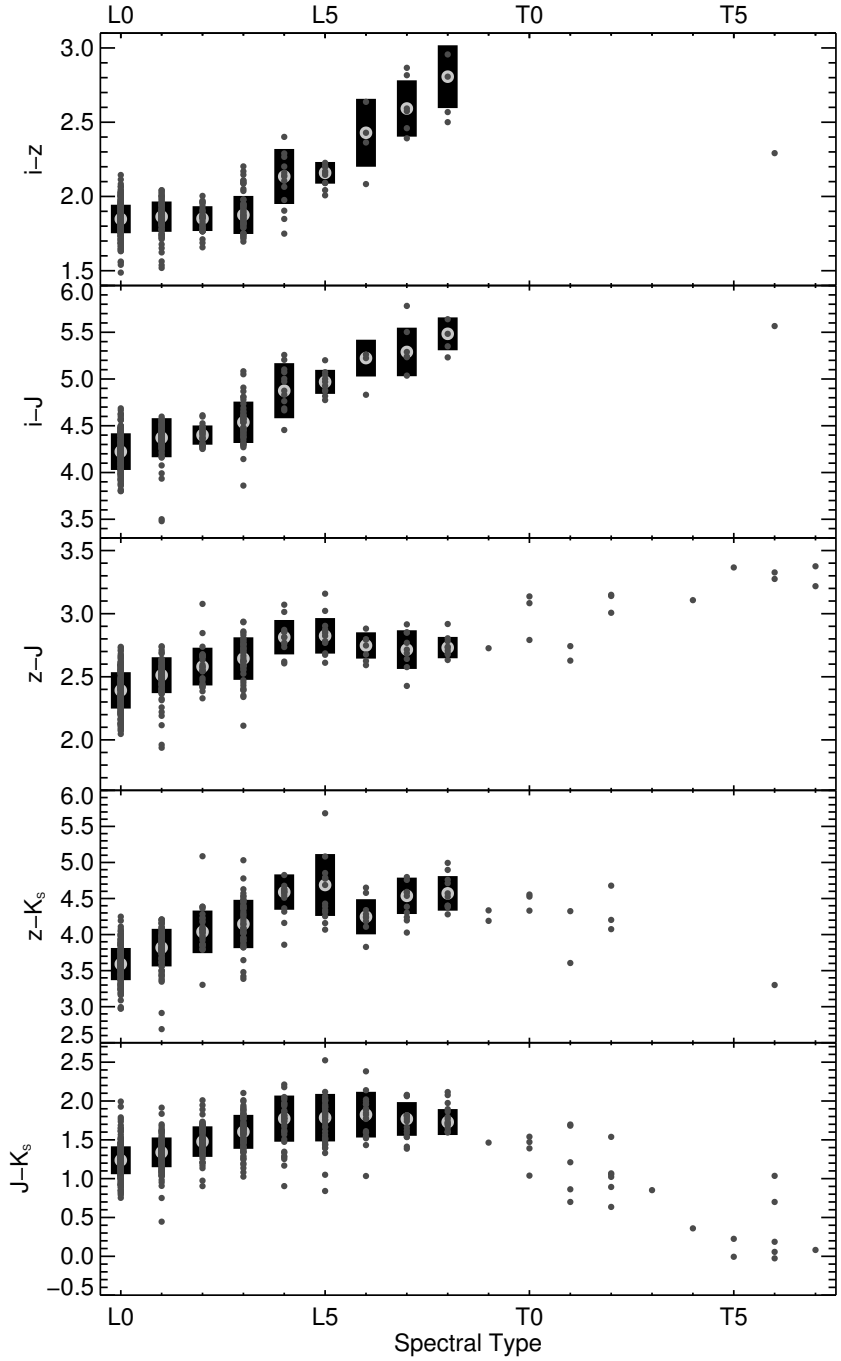

Figure 2.2 Color as a function of spectral type for five different colors. Individual dwarfs are shown (small dark grey circles) for L0-T7 dwarfs, as well as median colors (large light grey circles) and one sigma dispersions (black bars) for L0-L8 dwarfs.

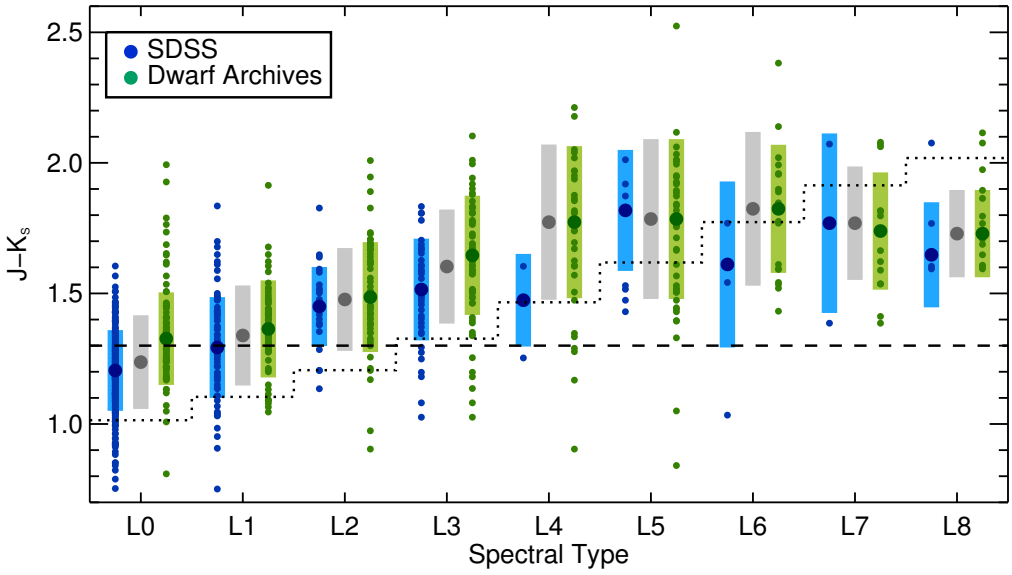

Figure 2.3]

$J - K_S$ color as a function of spectral type for the SDSS dwarfs (blue), all dwarfs (grey) and dwarfs from Dwarf Archives as of October 2009 (green). The median color per spectral type for each sample is shown (large circles) as well as the standard deviation of the colors in that spectral type (shaded bars) and the individual objects (small circles). The $J{-}K_S$ color selection criteria of Kirkpatrick et al. (1999, dashed line) and Cruz et al. (2003, dotted line) are shown; the latter is a combination of a color-magnitude cut and the Cruz et al. (2003) spectral type vs. M_J relation for dwarfs at 20 pc.

calculated from the photometric sample are consistently bluer than those found in previous work (Kirkpatrick et al. 2000; Faherty et al. 2009). Figure 2.3 shows the $J - K_S$ colors of all L dwarfs with 2MASS photometry compared to both the L dwarfs in the spectroscopic sample and the L dwarfs in Dwarf Archives; the data are given in Table 2.4. Early-L dwarfs in the SDSS spectroscopic sample are clearly bluer than the Dwarf Archives objects by $\sim$0.1 magnitude.

While the spectroscopic sample is likely to have no bias in $J - K_S$ color, the objects from Dwarf Archives were selected from a variety of criteria, including large numbers found

using 2MASS color criteria. Many known L dwarfs are the result of surveys that made cuts in $J-K_S$ to separate L dwarfs from the ubiquitous M dwarfs (Kirkpatrick et al. 1999, 2000; Cruz et al. 2003, 2007; Reid et al. 2008). The color selection criteria from Kirkpatrick et al. (1999) and Cruz et al. (2003) are shown in Figure 2.3. The Kirkpatrick et al. (1999) cut at $J-K_S > 1.3$ excludes many early-L dwarfs, and some objects at mid-L types. The Cruz et al. (2003) cut, though slightly bluer than the median color, still excludes some of the bluest objects at each type.

To test whether previously known L dwarfs are drawn from a different distribution than the SDSS spectroscopic sample, we performed a Kolmogorov-Smirnov test (KS test) on the color distribution of the two samples. In order to examine all of the L dwarfs as a single population, we used a color difference that is independent of spectral type, defined as $\delta_{J-K_S} = ((J-K_S) - (J-K_S)_{med})/\sigma_{J-K_S}$. We used the median $J-K_S$ and $\sigma_{(J-K_S)}$ for all L dwarfs given in Table 2.3. The KS test shows that the two samples are *not* drawn from the same distribution at a high confidence level (P<0.01).

This selection bias can lead to systematic problems when $J-K_S$ color criteria are used to assemble large statistical samples of L dwarfs. There is a strong potential to miss nearby blue objects (Section 2.3.5; Schmidt et al. 2010b; Bowler et al. 2010) and to bias all known L dwarfs towards redder colors. With mounting evidence that age and $J-K_S$ color are linked (Section 2.4.6; Folkes et al. 2007; Burgasser et al. 2008; Faherty et al. 2009), previous samples are likely biased towards younger dwarfs. Past kinematic studies have noted that the L dwarf population seems unusually young (e.g., Zapatero Osorio et al. 2007) – this could be in part due to a color selection bias.

2.3.3 Color-color relations

Figure 2.4 shows six color-color plots for our combined photometric sample. To examine the different color spaces for each spectral type, we distinguish between early-L, late-L, and T dwarfs.

The first four panels show updated color-color plots similar to those from the SDSS Early Data Release (H02). The $i-z$, $z-J$ and $i-J$, $z-J$ plots show the same general

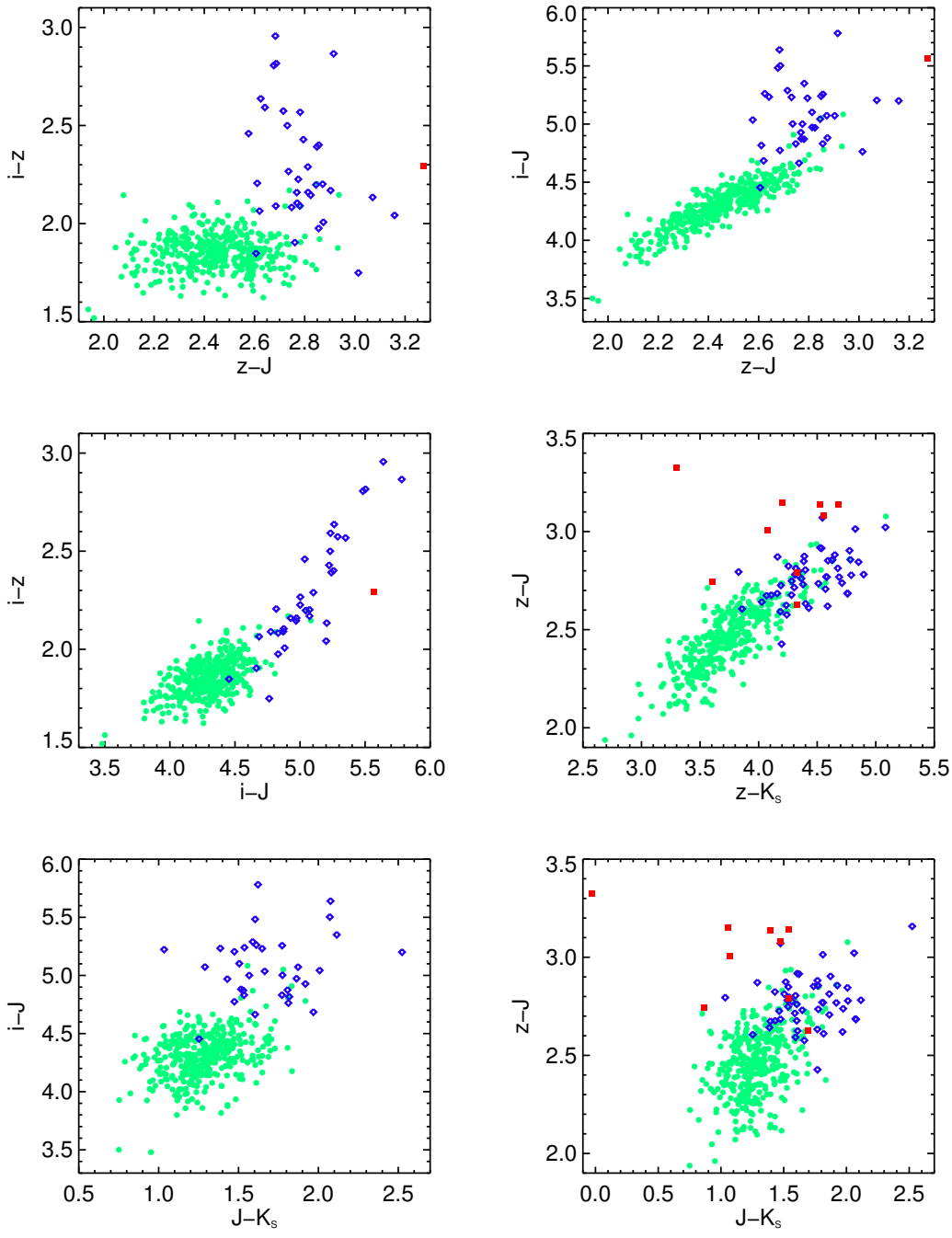

Figure 2.4 Color color plots for six different color combinations. Early-L dwarfs (L0-L3; green circles), mid- to late- L dwarfs (L4-L8; blue diamonds) and T dwarfs (red squares) are distinguished.

shape as in H02. The $i-z$ and $i-J$ colors are relatively linear with spectral type. The $z-J$, $i-J$ plot is useful for classifying L0 to L3 dwarfs, but the $z-J$ color saturates for mid- to late- L dwarfs. The $i-z$, $i-J$ plot shows a remarkably straight line in color-color space for $i-J>4.8$ and is most useful for classifying L4 and later types. In $z-J$, $z-K_S$ the early-L dwarfs are spread out, while the late-L and T dwarfs are clumped. A turnover in $z-K_S$ color is also apparent, similar to the one seen in H02.

The last two panels show $i-J$ and $z-J$ as a function of $J-K_S$. Both $i-J$ and $z-J$ colors separate the early-L and T dwarfs into distinct groups despite their similar $J-K_S$ colors, and can be used to roughly classify objects as early-L, late-L or T dwarfs. This shows the value of including a bluer photometric band together with 2MASS colors when analyzing L and T dwarf photometry.

2.3.4 Photometric Distance Estimates

While spectral type is a relatively reliable predictor of absolute magnitude for L dwarfs (e.g., Vrba et al. 2004), spectrophotometric absolute magnitudes and distance estimates suffer from the uncertainty and coarse binning of spectral types, which are often good only to ± 1 subtype. When only 2MASS colors are available, spectral type relations are better because of the large spread in infrared colors with both absolute magnitude and spectral type. However, the $i-z$ and $i-J$ colors show much smaller scatter than the spectral type relations.

Figure 2.5 illustrates M_i as a function of $i-z$ and $i-J$ color based on photometry and parallax measurements for the 13 late-M and L dwarfs listed in Table 2.5. The reduced χ^2 value for each of the relations was minimized with third order polynomial fits, as follows:

$$(1.7 < i-z < 3.2) : M_i = -23.27 + 38.41(i-z) - 11.11(i-z)^2 + 1.064(i-z)^3 \quad (2.1)$$

$$(3.9 < i-J < 5.8) : M_i = 66.88 - 41.73(i-J) + 10.26(i-J)^2 - 0.7645(i-J)^3 \quad (2.2)$$

The relations have RMS scatters of 0.41 and 0.33 magnitudes in $i-z$ and $i-J$ respectively.

Distances computed from the derived absolute magnitudes are given in Table 2.6. We compare distance estimates from both of these relations to those from the Cruz et al. (2003)

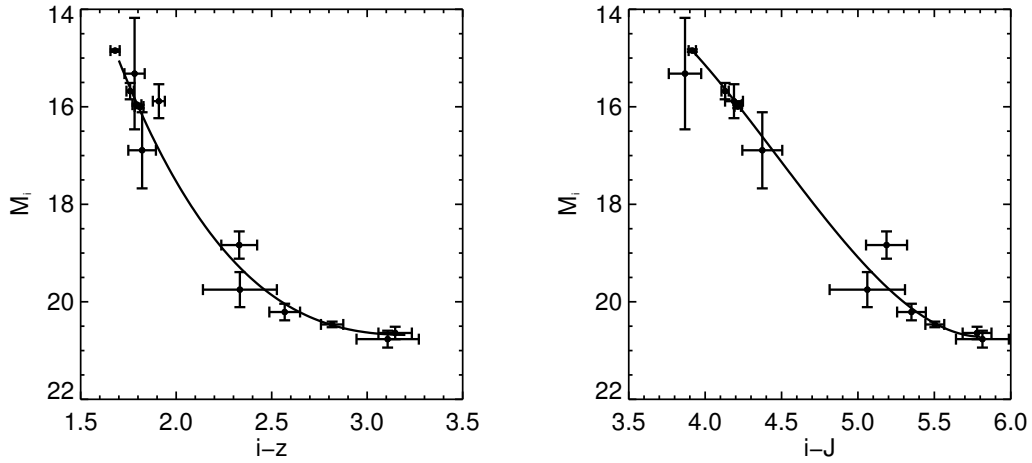

Figure 2.5 Absolute i magnitude as a function of $i - z$ (left) and $i - J$ (right) color, for M8-L8 dwarfs with SDSS photometry (given in Table 2.5). Third-order polynomial fits are shown (equations given in Section 2.3.4).

spectral type vs. M_J relation in Figure 2.6. There is a wide scatter about the one-to-one line, analogous to the scatter between $i - z$ or $i - J$ and spectral type, but 95% of the distance estimates agree within their uncertainties. Distances above 100 pc calculated from the $i - J$ vs. M_i relation seem to show a systematic offset from distances calculated from the spectral type vs. M_J relation. The dwarfs with these disparate distances estimates all have $i - J$ colors on the bluer end of the relation ($3.9 < i - J < 4.2$). The $i - J$ vs. M_i relation is steep in that color range, and while those $i - J$ colors are within the spread for L0/L1 dwarfs, the relation is also based on colors from M8/M9 dwarfs. This could be the reason for the disagreement between the distance estimates.

For the remainder of the paper, we use the $i - z$ distance estimates due to the better agreement with previous distances. For L dwarfs that fall outside the $i-z$ color limits given in Equation 1, we use the $i - J$ relation. For dwarfs outside both color limits but with L spectral types, we use the spectral type vs. M_J relation from Cruz et al. (2003).

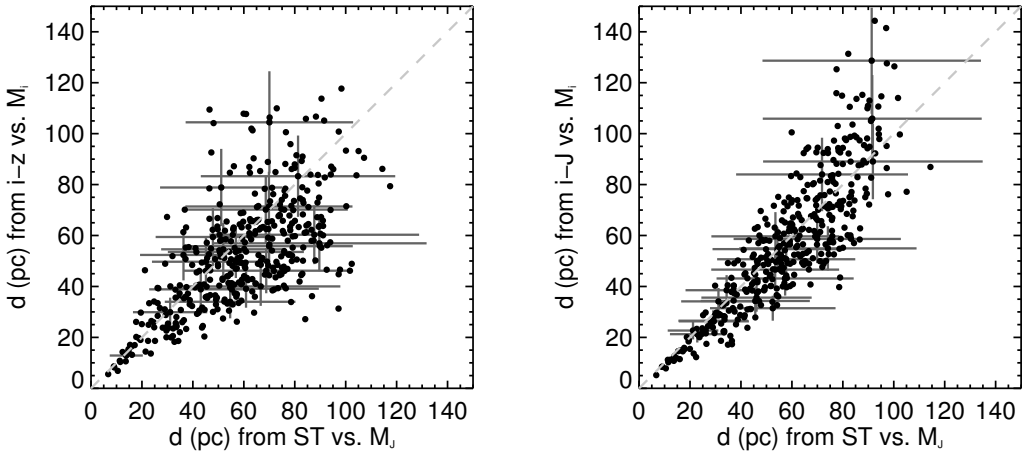

Figure 2.6 Comparison of spectrophotometric distance estimates using the Cruz et al. (2003) ST vs. M_J relation with distance estimates from our $i-z$ vs. M_i (left panel) and $i-J$ vs. M_i (right panel) relations. Uncertainties for a representative number ($\sim$5%) of the dwarfs (grey bars) and a one-to-one correspondence line are shown (grey dashed).

2.3.5 New L Dwarfs Within 30 pc

Previous searches for L dwarfs have focused on a census of nearby L dwarfs, probing distances of 20-30 pc from the Sun. Due to the comprehensive work done at these distances, the majority of newly discovered L dwarfs presented in this paper are early-L dwarfs at distances greater than 30 pc. There are, however, a few nearby dwarfs that were missed by previous selection criteria. Table 2.7 shows data for 5 L dwarfs which are placed within 30 pc of the Sun by the mean of all three distance estimates, weighted by the distance uncertainties.

Of the five L dwarfs, three are unusually blue for their spectral types, which is unsurprising given the bias of previous searches towards dwarfs with redder $J-K_S$ colors (Section 2.3.2). The nearest and bluest of these is SDSS J141624.09+134826.7 (hereafter SDSS1416+13), an exceptionally blue L dwarf within 10 pc of the Sun. Additional spectroscopic observations (Schmidt et al. 2010b) show that it is an L5 dwarf with an updated distance estimate of 8.9$\pm$2.1 pc.

The discovery of these new objects at $d < 30$ pc indicates that there is potential to

discover additional nearby L dwarfs. While SDSS is an excellent tool for uncovering dwarfs with peculiar 2MASS colors, the SDSS footprint does not cover the entire sky, and as yet there has been no comprehensive spectroscopic follow-up of all objects with L dwarf colors.

2.4 Kinematics

2.4.1 Proper Motions

Our combined photometric sample contains 586 objects that have both SDSS and 2MASS photometry. These two surveys are astrometrically calibrated and span a range of dates (2MASS 1997-2001; SDSS 2000-2008), which allowed us to calculate reliable proper motions for the majority of objects in our sample, using the difference between the SDSS and 2MASS positions. Objects were cross-matched using a search of the SDSS coordinates in the 2MASS database with a radius of $5''$. None of the objects with SDSS coordinates had multiple matches in the 2MASS database, and we found no mismatches by looking at outliers in color space. The number of mismatches between the two databases is likely low.

Proper motions were calculated for all objects with two sets of coordinates, but we only include measurements that had total proper motion uncertainties ($\sigma_{\mu}^{1/2} = (\sigma_{RA}^2 + \sigma_{dec}^2)^{1/2}$) of less than $\sigma_{\mu} < 0.08"/yr$ or $\sigma_{tot}/\mu_{tot} < 0.25$. The inclusion of dwarfs with $\sigma_{tot}/\mu_{tot} < 0.25$ allows for objects with relatively large proper motions to be included if their uncertainties are small compared to their proper motions. This should not bias the sample heavily towards faster moving objects because it only includes 14 dwarfs that would have been otherwise excluded. Table 2.6 gives proper motions for the 406 dwarfs (312 in the spectroscopic sample) that have reliable calculated proper motions. The distributions of μ_{α}, μ_{dec}, σ_{μ}, and time between observations are shown in Figure 2.7.

Of the 406 objects with measured proper motions, 135 have previous measurements (Faherty et al. 2009, and references therein). The bottom two panels of Figure 2.7 show the comparison of our measured proper motions to those from literature. There are only 9 objects that disagree by more than $0.08''$/yr in total proper motion. We were unable to calculate SDSS/2MASS proper motions for 35 objects in the spectroscopic sample that have measurements available from the literature. We include these literature measurements

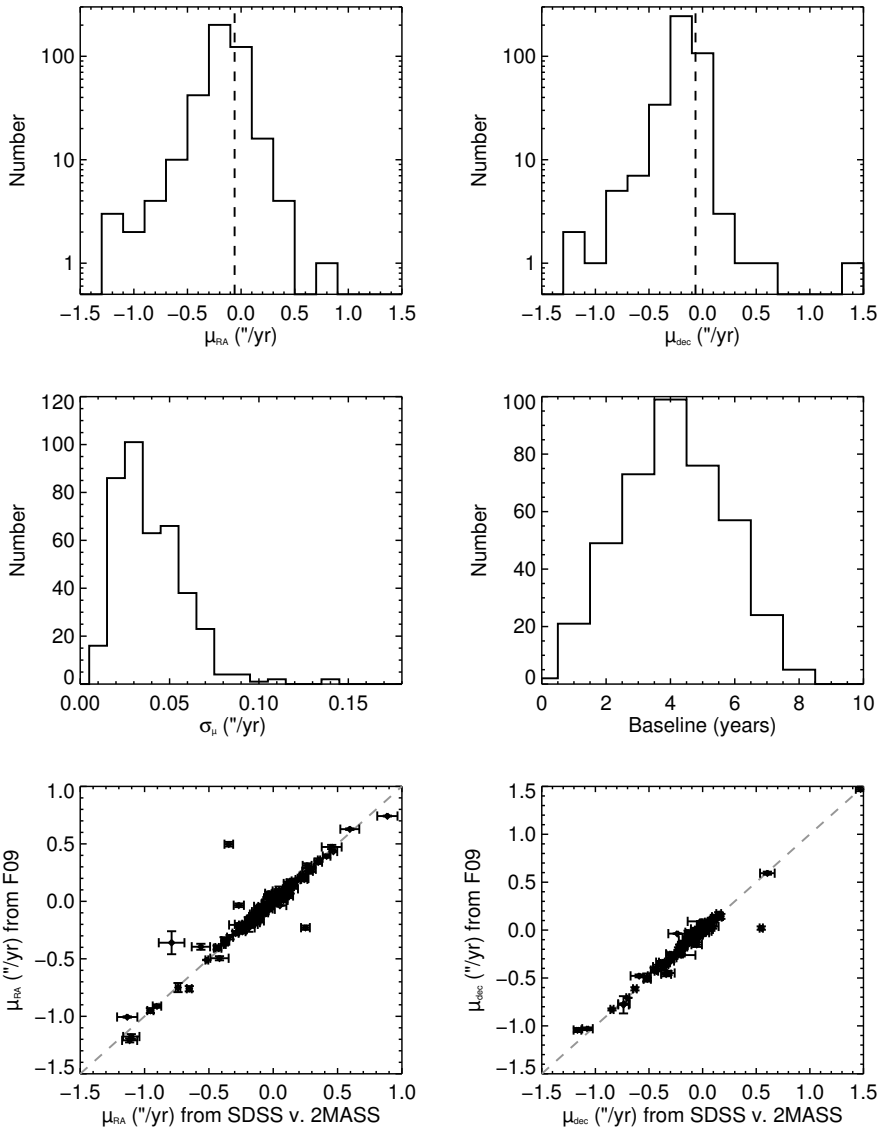

Figure 2.7]

Top panels: Histrograms showing the distribution of measured proper motions in RA (top left) and dec (top right). In both panels, the mean proper motion is shown (dashed line). Middle left panel: The distribution of total proper motion uncertainties. Note that cuts have been made of $\sigma_\mu < 0.8$ "/yr or $\sigma_\mu/\mu_{tot} < 0.25$. Middle right panel: The distribution of baselines used to measure proper motions. Bottom two panels: Comparison of our proper motions in RA (left) and dec (right) to measurements from Faherty et al. (2009) and references therein. A one-to-one correspondence line is shown.

(which are noted in Table 2.6) in order to calculate three dimensional velocities for these objects.

2.4.2 Tangential Velocities

While three dimensional velocities provide more accurate kinematic results, we could only measure reliable radial velocities for 413 dwarfs in the spectroscopic sample (see Section 2.4.3) and have no radial velocities for our photometric sample. By combining proper motions and distances from this paper and from the literature, we examined the tangential velocity distribution of 748 L dwarfs, shown in the left panel of Figure 2.8. The entire sample of velocities has a median of $V_{tan} = 28$ km s^{-1} and a dispersion of $\sigma_{tan} = 25$ km s^{-1}. These values are consistent with previous results for L dwarfs (Faherty et al. 2009; Schmidt et al. 2007).

The tangential velocity distributions for 347 L dwarfs in the spectroscopic sample and for 306 dwarfs with complete UVW kinematics are also shown in the left panel of Figure 2.8. They have dispersions of $\sigma_{tan} = 28$ km s^{-1} and $\sigma_{tan} = 27$ km s^{-1} respectively, which are consistent both with previous work and with the larger sample of L dwarfs discussed above.

2.4.3 Radial Velocities

Ten L dwarfs with spectra in the SDSS database also have radial velocities measured with high resolution spectroscopy (Mohanty & Basri 2003; Bailer-Jones 2004; Blake et al. 2007). We used these SDSS spectra as radial velocity templates. The template spectra span the entire L-dwarf spectral sequence with gaps no larger than one spectral type. We cross-correlated each spectrum from the spectroscopic sample with every template within one spectral type (in some cases there was only one such template). The minimum of the cross-correlation function was fit to determine the radial velocity. Each cross-correlation function was examined by eye to determine its quality. Cross-correlations that did not yield acceptable minima were skipped. All others were ranked according to the depth and symmetry of their form. Symmetric cross-correlation functions with troughs lower than 50% of the wings were assigned double the weight when computing the mean radial velocity

for each spectrum. Weighted standard deviations were also determined for each spectrum with more than one cross-correlation template within one spectral type. Measurements with uncertainties greater than 20 km s^{-1} were not used. Dwarfs cross-correlated with only one spectrum had no formal uncertainties, so we conservatively assign them uncertainties of 20 km s^{-1}.

Radial velocities are given in Table 2.6 and the distribution of radial velocities is shown in the right panel of Figure 2.8. The radial velocity distribution has a mean of $< V_{\rm rad} >= -4.7$ km s^{-1} and a dispersion of $< \sigma_{\rm rad} >= 34.3$ km s^{-1}. The deviation of the mean of the radial velocity distribution from $< V_{\rm rad} >= 0$ km s^{-1} is likely the effect of Solar motion, and not due to a systematic error in our measurements. Most of the sight lines to our L dwarfs are toward high northern Galactic latitudes (where most of the SDSS sky coverage is). In addition, the Sun's motion out of the Plane is $W = 7$ km s^{-1} (Dehnen & Binney 1998). Therefore, because the mean vertical motion of stars in the Galaxy is near 0 km s^{-1}, the distribution of stars in our sample appears to be moving toward us at the Solar vertical motion. We have corrected for the Solar motion in the W velocities described below.

2.4.4 UVW Motions

Using proper motions, photometric distances, and radial velocities for 306 dwarfs in the spectroscopic sample, we calculated UVW velocities and uncertainties with the method outlined in Johnson & Soderblom (1987). Our velocities (given in Table 2.6) were corrected to the Local Standard of Rest assuming $UVW_{\odot}$ = (-10, 5, 7) km s^{-1} (Dehnen & Binney 1998, with positive U defined toward the Galactic center). Because our L dwarfs are located within 120 pc, these UVW velocities are essentially equal to their Galactic V_r, V_ϕ, and V_z velocities.

To investigate possible biases due to the inclusion of fast moving objects (because of the proper motion cut, $\sigma_{tot}/\mu_{tot} < 0.25$) and poorer quality measurements, we compared our sample to a subsample of 175 objects with lower uncertainty cuts ($\sigma_\mu < 0.08''$ yr^{-1} and $\sigma_{rad} < 12$ km s^{-1}). Figure 2.9 shows UVW histograms of both the total sample and the subsample. We fit Gaussian functions to each of the velocity distributions to determine

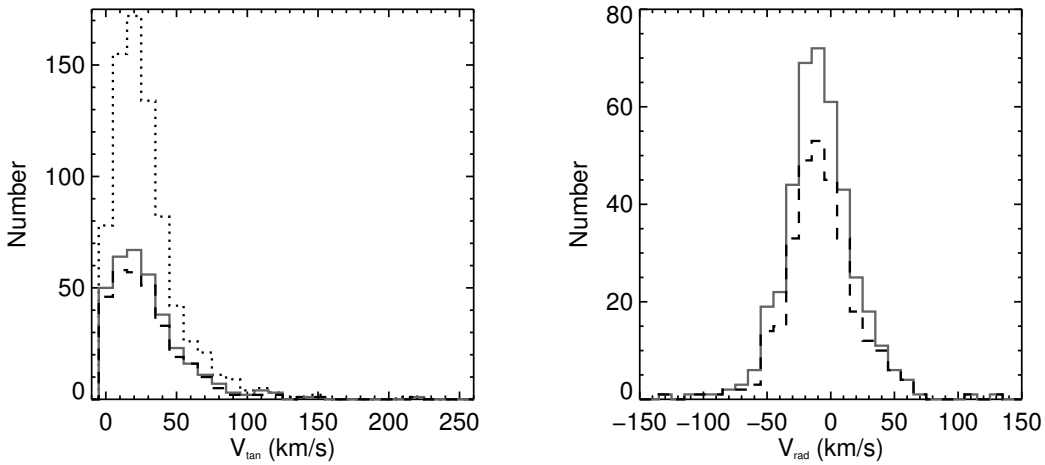

Figure 2.8 Histogram of tangential (left) and radial (right) velocities. In both panels, all dwarfs with complete UVW motions are shown (dashed lines). Dwarfs in the spectroscopic sample that only have tangential velocity measurements (left) or radial velocity measurements (right) are shown as the solid line. In the left panel, all dwarfs (including those previously known) with proper motions and distance estimates are also shown as the dotted line.

the mean and standard deviations (shown on each panel of Figure 2.9). The total sample shows good agreement with the lower uncertainty subsample; we use the total sample in the remainder of our analysis to take advantage of the larger number of velocities.

If we treat our kinematic distributions as a single population, our dispersions $(\sigma_U, \sigma_V, \sigma_W)$ = (25, 23, 20) km s^{-1} show reasonable agreement with those of previous studies. Zapatero Osorio et al. (2007) found dispersions of $(\sigma_U, \sigma_V, \sigma_W)$ = (30, 17, 16) km s^{-1} from complete kinematics of a sample of 20 L and T dwarfs, and Faherty et al. (2009) calculated $(\sigma_U, \sigma_V, \sigma_W)$ = (28, 23, 15) km s^{-1} from tangential velocities of a distance-limited sample of 114 L dwarfs.

2.4.5 Kinematic Models

Kinematics are useful tools to investigate the ages of populations of stars and brown dwarfs. As a population ages, its members have an increasing number of gravitational interactions with molecular clouds in the plane of the Galaxy. These interactions change the velocity

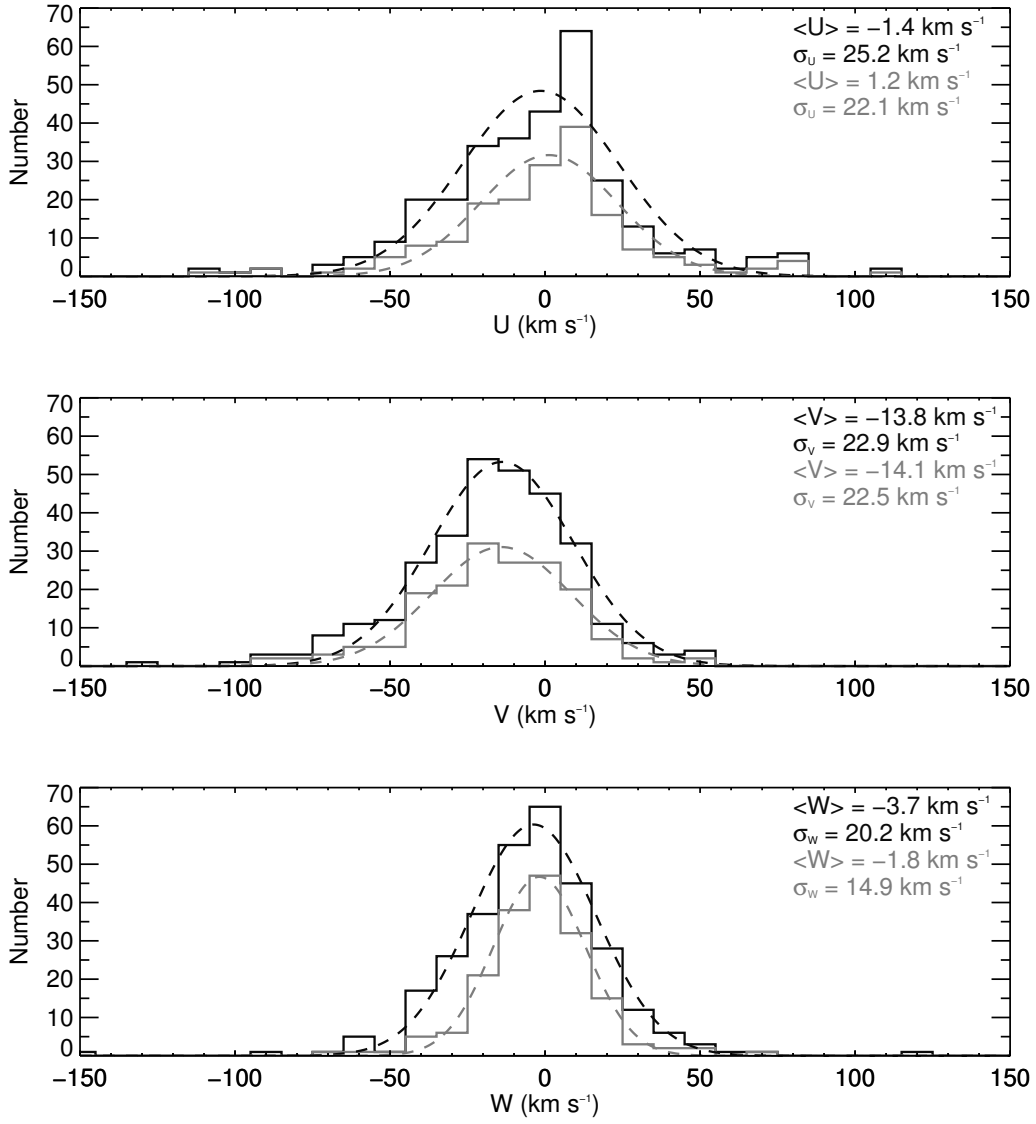

Figure 2.9 UVW histograms for all L dwarfs (black) and for dwarfs with good kinematics (grey). A Gaussian fit is shown (dashed line) for each distribution, and the best fit mean and dispersion for the Gaussian is given in the upper right corner of each plot.

of each star in a random direction and by a random amount, which increases the velocity dispersion of the population. Kinematically cooler populations (smaller dispersions) are typically younger than hotter populations (larger dispersions). The kinematics of disk stars are often fit with two components - a cooler, younger population and a hotter, older population (e.g., Reid et al. 2002).

While fitting the L dwarf velocities with a single Gaussian is useful for comparing our population to previous work, a two component analysis is important to examine how the L dwarf population compares to other disk dwarf populations (e.g. M dwarfs; Bochanski et al. 2007a). With large samples of objects, this can be easily accomplished by fitting two Gaussian functions to a histogram of the velocity distribution. The cold kinematic population dominates near the mean velocity, while the hotter kinematic population is usually only apparent a few standard deviations from the mean. For small samples like ours ($N < 400$), the hotter population is difficult to fit, with the Gaussian fit depending strongly on a few outliers in the wings of the velocity distribution.

This has been addressed in the past by fitting lines to a cumulative probability plot (shown for our data in Figure 2.10). In a cumulative probability plot, the data are shown as a function of the expected deviation from the mean for a Gaussian distribution; a population well-described by a single Gaussian function would be a straight line (Lutz & Upgren 1980). The dispersion of the cold population is then given by the slope of a line fit to the data near the mean, and the dispersion of the hot population is given by the average of the slopes of two lines fit to the data a few sigma in either direction from the mean (Reid et al. 2002; Bochanski et al. 2007a). While it is evident from Figure 2.10 that our sample contains both a hot and cold kinematic component, there are too few outlying points to use the slope of the wings to obtain velocity dispersions. We have therefore compared the velocity distributions to model kinematic populations.

We generated models by assigning a fraction of the total number of stars to each of the two components. We then randomly populated a comparison data set based on a mean and dispersion for each of the components, using the Box-Muller method (Box & Muller 1958). We used the Levenberg-Marquardt method for least squares fitting (Levenberg 1944; Marquardt 1963) to minimize the difference between the model distribution and the data

by varying the means and dispersions used to generate the model distribution. We repeated this process 1000 times for each fraction. The best fit parameters selected for the fraction are the mean of all the results. The uncertainties in the parameters are the standard deviation of all the results divided by the square root of the total number of stars. Once the best fit parameters for each fraction were found, we then determined the best fit fraction by choosing the fraction with the minimum average χ^2 fit. Only the W velocity showed a strong minimum χ^2, so we chose that fraction (90% cold, 10% hot) for the UV velocities as well.

Comparisons of our model and observed kinematic distributions are shown as cumulative probability plots in Figure 2.10. The means and dispersions of each of the populations are shown on each panel of Figure 2.10 and given in Table 2.8. As expected, the velocity dispersions for the cold component are similar to those obtained by fitting the entire population with one distribution. The dispersions of the cold and hot components are in good agreement with M dwarfs at Galactic heights $|z| < 100$ pc (Bochanski et al. 2007a; Pineda 2012, in prep.) indicating that the L dwarfs are kinematically similar to the local disk M dwarf population. This indicates that the L dwarfs have similar ages to local disk stars, instead of being a kinematically younger population, as has been previously suggested (Zapatero Osorio et al. 2007).

2.4.6 $J - K_S$ Outliers and Age

The spread in $J - K_S$ color within each spectral type is much wider than the spread in $i - z$, $i - J$, or $z - J$. Follow-up spectroscopic observations have shown that dwarfs with unusual $J - K_S$ colors are also sometimes spectroscopically peculiar. Red $J - K_S$ outliers often exhibit either distinctive low gravity features, indicating that these objects are young and still collapsing (Kirkpatrick et al. 2008; Cruz et al. 2009) or evidence of dusty photospheres, which can also be attributed to young ages (Looper et al. 2008). Blue outliers have been found to show strong H_2O and weak CO in their infrared spectra, possibly associated with high gravity and old age (Burgasser et al. 2008).

Additionally, a majority of the spectroscopically young red outliers have positions coin-

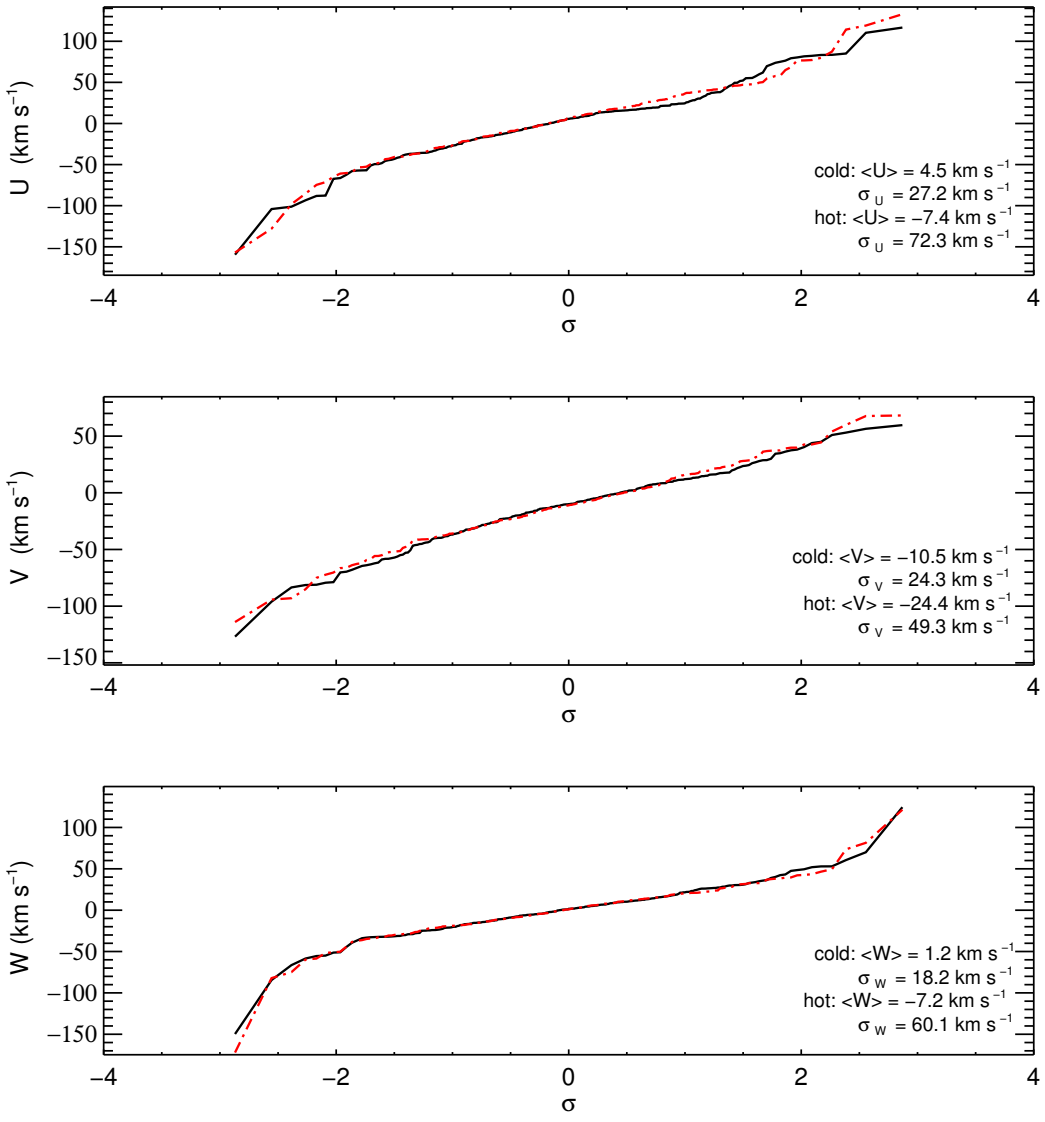

Figure 2.10 Probability plots for UVW data (black) compared to modeled data (red dot dashed). A population fit by a single Gaussian would appear to be a straight line. The means and dispersion for the dynamically hot (10% of total) and cold (90% of total) populations are given.

cident with young moving groups (Cruz et al. 2009), while many of the spectroscopically peculiar blue outliers have fast velocities consistent with being members of an older population. Faherty et al. (2009) investigated the kinematics of two groups of red and blue outliers (regardless of spectroscopic peculiarities), and found that the red outliers (more than 2σ from mean $J-K_S$ color) have a smaller tangential velocity dispersion ($\sigma_{\rm tan}$ = 16 km/s) and the blue outliers have a larger tangential velocity dispersion ($\sigma_{\rm tan}$ = 47 km/s) compared to the full sample dispersion of $\sigma_{\rm tan}$ = 23 km/s. This provides additional evidence that the features that cause unusually blue or red color can be associated with age.

In order to test this, we again used a color difference (δ_{J-K_S}; see section 2.3.2) to compare the spread in color across spectral types. We separated our sample into five bins based on their color difference and then examined the kinematics in each color difference bin. There were not sufficient objects in each bin to analyze the kinematics with two components, so we found one component velocity dispersions for each bin by fitting lines to their probability plots (similar to fitting a single Gaussian function to each distribution). Figure 2.11 shows the resulting σ_U, σ_V, and σ_W for the 5 color difference bins. It appears that the bluer L dwarfs ($\delta_{J-K_S} < -1.5$) have higher dispersions, indicating an older population.

To test whether color difference and velocity dispersion were correlated, we used Spearman's rank test. The correlation between color difference and dispersion is significant (P < 0.05) for σ_V and σ_W, with each having a correlation coefficient of $\rho = -0.9$. The correlation between color difference and dispersion is not significant for σ_U (P = 0.14, $\rho = -0.7$). The lack of significant correlation for σ_U is due to the higher dispersion found in the $0.5 > \delta_{J-K_S} > 1.5$ bin, likely an effect of small number statistics. These correlations support the idea that the color difference is primarily due to an age effect. Using the relation from Wielen (1977), we derive a mean age of 4.4 Gyr for our blue outliers ($\delta_{J-K_S} < -1.5$) and 0.9 Gyr for our red outliers ($\delta_{J-K_S} > 1.5$) . We do not provide a full relation between δ_{J-K_S} and age here. Our sample is too small to derive a reliable relation, and the kinematics and colors of L dwarfs should be examined in greater detail before an explicit relation can be given. Whether the specific mechanism is the effect of clouds, gravity, metallicity, or some combination of those three properties remains to be investigated.

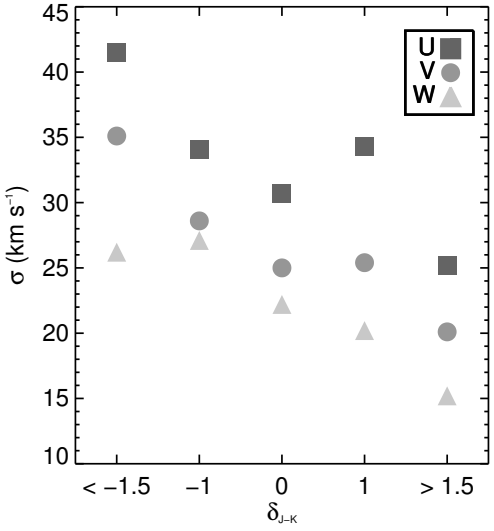

Figure 2.11 UVW velocity dispersions for L dwarfs divided into color difference bins.

2.5 Summary

We identified a sample of 484 L dwarfs using a search of the SDSS spectroscopic database, 210 of which are newly discovered. Combined with previously known dwarfs, this sample has allowed us to provide updated SDSS/2MASS colors for L and T dwarfs, revealing a systematic bias in previous selection based on $J - K_S$ color criteria.

We combined photometric distance estimates, proper motions, and radial velocities to examine the three dimensional kinematics of 306 L dwarfs. The L dwarf population is best fit by models generated from two Gaussian components, suggesting that it is made up of a combination of old and young disk stars. There is a correlation between $J - K_S$ color and velocity dispersion, which confirms a suggested relationship between age and color, with younger L dwarfs having redder colors.

This correlation is especially interesting given the bias towards the selection of redder objects in previous samples of L dwarfs. The current sample of L dwarfs is likely younger than the actual population, thus explaining suggestions that the L dwarf population is younger than the local disk (as measured by the field M dwarfs). Future work is needed to

ensure that the current sample of nearby dwarfs includes those with peculiar colors, and to further examine the relationship between age and color.

Table 2.1. SDSS spectroscopic sample

SDSS Designation (SDSS J +)	Other Name	ST	i	z	J	H	K_S	Discovery Reference
000632.60+140606.2	···	L0	20.11 ± 0.03	18.29 ± 0.03	15.85 ± 0.06	15.30 ± 0.07	15.06 ± 0.15	1
001637.61-103911.1	···	L0	19.73 ± 0.03	17.78 ± 0.02	15.46 ± 0.05	14.78 ± 0.07	14.53 ± 0.10	1
001911.64+003017.6	···	L0	19.36 ± 0.03	17.57 ± 0.02	14.92 ± 0.04	14.18 ± 0.04	13.57 ± 0.03	2
002209.34-011039.7	···	L0	19.74 ± 0.04	17.98 ± 0.02	15.82 ± 0.07	15.09 ± 0.08	14.70 ± 0.10	1
002611.45-094341.1	···	L1	19.98 ± 0.03	18.18 ± 0.03	15.60 ± 0.07	15.00 ± 0.08	14.38 ± 0.07	3
003524.43+144739.7	···	L2	21.12 ± 0.08	19.32 ± 0.08	···	···	···	2
003843.99+134339.3	···	L1	20.34 ± 0.05	18.42 ± 0.03	15.91 ± 0.07	15.20 ± 0.07	14.76 ± 0.10	2
004058.93+152845.0	···	L1	20.62 ± 0.06	18.90 ± 0.04	16.96 ± 0.21	15.58 ± 0.15	15.60 ± 0.23	3
004221.15+145923.8	···	L0	21.06 ± 0.07	19.03 ± 0.05	16.68 ± 0.15	16.09 ± 0.18	15.58 ± 0.20	2
005406.60-003102.4	···	L3	20.05 ± 0.03	18.20 ± 0.03	15.73 ± 0.05	14.89 ± 0.05	14.38 ± 0.07	4
005705.56-084624.1	···	L0	19.95 ± 0.04	18.14 ± 0.03	15.70 ± 0.06	14.92 ± 0.07	14.36 ± 0.08	1
010718.70+132656.1	···	L0	20.73 ± 0.06	18.66 ± 0.04	···	···	···	1
010840.48+134739.2	···	L0	20.48 ± 0.06	18.66 ± 0.05	···	···	···	1
010859.24-104546.3	···	L0	20.60 ± 0.06	18.76 ± 0.05	16.33 ± 0.08	15.72 ± 0.10	15.34 ± 0.15	1
011816.78+141841.4	···	L1	21.27 ± 0.08	19.43 ± 0.06	···	···	···	3
014658.14+002132.7	···	L0	20.77 ± 0.04	18.85 ± 0.04	16.56 ± 0.11	16.30 ± 0.23	15.40 ± 0.15	3
015354.23+140452.8	···	L0	19.39 ± 0.03	17.47 ± 0.03	15.21 ± 0.04	14.48 ± 0.05	13.96 ± 0.06	1
020551.36-075925.0	···	L3	20.77 ± 0.07	18.83 ± 0.05	16.03 ± 0.08	15.17 ± 0.06	14.36 ± 0.08	3
020735.59+135556.2	···	L3	19.85 ± 0.03	18.06 ± 0.02	15.46 ± 0.05	14.47 ± 0.04	13.81 ± 0.05	2
021128.26+141003.8	···	L0	20.51 ± 0.07	18.67 ± 0.04	16.13 ± 0.08	15.42 ± 0.09	15.01 ± 0.12	2
021248.51+221822.0	···	L0	21.36 ± 0.07	19.54 ± 0.06	···	···	···	3
022754.94+002619.9	···	L0	20.47 ± 0.04	18.84 ± 0.03	16.53 ± 0.11	15.87 ± 0.13	15.32 ± 0.15	1
023547.55-084919.9	···	L2	19.86 ± 0.04	17.99 ± 0.03	15.57 ± 0.05	14.81 ± 0.06	14.19 ± 0.07	2
025357.79+010934.3	···	L0	20.86 ± 0.07	19.22 ± 0.06	···	···	···	1
025601.88+011046.7	···	L0	20.04 ± 0.04	18.10 ± 0.03	16.21 ± 0.10	15.70 ± 0.18	15.22 ± 0.18	2
030536.55-064216.1	···	L0	20.30 ± 0.05	18.52 ± 0.04	15.99 ± 0.09	15.51 ± 0.13	14.76 ± 0.13	1
031740.38+061303.8	···	L3	20.93 ± 0.08	18.99 ± 0.05	16.37 ± 0.10	15.60 ± 0.13	14.91 ± 0.09	3
032817.43+003257.1	···	L2	20.04 ± 0.04	18.10 ± 0.03	15.99 ± 0.09	14.98 ± 0.07	14.16 ± 0.08	4
033035.19-002535.7	···	L5	20.09 ± 0.03	18.00 ± 0.03	15.31 ± 0.05	14.42 ± 0.04	13.84 ± 0.05	5
034408.91+011124.9	···	L1	20.04 ± 0.04	18.10 ± 0.03	14.74 ± 0.03	13.91 ± 0.04	13.52 ± 0.05	3
035048.62-051812.8	···	L0	20.78 ± 0.08	18.92 ± 0.05	16.33 ± 0.09	15.53 ± 0.09	15.13 ± 0.13	2
035308.54+103056.0	···	L1	19.91 ± 0.03	17.94 ± 0.03	15.45 ± 0.06	14.65 ± 0.05	14.18 ± 0.04	3
035721.12-064125.9	···	L0	20.20 ± 0.04	18.28 ± 0.03	15.95 ± 0.08	15.06 ± 0.09	14.60 ± 0.09	2
042230.66+072342.9	···	L1	20.07 ± 0.03	18.21 ± 0.03	15.77 ± 0.07	14.92 ± 0.07	14.45 ± 0.06	3
073519.59+410850.3	···	L0	19.70 ± 0.03	17.83 ± 0.03	15.78 ± 0.07	15.25 ± 0.09	14.85 ± 0.10	1
074227.46+412620.8	···	L0	18.86 ± 0.02	17.07 ± 0.01	14.78 ± 0.03	14.02 ± 0.03	13.59 ± 0.04	1

Table 2.1 (cont'd)

SDSS Designation (SDSS J +)	Other Name	ST	i	z	J	H	K_S	Discovery Reference
074434.60+320705.1	···	L0	20.57 ± 0.05	18.66 ± 0.05	16.33 ± 0.09	15.66 ± 0.12	15.41 ± 0.16	1
074515.07+254619.1	···	L1	20.74 ± 0.05	18.82 ± 0.05	16.44 ± 0.12	15.66 ± 0.13	15.33 ± 0.15	1
074642.42+200031.8	2MASSI J0746425+200032	L1	16.09 ± 0.01	14.24 ± 0.02	11.76 ± 0.02	11.01 ± 0.02	10.47 ± 0.02	6
074656.83+251019.0	···	L0	20.29 ± 0.04	18.75 ± 0.04	16.76 ± 0.22	15.72 ± 0.16	15.74 ± 0.22	3
074756.32+394732.8	···	L0	19.23 ± 0.02	17.42 ± 0.03	15.08 ± 0.04	14.16 ± 0.04	13.72 ± 0.04	2
075004.93+330617.9	···	L0	20.23 ± 0.04	18.45 ± 0.03	16.14 ± 0.07	15.37 ± 0.08	15.20 ± 0.12	1
075259.43+413634.6	···	L2	20.85 ± 0.06	19.08 ± 0.04	···	···	···	2
075332.13+291711.4	2MASSI J0753321+291711	L3	19.97 ± 0.03	18.14 ± 0.03	15.52 ± 0.05	14.53 ± 0.04	13.85 ± 0.04	7
075414.04+431534.1	···	L1	20.66 ± 0.04	18.87 ± 0.04	16.41 ± 0.18	15.60 ± 0.17	15.06 ± 0.17	1
075910.44+242712.4	···	L0	20.09 ± 0.04	18.17 ± 0.03	15.74 ± 0.05	14.98 ± 0.05	14.48 ± 0.07	1
080027.57+551134.1	···	L1	19.07 ± 0.02	17.17 ± 0.02	14.62 ± 0.03	13.82 ± 0.02	13.36 ± 0.03	3
080048.12+465825.6	···	L3	19.99 ± 0.03	18.14 ± 0.03	15.51 ± 0.07	14.55 ± 0.06	14.32 ± 0.08	2
080054.26+241316.8	···	L0	19.60 ± 0.03	17.87 ± 0.02	15.80 ± 0.06	14.99 ± 0.06	14.68 ± 0.09	1
080159.52+480628.5	···	L0	20.30 ± 0.05	18.33 ± 0.03	16.01 ± 0.09	15.06 ± 0.10	14.82 ± 0.11	1
080255.75+332143.6	···	L2	20.15 ± 0.05	18.39 ± 0.04	15.85 ± 0.08	14.80 ± 0.07	14.20 ± 0.07	3
080322.77+123845.3	···	L3	20.74 ± 0.05	18.65 ± 0.03	16.31 ± 0.08	15.44 ± 0.08	15.23 ± 0.11	8
080519.69+492504.8	···	L0	20.75 ± 0.06	18.84 ± 0.04	···	···	···	3
080549.90+511312.6	···	L1	19.61 ± 0.03	17.71 ± 0.03	15.26 ± 0.05	14.38 ± 0.06	13.85 ± 0.05	3
080550.07+533531.4	···	L0	20.07 ± 0.03	18.33 ± 0.03	16.21 ± 0.11	15.50 ± 0.16	15.04 ± 0.15	1
080858.99+410741.0	···	L2	20.14 ± 0.03	18.17 ± 0.03	15.74 ± 0.08	14.88 ± 0.08	14.33 ± 0.07	3
081253.19+372104.2	···	L3	20.21 ± 0.03	18.34 ± 0.03	15.75 ± 0.07	14.98 ± 0.08	14.28 ± 0.07	3
081301.02+322807.9	···	L3	20.24 ± 0.03	18.38 ± 0.03	15.95 ± 0.08	15.09 ± 0.08	14.54 ± 0.08	3
081556.74+452411.8	···	L0	20.53 ± 0.05	18.53 ± 0.03	16.06 ± 0.08	15.23 ± 0.09	14.81 ± 0.10	2
081653.72+344535.8	···	L2	20.72 ± 0.05	18.79 ± 0.04	16.12 ± 0.09	15.41 ± 0.11	14.99 ± 0.12	3
081733.99+393606.0	···	L0	20.74 ± 0.05	18.81 ± 0.04	···	···	···	3
081752.62+194727.5	···	L0	19.74 ± 0.03	17.99 ± 0.02	15.57 ± 0.05	14.83 ± 0.06	14.35 ± 0.05	1
081757.49+182405.0	···	L1	19.44 ± 0.02	17.50 ± 0.02	15.09 ± 0.04	14.29 ± 0.04	13.82 ± 0.03	3
081802.24+582920.9	···	L0	20.78 ± 0.05	18.82 ± 0.04	16.33 ± 0.10	15.50 ± 0.10	15.24 ± 0.18	3
081812.28+331048.2	···	L0	20.44 ± 0.04	18.60 ± 0.04	15.99 ± 0.09	15.37 ± 0.11	15.06 ± 0.14	3
081814.38+245337.4	···	L0	20.04 ± 0.04	18.10 ± 0.03	16.37 ± 0.09	15.54 ± 0.09	14.91 ± 0.09	3
082115.03+333651.3	···	L0	···	···	16.50 ± 0.17	15.63 ± 0.15	15.06 ± 0.16	1
082346.99+154947.4	···	L1	···	···	16.46 ± 0.11	15.58 ± 0.12	14.96 ± 0.13	3
082348.15+242857.9	2MASS J08234818+2428577	L3	19.56 ± 0.02	17.75 ± 0.02	14.99 ± 0.04	14.06 ± 0.04	13.38 ± 0.03	9
082519.45+211550.3	2MASSI J0825196+211552	L7	20.60 ± 0.05	17.79 ± 0.03	15.10 ± 0.03	13.79 ± 0.03	13.03 ± 0.03	7
082539.87+310040.7	···	L1	20.37 ± 0.04	18.47 ± 0.03	16.44 ± 0.14	15.36 ± 0.12	15.13 ± 0.16	3
082612.27+544735.4	···	L0	20.45 ± 0.06	18.60 ± 0.04	16.36 ± 0.11	15.59 ± 0.11	15.26 ± 0.18	1

Table 2.1 (cont'd)

SDSS Designation (SDSS J +)	Other Name	ST	i	z	J	H	K_S	Discovery Reference
082906.61+145620.7	2MASSW J0829066+145622	L3	19.17 ± 0.02	17.35 ± 0.02	14.75 ± 0.03	13.80 ± 0.04	13.17 ± 0.03	7
082928.21+343954.0	···	L0	20.49 ± 0.04	18.55 ± 0.04	16.10 ± 0.10	15.43 ± 0.11	15.06 ± 0.14	3
083008.11+482847.4	···	L8	21.22 ± 0.08	18.08 ± 0.03	15.44 ± 0.05	14.34 ± 0.04	13.68 ± 0.04	10
083027.24+220345.0	···	L0	19.86 ± 0.02	17.98 ± 0.02	15.66 ± 0.06	14.81 ± 0.05	14.46 ± 0.09	1
083122.08+153850.3	···	L1	19.99 ± 0.03	18.04 ± 0.03	15.79 ± 0.09	14.89 ± 0.07	14.54 ± 0.09	3
083424.12+071916.2	···	L0	20.63 ± 0.04	18.88 ± 0.04	16.54 ± 0.11	15.84 ± 0.14	15.43 ± 0.14	1
083429.19+230855.1	···	L1	20.69 ± 0.04	18.89 ± 0.04	16.51 ± 0.11	15.42 ± 0.10	14.68 ± 0.07	1
083545.33+222430.8	···	L0	19.73 ± 0.02	17.83 ± 0.02	15.74 ± 0.06	14.93 ± 0.06	14.45 ± 0.07	1
083611.43+450319.5	···	L1	19.56 ± 0.02	17.75 ± 0.02	15.27 ± 0.05	14.42 ± 0.06	13.93 ± 0.05	3
083621.99+494931.5	···	L0	19.62 ± 0.04	17.78 ± 0.03	15.42 ± 0.06	14.64 ± 0.07	14.54 ± 0.12	1
083646.34+052642.6	···	L0	18.72 ± 0.02	16.93 ± 0.02	14.58 ± 0.04	13.91 ± 0.04	13.29 ± 0.03	1
083652.36+183544.9	···	L0	20.87 ± 0.05	18.98 ± 0.04	16.51 ± 0.12	15.88 ± 0.15	15.18 ± 0.10	3
083724.77+081603.9	···	L0	20.27 ± 0.05	18.43 ± 0.03	16.13 ± 0.09	15.31 ± 0.10	14.76 ± 0.09	1
083732.80+161737.5	···	L0	20.74 ± 0.05	18.88 ± 0.04	16.59 ± 0.12	15.56 ± 0.10	15.11 ± 0.11	3
083759.75+195727.7	···	L0	20.24 ± 0.03	18.55 ± 0.03	16.36 ± 0.10	15.57 ± 0.11	14.93 ± 0.09	3
083926.23+433935.7	···	L0	20.55 ± 0.06	18.64 ± 0.03	16.51 ± 0.16	15.66 ± 0.17	15.28 ± 0.22	1
084001.62+451752.3	···	L1	20.12 ± 0.03	18.30 ± 0.03	15.73 ± 0.07	14.93 ± 0.08	14.30 ± 0.06	1
084016.42+543002.1	···	L1	20.83 ± 0.06	18.79 ± 0.05	16.39 ± 0.12	15.51 ± 0.13	15.35 ± 0.15	8
084036.04+143424.3	···	L1	20.30 ± 0.04	18.59 ± 0.03	16.23 ± 0.09	15.08 ± 0.07	14.62 ± 0.08	3
084106.85+603506.3	···	L4	20.40 ± 0.04	18.55 ± 0.03	15.94 ± 0.09	15.03 ± 0.10	14.69 ± 0.09	3
084149.77+005844.6	···	L0	20.91 ± 0.07	18.95 ± 0.05	···	···	···	3
084217.14+432506.3	···	L0	20.51 ± 0.05	18.64 ± 0.04	16.25 ± 0.10	15.67 ± 0.17	15.01 ± 0.11	1
084307.94+314129.2	···	L3	20.45 ± 0.05	18.52 ± 0.03	15.99 ± 0.10	15.22 ± 0.12	14.65 ± 0.11	1
084333.28+102443.5	···	L1	19.31 ± 0.02	17.48 ± 0.02	14.87 ± 0.04	14.09 ± 0.04	13.67 ± 0.04	3
084407.00+284702.1	···	L2	20.36 ± 0.04	18.41 ± 0.03	15.87 ± 0.06	14.82 ± 0.05	14.34 ± 0.06	3
084444.58+403620.0	···	L1	20.53 ± 0.05	18.75 ± 0.05	16.20 ± 0.09	15.54 ± 0.11	15.07 ± 0.14	3
084520.22+360551.4	···	L0	20.17 ± 0.03	18.38 ± 0.02	15.82 ± 0.07	15.01 ± 0.07	14.45 ± 0.08	1
084751.48+013811.0	···	L3	20.92 ± 0.08	18.88 ± 0.06	16.23 ± 0.13	15.12 ± 0.10	14.41 ± 0.08	8
084934.05+591622.9	···	L0	20.62 ± 0.05	18.74 ± 0.05	16.29 ± 0.10	15.38 ± 0.13	15.03 ± 0.12	3
085213.94+421921.3	···	L0	19.84 ± 0.03	18.00 ± 0.02	15.64 ± 0.07	15.00 ± 0.09	14.44 ± 0.09	1
085214.41+094048.0	···	L0	20.32 ± 0.03	18.39 ± 0.03	16.08 ± 0.08	15.36 ± 0.10	14.91 ± 0.09	1
085359.10+223335.8	···	L2	20.73 ± 0.06	18.96 ± 0.04	16.30 ± 0.10	15.29 ± 0.09	14.85 ± 0.10	3
085602.05+124014.3	···	L0	19.78 ± 0.03	17.93 ± 0.02	15.45 ± 0.05	14.67 ± 0.05	14.28 ± 0.05	3
085758.44+570851.4	···	L8	20.68 ± 0.07	17.72 ± 0.03	15.04 ± 0.04	13.79 ± 0.04	12.96 ± 0.03	10
085805.47+221457.8	···	L1	19.58 ± 0.02	17.72 ± 0.03	15.23 ± 0.05	14.42 ± 0.05	13.84 ± 0.05	3
085836.97+271050.8	···	L0	19.44 ± 0.03	17.63 ± 0.02	15.05 ± 0.05	14.23 ± 0.05	13.66 ± 0.05	1

Table 2.1 (cont'd)

SDSS Designation (SDSS J +)	Other Name	ST	i	z	J	H	K_S	Discovery Reference
085858.92+180445.7	···	L2	20.83 ± 0.06	18.98 ± 0.04	16.35 ± 0.09	15.76 ± 0.11	15.14 ± 0.11	3
085938.50+634133.5	2MASS J08593854+6341355	L0	17.95 ± 0.01	16.14 ± 0.01	13.70 ± 0.03	12.89 ± 0.03	12.39 ± 0.03	9
085959.77+292205.3	···	L0	20.19 ± 0.03	18.38 ± 0.03	15.80 ± 0.07	14.95 ± 0.06	14.62 ± 0.08	1
090023.68+253934.3	···	L7	21.45 ± 0.08	18.85 ± 0.04	16.43 ± 0.11	15.41 ± 0.12	14.66 ± 0.08	3
090040.61+422721.5	···	L0	20.71 ± 0.05	18.89 ± 0.04	···	···	···	3
090154.72+381837.5	···	L0	19.53 ± 0.02	17.75 ± 0.03	15.31 ± 0.05	14.57 ± 0.06	14.09 ± 0.05	1
090238.98+301840.3	···	L0	20.15 ± 0.05	18.37 ± 0.03	16.24 ± 0.09	15.44 ± 0.10	15.05 ± 0.14	1
090347.55+011446.0	···	L3	21.04 ± 0.07	18.93 ± 0.05	16.45 ± 0.14	15.60 ± 0.10	14.89 ± 0.13	8
090509.01+043819.9	···	L0	20.17 ± 0.03	18.68 ± 0.03	16.70 ± 0.18	16.08 ± 0.16	15.74 ± 0.27	1
090531.00+195433.0	···	L0	20.26 ± 0.04	18.43 ± 0.03	15.94 ± 0.07	15.10 ± 0.06	14.54 ± 0.06	3
090837.91+503207.5	2MASSI J0908380+503208	L8	20.03 ± 0.04	17.23 ± 0.02	14.55 ± 0.02	13.48 ± 0.03	12.95 ± 0.03	11
090948.13+194043.9	···	L1	19.13 ± 0.02	17.25 ± 0.02	14.73 ± 0.03	13.93 ± 0.03	13.44 ± 0.03	3
091128.95+320644.7	···	L0	20.31 ± 0.03	18.38 ± 0.03	15.90 ± 0.08	15.22 ± 0.10	14.78 ± 0.12	1
091206.35+420330.5	···	L0	20.09 ± 0.03	18.24 ± 0.03	15.99 ± 0.09	15.38 ± 0.10	14.93 ± 0.12	2
091414.38+105719.5	···	L0	19.66 ± 0.03	17.84 ± 0.02	15.50 ± 0.07	14.81 ± 0.08	14.26 ± 0.10	1
091524.33+383128.3	···	L0	20.38 ± 0.05	18.62 ± 0.04	16.24 ± 0.11	15.32 ± 0.11	14.74 ± 0.11	1
091656.32+105740.0	···	L1	20.53 ± 0.05	18.88 ± 0.05	···	···	···	3
091659.10+512450.4	···	L0	18.53 ± 0.02	16.75 ± 0.02	14.41 ± 0.03	13.73 ± 0.03	13.18 ± 0.03	1
091714.76+314824.8	···	L1	20.87 ± 0.04	18.85 ± 0.03	16.30 ± 0.10	15.73 ± 0.14	15.01 ± 0.13	8
091750.33+294444.9	···	L0	20.20 ± 0.03	18.25 ± 0.03	15.85 ± 0.08	14.97 ± 0.09	14.50 ± 0.08	1
092026.43+265157.7	···	L0	19.94 ± 0.04	18.31 ± 0.03	15.83 ± 0.07	14.97 ± 0.08	14.62 ± 0.09	1
092142.52+084202.7	···	L2	20.07 ± 0.04	18.26 ± 0.03	15.79 ± 0.08	14.89 ± 0.09	14.34 ± 0.07	3
092300.89+052801.5	···	L0	20.39 ± 0.04	18.83 ± 0.04	···	···	···	3
092308.70+234013.7	···	L1	18.23 ± 0.02	16.23 ± 0.02	13.85 ± 0.03	13.16 ± 0.03	12.81 ± 0.02	3
092532.11+283550.9	···	L0	20.80 ± 0.04	18.89 ± 0.03	16.53 ± 0.12	15.85 ± 0.15	15.24 ± 0.16	3
092757.43+602746.3	···	L0	19.93 ± 0.03	18.07 ± 0.03	15.52 ± 0.05	14.74 ± 0.05	14.23 ± 0.06	2
093113.23+280227.1	···	L3	19.62 ± 0.03	17.67 ± 0.02	14.98 ± 0.03	14.26 ± 0.04	13.73 ± 0.04	3
093146.83+544227.1	···	L0	20.10 ± 0.04	18.31 ± 0.03	16.08 ± 0.07	15.42 ± 0.08	14.91 ± 0.10	1
093215.46+345624.8	···	L0	20.62 ± 0.04	18.85 ± 0.03	16.73 ± 0.15	15.70 ± 0.14	14.98 ± 0.14	3
093237.47+672514.5	···	L0	20.20 ± 0.04	18.37 ± 0.04	15.91 ± 0.09	15.37 ± 0.13	14.99 ± 0.12	3
093535.49+234217.5	···	L1	20.52 ± 0.05	18.71 ± 0.05	16.64 ± 0.12	15.84 ± 0.14	15.28 ± 0.13	3
093600.12+043147.9	···	L2	20.87 ± 0.07	18.99 ± 0.04	···	···	···	3
093706.71+284705.6	···	L0	···	18.32 ± 0.03	15.80 ± 0.07	15.29 ± 0.11	14.68 ± 0.07	1
093824.88+290328.9	···	L0	21.26 ± 0.10	19.41 ± 0.07	16.83 ± 0.19	15.84 ± 0.22	15.53 ± 0.20	3
093858.88+044343.9	···	L0	20.04 ± 0.04	18.10 ± 0.03	15.24 ± 0.05	14.50 ± 0.05	14.00 ± 0.07	3
093906.46+341257.4	···	L0	19.74 ± 0.02	17.86 ± 0.02	15.58 ± 0.05	14.88 ± 0.06	14.30 ± 0.06	1

Table 2.1 (cont'd)

SDSS Designation (SDSS J +)	Other Name	ST	i	z	J	H	K_S	Discovery Reference
094043.19+565049.1	···	L0	19.84 ± 0.04	18.07 ± 0.03	15.71 ± 0.06	14.90 ± 0.07	14.28 ± 0.05	1
094047.88+294653.0	···	L1	19.79 ± 0.02	17.86 ± 0.03	15.29 ± 0.07	14.34 ± 0.06	13.92 ± 0.05	3
094134.92+100942.1	···	L0	18.84 ± 0.02	17.03 ± 0.02	14.58 ± 0.02	13.78 ± 0.03	13.37 ± 0.04	1
094350.20+151909.2	···	L1	20.18 ± 0.03	18.24 ± 0.02	15.75 ± 0.06	15.03 ± 0.09	14.56 ± 0.07	3
094402.80+313132.5	2MASSW J0944027+313132	L3	20.11 ± 0.03	18.33 ± 0.02	15.50 ± 0.05	14.63 ± 0.05	14.01 ± 0.04	7
094427.31+641037.3	···	L0	20.96 ± 0.08	18.93 ± 0.06	16.67 ± 0.16	15.88 ± 0.17	15.46 ± 0.18	3
094436.31+364920.8	···	L2	20.30 ± 0.03	18.54 ± 0.03	15.99 ± 0.08	14.98 ± 0.07	14.47 ± 0.07	3
094818.61+132320.0	···	L0	20.43 ± 0.04	18.52 ± 0.03	15.87 ± 0.08	15.25 ± 0.11	14.47 ± 0.08	3
094903.15+264944.2	···	L0	20.64 ± 0.04	18.75 ± 0.04	16.22 ± 0.09	15.55 ± 0.09	15.11 ± 0.10	3
095415.73+500140.3	···	L0	20.77 ± 0.08	18.95 ± 0.05	16.54 ± 0.12	15.55 ± 0.11	14.94 ± 0.10	3
095850.68+200150.6	···	L0	20.50 ± 0.03	18.66 ± 0.04	16.08 ± 0.08	15.25 ± 0.09	14.61 ± 0.07	3
095908.97+312557.3	···	L0	19.37 ± 0.02	17.53 ± 0.03	15.42 ± 0.05	14.80 ± 0.06	14.29 ± 0.06	1
095916.66+364157.6	···	L0	19.93 ± 0.04	18.06 ± 0.03	15.94 ± 0.08	15.26 ± 0.09	14.76 ± 0.11	1
100016.92+321829.4	···	L1	21.05 ± 0.10	18.81 ± 0.05	16.62 ± 0.12	15.70 ± 0.11	15.36 ± 0.17	8
100435.88+565757.4	···	L0	20.89 ± 0.07	18.74 ± 0.04	16.67 ± 0.11	15.81 ± 0.10	15.43 ± 0.17	3
100442.60+614628.5	···	L0	19.78 ± 0.03	17.89 ± 0.03	15.55 ± 0.05	14.79 ± 0.07	14.28 ± 0.06	1
100559.85+035842.3	···	L0	20.31 ± 0.03	18.50 ± 0.03	15.95 ± 0.10	15.09 ± 0.07	14.65 ± 0.11	1
100844.63+470738.0	···	L0	20.09 ± 0.04	18.29 ± 0.03	15.93 ± 0.09	15.24 ± 0.11	14.91 ± 0.12	1
100942.68+580217.6	···	L3	20.38 ± 0.05	18.63 ± 0.04	16.04 ± 0.08	15.15 ± 0.07	14.60 ± 0.07	3
101304.34+071050.7	···	L0	20.51 ± 0.04	18.61 ± 0.03	16.22 ± 0.13	15.47 ± 0.14	15.09 ± 0.18	3
101517.63+075211.9	···	L0	19.94 ± 0.03	18.00 ± 0.03	15.51 ± 0.09	14.85 ± 0.08	14.41 ± 0.09	1
101707.55+130839.3	2MASSI J1017075+130839	L2	18.54 ± 0.02	16.75 ± 0.02	14.10 ± 0.02	13.28 ± 0.03	12.71 ± 0.02	11
101742.51+431057.9	···	L1	19.95 ± 0.03	18.14 ± 0.04	15.55 ± 0.07	14.89 ± 0.08	14.52 ± 0.10	3
102116.05+354607.8	···	L0	20.80 ± 0.05	18.92 ± 0.04	16.47 ± 0.11	15.99 ± 0.16	15.41 ± 0.18	1
102204.88+020047.5	···	L0	18.34 ± 0.03	16.49 ± 0.02	14.10 ± 0.03	13.40 ± 0.03	12.90 ± 0.03	1
102436.10+624514.0	···	L0	19.96 ± 0.04	18.06 ± 0.03	15.68 ± 0.07	15.04 ± 0.09	14.45 ± 0.09	1
102600.05+395509.6	···	L0	20.43 ± 0.03	18.50 ± 0.03	16.12 ± 0.09	15.71 ± 0.14	15.27 ± 0.15	1
102921.85+162649.8	2MASSI J1029216+162652	L3	18.76 ± 0.02	17.02 ± 0.03	14.29 ± 0.02	13.33 ± 0.03	12.62 ± 0.02	7
102947.68+483412.2	···	L0	20.89 ± 0.07	18.88 ± 0.05	16.76 ± 0.19	16.04 ± 0.21	15.59 ± 0.24	8
103225.19+330042.0	···	L0	19.45 ± 0.02	17.66 ± 0.03	15.26 ± 0.05	14.56 ± 0.06	13.94 ± 0.04	1
103309.10+121625.9	···	L0	19.35 ± 0.02	17.63 ± 0.03	15.07 ± 0.04	14.44 ± 0.05	13.95 ± 0.05	1
103405.67+035016.3	···	L0	20.04 ± 0.04	18.10 ± 0.03	14.70 ± 0.04	14.02 ± 0.04	13.63 ± 0.05	3
103428.24+414000.7	···	L0	20.54 ± 0.04	18.65 ± 0.04	16.49 ± 0.14	15.95 ± 0.20	15.22 ± 0.15	1
103451.12+125840.7	···	L0	20.51 ± 0.04	18.65 ± 0.04	16.01 ± 0.08	15.54 ± 0.12	14.88 ± 0.12	3
103528.61+231840.0	···	L0	20.54 ± 0.04	18.64 ± 0.03	16.50 ± 0.10	15.61 ± 0.10	15.10 ± 0.12	3
103602.44+372448.4	···	L0	20.86 ± 0.06	18.77 ± 0.04	16.42 ± 0.12	15.54 ± 0.13	14.99 ± 0.11	8

Table 2.1 (cont'd)

SDSS Designation (SDSS J +)	Other Name	ST	i	z	J	H	K_S	Discovery Reference
103730.42+461826.6	···	L0	20.22 ± 0.03	18.29 ± 0.03	16.08 ± 0.08	15.62 ± 0.13	14.76 ± 0.07	3
104014.50+413116.4	···	L0	20.29 ± 0.03	18.73 ± 0.03	16.72 ± 0.16	16.04 ± 0.18	15.80 ± 0.23	1
104121.86+244228.0	···	L0	20.80 ± 0.05	18.91 ± 0.04	16.49 ± 0.14	15.60 ± 0.12	15.50 ± 0.21	3
104319.44+071232.4	···	L0	20.53 ± 0.04	18.62 ± 0.05	16.13 ± 0.10	15.42 ± 0.11	14.97 ± 0.14	3
104407.47+015742.0	···	L2	20.87 ± 0.06	18.87 ± 0.05	16.58 ± 0.16	15.65 ± 0.13	15.22 ± 0.20	8
104426.79+272033.2	···	L1	20.39 ± 0.04	18.67 ± 0.04	···	···	···	3
104617.01+351305.8	···	L1	20.64 ± 0.05	18.81 ± 0.05	16.37 ± 0.10	15.57 ± 0.10	15.06 ± 0.10	1
104729.03+301639.7	···	L0	20.48 ± 0.05	18.71 ± 0.03	16.33 ± 0.12	15.41 ± 0.13	15.15 ± 0.12	3
104842.70+300650.5	···	L1	20.47 ± 0.05	18.53 ± 0.04	15.90 ± 0.07	15.06 ± 0.08	14.61 ± 0.06	3
104842.80+011158.0	···	L1	17.25 ± 0.02	15.44 ± 0.02	12.92 ± 0.02	12.14 ± 0.02	11.62 ± 0.02	2
104922.45+012559.2	···	L6	21.00 ± 0.09	18.76 ± 0.04	15.88 ± 0.07	14.95 ± 0.07	14.11 ± 0.06	8
104928.24+253723.2	···	L1	19.96 ± 0.03	18.10 ± 0.03	15.67 ± 0.06	14.83 ± 0.07	14.37 ± 0.06	3
104934.84+602029.4	···	L0	20.67 ± 0.06	18.82 ± 0.05	16.21 ± 0.12	15.44 ± 0.15	15.08 ± 0.15	3
105012.46+005803.1	···	L0	20.40 ± 0.06	18.51 ± 0.04	···	···	···	2
105044.04+325843.5	···	L0	20.53 ± 0.04	18.67 ± 0.04	16.42 ± 0.10	15.73 ± 0.12	15.28 ± 0.14	1
105110.69+314130.0	···	L0	20.20 ± 0.04	18.38 ± 0.03	15.79 ± 0.06	14.96 ± 0.06	14.70 ± 0.08	3
105118.96+561308.0	2MASS J10511900+5613086	L1	17.65 ± 0.01	15.83 ± 0.01	13.24 ± 0.02	12.42 ± 0.03	11.91 ± 0.02	9
105259.70+334406.1	···	L0	20.69 ± 0.05	18.88 ± 0.03	16.48 ± 0.15	15.75 ± 0.19	15.31 ± 0.20	3
105318.15+433306.1	···	L0	20.08 ± 0.03	18.27 ± 0.03	15.88 ± 0.10	15.21 ± 0.11	14.83 ± 0.14	1
105339.22+642351.5	···	L0	20.30 ± 0.04	18.55 ± 0.04	16.32 ± 0.12	15.34 ± 0.12	15.16 ± 0.17	3
105355.39+385737.5	···	L0	20.37 ± 0.04	18.55 ± 0.04	16.09 ± 0.08	15.42 ± 0.10	14.86 ± 0.09	1
105510.41+511026.1	···	L0	20.68 ± 0.05	18.95 ± 0.04	16.51 ± 0.10	16.08 ± 0.19	15.57 ± 0.17	3
105814.54+303159.8	···	L0	19.78 ± 0.03	17.97 ± 0.03	15.62 ± 0.06	15.07 ± 0.07	14.60 ± 0.09	1
110008.19+295516.1	···	L0	20.03 ± 0.03	18.30 ± 0.03	15.70 ± 0.07	14.99 ± 0.09	14.45 ± 0.08	1
110009.62+495746.5	···	L3	20.09 ± 0.03	18.00 ± 0.02	15.28 ± 0.04	14.19 ± 0.04	13.47 ± 0.03	8
110148.04+544009.1	···	L0	19.44 ± 0.02	17.71 ± 0.02	15.36 ± 0.04	14.63 ± 0.05	14.15 ± 0.06	1
110212.06+162938.7	···	L0	20.62 ± 0.05	18.76 ± 0.04	16.52 ± 0.14	15.57 ± 0.15	15.23 ± 0.14	3
110401.29+195922.3	2MASSI J1104012+195921	L5	19.35 ± 0.02	17.20 ± 0.02	14.38 ± 0.02	13.48 ± 0.03	12.95 ± 0.03	11
110555.02+042145.3	···	L0	20.91 ± 0.06	18.93 ± 0.04	···	···	···	1
110705.31+245448.5	···	L0	20.51 ± 0.06	18.67 ± 0.04	16.23 ± 0.10	15.47 ± 0.14	14.76 ± 0.12	3
110927.19-160653.7	···	L0	19.28 ± 0.02	17.25 ± 0.02	14.97 ± 0.04	14.35 ± 0.04	13.89 ± 0.06	3
110938.29+235339.6	···	L0	19.98 ± 0.03	18.17 ± 0.02	15.70 ± 0.05	15.01 ± 0.06	14.58 ± 0.07	3
111143.85+295823.8	···	L1	20.50 ± 0.05	18.69 ± 0.03	16.57 ± 0.12	16.03 ± 0.14	15.09 ± 0.12	3
111316.95-000246.7	···	L0	19.44 ± 0.02	17.56 ± 0.02	15.08 ± 0.03	14.30 ± 0.04	13.80 ± 0.05	2
111647.97+603730.7	···	L0	20.18 ± 0.05	18.53 ± 0.04	16.38 ± 0.10	15.50 ± 0.13	15.45 ± 0.18	3
111736.93+360935.9	2MASSI J1117369+360936	L0	18.64 ± 0.02	16.75 ± 0.01	14.27 ± 0.03	13.46 ± 0.03	12.96 ± 0.03	11

Table 2.1 (cont'd)

SDSS Designation (SDSS J +)	Other Name	ST	i	z	J	H	K_S	Discovery Reference
112210.27+340432.5	···	L1	20.66 ± 0.05	18.70 ± 0.04	16.12 ± 0.08	15.30 ± 0.10	14.74 ± 0.09	3
112505.01+055642.3	···	L0	20.04 ± 0.04	18.10 ± 0.03	15.53 ± 0.06	14.85 ± 0.07	14.49 ± 0.09	3
112647.03+581632.2	···	L3	20.14 ± 0.03	18.19 ± 0.03	15.84 ± 0.08	15.11 ± 0.08	14.54 ± 0.08	3
112706.62+470548.1	···	L1	19.57 ± 0.03	17.64 ± 0.02	15.20 ± 0.03	14.50 ± 0.03	13.91 ± 0.04	3
112720.55+593633.0	···	L0	20.60 ± 0.04	18.80 ± 0.04	16.82 ± 0.16	15.76 ± 0.17	15.56 ± 0.21	1
113035.14-005225.7	···	L0	19.03 ± 0.02	17.33 ± 0.01	15.12 ± 0.04	14.46 ± 0.05	13.88 ± 0.05	1
113344.68+131126.4	···	L1	20.11 ± 0.04	18.24 ± 0.03	15.70 ± 0.05	14.93 ± 0.06	14.42 ± 0.05	3
113826.35+333114.1	···	L0	20.07 ± 0.04	18.20 ± 0.03	15.59 ± 0.06	14.77 ± 0.07	14.31 ± 0.07	3
113833.07+674040.2	···	L0	19.35 ± 0.03	17.56 ± 0.02	15.22 ± 0.04	14.48 ± 0.05	13.95 ± 0.05	2
113941.90-031004.1	···	L0	18.63 ± 0.03	16.66 ± 0.02	14.40 ± 0.03	13.71 ± 0.03	13.20 ± 0.04	1
114144.14+411656.7	···	L0	19.65 ± 0.03	17.89 ± 0.02	15.68 ± 0.07	14.78 ± 0.06	14.57 ± 0.07	1
114251.67+640020.0	···	L0	20.78 ± 0.05	18.97 ± 0.04	16.60 ± 0.12	16.19 ± 0.19	15.76 ± 0.25	1
114634.52+223053.1	2MASSW J1146345+223053	L3	18.85 ± 0.05	16.95 ± 0.02	14.17 ± 0.03	13.18 ± 0.02	12.59 ± 0.03	12
114804.25+025405.6	···	L0	20.36 ± 0.05	18.53 ± 0.04	16.11 ± 0.10	15.38 ± 0.12	15.20 ± 0.21	2
114805.02+020350.8	···	L0	19.93 ± 0.03	17.88 ± 0.03	15.52 ± 0.07	15.01 ± 0.11	14.51 ± 0.12	2
114912.31-015300.6	···	L0	18.68 ± 0.02	16.88 ± 0.02	14.67 ± 0.04	14.13 ± 0.04	13.71 ± 0.07	1
115013.17+052012.3	···	L6	21.30 ± 0.07	18.93 ± 0.04	16.25 ± 0.14	15.46 ± 0.14	15.02 ± 0.17	8
115250.06+643252.5	···	L2	20.01 ± 0.03	18.15 ± 0.02	15.60 ± 0.05	14.64 ± 0.06	14.09 ± 0.06	3
115306.12+371653.4	···	L0	20.37 ± 0.04	18.55 ± 0.03	16.38 ± 0.10	15.79 ± 0.13	15.56 ± 0.15	1
115339.67+503209.4	2MASS J11533966+5032092	L0	18.46 ± 0.01	16.64 ± 0.01	14.19 ± 0.03	13.31 ± 0.02	12.85 ± 0.03	9
115435.31+623438.2	···	L0	19.62 ± 0.03	17.82 ± 0.03	15.40 ± 0.05	14.80 ± 0.07	14.26 ± 0.07	3
115553.84+055957.5	···	L6	21.28 ± 0.12	18.46 ± 0.04	15.66 ± 0.08	14.70 ± 0.07	14.12 ± 0.07	13
115804.70+644720.4	···	L0	20.43 ± 0.05	18.53 ± 0.03	16.13 ± 0.10	15.77 ± 0.15	15.09 ± 0.16	3
115938.50+005726.9	DENIS-P J1159+0057	L0	18.51 ± 0.02	16.59 ± 0.03	14.08 ± 0.03	13.31 ± 0.02	12.81 ± 0.03	14
115940.72+540938.6	···	L2	20.04 ± 0.04	18.10 ± 0.03	15.22 ± 0.04	14.34 ± 0.04	13.76 ± 0.04	3
115948.00+383016.2	···	L0	20.63 ± 0.05	18.94 ± 0.04	16.39 ± 0.11	15.74 ± 0.15	15.30 ± 0.14	1
120020.66+340615.4	···	L1	20.60 ± 0.04	18.69 ± 0.03	···	···	···	3
120249.99+420452.1	···	L0	18.89 ± 0.02	16.94 ± 0.03	···	···	···	1
120252.65-022748.6	···	L1	20.17 ± 0.05	18.35 ± 0.04	15.74 ± 0.06	15.04 ± 0.07	14.37 ± 0.09	1
120358.19+001550.2	···	L5	18.88 ± 0.02	16.79 ± 0.02	14.01 ± 0.02	13.06 ± 0.02	12.48 ± 0.02	5
120430.38+321259.4	2MASSI J1204303+321259	L0	18.16 ± 0.02	16.37 ± 0.02	13.82 ± 0.03	13.09 ± 0.04	12.52 ± 0.03	11
120543.42+605728.3	···	L0	20.76 ± 0.06	18.76 ± 0.04	16.32 ± 0.11	15.43 ± 0.12	15.21 ± 0.19	3
120610.49+624257.2	···	L1	20.00 ± 0.04	18.10 ± 0.04	15.65 ± 0.07	14.75 ± 0.07	13.95 ± 0.07	3
120637.41-014332.2	···	L1	21.12 ± 0.08	19.50 ± 0.07	···	···	···	3
120747.17+024424.8	···	L8	21.46 ± 0.11	18.38 ± 0.04	15.58 ± 0.07	14.56 ± 0.06	13.99 ± 0.06	2
120821.72+445224.6	···	L0	20.24 ± 0.04	18.35 ± 0.03	15.93 ± 0.09	15.11 ± 0.10	14.71 ± 0.09	1

Table 2.1 (cont'd)

SDSS Designation (SDSS J +)	Other Name	ST	i	z	J	H	K_S	Discovery Reference
120831.50+014924.7	DENIS-P J1208.5+0149	L0	19.29 ± 0.02	17.37 ± 0.03	15.13 ± 0.04	14.42 ± 0.05	14.10 ± 0.07	14
120906.49+323327.5	···	L0	19.69 ± 0.03	17.69 ± 0.03	15.30 ± 0.05	14.61 ± 0.05	14.17 ± 0.06	3
120916.20+542949.5	···	L1	19.79 ± 0.03	17.97 ± 0.03	15.52 ± 0.06	14.66 ± 0.06	14.22 ± 0.06	3
121210.99+605948.0	···	L0	19.07 ± 0.03	17.29 ± 0.03	14.87 ± 0.04	14.26 ± 0.05	13.71 ± 0.06	1
121304.77+152922.2	···	L1	20.65 ± 0.07	18.79 ± 0.05	16.33 ± 0.11	15.66 ± 0.12	15.42 ± 0.16	3
121409.75+332356.0	···	L0	20.61 ± 0.06	18.86 ± 0.06	16.46 ± 0.11	15.77 ± 0.12	15.45 ± 0.14	1
121433.60+372111.8	···	L0	20.18 ± 0.03	18.31 ± 0.03	16.19 ± 0.08	15.50 ± 0.12	15.07 ± 0.12	1
121645.58+492744.9	···	L1	20.19 ± 0.03	18.19 ± 0.03	15.59 ± 0.06	14.77 ± 0.07	14.11 ± 0.05	3
121855.72+352022.9	···	L0	20.66 ± 0.04	18.78 ± 0.04	16.49 ± 0.13	15.69 ± 0.15	15.19 ± 0.15	3
121950.22+654136.5	···	L0	19.76 ± 0.03	18.01 ± 0.03	15.61 ± 0.06	15.09 ± 0.09	14.57 ± 0.07	1
122048.34-014237.8	···	L0	20.27 ± 0.05	18.54 ± 0.04	16.20 ± 0.10	15.95 ± 0.14	15.38 ± 0.21	1
122127.70+025719.7	2MASS J12212770+0257198	L0	17.41 ± 0.02	15.61 ± 0.02	13.17 ± 0.02	12.41 ± 0.02	11.95 ± 0.02	9
122524.00-021559.7	···	L3	20.70 ± 0.06	18.95 ± 0.06	16.55 ± 0.10	15.65 ± 0.11	15.04 ± 0.13	3
122818.53+583342.2	···	L0	20.00 ± 0.03	18.22 ± 0.03	15.91 ± 0.10	15.21 ± 0.10	14.89 ± 0.14	1
123045.43+282758.0	2MASS J12304562+2827583	L2	20.33 ± 0.04	18.67 ± 0.04	16.07 ± 0.09	15.01 ± 0.08	14.43 ± 0.06	15
123112.97+405027.9	···	L0	19.26 ± 0.02	17.50 ± 0.02	15.24 ± 0.05	14.57 ± 0.05	14.10 ± 0.05	1
123121.38+495923.3	2MASS J12312141+4959234	L3	19.23 ± 0.02	17.28 ± 0.02	14.62 ± 0.03	13.71 ± 0.03	13.14 ± 0.03	16
123322.63+213805.1	···	L0	20.47 ± 0.05	18.55 ± 0.04	16.21 ± 0.11	15.51 ± 0.12	14.99 ± 0.12	3
123517.24+315815.6	···	L0	20.33 ± 0.04	18.48 ± 0.04	16.50 ± 0.13	15.39 ± 0.12	15.27 ± 0.15	1
123815.58+621925.9	···	L0	20.43 ± 0.05	18.76 ± 0.05	16.30 ± 0.11	15.76 ± 0.15	15.22 ± 0.14	1
123927.32+551537.3	2MASSW J1239272+551537	L5	19.64 ± 0.04	17.48 ± 0.03	14.71 ± 0.03	13.57 ± 0.03	12.79 ± 0.03	7
124036.80+152517.1	···	L0	19.83 ± 0.05	17.94 ± 0.03	15.59 ± 0.05	14.66 ± 0.05	14.50 ± 0.06	1
124352.25+131021.3	···	L0	19.60 ± 0.03	17.79 ± 0.03	15.58 ± 0.04	14.85 ± 0.06	14.45 ± 0.06	1
124510.86-013230.9	···	L0	20.76 ± 0.07	18.94 ± 0.05	16.60 ± 0.14	16.08 ± 0.16	15.61 ± 0.24	3
124514.95+120442.0	···	L1	20.54 ± 0.04	18.67 ± 0.03	16.05 ± 0.08	15.32 ± 0.11	14.73 ± 0.09	3
124555.66+490210.9	···	L1	19.45 ± 0.02	17.89 ± 0.02	15.95 ± 0.07	15.36 ± 0.09	15.20 ± 0.14	3
124908.66+415728.5	···	L0	19.60 ± 0.03	17.72 ± 0.02	15.44 ± 0.04	14.69 ± 0.06	14.29 ± 0.05	1
124921.22+541340.1	···	L0	18.98 ± 0.02	17.18 ± 0.02	14.83 ± 0.03	14.10 ± 0.04	13.65 ± 0.04	1
125044.67+041758.2	···	L0	20.63 ± 0.06	18.80 ± 0.04	16.49 ± 0.14	16.01 ± 0.18	15.47 ± 0.24	1
125045.66+441853.6	···	L0	19.84 ± 0.03	18.16 ± 0.03	16.45 ± 0.14	16.16 ± 0.26	15.11 ± 0.19	1
125214.08+142239.3	···	L3	20.57 ± 0.04	18.76 ± 0.03	16.00 ± 0.07	15.16 ± 0.08	14.49 ± 0.07	3
125230.79+183506.0	···	L1	20.62 ± 0.06	18.88 ± 0.04	16.31 ± 0.12	15.23 ± 0.10	14.72 ± 0.13	3
125253.62+342138.8	···	L2	20.54 ± 0.04	18.76 ± 0.03	16.27 ± 0.10	15.26 ± 0.09	14.68 ± 0.08	3
125437.60+293832.6	···	L0	19.71 ± 0.02	17.93 ± 0.02	15.46 ± 0.05	14.60 ± 0.06	14.18 ± 0.06	1
125459.33+263107.2	···	L1	20.78 ± 0.05	18.80 ± 0.03	16.83 ± 0.15	15.56 ± 0.12	15.33 ± 0.14	3
125550.62+170059.7	···	L0	20.45 ± 0.04	18.61 ± 0.04	16.19 ± 0.07	15.35 ± 0.11	15.01 ± 0.10	3

Table 2.1 (cont'd)

SDSS Designation (SDSS J +)	Other Name	ST	i	z	J	H	K_S	Discovery Reference
125737.25-011336.2	···	L5	20.76 ± 0.05	18.55 ± 0.04	15.94 ± 0.08	14.72 ± 0.06	14.12 ± 0.07	10
130148.19+584104.1	···	L1	20.26 ± 0.04	18.42 ± 0.03	16.10 ± 0.08	15.45 ± 0.11	14.86 ± 0.10	3
130234.70+512600.8	···	L0	20.02 ± 0.04	18.04 ± 0.05	15.54 ± 0.07	15.02 ± 0.09	14.37 ± 0.08	2
130250.94+564037.8	···	L0	20.55 ± 0.04	18.73 ± 0.04	16.14 ± 0.12	15.49 ± 0.12	14.99 ± 0.12	3
130317.69+181522.0	···	L0	20.59 ± 0.06	18.90 ± 0.05	16.31 ± 0.09	15.37 ± 0.08	15.04 ± 0.11	3
130433.16+090706.9	···	L0	19.68 ± 0.03	17.79 ± 0.02	···	···	···	3
130541.04+204639.8	2MASSI J1305410+204639	L3	20.11 ± 0.05	17.94 ± 0.02	15.20 ± 0.05	14.04 ± 0.04	13.37 ± 0.04	11
130617.23+382029.6	2MASS J13061727+3820296	L0	19.13 ± 0.02	17.30 ± 0.02	14.63 ± 0.03	13.80 ± 0.04	13.22 ± 0.03	9
130831.01+081852.3	···	L0	19.60 ± 0.03	17.83 ± 0.02	15.13 ± 0.05	14.35 ± 0.06	13.85 ± 0.07	3
131002.88+055404.2	···	L0	20.12 ± 0.04	18.34 ± 0.03	16.08 ± 0.10	15.40 ± 0.10	14.78 ± 0.13	1
131113.82+240105.0	···	L3	20.73 ± 0.04	18.81 ± 0.03	16.19 ± 0.11	15.69 ± 0.16	14.79 ± 0.15	3
131221.79+290935.0	···	L0	19.89 ± 0.03	17.94 ± 0.03	15.33 ± 0.06	14.78 ± 0.09	14.30 ± 0.07	3
131223.11+493126.3	···	L0	20.35 ± 0.03	18.50 ± 0.04	16.20 ± 0.08	15.43 ± 0.08	14.99 ± 0.10	1
131448.64+240532.1	···	L3	20.54 ± 0.03	18.79 ± 0.04	16.68 ± 0.11	15.64 ± 0.10	15.40 ± 0.13	3
131543.68+233458.0	···	L1	20.29 ± 0.03	18.39 ± 0.03	15.81 ± 0.07	15.04 ± 0.08	14.77 ± 0.09	3
131545.55+245407.3	···	L0	19.84 ± 0.03	18.00 ± 0.02	15.54 ± 0.06	14.77 ± 0.07	14.36 ± 0.07	3
131614.35+213329.9	···	L0	20.84 ± 0.06	18.94 ± 0.04	16.21 ± 0.10	15.53 ± 0.16	14.96 ± 0.13	3
131839.06+213043.0	···	L0	20.64 ± 0.05	18.74 ± 0.03	16.44 ± 0.12	15.50 ± 0.13	15.04 ± 0.12	3
132511.10+051704.2	···	L1	19.64 ± 0.03	17.80 ± 0.02	15.09 ± 0.04	14.52 ± 0.05	13.91 ± 0.05	3
132715.21+075937.5	···	L1	19.17 ± 0.03	17.34 ± 0.02	14.60 ± 0.04	13.79 ± 0.04	13.24 ± 0.04	3
132937.21+035729.6	···	L0	20.21 ± 0.03	18.32 ± 0.03	16.04 ± 0.10	15.15 ± 0.09	15.05 ± 0.14	1
133010.03+141113.3	···	L0	20.44 ± 0.04	18.57 ± 0.03	16.44 ± 0.11	15.76 ± 0.16	15.21 ± 0.15	3
133132.83+623301.4	···	L0	20.29 ± 0.04	18.59 ± 0.04	16.17 ± 0.08	15.41 ± 0.12	15.13 ± 0.10	1
133132.98+340757.5	2MASS J13313310+3407583	L0	18.55 ± 0.02	16.77 ± 0.02	14.33 ± 0.02	13.40 ± 0.03	12.89 ± 0.02	9
133148.88-011652.5	···	L7	20.69 ± 0.07	18.10 ± 0.04	15.46 ± 0.04	14.48 ± 0.04	14.07 ± 0.07	2
133312.79+150956.6	···	L0	19.77 ± 0.03	18.06 ± 0.03	15.84 ± 0.07	15.28 ± 0.09	15.09 ± 0.14	3
133345.36-021600.2	···	L3	19.65 ± 0.03	17.77 ± 0.02	15.38 ± 0.04	14.37 ± 0.04	13.85 ± 0.05	3
133406.17+194035.8	2MASSW J1334062+194034	L1	19.88 ± 0.03	18.11 ± 0.02	15.48 ± 0.06	14.83 ± 0.07	14.00 ± 0.05	12
133506.46+431725.1	···	L0	20.65 ± 0.05	18.70 ± 0.04	16.45 ± 0.13	16.20 ± 0.24	15.38 ± 0.19	1
133640.53+374322.6	2MASS J13364062+3743230	L1	18.72 ± 0.02	16.82 ± 0.02	14.41 ± 0.03	13.63 ± 0.03	13.10 ± 0.02	16
133849.45+043731.2	2MASS J13384944+0437315	L1	18.53 ± 0.01	16.72 ± 0.02	14.16 ± 0.03	13.25 ± 0.03	12.74 ± 0.03	9
134148.85+551046.2	···	L1	19.74 ± 0.03	17.70 ± 0.02	15.21 ± 0.04	14.39 ± 0.04	14.04 ± 0.05	3
134224.93+603731.5	···	L0	20.84 ± 0.05	19.07 ± 0.05	16.36 ± 0.10	15.64 ± 0.12	15.51 ± 0.15	1
134228.41-002705.6	···	L0	19.74 ± 0.03	17.95 ± 0.02	15.59 ± 0.06	14.88 ± 0.05	14.30 ± 0.08	1
134316.54+394509.2	2MASSW J1343167+394508	L5	21.30 ± 0.08	18.94 ± 0.04	16.16 ± 0.07	14.86 ± 0.05	14.15 ± 0.05	7
134322.51-030100.2	···	L0	20.39 ± 0.04	18.45 ± 0.03	16.13 ± 0.09	15.44 ± 0.09	15.03 ± 0.14	3

Table 2.1 (cont'd)

SDSS Designation (SDSS J +)	Other Name	ST	i	z	J	H	K_S	Discovery Reference
134329.01+131226.2	···	L1	20.29 ± 0.04	18.55 ± 0.03	16.02 ± 0.08	15.44 ± 0.12	14.89 ± 0.12	3
134338.73-022044.5	···	L1	20.41 ± 0.05	18.64 ± 0.04	16.30 ± 0.12	15.53 ± 0.12	15.02 ± 0.15	1
134515.82-025514.4	···	L0	20.32 ± 0.04	18.43 ± 0.04	16.09 ± 0.08	15.29 ± 0.10	14.88 ± 0.10	1
134544.36+654217.9	···	L1	20.20 ± 0.04	18.34 ± 0.03	···	···	···	1
134607.41+084234.5	···	L2	20.02 ± 0.03	18.16 ± 0.03	15.74 ± 0.07	14.79 ± 0.08	14.16 ± 0.07	3
134845.94+035354.2	2MASS J13484591+0353545	L1	19.05 ± 0.02	17.11 ± 0.03	14.63 ± 0.03	13.76 ± 0.03	13.23 ± 0.04	9
134925.25+504954.5	···	L0	19.16 ± 0.02	17.28 ± 0.02	14.72 ± 0.03	13.97 ± 0.04	13.57 ± 0.05	1
135238.65+324002.4	···	L0	20.44 ± 0.04	18.51 ± 0.04	16.05 ± 0.09	15.29 ± 0.11	14.99 ± 0.13	3
135439.54+504451.0	···	L1	18.68 ± 0.02	16.77 ± 0.02	14.35 ± 0.03	13.58 ± 0.03	13.16 ± 0.04	3
135712.40+142839.8	···	L3	20.12 ± 0.03	18.27 ± 0.02	15.58 ± 0.06	14.65 ± 0.06	13.88 ± 0.04	3
135825.72+423434.4	···	L0	20.34 ± 0.04	18.42 ± 0.04	16.16 ± 0.09	15.32 ± 0.09	14.90 ± 0.11	3
135955.19+324719.0	···	L0	19.81 ± 0.03	17.87 ± 0.03	15.58 ± 0.05	14.82 ± 0.06	14.31 ± 0.07	3
140231.75+014830.2	···	L1	19.92 ± 0.03	17.96 ± 0.02	15.45 ± 0.06	14.65 ± 0.07	14.18 ± 0.07	2
140307.47+201859.3	···	L0	20.82 ± 0.05	18.84 ± 0.03	···	···	···	3
140347.84+351313.1	···	L0	20.60 ± 0.05	18.80 ± 0.04	16.41 ± 0.12	16.13 ± 0.18	15.46 ± 0.18	1
140409.90+400214.0	···	L0	20.88 ± 0.05	18.95 ± 0.03	···	···	···	1
140412.19+133922.1	···	L0	20.67 ± 0.05	18.78 ± 0.04	16.36 ± 0.11	15.70 ± 0.15	15.04 ± 0.10	1
140441.67+023550.1	···	L0	···	···	15.60 ± 0.06	14.91 ± 0.07	14.53 ± 0.10	2
140442.38-022426.0	···	L0	20.26 ± 0.04	18.43 ± 0.04	16.19 ± 0.08	15.44 ± 0.11	15.00 ± 0.14	1
140444.86+463430.4	2MASS J14044495+4634297	L0	18.66 ± 0.02	16.78 ± 0.02	14.34 ± 0.03	13.53 ± 0.02	13.06 ± 0.03	16
140601.48+524930.9	···	L0	19.89 ± 0.03	18.10 ± 0.03	15.56 ± 0.05	14.97 ± 0.08	14.56 ± 0.10	1
140633.17+360449.2	···	L0	20.61 ± 0.04	18.64 ± 0.03	16.31 ± 0.10	15.89 ± 0.15	15.21 ± 0.15	1
140753.53+124110.1	2MASS J14075361+1241099	L3	20.43 ± 0.04	18.23 ± 0.03	15.38 ± 0.05	14.34 ± 0.05	13.60 ± 0.04	9
140818.89+064954.3	···	L1	20.12 ± 0.03	18.23 ± 0.04	15.79 ± 0.08	14.92 ± 0.05	14.35 ± 0.08	3
140909.45+432749.9	···	L0	20.13 ± 0.04	18.23 ± 0.04	15.92 ± 0.07	15.11 ± 0.09	14.61 ± 0.07	1
141117.12+393636.8	2MASSW J1411175+393636	L2	19.11 ± 0.02	17.21 ± 0.02	14.64 ± 0.03	13.77 ± 0.04	13.24 ± 0.03	7
141133.55+172530.6	···	L1	20.51 ± 0.04	18.63 ± 0.03	16.26 ± 0.10	15.40 ± 0.13	14.78 ± 0.09	3
141624.09+134826.7	···	L6	18.37 ± 0.02	15.94 ± 0.02	13.15 ± 0.02	12.46 ± 0.03	12.11 ± 0.02	17
141838.08+145522.4	···	L0	19.49 ± 0.02	17.68 ± 0.02	15.22 ± 0.05	14.55 ± 0.05	14.21 ± 0.06	3
141910.99+484257.0	···	L0	19.97 ± 0.03	18.29 ± 0.02	16.15 ± 0.10	15.47 ± 0.12	14.76 ± 0.12	1
141942.82+420524.0	···	L0	20.24 ± 0.04	18.41 ± 0.03	16.11 ± 0.09	15.36 ± 0.10	14.96 ± 0.14	1
142058.30+213156.6	···	L1	19.50 ± 0.02	17.55 ± 0.02	15.12 ± 0.04	14.52 ± 0.05	14.06 ± 0.06	3
142241.28+234011.8	···	L0	20.62 ± 0.04	18.75 ± 0.04	16.53 ± 0.12	16.10 ± 0.16	15.56 ± 0.16	3
142257.15+082752.1	···	L2	19.47 ± 0.02	17.68 ± 0.03	15.10 ± 0.05	14.22 ± 0.03	13.65 ± 0.05	3
142806.99+512022.4	···	L0	20.40 ± 0.04	18.61 ± 0.03	16.32 ± 0.12	15.44 ± 0.12	14.99 ± 0.16	1
142831.28+592335.3	2MASS J14283132+5923354	L5	19.66 ± 0.03	17.66 ± 0.03	14.78 ± 0.04	13.88 ± 0.04	13.27 ± 0.03	9

Table 2.1 (cont'd)

SDSS Designation (SDSS J +)	Other Name	ST	i	z	J	H	K_S	Discovery Reference
142843.13+331036.8	LHS 2924	L0	16.20 ± 0.01	14.40 ± 0.02	11.99 ± 0.02	11.23 ± 0.03	10.74 ± 0.02	18
142935.19+383221.4	···	L0	19.85 ± 0.03	18.10 ± 0.03	15.97 ± 0.08	14.93 ± 0.06	14.53 ± 0.08	1
143043.51+291541.3	2MASSI J1430435+291540	L2	18.76 ± 0.02	16.94 ± 0.03	14.27 ± 0.03	13.44 ± 0.03	12.77 ± 0.02	19
143130.78+143653.4	2MASS J14313097+1436539	L3	19.71 ± 0.03	17.60 ± 0.02	15.15 ± 0.04	14.50 ± 0.05	14.13 ± 0.06	15
143132.79+351300.6	···	L1	20.03 ± 0.03	18.17 ± 0.03	15.59 ± 0.05	14.77 ± 0.05	14.16 ± 0.05	3
143147.92+124329.0	···	L0	20.48 ± 0.04	18.63 ± 0.04	16.38 ± 0.10	15.57 ± 0.12	15.32 ± 0.17	1
143242.10+345142.7	···	L1	20.12 ± 0.04	18.16 ± 0.03	15.75 ± 0.11	15.05 ± 0.13	14.77 ± 0.10	3
143251.01+363643.6	···	L0	18.52 ± 0.02	16.56 ± 0.02	14.30 ± 0.03	13.60 ± 0.03	13.07 ± 0.03	1
143517.20-004612.8	···	L0	20.35 ± 0.05	18.57 ± 0.03	16.48 ± 0.10	15.61 ± 0.12	15.32 ± 0.18	2
143832.63+572216.9	···	L3	20.83 ± 0.06	18.74 ± 0.04	15.96 ± 0.07	15.10 ± 0.08	14.37 ± 0.06	8
143911.87+082315.6	···	L0	19.87 ± 0.03	17.97 ± 0.03	15.39 ± 0.04	14.65 ± 0.05	14.09 ± 0.07	3
143925.23+424141.7	···	L0	19.84 ± 0.03	17.98 ± 0.03	15.50 ± 0.04	14.79 ± 0.06	14.20 ± 0.05	1
143933.43+031759.1	···	L3	20.65 ± 0.06	18.72 ± 0.05	15.99 ± 0.10	15.67 ± 0.15	14.81 ± 0.13	2
143940.91+182637.0	2MASSW J1439409+182637	L1	20.64 ± 0.05	18.73 ± 0.03	16.22 ± 0.10	15.45 ± 0.11	14.54 ± 0.10	12
144139.88+353809.5	···	L0	19.64 ± 0.02	17.77 ± 0.03	15.44 ± 0.05	14.78 ± 0.06	14.19 ± 0.06	1
144430.15+485807.4	···	L0	20.67 ± 0.05	18.90 ± 0.05	16.67 ± 0.16	15.65 ± 0.16	15.24 ± 0.15	1
144635.65+164337.3	···	L0	20.90 ± 0.07	18.96 ± 0.04	16.42 ± 0.13	15.97 ± 0.23	15.15 ± 0.15	3
144804.96+060802.2	···	L0	20.00 ± 0.03	18.04 ± 0.03	15.77 ± 0.09	15.00 ± 0.10	14.58 ± 0.11	1
144825.69+103158.8	2MASSW J1448256+103159	L5	19.63 ± 0.02	17.46 ± 0.02	14.56 ± 0.03	13.43 ± 0.03	12.68 ± 0.03	19
144842.75+371932.0	···	L0	19.80 ± 0.03	17.96 ± 0.02	···	···	···	1
144927.99+205434.1	···	L0	20.70 ± 0.06	18.91 ± 0.04	16.88 ± 0.18	16.46 ± 0.23	15.83 ± 0.23	3
144937.86+235537.8	2MASSW J1449378+235537	L0	19.93 ± 0.03	18.09 ± 0.03	15.82 ± 0.07	15.00 ± 0.09	14.31 ± 0.08	7
145017.31+461739.3	···	L0	19.53 ± 0.02	17.72 ± 0.02	15.51 ± 0.05	14.84 ± 0.08	14.42 ± 0.06	1
145037.69+082807.1	···	L0	20.60 ± 0.04	18.75 ± 0.04	16.33 ± 0.11	15.88 ± 0.15	15.40 ± 0.20	3
145255.58+272324.4	···	L0	19.21 ± 0.02	17.24 ± 0.02	14.92 ± 0.04	14.36 ± 0.04	14.08 ± 0.06	3
145325.89+142041.8	···	L1	19.64 ± 0.02	17.77 ± 0.02	15.07 ± 0.04	14.40 ± 0.06	13.89 ± 0.03	3
145447.76+371823.1	···	L0	20.33 ± 0.04	18.43 ± 0.03	16.27 ± 0.11	15.64 ± 0.15	15.32 ± 0.21	1
145502.93+261919.6	···	L1	19.66 ± 0.03	17.78 ± 0.02	15.14 ± 0.05	14.53 ± 0.06	13.87 ± 0.06	3
145658.17+070104.7	···	L3	20.58 ± 0.04	18.69 ± 0.03	16.28 ± 0.11	15.20 ± 0.09	14.60 ± 0.10	3
150238.47+182539.8	···	L0	20.77 ± 0.05	18.91 ± 0.05	16.47 ± 0.13	15.54 ± 0.12	15.28 ± 0.18	3
150240.80+613815.5	···	L0	20.71 ± 0.05	18.81 ± 0.05	16.35 ± 0.12	16.08 ± 0.23	15.39 ± 0.21	2
150309.53+115323.1	···	L2	20.64 ± 0.04	18.74 ± 0.04	16.30 ± 0.10	15.40 ± 0.10	14.79 ± 0.09	3
150844.43+433955.5	···	L0	20.35 ± 0.04	18.57 ± 0.04	16.28 ± 0.11	15.25 ± 0.11	15.07 ± 0.11	1
151136.24+353511.4	···	L0	20.72 ± 0.05	18.71 ± 0.03	16.29 ± 0.10	15.62 ± 0.11	14.95 ± 0.12	8
151240.67+340350.1	···	L3	19.34 ± 0.02	17.63 ± 0.02	15.04 ± 0.04	14.05 ± 0.04	13.41 ± 0.04	3
151500.62+484744.8	2MASSW J1515008+484742	L6	19.37 ± 0.02	16.74 ± 0.02	14.11 ± 0.03	13.10 ± 0.03	12.50 ± 0.02	19

Table 2.1 (cont'd)

SDSS Designation (SDSS J +)	Other Name	ST	i	z	J	H	K_S	Discovery Reference
151527.14+341232.7	···	L1	20.63 ± 0.05	18.80 ± 0.04	16.27 ± 0.08	15.17 ± 0.07	14.65 ± 0.06	3
151542.28+325543.2	···	L0	20.30 ± 0.04	18.41 ± 0.03	16.22 ± 0.07	15.57 ± 0.09	14.96 ± 0.08	1
151603.96+573907.6	···	L0	20.17 ± 0.04	18.46 ± 0.03	16.15 ± 0.09	15.48 ± 0.09	15.20 ± 0.14	1
152314.46+105258.9	···	L0	20.54 ± 0.04	18.58 ± 0.03	16.09 ± 0.10	15.15 ± 0.07	14.82 ± 0.12	3
152324.45-021133.9	···	L0	19.67 ± 0.02	17.91 ± 0.03	15.61 ± 0.06	14.93 ± 0.06	14.39 ± 0.08	1
152529.74+200407.9	···	L1	19.81 ± 0.02	17.91 ± 0.03	15.51 ± 0.05	14.61 ± 0.05	14.02 ± 0.05	3
152621.06+280806.9	···	L1	20.32 ± 0.03	18.44 ± 0.03	15.92 ± 0.10	15.45 ± 0.14	14.47 ± 0.10	3
153108.87+060111.2	ULAS J153108.89+060111.1	L1	20.21 ± 0.03	18.27 ± 0.03	16.05 ± 0.10	15.06 ± 0.06	14.40 ± 0.11	20
153119.91+262835.2	···	L0	20.79 ± 0.04	18.78 ± 0.04	···	···	···	3
153223.34+261118.8	···	L1	20.63 ± 0.04	18.69 ± 0.03	16.12 ± 0.10	15.33 ± 0.10	14.90 ± 0.12	3
153721.97+140507.5	···	L0	20.27 ± 0.04	18.49 ± 0.03	16.13 ± 0.10	15.46 ± 0.14	15.05 ± 0.15	3
154050.74+503324.4	···	L0	20.57 ± 0.04	18.91 ± 0.04	16.66 ± 0.14	16.42 ± 0.27	15.70 ± 0.26	3
154343.91-014737.2	···	L0	20.17 ± 0.03	18.39 ± 0.03	15.96 ± 0.09	15.26 ± 0.10	14.95 ± 0.15	1
154501.09+033714.3	···	L0	20.39 ± 0.05	18.74 ± 0.04	16.34 ± 0.09	15.63 ± 0.13	15.29 ± 0.15	1
154502.88+061807.8	···	L1	20.85 ± 0.05	18.84 ± 0.04	16.37 ± 0.11	15.60 ± 0.12	15.28 ± 0.16	8
154625.94+160917.9	···	L0	19.82 ± 0.03	18.05 ± 0.03	15.71 ± 0.05	14.81 ± 0.06	14.19 ± 0.06	3
154628.39+253634.3	···	L0	20.15 ± 0.03	18.11 ± 0.03	15.76 ± 0.07	15.07 ± 0.08	14.71 ± 0.08	8
154727.23+033636.3	···	L3	20.45 ± 0.05	18.72 ± 0.04	16.08 ± 0.07	15.07 ± 0.06	14.27 ± 0.07	2
154849.02+172235.3	···	L8	21.34 ± 0.08	18.84 ± 0.04	16.10 ± 0.11	15.14 ± 0.11	14.46 ± 0.08	21
154910.12+551203.2	···	L3	20.86 ± 0.06	18.88 ± 0.04	16.49 ± 0.13	15.52 ± 0.10	15.17 ± 0.17	3
154914.17+502235.8	···	L0	20.64 ± 0.05	18.86 ± 0.04	16.26 ± 0.09	15.70 ± 0.12	15.20 ± 0.14	3
154951.38+490450.1	···	L0	20.71 ± 0.05	18.84 ± 0.04	16.25 ± 0.10	15.32 ± 0.12	15.07 ± 0.16	1
155008.50+145517.0	2MASS J15500845+1455180	L3	19.58 ± 0.02	17.71 ± 0.02	14.78 ± 0.04	13.80 ± 0.04	13.26 ± 0.03	16
155120.86+432930.3	···	L3	19.58 ± 0.02	17.71 ± 0.02	15.13 ± 0.04	14.20 ± 0.05	13.63 ± 0.04	3
155132.71+544201.2	···	L0	20.04 ± 0.04	18.10 ± 0.03	14.86 ± 0.04	14.04 ± 0.04	13.50 ± 0.05	3
155215.39+065041.5	···	L0	21.01 ± 0.05	19.00 ± 0.04	16.78 ± 0.15	15.91 ± 0.14	15.63 ± 0.21	8
155252.32-003501.9	···	L0	20.04 ± 0.04	18.10 ± 0.03	15.99 ± 0.09	15.40 ± 0.12	15.01 ± 0.13	1
155259.02+294848.3	2MASSW J1552591+294849	L0	18.11 ± 0.02	16.22 ± 0.02	13.48 ± 0.02	12.61 ± 0.02	12.02 ± 0.03	19
155644.35+172308.9	···	L0	19.13 ± 0.02	17.26 ± 0.02	14.67 ± 0.03	13.87 ± 0.05	13.35 ± 0.04	3
160140.86+215945.4	···	L1	20.78 ± 0.04	18.79 ± 0.04	16.27 ± 0.10	15.48 ± 0.11	15.13 ± 0.17	3
160510.15+042152.1	···	L0	19.47 ± 0.02	17.71 ± 0.03	15.24 ± 0.05	14.38 ± 0.04	13.82 ± 0.04	1
160743.08+345947.3	···	L0	19.91 ± 0.04	17.95 ± 0.03	15.42 ± 0.04	14.51 ± 0.06	13.96 ± 0.04	1
161106.31+002547.0	···	L0	21.42 ± 0.09	19.53 ± 0.05	17.02 ± 0.21	16.53 ± 0.27	15.83 ± 0.26	3
161312.06+472918.2	···	L0	20.27 ± 0.03	18.41 ± 0.03	15.96 ± 0.08	15.23 ± 0.09	14.79 ± 0.13	1
161349.44+134608.6	···	L0	20.20 ± 0.04	18.48 ± 0.03	···	···	···	3
161420.49+004643.5	···	L2	20.84 ± 0.06	19.07 ± 0.05	16.23 ± 0.10	15.59 ± 0.13	14.85 ± 0.11	2

Table 2.1 (cont'd)

SDSS Designation (SDSS J +)	Other Name	ST	i	z	J	H	K_S	Discovery Reference
161544.16+355858.3	2MASSW J1615441+355900	L4	19.20 ± 0.02	17.30 ± 0.02	14.54 ± 0.03	13.52 ± 0.03	12.94 ± 0.03	7
161611.36+521327.9	···	L0	19.96 ± 0.04	17.96 ± 0.03	15.40 ± 0.04	14.63 ± 0.05	14.18 ± 0.07	1
161840.27+202045.6	···	L0	20.62 ± 0.03	18.60 ± 0.03	16.15 ± 0.09	15.20 ± 0.07	14.81 ± 0.09	3
161928.30+005011.7	···	L2	18.88 ± 0.02	17.05 ± 0.01	14.39 ± 0.03	13.67 ± 0.04	13.19 ± 0.04	2
162124.66+274702.7	···	L1	20.43 ± 0.04	18.76 ± 0.03	16.44 ± 0.12	15.73 ± 0.14	15.54 ± 0.19	3
162208.04+454813.0	···	L1	20.29 ± 0.03	18.35 ± 0.03	15.86 ± 0.07	15.08 ± 0.08	14.44 ± 0.09	1
162307.37+290827.7	···	L1	20.57 ± 0.05	18.63 ± 0.04	16.08 ± 0.09	15.50 ± 0.11	14.97 ± 0.10	3
162321.84+153039.2	···	L0	20.12 ± 0.03	18.29 ± 0.03	15.94 ± 0.09	15.13 ± 0.08	14.63 ± 0.08	3
162559.01+334705.4	···	L0	19.67 ± 0.03	17.82 ± 0.03	15.62 ± 0.05	14.69 ± 0.06	14.23 ± 0.05	1
162603.03+211313.0	···	L3	20.56 ± 0.04	18.41 ± 0.03	15.48 ± 0.05	14.59 ± 0.06	13.92 ± 0.05	3
162834.35+242847.2	···	L1	20.12 ± 0.03	18.28 ± 0.03	15.90 ± 0.07	15.00 ± 0.08	14.48 ± 0.09	3
162838.35+625945.7	···	L0	20.12 ± 0.03	18.29 ± 0.03	15.77 ± 0.07	15.16 ± 0.09	14.66 ± 0.11	3
163041.37+093844.3	2MASS J16304139+0938446	L0	19.49 ± 0.02	17.55 ± 0.02	14.87 ± 0.03	13.94 ± 0.04	13.30 ± 0.04	9
163050.00+005101.3	···	L3	20.48 ± 0.04	18.76 ± 0.04	16.00 ± 0.08	15.25 ± 0.06	14.62 ± 0.08	2
163142.02+243359.7	···	L0	20.71 ± 0.05	18.85 ± 0.05	···	···	···	3
163355.23+010027.0	···	L0	19.55 ± 0.02	17.88 ± 0.02	15.61 ± 0.05	15.04 ± 0.05	14.49 ± 0.09	1
163600.79-003452.5	···	L0	18.80 ± 0.02	16.88 ± 0.02	14.59 ± 0.04	13.90 ± 0.04	13.42 ± 0.04	5
163655.90+002526.3	···	L1	21.03 ± 0.06	19.50 ± 0.05	···	···	···	3
163817.31+321144.0	···	L0	19.83 ± 0.03	17.93 ± 0.03	15.39 ± 0.05	14.64 ± 0.05	14.16 ± 0.07	1
164230.27+202048.1	···	L1	20.47 ± 0.04	18.74 ± 0.04	16.22 ± 0.11	15.31 ± 0.12	14.67 ± 0.12	3
164438.14+284614.5	···	L2	19.91 ± 0.03	18.04 ± 0.03	15.66 ± 0.07	14.69 ± 0.06	14.18 ± 0.08	3
164439.66+260013.3	···	L1	19.92 ± 0.03	17.97 ± 0.03	15.47 ± 0.05	14.71 ± 0.06	14.21 ± 0.09	3
164522.06+300406.9	2MASS J16452207+3004071	L3	19.77 ± 0.04	17.95 ± 0.03	15.19 ± 0.04	14.21 ± 0.04	13.59 ± 0.04	16
164540.16+290744.5	···	L0	20.71 ± 0.04	18.86 ± 0.04	···	···	···	1
165031.33+352359.5	···	L2	20.19 ± 0.03	18.40 ± 0.03	15.82 ± 0.07	14.89 ± 0.08	14.54 ± 0.09	3
165301.98+413847.5	···	L0	20.76 ± 0.05	18.90 ± 0.05	16.73 ± 0.17	16.22 ± 0.27	15.48 ± 0.20	3
165309.93+245039.8	···	L0	20.68 ± 0.04	18.77 ± 0.03	16.59 ± 0.16	15.87 ± 0.18	15.40 ± 0.16	3
165329.69+623136.4	···	L2	19.52 ± 0.03	17.61 ± 0.02	···	···	···	2
165450.79+374714.6	···	L2	19.30 ± 0.02	17.44 ± 0.02	15.01 ± 0.04	14.18 ± 0.04	13.66 ± 0.04	3
165850.26+182000.5	···	L0	19.93 ± 0.03	18.11 ± 0.02	15.48 ± 0.06	14.91 ± 0.07	14.57 ± 0.10	1
170219.44+385841.2	···	L1	21.05 ± 0.06	19.20 ± 0.05	16.89 ± 0.18	15.95 ± 0.17	15.17 ± 0.14	3
170302.53+355824.2	···	L0	19.04 ± 0.02	17.27 ± 0.02	15.07 ± 0.03	14.41 ± 0.05	13.97 ± 0.05	1
171113.52+232633.2	2MASS J17111353+2326333	L0	19.09 ± 0.02	17.17 ± 0.02	14.50 ± 0.02	13.67 ± 0.03	13.06 ± 0.03	16
171319.23+292816.1	···	L0	···	···	16.23 ± 0.09	15.59 ± 0.09	14.86 ± 0.10	3
172244.26+632946.9	···	L0	19.67 ± 0.04	17.82 ± 0.02	15.37 ± 0.05	14.55 ± 0.05	14.08 ± 0.07	2
172543.84+532534.9	···	L1	18.64 ± 0.02	17.12 ± 0.02	15.16 ± 0.04	14.62 ± 0.06	14.21 ± 0.08	3

Table 2.1 (cont'd)

SDSS Designation (SDSS J +)	Other Name	ST	i	z	J	H	K_S	Discovery Reference
172822.18+584509.8	···	L2	21.03 ± 0.07	19.07 ± 0.05	···	···	···	2
205755.92-005006.7	···	L0	19.07 ± 0.02	17.20 ± 0.02	14.97 ± 0.03	14.23 ± 0.04	13.77 ± 0.04	1
211846.76-001044.6	···	L0	20.89 ± 0.06	18.78 ± 0.04	16.20 ± 0.11	15.62 ± 0.16	15.07 ± 0.13	8
214046.53+011259.2	···	L4	21.10 ± 0.08	18.96 ± 0.05	15.89 ± 0.08	15.31 ± 0.09	14.42 ± 0.08	2
214527.82-073434.1	···	L0	19.81 ± 0.03	18.03 ± 0.03	15.59 ± 0.07	14.92 ± 0.08	14.31 ± 0.08	1
215125.92-000200.7	···	L0	19.97 ± 0.03	18.18 ± 0.03	15.75 ± 0.07	15.09 ± 0.09	14.86 ± 0.12	3
221743.53+000253.8	···	L1	20.99 ± 0.06	19.39 ± 0.07	···	···	···	3
222000.97+121436.5	···	L0	20.61 ± 0.05	18.61 ± 0.04	···	···	···	1
222412.13+001040.8	···	L0	19.98 ± 0.03	18.24 ± 0.03	15.90 ± 0.07	15.16 ± 0.10	14.74 ± 0.10	1
223550.14+122737.3	···	L0	19.18 ± 0.02	17.47 ± 0.02	15.21 ± 0.04	14.50 ± 0.05	14.04 ± 0.07	1
225529.07-003434.0	···	L0	19.84 ± 0.02	17.93 ± 0.02	15.65 ± 0.05	14.76 ± 0.06	14.44 ± 0.08	4
233358.42+005012.1	···	L0	19.19 ± 0.02	17.37 ± 0.02	15.01 ± 0.04	14.40 ± 0.04	13.84 ± 0.05	1
233526.42+081721.3	···	L0	19.08 ± 0.01	17.32 ± 0.02	14.72 ± 0.03	13.95 ± 0.04	13.38 ± 0.03	3
233615.99+004253.4	···	L0	20.91 ± 0.07	19.06 ± 0.04	17.08 ± 0.20	15.71 ± 0.14	15.29 ± 0.16	3
234034.42-001351.6	···	L1	20.75 ± 0.06	18.87 ± 0.05	···	···	···	3
234406.88+011515.6	···	L3	20.81 ± 0.06	18.99 ± 0.05	16.41 ± 0.10	15.73 ± 0.16	15.04 ± 0.11	3

References. — (1) West et al. (2008); (2) Hawley et al. (2002); (3) this paper; (4) Schneider et al. (2002); (5) Fan et al. (2000); (6) Reid et al. (2000); (7) Kirkpatrick et al. (2000); (8) Zhang et al. (2009); (9) Reid et al. (2008); (10) Geballe et al. (2002); (11) Cruz et al. (2003); (12) Kirkpatrick et al. (1999); (13) Knapp et al. (2004) (14) Martín et al. (1999); (15) Sheppard & Cushing (2009); (16) Cruz et al. (2007); (17) Schmidt et al. (2010b); (18) Probst & Liebert (1984); (19) Wilson et al. (2003); (20) Kendall et al. (2007); (21) Chiu et al. (2006)

Table 2.2. Activity

SDSS Designation (SDSS J +)	Other Name	ST	Active?	Hα EW (Å)
074227.46+412620.8	···	L0	y	12.93 ± 0.84
074642.42+200031.8	2MASSI J0746425+200032	L1	y	2.44 ± 0.15
081301.02+322807.9	···	L3	n	0.09 ± 0.00
092308.70+234013.7	···	L1	n	3.47 ± 0.52
093600.12+043147.9	···	L2	n	-0.54 ± 1.35
101707.55+130839.3	2MASSI J1017075+130839	L2	y	7.20 ± 0.74
102204.88+020047.5	···	L0	n	0.44 ± 0.61
102921.85+162649.8[1]	2MASSI J1029216+162652	L3	y	3.60 ± 1.05
104842.80+011158.0[2]	···	L1	y	5.39 ± 0.37
105118.96+561308.0	2MASS J10511900+5613086	L1	y	1.75 ± 0.41
111736.93+360935.9	2MASSI J1117369+360936	L0	y	3.32 ± 0.98
114634.52+223053.1	2MASSW J1146345+223053	L3	y	1.66 ± 0.74
115339.67+503209.4	2MASS J11533966+5032092	L0	m	2.48 ± 0.90
115938.50+005726.9	DENIS-P J1159+0057	L0	y	2.13 ± 0.71
120249.99+420452.1	···	L0	y	4.05 ± 1.01
120430.38+321259.4	2MASSI J1204303+321259	L0	y	1.80 ± 0.57
122127.70+025719.7[3]	2MASS J12212770+0257198	L0	y	7.47 ± 0.36
130617.23+382029.6	2MASS J13061727+3820296	L0	m	2.98 ± 0.68
133132.98+340757.5	2MASS J13313310+3407583	L0	y	2.96 ± 0.72
133640.53+374322.6[4]	2MASS J13364062+3743230	L1	y	2.64 ± 0.94
133849.45+043731.2[5]	2MASS J13384944+0437315	L1	y	8.06 ± 0.72
135439.54+504451.0	···	L1	y	2.64 ± 0.81
140444.86+463430.4	2MASS J14044495+4634297	L0	y	7.82 ± 1.07
141624.09+134826.7	···	L6	n	-0.16 ± 0.43
142843.13+331036.8[6]	LHS 2924	L0	y	4.48 ± 0.34
143043.51+291541.3	2MASSI J1430435+291540	L2	n	0.53 ± 0.82
155259.02+294848.3	2MASSW J1552591+294849	L0	y	1.93 ± 0.55
161928.30+005011.7	···	L2	m	1.85 ± 0.78
163600.79−003452.5	···	L0	y	3.80 ± 0.72
165329.69+623136.4	···	L2	y	3.55 ± 1.03
172543.84+532534.9	···	L1	y	5.30 ± 0.85
233526.42+081721.3	···	L0	y	4.07 ± 0.60

[1]EW = 0.5Å (Kirkpatrick et al. 2000); EW = 1.96Å (Reiners & Basri 2008)

[2]EW = 1.08Å, EW = 3.19Å (Reiners & Basri 2008)

[3]EW = 6Å (Schmidt et al. 2007); EW = 5.01Å, EW = 25.65Å (Reiners & Basri 2008)

[4]EW = 15Å, EW <5Å (hour apart) (Schmidt et al. 2007)

[5]EW = 11ÅEW = 28Å (year apart) (Schmidt et al. 2007)

[6]EW = 5Å (Schmidt et al. 2007); EW = 5.76Å (Reiners et al. 2007)

Table 2.3. Median Colors

	$i-z$			$i-J$			$z-J$			$z-K_S$			$J-K_S$		
ST	N	median	σ	N	median	σ	N	median	σ	N	median	σ	N	median	σ
L0	301	1.85 ± 0.01	0.10	243	4.23 ± 0.01	0.17	243	2.39 ± 0.01	0.14	238	3.59 ± 0.01	0.22	289	1.24 ± 0.01	0.18
L1	100	1.86 ± 0.01	0.10	84	4.39 ± 0.02	0.18	85	2.51 ± 0.02	0.14	88	3.82 ± 0.03	0.26	135	1.34 ± 0.02	0.19
L2	34	1.85 ± 0.01	0.08	29	4.40 ± 0.02	0.10	30	2.58 ± 0.03	0.15	30	4.04 ± 0.05	0.30	76	1.48 ± 0.02	0.20
L3	50	1.88 ± 0.02	0.13	46	4.54 ± 0.03	0.23	46	2.64 ± 0.02	0.17	49	4.15 ± 0.05	0.34	83	1.60 ± 0.02	0.22
L4	13	2.13 ± 0.05	0.19	12	4.97 ± 0.07	0.24	12	2.81 ± 0.04	0.14	14	4.59 ± 0.07	0.25	36	1.77 ± 0.05	0.30
L5	10	2.16 ± 0.02	0.07	10	4.97 ± 0.04	0.13	14	2.82 ± 0.04	0.14	14	4.69 ± 0.11	0.43	42	1.78 ± 0.05	0.31
L6	4	2.43 ± 0.11	0.23	3	5.22 ± 0.14	0.24	7	2.75 ± 0.04	0.10	9	4.25 ± 0.08	0.24	20	1.82 ± 0.07	0.29
L7	6	2.59 ± 0.08	0.19	6	5.29 ± 0.11	0.26	9	2.72 ± 0.05	0.15	10	4.54 ± 0.08	0.25	16	1.77 ± 0.05	0.22
L8	4	2.81 ± 0.11	0.21	4	5.48 ± 0.09	0.18	9	2.73 ± 0.03	0.08	10	4.57 ± 0.08	0.24	15	1.73 ± 0.04	0.17
L9	0	···	···	0	···	···	1	2.73	···	2	4.34 ± 0.07	0.10	1	1.46	···
T0	0	···	···	0	···	···	3	3.08 ± 0.11	0.19	3	4.53 ± 0.07	0.12	4	1.47 ± 0.11	0.22
T1	0	···	···	0	···	···	2	2.74 ± 0.06	0.08	2	4.32 ± 0.36	0.51	5	1.21 ± 0.20	0.46
T2	0	···	···	0	···	···	3	3.14 ± 0.05	0.08	3	4.20 ± 0.18	0.32	6	1.05 ± 0.12	0.29
T3	0	···	···	0	···	···	0	···	···	0	···	···	1	0.85	···
T4	0	···	···	0	···	···	1	3.11	···	0	···	···	1	0.36	···
T5	0	···	···	0	···	···	1	3.37	···	0	···	···	2	0.23 ± 0.12	0.16
T6	1	2.29	···	1	5.57	···	2	3.33 ± 0.03	0.04	1	3.30	···	5	0.19 ± 0.20	0.46

Table 2.4. Median $J - K_S$ Colors

	All Dwarfs			SDSS Spectra			Dwarf Archives		
ST	N	median	σ	N	median	σ	N	median	σ
L0	289	1.24 ± 0.01	0.18	218	1.20 ± 0.01	0.15	102	1.33 ± 0.02	0.18
L1	135	1.34 ± 0.02	0.19	75	1.29 ± 0.02	0.19	74	1.36 ± 0.02	0.19
L2	76	1.48 ± 0.02	0.20	25	1.45 ± 0.03	0.15	59	1.49 ± 0.03	0.21
L3	83	1.60 ± 0.02	0.22	40	1.52 ± 0.03	0.19	64	1.65 ± 0.03	0.23
L4	36	1.77 ± 0.05	0.30	3	1.47 ± 0.10	0.18	35	1.77 ± 0.05	0.29
L5	42	1.78 ± 0.05	0.31	8	1.82 ± 0.08	0.23	42	1.78 ± 0.05	0.31
L6	20	1.82 ± 0.07	0.29	4	1.61 ± 0.16	0.32	19	1.82 ± 0.06	0.25
L7	16	1.77 ± 0.05	0.22	3	1.77 ± 0.20	0.34	15	1.74 ± 0.06	0.22
L8	15	1.73 ± 0.04	0.17	5	1.65 ± 0.09	0.20	15	1.73 ± 0.04	0.17

Table 2.5. Dwarfs with parallaxes and SDSS photometry

SDSS coordinates	ST	M_i	$i - z$	$i - J$	plx ref
03 20 59.8 +18 54 20.9	M8	14.85 ± 0.03	1.68 ± 0.02	3.92 ± 0.02	1
14 35 17.2 -00 46 12.8	L0	15.32 ± 1.14	1.78 ± 0.05	3.87 ± 0.11	2
15 10 16.7 -02 41 07.8	M9	15.68 ± 0.17	1.76 ± 0.02	4.13 ± 0.02	3
22 55 29.0 -00 34 34.0	L0	15.88 ± 0.35	1.91 ± 0.03	4.19 ± 0.06	2
15 01 08.1 +22 50 01.7	M8.5	15.96 ± 0.02	1.79 ± 0.02	4.22 ± 0.02	1
14 28 43.1 +33 10 36.8	M9	15.99 ± 0.03	1.81 ± 0.02	4.21 ± 0.02	4
14 35 35.7 -00 43 47.1	L3	16.89 ± 0.78	1.82 ± 0.07	4.37 ± 0.13	2
13 28 55.1 +21 14 46.0	L5	18.84 ± 0.28	2.33 ± 0.09	5.19 ± 0.13	1
17 11 45.7 +22 32 04.3	L6.5	19.75 ± 0.36	2.33 ± 0.19	5.06 ± 0.25	2
01 07 52.4 +00 41 56.3	L8	20.21 ± 0.17	2.57 ± 0.08	5.35 ± 0.09	2
08 25 19.4 +21 15 50.2	L7	20.46 ± 0.06	2.82 ± 0.06	5.50 ± 0.06	1
08 30 08.1 +48 28 47.3	L8	20.64 ± 0.13	3.15 ± 0.09	5.78 ± 0.09	2
16 32 29.2 +19 04 40.3	L8	20.77 ± 0.17	3.11 ± 0.16	5.81 ± 0.17	1

References. — (1) Dahn et al. (2002); (2) Vrba et al. (2004); (3) Tinney et al. (1995); (4) Monet et al. (1992)

Table 2.6. Kinematics

SDSS Designation (SDSS J +)	Other Name	Spectral Type	ST ref	μ_{RA} (mas yr^{-1})	μ_{dec} (mas yr^{-1})	μ ref	distance (pc)	radial velocity (km s^{-1})	U (km s^{-1})	V (km s^{-1})	W (km s^{-1})
000250.97+245413.8	···	L5.5	1	3.0 ± 23.1	-57.8 ± 50.9	2	50.3 ± 10.4	···	···	···	···
000632.60+140606.3	···	L0	2	74.1 ± 44.6	-42.2 ± 42.9	2	63.0 ± 12.0	26.80 ± 13.70	-8.86 ± 13.47	4.58 ± 13.72	-24.80 ± 13.51
001637.62-103911.1	···	L0	2	-46.5 ± 63.8	-263.1 ± 44.5	2	32.9 ± 6.3	25.20 ± 13.40	36.05 ± 10.61	-17.24 ± 10.30	-27.66 ± 13.10
001911.64+003017.6	···	L0	2	-29.0 ± 18.0	-25.0 ± 11.0	3	49.4 ± 9.4	-4.50 ± 15.30	19.30 ± 4.66	1.86 ± 7.60	9.08 ± 13.49
002209.33-011039.7	···	L0	2	···	···	···	66.2 ± 12.7	31.80 ± 17.80	···	···	···
002611.45-094341.1	···	L1	2	···	···	···	61.9 ± 11.8	-20.70 ± 3.10	···	···	···
002855.49-192716.3	2MASS J00285545-1927165	L0:	4	99.5 ± 19.2	32.2 ± 20.9	2	23.9 ± 4.6	···	···	···	···
003524.44+144739.7	···	L2	2	···	···	···	104.6 ± 20.6	-2.40 ± 10.20	···	···	···
003609.26+241343.2	···	L5.5	1	26.5 ± 62.3	-40.7 ± 26.6	2	30.3 ± 8.0	···	···	···	···
003843.99+134339.4	···	L1	2	58.4 ± 72.4	-86.8 ± 33.0	2	47.2 ± 9.1	28.00 ± 12.70	-1.61 ± 14.71	2.15 ± 12.66	-27.50 ± 11.07
004058.92+152845.0	···	L1	2	···	···	···	117.7 ± 22.7	-16.00 ± 9.60	···	···	···
004221.15+145923.8	···	L0	2	···	···	···	46.6 ± 9.1	-14.20 ± 20.00	···	···	···
004648.45+071517.4	2MASS J00464841+0715177	L0::	4	115.1 ± 25.2	-58.0 ± 15.8	2	13.1 ± 2.5	···	···	···	···
005406.60-003102.4	···	L3	2	231.5 ± 42.4	-201.1 ± 29.3	2	55.0 ± 10.5	-5.70 ± 13.00	-13.56 ± 11.54	-69.56 ± 16.86	-10.78 ± 12.88
005705.56-084624.1	···	L0	2	···	···	···	59.8 ± 11.5	-5.50 ± 16.30	···	···	···
010407.60-005328.5	2MASSI J0104075-005328	L4.5	5	454.1 ± 77.5	-66.7 ± 29.4	2	35.1 ± 6.9	···	···	···	···
010718.70+132656.1	···	L0	2	···	···	···	36.1 ± 7.0	25.50 ± 12.50	···	···	···
010752.47+004156.3	···	L8	6	595.0 ± 73.7	-18.2 ± 121.2	2	16.9 ± 3.3	···	···	···	···
010840.48+134739.2	···	L0	2	···	···	···	72.8 ± 14.1	-11.60 ± 10.90	···	···	···
010859.24-104546.3	···	L0	2	···	···	···	72.8 ± 14.1	20.50 ± 6.30	···	···	···
011816.78+141841.4	···	L1	2	···	···	···	98.9 ± 19.3	-7.60 ± 15.00	···	···	···
014658.14+002132.7	···	L0	2	···	···	···	56.1 ± 10.8	-11.50 ± 10.0	···	···	···
015141.68+124429.5	···	T1	7	887.0 ± 78.8	-236.0 ± 83.9	2	···	···	···	···	···
015354.23+140452.8	···	L0	2	···	···	···	31.1 ± 5.9	16.20 ± 6.80	···	···	···
020529.59-115929.7	DENIS-P J0205.4-1159	L7	8	467.1 ± 30.3	-18.9 ± 32.2	2	9.2 ± 1.8	···	···	···	···
020551.36-075925.0	···	L3	2	···	···	···	54.9 ± 10.6	-14.40 ± 9.30	···	···	···
020608.97+223559.0	···	L5.5	1	349.2 ± 30.3	-38.3 ± 13.0	2	21.9 ± 4.6	···	···	···	···
020735.59+135556.2	···	L3	2	260.0 ± 17.0	-161.0 ± 18.0	9	61.3 ± 11.7	13.70 ± 10.0	-35.97 ± 10.22	-70.25 ± 16.43	-10.94 ± 8.12
021248.51+221822.0	···	L0	2	···	···	···	112.3 ± 21.9	5.20 ± 14.34	···	···	···
022754.95+002619.9	···	L0	2	···	···	···	91.3 ± 42.9	1.60 ± 8.40	···	···	···
023015.61+270406.0	2MASS J02301551+2704061	L0:	10	191.9 ± 18.6	-20.4 ± 11.6	2	34.7 ± 6.6	···	···	···	···
023547.55-084919.9	···	L2	2	-44.0 ± 13.0	13.0 ± 13.0	9	46.1 ± 8.8	22.80 ± 6.10	2.94 ± 4.05	13.20 ± 3.27	-15.43 ± 5.47
024256.98+212319.6	···	L4	1	96.6 ± 47.7	-108.9 ± 17.5	2	53.3 ± 11.2	···	···	···	···
030321.24-000938.3	···	L0	11	48.4 ± 60.9	-135.8 ± 25.4	2	57.9 ± 11.1	···	···	···	···
030536.55-064216.1	···	L0	2	···	···	···	78.7 ± 15.2	-50.10 ± 18.50	···	···	···
031740.38+061303.8	···	L3	2	11.4 ± 21.2	-166.6 ± 42.6	2	57.8 ± 11.2	-14.16 ± 10.78	37.43 ± 10.36	-31.96 ± 11.84	-6.20 ± 10.86
033035.19-002535.7	···	L5	2	414.8 ± 29.6	-355.2 ± 51.7	2	25.0 ± 4.8	-20.80 ± 20.00	21.75 ± 14.90	-57.65 ± 13.29	30.30 ± 14.26
035048.62-051812.8	···	L0	2	12.0 ± 22.0	-28.0 ± 22.0	9	74.0 ± 14.4	-1.10 ± 16.60	14.45 ± 13.11	-4.76 ± 8.38	6.49 ± 12.52
035104.35+481046.7	···	T1+/-1.5	1	263.4 ± 34.5	-214.5 ± 18.5	2	···	···	···	···	···
035308.54+103056.0	···	L1	2	188.4 ± 32.6	-73.9 ± 28.4	2	32.9 ± 6.3	16.72 ± 8.82	-12.43 ± 8.06	-22.63 ± 7.13	10.28 ± 6.62
035523.48+113339.3	2MASS J03552337+1133437	L5gamma	12	241.1 ± 24.2	-631.2 ± 17.9	2	19.4 ± 3.7	···	···	···	···
035721.12-064125.9	···	L0	2	133.3 ± 58.9	60.1 ± 36.5	2	44.4 ± 8.5	38.70 ± 14.50	-36.17 ± 12.82	-12.48 ± 10.46	4.31 ± 13.56
040707.56+154645.2	2MASS J04070752+1546457	L3.5	4	81.8 ± 26.1	-75.8 ± 29.6	2	45.6 ± 8.7	···	···	···	···
042230.66+072342.9	···	L1	2	198.5 ± 22.0	-275.3 ± 18.7	2	53.5 ± 10.2	29.08 ± 12.92	-4.88 ± 11.73	-83.52 ± 17.16	-7.56 ± 7.72
050213.49+144236.6	2MASSI J0502134+144236	L0	13	66.6 ± 12.7	-11.2 ± 15.0	2	29.9 ± 5.7	···	···	···	···
053012.60+625325.2	2MASS J05301261+6253254	L1	4	-11.0 ± 14.3	-47.1 ± 8.0	2	29.0 ± 5.5	···	···	···	···
060222.14+633637.9	2MASS J06022216+6336391	L1:	4	-27.4 ± 11.8	-202.5 ± 5.5	2	30.1 ± 5.7	···	···	···	···
063206.15+830501.1	2MASS J06320617+8305014	L0.5	4	-5.2 ± 1.8	-44.8 ± 13.2	2	18.1 ± 3.5	···	···	···	···
065405.61+652805.7	···	L6+/-1	1	-25.0 ± 14.1	94.1 ± 16.1	2	38.2 ± 7.3	···	···	···	···

Table 2.6 (cont'd)

SDSS Designation (SDSS J +)	Other Name	Spectral Type	ST ref	μ_{RA} (mas yr^{-1})	μ_{dec} (mas yr^{-1})	μ ref	distance (pc)	radial velocity (km s^{-1})	U (km s^{-1})	V (km s^{-1})	W (km s^{-1})
070821.36+295033.3	2MASSW J0708213+295035	L5	14	50.6 ± 22.5	-196.9 ± 13.9	2	27.9 ± 5.7	···	···	···	···
073519.58+410850.3	···	L0	2	-186.6 ± 20.0	-114.4 ± 16.8	2	41.1 ± 7.9	12.90 ± 11.90	-19.59 ± 11.40	-6.09 ± 4.00	-24.44 ± 9.37
074007.07+200920.9	···	L6+/-1.5	1	-127.8 ± 24.1	-149.4 ± 72.2	2	28.9 ± 7.7	···	···	···	···
074227.46+412620.8	···	L0	2	-217.5 ± 33.3	-192.3 ± 45.9	2	39.6 ± 7.5	28.30 ± 17.00	-37.87 ± 16.05	-18.63 ± 9.70	-23.40 ± 12.59
074434.60+320705.1	···	L0	2	-120.0 ± 57.0	-95.0 ± 55.8	2	55.3 ± 10.7	-94.50 ± 9.50	81.61 ± 11.05	0.70 ± 14.92	-66.46 ± 15.58
074515.07+254619.1	···	L1	2	···	···	···	58.0 ± 11.2	5.60 ± 6.30	···	···	···
074642.42+200031.8	2MASSI J0746425+200032	L1	2	-376.8 ± 7.5	-72.2 ± 14.0	2	8.6 ± 1.6	51.90 ± 2.70	-41.66 ± 2.65	-10.91 ± 1.04	11.12 ± 2.91
074656.83+251019.1	···	L0	2	···	···	···	101.6 ± 47.7	35.10 ± 11.50	···	···	···
074756.32+394732.8	···	L0	2	84.6 ± 35.2	-52.6 ± 48.1	2	42.6 ± 8.1	5.70 ± 7.50	11.37 ± 7.56	-9.40 ± 9.98	22.12 ± 7.72
075004.93+330617.9	···	L0	2	-106.6 ± 30.4	-45.7 ± 50.0	2	78.4 ± 15.0	···	···	···	···
075332.13+291711.3	2MASSI J0753321+291711	L3	2	-127.1 ± 38.5	-139.6 ± 41.5	2	55.3 ± 10.6	···	···	···	···
075547.87+221215.6	2MASSI J0755480+221218	T6	15	-267.6 ± 39.7	-301.2 ± 39.7	2	27.2 ± 5.3	···	···	···	···
075625.29+124455.3	2MASSI J0756252+124456	L6	14	-2.0 ± 22.9	-104.8 ± 12.5	2	30.3 ± 6.0	···	···	···	···
075656.35+231457.0	···	L3.5+/-1	1	140.3 ± 19.3	-171.7 ± 31.0	2	32.9 ± 7.7	···	···	···	···
075840.32+324723.2	···	T2	7	-170.0 ± 28.7	-351.4 ± 22.4	2	···	···	···	···	···
075910.44+242712.4	···	L0	2	8.9 ± 33.4	-237.2 ± 30.5	2	42.9 ± 8.2	61.50 ± 11.60	-35.71 ± 10.69	-57.11 ± 11.06	19.81 ± 8.23
080027.57+551134.1	···	L1	2	-11.4 ± 16.8	-113.5 ± 11.8	2	28.0 ± 5.3	-4.70 ± 11.80	8.24 ± 9.72	-10.13 ± 4.28	2.59 ± 6.49
080048.13+465825.6	···	L3	2	-103.8 ± 47.9	12.7 ± 58.2	2	50.8 ± 9.7	-29.30 ± 16.40	23.36 ± 15.45	9.72 ± 14.04	-28.94 ± 13.62
080054.27+241316.8	···	L0	2	-26.6 ± 33.4	-85.0 ± 28.8	2	71.2 ± 13.6	21.20 ± 11.40	-8.54 ± 11.33	-25.92 ± 11.03	-0.34 ± 11.58
080140.52+462849.0	2MASSW J0801405+462850	L6.5	14	-209.6 ± 89.3	-392.8 ± 40.8	2	19.1 ± 3.7	···	···	···	···
080159.51+480628.5	···	L0	2	-8.3 ± 24.7	55.3 ± 14.6	2	38.8 ± 7.4	-51.60 ± 19.20	55.01 ± 16.37	8.34 ± 4.24	-20.05 ± 10.70
080255.74+332143.6	···	L2	2	76.2 ± 46.4	-85.7 ± 34.7	2	78.9 ± 15.2	···	···	···	···
080322.77+123845.3	···	L3	2	-66.2 ± 21.5	-95.2 ± 21.1	2	33.3 ± 6.4	4.10 ± 10.90	6.22 ± 9.05	-7.85 ± 6.16	-6.11 ± 5.81
080519.69+492504.7	···	L0	2	···	···	···	59.0 ± 11.4	23.60 ± 16.50	···	···	···
080549.89+511312.6	···	L1	2	-19.1 ± 18.8	-86.0 ± 18.2	2	35.8 ± 6.8	-11.40 ± 19.90	14.05 ± 16.56	-10.56 ± 5.40	-2.76 ± 10.97
080550.06+533531.4	···	L0	2	-22.5 ± 15.2	-170.0 ± 28.7	2	86.1 ± 16.5	-37.30 ± 19.00	15.68 ± 16.83	-67.92 ± 17.25	-23.66 ± 11.64
080858.99+410741.1	···	L2	2	15.2 ± 47.0	-70.0 ± 60.0	2	36.5 ± 7.0	-16.80 ± 9.60	24.43 ± 9.25	-7.55 ± 10.59	-1.37 ± 8.62
081253.20+372104.2	···	L3	2	23.3 ± 27.9	-164.8 ± 21.6	2	53.5 ± 10.2	50.00 ± 20.00	-31.11 ± 17.41	-40.00 ± 9.82	30.78 ± 12.06
081301.02+322807.9	···	L3	2	-50.5 ± 36.1	1.1 ± 24.6	2	57.2 ± 10.9	-21.70 ± 8.90	21.26 ± 9.25	10.67 ± 6.85	-15.35 ± 9.69
081556.74+452411.8	···	L0	2	-11.0 ± 47.9	-54.0 ± 47.2	2	39.3 ± 7.6	51.90 ± 18.20	-35.80 ± 15.93	-0.46 ± 9.07	32.91 ± 12.49
081653.72+344535.7	···	L2	2	57.5 ± 33.9	-54.8 ± 33.8	2	54.1 ± 10.4	1.40 ± 10.70	16.78 ± 10.28	-11.28 ± 9.24	17.29 ± 9.47
081752.62+194727.5	···	L0	2	-84.0 ± 14.2	-68.4 ± 18.6	2	68.8 ± 13.1	45.60 ± 8.80	-36.86 ± 7.91	-27.51 ± 7.15	-1.65 ± 8.19
081757.49+182404.9	···	L1	2	9.2 ± 12.1	24.9 ± 17.2	2	29.2 ± 5.6	46.70 ± 14.20	-27.80 ± 11.50	-9.69 ± 5.82	30.44 ± 6.67
081802.24+582920.9	···	L0	2	45.7 ± 34.8	-45.6 ± 17.1	2	50.1 ± 9.7	-5.72 ± 5.79	16.66 ± 6.48	-8.59 ± 4.96	13.21 ± 7.79
081812.28+331048.2	···	L0	2	-187.3 ± 20.2	67.5 ± 35.2	2	65.6 ± 12.6	0.80 ± 18.00	-22.76 ± 16.69	34.46 ± 12.39	-36.52 ± 13.86
082029.92+450030.6	2MASSW J0820299+450031	L5	14	-132.2 ± 49.4	-296.2 ± 29.7	2	42.7 ± 8.4	···	···	···	···
082030.12+103736.9	···	L9.5+/-2	1	-58.0 ± 22.0	-42.0 ± 52.8	2	44.3 ± 10.1	···	···	···	···
082115.03+333651.3	···	L0	2	53.2 ± 22.6	125.7 ± 75.4	2	89.8 ± 42.2	-43.50 ± 17.00	57.38 ± 16.03	59.72 ± 39.15	12.58 ± 19.16
082346.99+154947.4	···	L1	2	-7.2 ± 9.8	-24.8 ± 22.4	2	78.0 ± 36.6	11.20 ± 10.40	2.35 ± 8.70	-7.58 ± 9.38	6.83 ± 6.78
082348.15+242857.9	2MASS J08234818+2428577	L3	2	-103.4 ± 31.0	65.9 ± 37.1	2	48.9 ± 9.3	40.60 ± 20.00	-38.90 ± 17.10	11.37 ± 10.54	12.06 ± 12.31
082519.45+211550.2	2MASSI J0825196+211552	L7	2	-516.2 ± 11.2	-295.8 ± 14.7	2	10.6 ± 2.0	20.50 ± 20.00	-17.89 ± 16.17	-12.24 ± 7.04	-8.40 ± 11.07
082539.88+310040.7	···	L1	2	7.4 ± 24.7	-102.3 ± 58.7	2	52.4 ± 10.	55.90 ± 10.20	-33.25 ± 9.16	-29.73 ± 15.16	33.40 ± 8.07
082612.27+544735.4	···	L0	2	-104.3 ± 55.5	-88.5 ± 15.7	2	63.9 ± 12.3	-3.60 ± 6.80	-12.20 ± 11.97	-17.49 ± 6.77	-20.06 ± 15.06
082906.61+145620.7	2MASSW J0829066+145622	L3	2	-53.4 ± 12.5	-254.8 ± 7.0	2	39.4 ± 7.5	-1.10 ± 9.40	19.26 ± 7.49	-35.66 ± 8.93	-18.07 ± 6.74
082928.21+343954.1	···	L0	2	47.3 ± 23.3	62.0 ± 52.7	2	47.3 ± 9.1	···	···	···	···
082957.04+265509.8	2MASSW J0829570+265510	L6.5	14	-72.4 ± 32.5	-25.3 ± 17.2	2	28.7 ± 6.1	···	···	···	···
083008.11+482847.3	···	L8	2	-1134.7 ± 78.8	-733.4 ± 54.1	2	12.9 ± 2.5	···	···	···	···
083027.24+220345.0	···	L0	2	-6.8 ± 15.0	-106.4 ± 22.6	2	43.4 ± 8.3	-4.00 ± 12.50	16.76 ± 10.12	-14.04 ± 7.12	-2.38 ± 7.18
083122.07+153850.3	···	L1	2	-281.7 ± 10.8	-113.2 ± 14.2	2	36.9 ± 7.0	0.20 ± 5.70	-12.97 ± 6.29	-7.05 ± 4.02	-39.35 ± 9.45

Table 2.6 (cont'd)

SDSS Designation (SDSS J +)	Other Name	Spectral Type	ST ref	μ_{RA} (mas yr^{-1})	μ_{dec} (mas yr^{-1})	μ ref	distance (pc)	radial velocity (km s^{-1})	U (km s^{-1})	V (km s^{-1})	W (km s^{-1})
083204.51-012836.0	2MASSW J0832045-012835	L1.5	14	-35.3 ± 27.9	18.2 ± 40.2	2	27.5 ± 5.2	···	···	···	···
083424.12+071916.2	···	L0	2	-456.4 ± 86.8	40.6 ± 32.7	2	105.1 ± 20.2	39.50 ± 16.70	-159.59 ± 39.57	24.47 ± 18.75	-149.75 ± 49.15
083429.19+230855.0	···	L1	2	-60.9 ± 20.4	-42.1 ± 13.0	2	86.6 ± 16.6	5.10 ± 2.90	-5.43 ± 5.93	-10.19 ± 5.81	-14.92 ± 8.47
083506.15+195304.2	···	L4.5	1	-167.5 ± 21.8	-124.2 ± 14.2	2	26.1 ± 5.1	···	···	···	···
083545.33+222430.8	···	L0	2	-118.7 ± 14.9	-43.3 ± 22.5	2	38.0 ± 7.2	71.50 ± 9.20	-56.91 ± 7.70	-23.14 ± 4.94	26.05 ± 6.60
083558.28+054830.7	2MASS J08355829+0548308	L2:	4	-102.6 ± 40.4	-27.6 ± 46.1	2	32.1 ± 6.1	···	···	···	···
083611.42+450319.5	···	L1	2	···	···	···	49.7 ± 9.5	-9.70 ± 16.70	···	···	···
083621.97+494931.5	···	L0	2	···	···	···	44.9 ± 8.6	-54.00 ± 16.30	···	···	···
083646.34+052642.6	···	L0	2	-61.9 ± 32.2	-1.4 ± 51.6	2	35.9 ± 6.8	31.90 ± 9.30	-18.02 ± 8.14	-12.72 ± 8.94	12.41 ± 7.19
083652.36+183544.9	···	L0	2	-63.7 ± 14.5	-100.3 ± 32.3	2	67.3 ± 13.0	30.40 ± 7.40	-17.14 ± 6.84	-33.99 ± 11.18	-3.18 ± 7.96
083724.77+081603.9	···	L0	2	-104.6 ± 42.0	-55.9 ± 56.4	2	60.8 ± 11.7	14.50 ± 13.40	-11.95 ± 13.62	-13.29 ± 15.56	-16.71 ± 14.33
083732.80+161737.5	···	L0	2	-46.0 ± 10.	-62.2 ± 25.6	2	70.0 ± 13.5	···	···	···	···
083759.75+195727.7	···	L0	2	-48.7 ± 25.5	-27.1 ± 24.8	2	84.6 ± 39.7	45.80 ± 17.60	-34.18 ± 15.59	-19.77 ± 11.89	12.60 ± 15.47
084001.61+451752.3	···	L1	2	···	···	···	62.5 ± 11.9	40.30 ± 13.40	···	···	···
084036.04+143424.3	···	L1	2	-150.8 ± 14.1	-51.8 ± 11.3	2	106.4 ± 20.4	12.80 ± 15.00	-37.33 ± 13.98	-17.03 ± 9.00	-55.45 ± 16.37
084106.85+603506.3	···	L4	2	-6.9 ± 19.1	-98.9 ± 25.7	2	63.2 ± 12.1	-10.13 ± 20.00	6.92 ± 15.35	-25.99 ± 11.11	3.26 ± 12.84
084149.77+005844.6	···	L0	2	···	···	···	53.1 ± 10.3	-405.60 ± 20.00	···	···	···
084307.94+314129.2	···	L3	2	-34.9 ± 48.1	-114.0 ± 35.5	2	47.5 ± 9.1	19.40 ± 10.70	-7.93 ± 10.75	-22.85 ± 9.39	8.01 ± 10.91
084333.28+102443.5	···	L1	2	131.3 ± 11.6	-587.8 ± 16.6	2	39.7 ± 7.6	-19.90 ± 6.30	79.33 ± 11.57	-81.36 ± 18.88	-24.68 ± 5.60
084407.00+284702.1	···	L2	2	46.4 ± 25.9	-98.8 ± 19.6	2	43.1 ± 8.2	2.10 ± 11.50	16.69 ± 9.67	-15.85 ± 6.08	11.68 ± 8.00
084444.58+403619.9	···	L1	2	180.1 ± 58.1	19.3 ± 22.9	2	88.9 ± 17.1	-22.80 ± 10.80	75.01 ± 19.54	7.44 ± 9.82	52.95 ± 23.36
084520.21+360551.4	···	L0	2	-10.6 ± 19.7	-15.4 ± 26.4	2	71.6 ± 13.7	15.90 ± 6.50	-4.58 ± 6.59	-1.41 ± 8.98	13.29 ± 6.69
084751.48+013811.0	···	L3	2	···	···	···	42.6 ± 8.3	15.90 ± 13.20	···	···	···
084934.05+591622.9	···	L0	2	-58.6 ± 27.7	-99.0 ± 12.3	2	63.3 ± 12.2	50.03 ± 19.60	-45.61 ± 15.66	-6.88 ± 8.68	28.49 ± 13.82
085035.85+105715.4	2MASSs J0850359+105716	L6	8	-152.8 ± 11.3	-22.5 ± 16.8	2	22.9 ± 4.7	···	···	···	···
085116.20+181730.0	···	L4.5+/-1.5	1	-166.6 ± 15.1	-29.0 ± 32.1	2	29.4 ± 6.0	···	···	···	···
085213.94+421921.3	···	L0	2	-157.3 ± 44.2	-73.7 ± 30.8	2	49.4 ± 9.4	···	···	···	···
085214.41+094048.0	···	L0	2	-35.6 ± 17.3	-4.6 ± 29.8	2	45.1 ± 8.6	18.20 ± 4.10	-6.73 ± 4.43	-4.99 ± 5.82	10.21 ± 4.44
085234.90+472034.8	···	L9.5+/-1	16	-43.2 ± 55.2	-453.1 ± 30.0	2	18.4 ± 3.8	···	···	···	···
085359.09+223335.8	···	L2	2	-171.2 ± 14.7	-76.9 ± 18.4	2	102.0 ± 19.7	···	···	···	···
085602.05+124014.3	···	L0	2	-105.9 ± 17.9	-93.9 ± 11.3	2	48.1 ± 9.2	···	···	···	···
085647.83+223518.3	2MASSI J0856479+223518	L3:	17	-225.1 ± 23.6	21.8 ± 24.0	2	71.6 ± 13.7	···	···	···	···
085758.45+570851.3	···	L8	2	-413.0 ± 6.0	-349.0 ± 12.0	9	10.3 ± 2.0	-123.50 ± 20.00	82.26 ± 14.85	-43.69 ± 6.17	-84.45 ± 12.97
085805.47+221457.8	···	L1	2	-51.9 ± 12.3	-61.8 ± 31.7	2	40.8 ± 7.8	···	···	···	···
085834.42+325627.6	···	T1	1	-652.5 ± 19.4	20.9 ± 19.5	2	19.6 ± 4.0	···	···	···	···
085836.97+271050.8	···	L0	2	89.5 ± 16.4	-195.4 ± 31.0	2	47.8 ± 9.1	-10.20 ± 7.20	38.04 ± 7.13	-36.06 ± 10.89	7.49 ± 5.63
085858.92+180445.7	···	L2	2	23.4 ± 12.6	-100.4 ± 31.9	2	76.4 ± 14.7	24.20 ± 10.0	8.68 ± 8.83	-38.30 ± 13.05	17.18 ± 7.63
085938.50+634133.5	2MASS J08593854+6341355	L0	2	-65.4 ± 12.0	-520.9 ± 23.7	2	23.9 ± 4.6	11.44 ± 8.70	-20.82 ± 7.52	-45.20 ± 11.15	21.55 ± 5.69
085959.77+292205.3	···	L0	2	27.4 ± 24.7	-12.7 ± 30.1	2	66.1 ± 12.6	14.50 ± 15.70	5.41 ± 12.82	-2.25 ± 9.82	22.03 ± 11.72
090023.68+253934.3	···	L7	2	42.2 ± 33.5	-45.0 ± 19.0	2	18.6 ± 3.6	···	···	···	···
090154.73+381837.5	···	L0	2	54.1 ± 25.4	-38.1 ± 31.6	2	54.6 ± 10.4	3.00 ± 15.80	17.25 ± 12.75	-5.42 ± 8.45	18.88 ± 11.69
090238.98+301840.3	···	L0	2	-50.8 ± 31.5	-74.9 ± 44.0	2	73.6 ± 14.1	31.60 ± 11.80	-21.67 ± 11.63	-26.32 ± 15.96	10.24 ± 11.91
090347.56+011446.1	···	L3	2	···	···	···	37.1 ± 7.2	-15.20 ± 18.70	···	···	···
090509.00+043819.9	···	L0	2	···	···	···	98.7 ± 46.3	27.30 ± 18.40	···	···	···
090531.00+195433.0	···	L0	2	-52.5 ± 17.7	-64.0 ± 25.9	2	62.6 ± 12.0	···	···	···	···
090837.91+503207.5	2MASSI J0908380+503208	L8	2	-562.3 ± 71.3	-591.6 ± 80.1	2	8.2 ± 1.6	-33.20 ± 20.00	16.54 ± 15.01	-22.59 ± 6.12	-29.08 ± 13.83
090900.72+652527.1	···	T1.5	1	-205.8 ± 15.4	-121.8 ± 36.9	2	···	···	···	···	···
090948.13+194043.9	···	L1	2	-198.6 ± 19.0	169.2 ± 10.1	2	30.8 ± 5.9	0.30 ± 3.10	-16.59 ± 5.79	27.97 ± 4.75	-7.63 ± 4.01
091128.95+320644.7	···	L0	2	-156.4 ± 13.9	-10.6 ± 26.4	2	44.6 ± 8.5	-49.60 ± 14.90	23.27 ± 11.73	11.07 ± 6.05	-50.87 ± 11.31

Table 2.6 (cont'd)

SDSS Designation (SDSS J +)	Other Name	Spectral Type	ST ref	μ_{RA} (mas yr^{-1})	μ_{dec} (mas yr^{-1})	μ ref	distance (pc)	radial velocity (km s^{-1})	U (km s^{-1})	V (km s^{-1})	W (km s^{-1})
091206.35+420330.5	···	L0	2	-139.8 ± 40.7	18.5 ± 21.4	2	54.1 ± 10.3	-16.00 ± 15.40	-2.92 ± 14.10	9.63 ± 5.56	-30.07 ± 13.93
091303.22+184148.8	2MASSW J0913032+184150	L3	8	39.9 ± 15.6	-181.0 ± 11.3	2	52.7 ± 8.2	···	···	···	···
091414.38+105719.5	···	L0	2	-25.6 ± 30.0	-3.1 ± 45.5	2	49.8 ± 9.5	-0.80 ± 7.10	6.59 ± 7.74	4.74 ± 9.91	1.89 ± 7.68
091524.33+383128.3	···	L0	2	-77.1 ± 20.9	-33.7 ± 35.9	2	87.9 ± 16.9	40.70 ± 9.70	-40.89 ± 10.14	-11.58 ± 15.20	11.64 ± 10.25
091656.32+105740.0	···	L1	2	···	···	···	···	-27.90 ± 13.80	···	···	···
091659.09+512450.4	···	L0	2	···	···	···	35.6 ± 6.8	-20.60 ± 9.90	···	···	···
091714.76+314824.8	···	L1	2	-12.6 ± 43.5	-21.0 ± 12.6	2	43.6 ± 8.3	···	···	···	···
091750.33+294444.9	···	L0	2	-46.9 ± 14.8	-119.0 ± 33.6	2	40.0 ± 7.7	13.30 ± 7.80	-1.90 ± 5.89	-19.97 ± 7.71	6.79 ± 6.05
092026.43+265157.6	···	L0	2	-77.5 ± 17.5	-138.1 ± 23.2	2	66.0 ± 31.0	9.20 ± 4.80	-4.85 ± 6.63	-39.74 ± 21.15	-10.94 ± 12.54
092142.51+084202.7	···	L2	2	-173.5 ± 43.5	-111.7 ± 56.7	2	62.4 ± 11.9	40.40 ± 17.00	-36.61 ± 15.67	-46.14 ± 17.74	-16.95 ± 17.68
092308.70+234013.6	···	L1	2	294.2 ± 35.5	-395.8 ± 19.8	2	13.7 ± 2.6	-29.90 ± 4.30	49.42 ± 4.99	-9.53 ± 4.87	-5.16 ± 3.72
092532.11+283550.8	···	L0	2	-2.8 ± 15.8	-26.5 ± 46.9	2	60.1 ± 11.5	-19.70 ± 8.20	24.08 ± 6.85	2.06 ± 13.22	-8.45 ± 6.83
092757.43+602746.3	···	L0	2	3.0 ± 13.0	16.0 ± 25.0	9	49.6 ± 9.5	-3.30 ± 18.40	13.42 ± 12.48	7.52 ± 8.16	4.27 ± 12.67
092933.56+342952.4	2MASSW J0929336+342952	L8	14	-211.3 ± 27.0	-57.5 ± 15.9	2	25.1 ± 5.2	···	···	···	···
093113.23+280227.1	···	L3	2	291.3 ± 13.6	-292.5 ± 22.8	2	31.0 ± 5.9	-8.40 ± 7.60	55.29 ± 9.22	-32.40 ± 8.38	24.43 ± 7.21
093146.84+544227.1	···	L0	2	-206.8 ± 47.5	-28.4 ± 60.1	2	68.1 ± 13.0	39.50 ± 12.50	-66.39 ± 17.09	1.24 ± 19.26	-8.79 ± 16.48
093215.45+345624.8	···	L0	2	33.6 ± 21.3	-110.9 ± 44.6	2	93.3 ± 17.9	···	···	···	···
093237.47+672514.5	···	L0	2	-39.9 ± 11.7	-157.2 ± 24.1	2	62.6 ± 12.0	-61.80 ± 15.99	28.34 ± 11.29	-64.50 ± 12.51	-24.10 ± 10.96
093535.49+234217.5	···	L1	2	-28.6 ± 11.8	-35.4 ± 28.7	2	77.6 ± 14.9	-2.00 ± 14.30	6.78 ± 9.91	-7.47 ± 11.24	-3.88 ± 11.00
093706.71+284705.5	···	L0	2	-19.6 ± 18.2	-2.1 ± 30.8	2	65.1 ± 30.6	24.80 ± 15.10	-10.24 ± 10.89	-1.50 ± 9.83	21.14 ± 11.93
093824.88+290328.9	···	L0	2	-21.6 ± 19.4	-53.5 ± 44.9	2	93.2 ± 18.5	···	···	···	···
093906.46+341257.4	···	L0	2	-157.8 ± 31.8	-0.5 ± 17.8	2	40.8 ± 7.8	···	···	···	···
094043.19+565049.1	···	L0	2	···	···	···	66.4 ± 12.7	-24.10 ± 9.20	···	···	···
094047.88+294652.9	···	L1	2	-125.3 ± 27.9	-79.0 ± 16.3	2	36.1 ± 6.9	4.10 ± 7.10	-6.02 ± 6.31	-10.81 ± 4.22	-5.37 ± 6.84
094134.92+100942.1	···	L0	2	-35.2 ± 56.7	-335.7 ± 27.4	2	35.9 ± 6.8	27.20 ± 5.10	13.76 ± 8.65	-58.19 ± 10.53	1.81 ± 8.62
094350.20+151909.1	···	L1	2	-135.2 ± 18.7	-47.2 ± 24.9	2	40.7 ± 7.8	13.60 ± 15.40	-14.04 ± 9.66	-11.50 ± 8.25	-2.87 ± 11.82
094402.80+313132.4	2MASSW J0944027+313132	L3	2	27.2 ± 16.4	-54.2 ± 23.0	2	70.1 ± 13.4	-10.80 ± 13.10	26.89 ± 9.53	-10.0 ± 8.47	3.42 ± 10.59
094427.31+641037.3	···	L0	2	-18.1 ± 54.8	20.0 ± 15.0	2	44.8 ± 8.7	5.55 ± 7.29	4.40 ± 9.93	10.67 ± 4.25	6.78 ± 9.11
094436.32+364920.8	···	L2	2	-96.6 ± 20.2	-62.6 ± 42.1	2	84.6 ± 16.2	30.20 ± 14.10	-35.62 ± 12.21	-25.98 ± 17.68	4.92 ± 12.88
094818.61+132319.9	···	L0	2	-43.5 ± 21.5	-17.8 ± 29.4	2	51.2 ± 9.8	-8.90 ± 15.80	8.26 ± 9.70	4.24 ± 9.72	-7.34 ± 11.98
094903.15+264944.1	···	L0	2	66.2 ± 29.9	-18.2 ± 20.3	2	59.6 ± 11.4	-0.70 ± 9.70	25.96 ± 9.28	2.21 ± 6.11	17.72 ± 9.41
095415.73+500140.2	···	L0	2	···	···	···	82.8 ± 16.1	22.40 ± 7.20	···	···	···
095850.68+200150.6	···	L0	2	-252.9 ± 13.6	-271.1 ± 18.9	2	67.8 ± 13.0	···	···	···	···
095908.97+312557.3	···	L0	2	44.7 ± 14.1	47.5 ± 22.5	2	39.6 ± 7.5	-1.50 ± 13.90	15.59 ± 8.51	15.08 ± 5.10	11.36 ± 11.19
095916.66+364157.6	···	L0	2	31.4 ± 22.1	-44.3 ± 14.2	2	48.2 ± 9.2	-41.10 ± 19.90	41.96 ± 12.72	-0.93 ± 4.00	-21.04 ± 16.12
100016.91+321829.4	···	L1	2	-352.4 ± 45.1	-204.6 ± 16.2	2	27.2 ± 5.4	114.90 ± 10.40	-87.69 ± 9.69	-44.34 ± 6.88	70.05 ± 10.59
100435.89+565757.2	···	L0	2	···	···	···	31.3 ± 6.1	-34.70 ± 13.70	···	···	···
100559.85+035842.3	···	L0	2	···	···	···	71.4 ± 13.6	35.40 ± 13.10	···	···	···
100711.73+193056.1	···	L8+/-1.5	1	-240.8 ± 25.6	-17.8 ± 15.7	2	28.3 ± 6.7	···	···	···	···
100844.63+470738.1	···	L0	2	-83.6 ± 49.0	-207.9 ± 39.0	2	65.3 ± 12.5	-7.20 ± 7.20	-2.09 ± 13.26	-63.13 ± 17.69	-1.85 ± 10.75
100942.69+580217.6	···	L3	2	157.5 ± 34.8	61.4 ± 63.9	2	92.6 ± 17.8	-5.30 ± 12.60	69.69 ± 18.06	40.30 ± 27.71	33.96 ± 17.00
101304.34+071050.7	···	L0	2	···	···	···	55.3 ± 10.6	-60.70 ± 19.40	···	···	···
101517.63+075211.9	···	L0	2	···	···	···	36.0 ± 6.9	18.00 ± 6.20	···	···	···
101707.55+130839.3	2MASSI J1017075+130839	L2	2	50.6 ± 11.9	-103.4 ± 29.4	2	33.4 ± 6.4	-6.20 ± 11.10	25.67 ± 5.89	-5.00 ± 6.91	1.93 ± 8.84
101742.51+431057.9	···	L1	2	-32.4 ± 21.8	-122.1 ± 29.2	2	58.4 ± 11.2	-14.40 ± 7.20	15.27 ± 6.50	-30.51 ± 10.43	-4.89 ± 6.89
102116.05+354607.8	···	L0	2	-66.8 ± 37.1	-105.0 ± 36.8	2	67.2 ± 12.9	29.40 ± 12.50	-16.21 ± 12.17	-34.20 ± 13.71	21.56 ± 12.45
102204.88+020047.4	···	L0	2	-173.0 ± 18.0	-398.0 ± 16.0	3	24.2 ± 4.6	-1.40 ± 18.70	15.82 ± 6.52	-33.28 ± 13.67	-24.45 ± 14.78
102248.13+582544.7	2MASS J10224821+5825453	L1beta	12	-789.8 ± 99.6	-737.7 ± 49.3	2	18.8 ± 3.6	···	···	···	···
102600.05+395509.6	···	L0	2	-188.0 ± 16.5	215.6 ± 48.5	2	47.8 ± 9.1	-28.00 ± 8.60	-18.70 ± 10.25	43.85 ± 13.07	-44.41 ± 9.28

Table 2.6 (cont'd)

SDSS Designation (SDSS J +)	Other Name	Spectral Type	ST ref	μ_{RA} (mas yr^{-1})	μ_{dec} (mas yr^{-1})	μ ref	distance (pc)	radial velocity (km s^{-1})	U (km s^{-1})	V (km s^{-1})	W (km s^{-1})
102921.85+162649.8	2MASSI J1029216+162652	L3	2	355.4 ± 9.0	-346.5 ± 14.1	2	46.4 ± 8.8	-15.70 ± 11.80	110.23 ± 18.64	-39.75 ± 11.10	16.77 ± 10.71
102947.67+483412.3	···	L0	2	···	···	···	46.2 ± 9.0	-26.40 ± 11.00	···	···	···
103225.18+330041.9	···	L0	2	-68.9 ± 14.4	-261.6 ± 27.0	2	51.7 ± 9.9	6.50 ± 10.40	9.18 ± 6.17	-61.58 ± 14.17	5.07 ± 9.25
103309.10+121625.9	···	L0	2	178.0 ± 21.8	-111.3 ± 30.8	2	66.6 ± 12.7	-24.40 ± 10.0	80.29 ± 14.12	-1.36 ± 10.21	5.34 ± 9.91
103428.24+414000.7	···	L0	2	-69.1 ± 61.3	103.5 ± 17.6	2	56.9 ± 10.9	···	···	···	···
103451.12+125840.7	···	L0	2	-218.5 ± 60.6	-8.4 ± 48.1	2	63.9 ± 12.3	14.40 ± 6.70	-49.42 ± 19.59	-19.07 ± 14.10	-14.95 ± 13.14
103528.60+231840.0	···	L0	2	189.4 ± 15.4	-63.2 ± 37.5	2	55.8 ± 10.7	-59.50 ± 15.30	83.30 ± 12.24	17.64 ± 10.24	-21.25 ± 14.04
103602.44+372448.4	···	L0	2	-0.2 ± 11.2	-108.0 ± 28.9	2	36.2 ± 7.0	-15.00 ± 9.80	21.67 ± 5.35	-12.39 ± 5.95	-4.37 ± 8.54
103730.42+461826.6	···	L0	2	38.3 ± 40.6	-21.3 ± 31.2	2	44.4 ± 8.5	-20.50 ± 14.20	28.21 ± 10.49	0.32 ± 6.86	-5.32 ± 12.80
104014.50+413116.4	···	L0	2	-134.1 ± 63.3	-120.6 ± 34.8	2	99.7 ± 46.8	···	···	···	···
104121.86+244228.0	···	L0	2	-86.6 ± 13.2	-102.8 ± 43.1	2	63.4 ± 12.2	-17.70 ± 18.70	6.03 ± 9.88	-26.13 ± 14.68	-24.00 ± 16.74
104307.51+222523.5	2MASS J10430758+2225236	L8	10	-134.7 ± 11.5	-5.7 ± 17.0	2	16.4 ± 3.2	···	···	···	···
104319.44+071232.4	···	L0	2	-0.5 ± 63.9	-80.5 ± 44.6	2	53.2 ± 10.2	-38.20 ± 17.10	30.26 ± 15.46	8.00 ± 13.77	-31.11 ± 16.31
104335.08+121314.0	···	L7+/-1	1	-0.2 ± 30.2	-204.3 ± 20.7	2	18.2 ± 3.8	···	···	···	···
104407.47+015742.0	···	L2	2	···	···	···	46.0 ± 8.9	-8.00 ± 13.20	···	···	···
104426.79+272033.1	···	L1	2	···	···	···	106.3 ± 20.4	1.90 ± 12.80	···	···	···
104523.97-014957.7	2MASSI J1045240-014957	L1	18	-417.9 ± 71.3	-65.4 ± 43.3	2	21.9 ± 4.2	···	···	···	···
104617.01+351305.8	···	L1	2	13.9 ± 34.4	4.4 ± 34.0	2	74.0 ± 14.3	-10.70 ± 8.60	18.65 ± 11.44	8.48 ± 11.94	-0.32 ± 9.48
104729.03+301639.7	···	L0	2	-9.2 ± 46.1	-110.2 ± 18.4	2	91.0 ± 17.5	-0.80 ± 11.20	21.60 ± 17.84	-41.17 ± 12.93	4.05 ± 13.51
104842.70+300650.5	···	L1	2	-122.9 ± 20.5	-21.4 ± 35.8	2	47.8 ± 9.2	···	···	···	···
104842.80+011158.0	···	L1	2	-442.0 ± 13.0	-209.0 ± 12.0	3	17.1 ± 3.3	35.50 ± 4.40	-20.22 ± 4.46	-38.55 ± 5.09	10.83 ± 5.69
104922.45+012559.2	···	L6	2	···	···	···	26.4 ± 5.2	-10.90 ± 13.20	···	···	···
104928.24+253723.2	···	L1	2	-1.2 ± 10.7	11.8 ± 14.2	2	49.2 ± 9.4	···	···	···	···
105012.46+005803.1	···	L0	2	···	···	···	54.0 ± 10.4	13.00 ± 11.20	···	···	···
105044.03+325843.5	···	L0	2	-48.9 ± 30.9	-15.2 ± 17.4	2	62.2 ± 12.0	10.90 ± 13.90	-5.73 ± 10.18	-4.37 ± 5.90	10.45 ± 13.13
105110.69+314129.9	···	L0	2	-45.5 ± 19.5	-62.8 ± 23.4	2	65.4 ± 12.5	-6.00 ± 10.70	6.49 ± 7.34	-16.75 ± 8.41	-4.33 ± 10.02
105118.95+561308.0	2MASS J10511900+5613086	L1	2	-189.5 ± 45.4	-268.6 ± 25.3	2	20.2 ± 3.8	-16.40 ± 3.80	5.57 ± 4.86	-28.30 ± 6.10	-4.38 ± 3.76
105213.49+442255.6	···	T0.5+/-1	1	-5.6 ± 19.5	-55.1 ± 49.0	2	···	···	···	···	···
105259.70+334406.1	···	L0	2	-109.3 ± 51.4	-74.0 ± 12.3	2	83.8 ± 16.1	···	···	···	···
105318.15+433306.1	···	L0	2	-27.1 ± 17.4	-59.6 ± 52.6	2	63.3 ± 12.1	-15.60 ± 12.90	14.33 ± 8.33	-15.66 ± 15.65	-6.60 ± 11.96
105339.22+642351.5	···	L0	2	-89.6 ± 30.8	5.1 ± 7.4	2	89.3 ± 17.1	66.47 ± 12.46	-57.06 ± 14.31	23.59 ± 7.12	38.91 ± 11.53
105355.39+385737.5	···	L0	2	-56.3 ± 12.3	-29.8 ± 24.5	2	70.4 ± 13.5	-5.60 ± 13.30	-0.95 ± 7.75	-9.93 ± 8.42	-4.86 ± 12.09
105510.41+511026.2	···	L0	2	199.6 ± 32.4	56.3 ± 67.8	2	113.7 ± 21.9	-39.00 ± 16.00	116.61 ± 24.46	56.45 ± 36.55	10.95 ± 20.64
105814.54+303159.7	···	L0	2	-18.9 ± 23.4	46.1 ± 26.1	2	54.7 ± 10.4	-9.70 ± 11.80	5.80 ± 7.52	16.13 ± 7.09	-3.93 ± 11.01
105951.45-211309.6	2MASSI J1059513-211308	L1	17	140.8 ± 16.2	-188.8 ± 12.9	2	20.5 ± 3.9	···	···	···	···
110008.19+295516.1	···	L0	2	-247.8 ± 33.8	28.6 ± 15.4	2	84.6 ± 16.2	64.10 ± 17.20	-104.09 ± 21.78	-23.20 ± 8.37	24.08 ± 18.40
110009.61+495746.5	···	L3	2	-125.1 ± 22.9	-174.8 ± 31.1	2	25.1 ± 4.8	-26.20 ± 14.40	13.56 ± 7.55	-23.94 ± 6.41	-15.17 ± 12.42
110148.04+544009.2	···	L0	2	59.4 ± 32.4	69.7 ± 24.1	2	65.5 ± 12.5	-1.50 ± 7.90	23.46 ± 9.84	30.02 ± 9.17	5.07 ± 8.25
110212.05+162938.7	···	L0	2	197.8 ± 47.3	-144.0 ± 21.6	2	65.9 ± 12.6	-10.90 ± 4.10	85.06 ± 18.99	-11.89 ± 8.61	12.98 ± 7.79
110401.29+195922.3	2MASSI J1104012+195921	L5	2	49.6 ± 17.5	109.8 ± 22.5	2	15.4 ± 2.9	-8.70 ± 6.60	12.64 ± 2.44	15.93 ± 2.95	1.86 ± 6.00
110555.02+042145.3	···	L0	2	···	···	···	49.5 ± 9.6	16.20 ± 14.20	···	···	···
110612.00+275420.0	2MASS J11061197+2754225	T2.5	19	250.2 ± 34.3	-322.8 ± 62.4	2	110.6 ± 54.5	···	···	···	···
110705.31+245448.5	···	L0	2	-48.1 ± 24.7	-27.3 ± 35.8	2	69.9 ± 13.5	-10.50 ± 9.60	3.19 ± 9.18	-6.21 ± 11.73	-9.56 ± 9.51
110927.19-160653.7	···	L0	2	-477.5 ± 15.2	-287.2 ± 17.2	2	20.3 ± 3.9	69.91 ± 10.02	-15.72 ± 5.16	-78.84 ± 9.66	16.16 ± 9.50
110938.29+235339.6	···	L0	2	-36.2 ± 13.0	-134.9 ± 12.7	2	60.9 ± 11.6	17.70 ± 13.50	10.37 ± 5.71	-38.19 ± 8.84	15.72 ± 12.58
111143.84+295823.8	···	L1	2	32.2 ± 12.9	15.9 ± 34.5	2	74.6 ± 14.3	-0.50 ± 10.60	18.04 ± 7.11	14.10 ± 11.70	10.76 ± 10.01
111225.55+354812.1	Gl 417BC	L4.5	14	-248.8 ± 12.5	-180.9 ± 26.1	2	16.3 ± 3.1	···	···	···	···
111316.95-000246.7	···	L0	2	42.0 ± 22.0	6.0 ± 13.0	3	36.6 ± 7.0	-32.60 ± 4.90	19.81 ± 3.70	26.95 ± 3.57	-16.21 ± 4.37
111320.16+343058.0	···	L3	1	132.0 ± 15.5	-37.7 ± 63.5	2	40.0 ± 8.1	···	···	···	···

Table 2.6 (cont'd)

SDSS Designation (SDSS J +)	Other Name	Spectral Type	ST ref	μ_{RA} (mas yr^{-1})	μ_{dec} (mas yr^{-1})	μ ref	distance (pc)	radial velocity (km s^{-1})	U (km s^{-1})	V (km s^{-1})	W (km s^{-1})
111647.97+603730.7	···	L0	2	···	···	···	85.0 ± 39.9	-17.30 ± 14.80	···	···	···
111736.93+360935.8	2MASSI J1117369+360936	L0	2	32.1 ± 10.7	-20.4 ± 47.6	2	23.5 ± 4.5	-15.00 ± 10.20	19.42 ± 4.36	4.37 ± 5.00	-5.40 ± 9.50
112210.27+340432.4	···	L1	2	-57.5 ± 11.3	-78.8 ± 21.8	2	48.5 ± 9.3	2.80 ± 15.40	3.88 ± 6.12	-16.77 ± 6.36	6.67 ± 14.48
112647.03+581632.1	···	L3	2	-55.0 ± 65.6	-206.2 ± 33.0	2	38.9 ± 7.4	-22.60 ± 10.80	18.66 ± 11.68	-39.32 ± 10.49	2.83 ± 10.49
112706.60+470548.1	···	L1	2	-15.1 ± 26.3	-18.1 ± 20.7	2	31.7 ± 6.1	-26.40 ± 6.50	19.40 ± 4.42	-2.84 ± 3.44	-16.66 ± 6.05
113035.14-005225.7	···	L0	2	···	···	···	62.3 ± 11.9	-14.70 ± 6.00	···	···	···
113344.68+131126.4	···	L1	2	-220.8 ± 30.8	-111.5 ± 31.1	2	50.7 ± 9.7	-18.70 ± 5.50	-21.14 ± 9.85	-31.56 ± 11.00	-32.69 ± 7.25
113826.35+333114.1	···	L0	2	78.0 ± 24.0	33.6 ± 15.0	2	49.2 ± 9.4	-34.30 ± 9.60	32.82 ± 6.30	20.52 ± 4.79	-21.41 ± 9.36
113833.08+674040.3	···	L0	2	24.0 ± 14.0	-127.0 ± 37.0	9	48.6 ± 9.3	18.60 ± 10.40	10.97 ± 5.98	-6.48 ± 9.31	40.18 ± 10.05
113941.90-031004.0	···	L0	2	···	···	···	18.6 ± 3.5	-2.50 ± 6.90	···	···	···
114144.13+411656.7	···	L0	2	76.3 ± 17.4	-2.3 ± 24.4	2	63.4 ± 12.1	-21.10 ± 7.70	37.28 ± 7.00	11.60 ± 7.23	-6.55 ± 7.63
114251.67+640019.9	···	L0	2	···	···	···	87.0 ± 16.8	-40.20 ± 12.50	···	···	···
114557.19+231729.3	2MASSW J1145572+231730	L1.5	8	110.6 ± 29.2	-68.5 ± 14.0	2	50.2 ± 7.8	···	···	···	···
114634.51+223053.0	2MASSW J1146345+223053	L3	2	69.2 ± 30.1	59.2 ± 12.2	2	25.2 ± 4.8	0.10 ± 4.60	14.04 ± 3.41	14.70 ± 2.86	9.81 ± 4.56
114805.02+020350.8	···	L0	2	237.0 ± 26.0	-322.0 ± 13.0	3	26.2 ± 5.0	-20.60 ± 14.80	55.19 ± 9.10	-3.17 ± 8.24	-20.79 ± 13.08
114912.31-015300.6	···	L0	2	···	···	···	34.7 ± 6.6	11.50 ± 3.60	···	···	···
115250.06+643252.4	···	L2	2	3.1 ± 23.2	73.4 ± 50.3	2	51.2 ± 9.8	-20.50 ± 19.20	15.23 ± 9.97	9.86 ± 13.43	-19.21 ± 16.76
115306.12+371653.4	···	L0	2	245.8 ± 50.8	-10.8 ± 16.5	2	71.2 ± 13.6	2.20 ± 0.80	83.43 ± 20.77	37.48 ± 10.87	28.28 ± 5.44
115339.68+503209.4	2MASS J11533966+5032092	L0	2	89.3 ± 13.5	58.6 ± 44.1	2	29.9 ± 5.7	1.00 ± 5.60	17.96 ± 3.67	17.90 ± 6.14	7.59 ± 5.57
115435.32+623438.1	···	L0	2	-114.5 ± 22.7	-50.4 ± 43.5	2	53.6 ± 10.2	-27.40 ± 7.20	-0.86 ± 7.76	-29.55 ± 10.55	-14.21 ± 8.53
115500.89+230705.7	2MASSW J1155009+230706	L4	8	40.5 ± 30.6	-14.1 ± 39.7	2	46.0 ± 8.8	···	···	···	···
115553.84+055957.5	···	L6	2	-406.0 ± 22.0	-26.0 ± 22.0	9	14.4 ± 2.9	136.80 ± 20.00	-14.98 ± 4.89	-66.13 ± 8.95	124.49 ± 18.20
115938.50+005726.9	DENIS-P J1159+0057	L0	2	12.0 ± 23.0	7.0 ± 17.0	3	20.0 ± 3.8	-5.30 ± 4.40	10.43 ± 2.08	8.56 ± 2.64	2.88 ± 3.94
115948.00+383016.2	···	L0	2	-127.4 ± 29.4	-61.6 ± 50.7	2	85.7 ± 40.3	-32.80 ± 17.60	-16.41 ± 21.69	-42.93 ± 28.67	-30.28 ± 17.73
120020.66+340615.4	···	L1	2	···	···	···	55.3 ± 10.6	25.10 ± 14.30	···	···	···
120249.99+420452.1	···	L0	2	···	···	···	21.5 ± 4.1	-33.60 ± 7.40	···	···	···
120252.65-022748.6	···	L1	2	···	···	···	63.2 ± 12.1	14.60 ± 8.20	···	···	···
120358.19+001550.2	···	L5	2	-1116.0 ± 58.7	-201.1 ± 133.9	2	14.3 ± 2.7	15.10 ± 14.20	-48.22 ± 12.62	-46.69 ± 12.95	0.23 ± 13.62
120430.38+321259.4	2MASSI J1204303+321259	L0	2	45.3 ± 24.1	-34.4 ± 16.9	2	28.5 ± 5.4	-2.20 ± 7.60	17.84 ± 3.65	3.67 ± 2.53	6.31 ± 7.48
120610.50+624257.3	···	L1	2	···	···	···	44.0 ± 8.4	-18.60 ± 7.40	···	···	···
120637.41-014332.2	···	L1	2	···	···	···	···	-10.80 ± 8.50	···	···	···
120747.17+024424.8	···	L8	2	-498.0 ± 18.0	138.0 ± 19.0	3	14.5 ± 2.9	-41.80 ± 20.00	-26.96 ± 7.04	15.01 ± 9.08	-32.24 ± 17.91
120821.72+445224.6	···	L0	2	-132.3 ± 18.8	47.8 ± 34.3	2	49.8 ± 9.5	-7.00 ± 8.10	-19.77 ± 8.22	-1.00 ± 7.51	-8.09 ± 8.18
120831.49+014924.7	DENIS-P J1208.5+0149	L0	2	···	···	···	30.0 ± 5.7	-20.90 ± 17.30	···	···	···
120906.49+323327.5	···	L0	2	-120.7 ± 19.0	171.0 ± 16.2	2	27.4 ± 5.2	59.10 ± 12.50	-24.71 ± 5.62	17.44 ± 3.23	60.60 ± 12.32
120916.19+542949.6	···	L1	2	12.8 ± 35.2	-129.2 ± 28.6	2	53.3 ± 10.2	8.70 ± 10.20	21.42 ± 9.28	-17.42 ± 9.33	29.79 ± 10.07
121210.98+605947.9	···	L0	2	33.6 ± 47.0	104.0 ± 34.8	2	46.1 ± 8.8	···	···	···	···
121304.77+152922.2	···	L1	2	-328.0 ± 33.8	-199.3 ± 82.2	2	67.6 ± 13.1	-10.20 ± 18.10	-49.46 ± 19.84	-96.04 ± 30.80	-31.55 ± 19.22
121409.75+332356.0	···	L0	2	-7.6 ± 50.1	-14.7 ± 20.5	2	106.7 ± 20.7	-15.30 ± 10.50	12.81 ± 22.58	-3.68 ± 15.17	-7.85 ± 11.01
121433.60+372111.8	···	L0	2	-148.9 ± 17.2	27.7 ± 35.5	2	52.6 ± 10.1	11.90 ± 7.00	-27.82 ± 8.81	-5.62 ± 8.35	12.13 ± 7.13
121645.58+492744.9	···	L1	2	-43.8 ± 20.1	-97.9 ± 35.3	2	34.0 ± 6.5	···	···	···	···
121855.72+352022.9	···	L0	2	-163.9 ± 13.9	-85.5 ± 36.9	2	63.8 ± 12.2	21.80 ± 15.00	-24.65 ± 9.08	-40.24 ± 13.40	25.74 ± 14.83
121950.20+654136.5	···	L0	2	-128.0 ± 25.3	-17.5 ± 52.5	2	69.0 ± 13.2	-23.10 ± 11.90	-15.46 ± 12.07	-30.87 ± 15.03	-12.58 ± 14.09
121951.45+312849.4	···	L8	1	-233.0 ± 23.7	-49.6 ± 14.7	2	18.1 ± 3.7	···	···	···	···
122127.70+025719.8	2MASS J12212770+0257198	L0	2	-115.0 ± 30.0	-18.0 ± 27.0	3	19.0 ± 3.6	-12.60 ± 4.10	0.44 ± 3.08	3.87 ± 3.09	-6.27 ± 3.87
122524.00-021559.7	···	L3	2	···	···	···	107.8 ± 20.9	-25.70 ± 16.40	···	···	···
122818.53+583342.3	···	L0	2	62.8 ± 32.3	141.9 ± 47.3	2	70.2 ± 13.4	-15.80 ± 12.50	14.71 ± 11.82	44.95 ± 16.66	-29.01 ± 14.11
123045.43+282758.0	2MASS J12304562+2827583	L2	2	-526.4 ± 24.7	-63.7 ± 48.0	2	56.7 ± 26.6	-20.00 ± 9.60	-101.23 ± 53.70	-81.11 ± 42.27	-23.92 ± 10.89
123112.97+405027.9	···	L0	2	-84.1 ± 33.0	49.4 ± 27.9	2	54.2 ± 10.3	-15.00 ± 10.0	-11.85 ± 9.50	2.30 ± 7.62	-12.21 ± 9.90

Table 2.6 (cont'd)

SDSS Designation (SDSS J +)	Other Name	Spectral Type	ST ref	μ_{RA} (mas yr^{-1})	μ_{dec} (mas yr^{-1})	μ ref	distance (pc)	radial velocity (km s^{-1})	U (km s^{-1})	V (km s^{-1})	W (km s^{-1})
123121.38+495923.3	2MASS J12312141+4959234	L3	2	-88.9 ± 22.8	-35.5 ± 29.8	2	25.9 ± 4.9	11.10 ± 13.10	-0.31 ± 4.69	-0.79 ± 5.38	18.04 ± 12.13
123147.38+084730.7	2MASS J12314753+0847331	T5.5	7	-1103.2 ± 63.3	-1167.1 ± 35.9	2	···	···	···	···	···
123322.63+213805.1	···	L0	2	-121.9 ± 33.4	-134.3 ± 18.5	2	50.0 ± 9.6	24.87 ± 15.56	1.46 ± 7.33	-39.82 ± 9.93	26.59 ± 15.49
123517.23+315815.6	···	L0	2	-52.9 ± 24.4	4.2 ± 20.3	2	60.7 ± 11.6	-18.70 ± 12.50	-1.82 ± 7.30	-2.53 ± 6.33	-12.65 ± 12.45
123815.59+621925.9	···	L0	2	···	···	···	82.3 ± 38.6	-21.30 ± 13.30	···	···	···
123927.31+551537.3	2MASSW J1239272+551537	L5	2	131.2 ± 25.8	76.1 ± 73.3	2	17.0 ± 3.2	-17.80 ± 20.00	21.28 ± 6.56	8.43 ± 9.11	-11.07 ± 17.85
124036.80+152517.1	···	L0	2	-3.6 ± 17.5	-18.2 ± 23.9	2	41.2 ± 7.9	-21.00 ± 10.30	9.75 ± 3.86	5.77 ± 4.75	-14.30 ± 10.12
124352.25+131021.3	···	L0	2	-81.4 ± 23.8	-47.2 ± 13.8	2	51.6 ± 9.8	47.20 ± 12.30	4.05 ± 5.78	-25.40 ± 6.25	49.41 ± 11.98
124510.86-013230.9	···	L0	2	···	···	···	84.0 ± 16.3	-3.40 ± 8.80	···	···	···
124514.95+120442.0	···	L1	2	-30.6 ± 34.5	-64.7 ± 13.4	2	61.7 ± 11.8	···	···	···	···
124555.66+490210.9	···	L1	2	4.2 ± 27.8	81.0 ± 27.9	2	61.8 ± 29.0	34.70 ± 13.60	-8.08 ± 9.83	34.95 ± 12.66	30.36 ± 13.63
124646.83+402714.6	2MASSW J1246467+402715	L4	14	156.7 ± 28.0	-113.3 ± 16.5	2	22.6 ± 4.3	···	···	···	···
124908.66+415728.5	···	L0	2	-241.0 ± 39.9	-41.9 ± 28.3	2	38.8 ± 7.4	21.40 ± 9.50	-26.42 ± 9.37	-20.70 ± 8.42	29.27 ± 9.28
124921.22+541340.1	···	L0	2	-39.2 ± 46.1	-135.6 ± 25.0	2	40.3 ± 7.7	5.00 ± 8.20	14.82 ± 8.12	-16.63 ± 8.08	23.20 ± 7.94
125011.65+392553.9	···	T4	1	-28.3 ± 58.6	-845.2 ± 15.4	2	···	···	···	···	···
125044.67+041758.2	···	L0	2	···	···	···	74.9 ± 14.4	-19.30 ± 11.30	···	···	···
125045.66+441853.7	···	L0	2	-24.9 ± 28.9	-304.2 ± 66.8	2	88.1 ± 41.4	···	···	···	···
125214.08+142239.3	···	L3	2	-78.0 ± 38.4	-79.6 ± 13.3	2	78.5 ± 15.0	6.70 ± 8.50	2.20 ± 12.43	-36.27 ± 11.77	7.09 ± 8.45
125230.79+183506.0	···	L1	2	-104.3 ± 16.3	-49.2 ± 35.3	2	109.9 ± 21.2	-0.40 ± 9.70	-21.78 ± 13.67	-45.88 ± 18.75	3.02 ± 10.0
125253.62+342138.8	···	L2	2	-51.6 ± 29.4	38.5 ± 18.9	2	86.9 ± 16.7	···	···	···	···
125437.59+293832.6	···	L0	2	-88.6 ± 27.6	-53.5 ± 17.5	2	60.3 ± 11.5	-20.80 ± 11.40	-2.49 ± 7.54	-22.55 ± 7.88	-12.80 ± 11.39
125459.33+263107.1	···	L1	2	37.8 ± 28.3	-8.7 ± 45.1	2	46.6 ± 8.9	7.50 ± 8.30	18.15 ± 7.72	7.97 ± 9.02	14.36 ± 8.30
125550.62+170059.7	···	L0	2	74.0 ± 20.3	-129.6 ± 14.1	2	67.8 ± 13.0	-1.50 ± 4.30	52.20 ± 10.09	-15.99 ± 6.62	-2.20 ± 4.56
125737.25-011336.2	···	L5	2	81.0 ± 20.0	-3.0 ± 11.0	3	25.4 ± 4.9	47.60 ± 20.00	31.66 ± 6.20	-8.13 ± 7.91	48.47 ± 17.61
130234.71+512600.8	···	L0	2	191.1 ± 24.7	-144.6 ± 45.0	2	33.5 ± 6.4	17.90 ± 7.50	43.63 ± 8.83	11.45 ± 6.36	31.42 ± 7.60
130250.93+564037.9	···	L0	2	-189.8 ± 21.9	-61.4 ± 58.9	2	75.6 ± 14.5	-22.10 ± 17.60	-29.60 ± 15.81	-58.29 ± 20.14	1.64 ± 18.68
130317.69+181522.0	···	L0	2	-151.3 ± 19.2	14.3 ± 24.5	2	82.6 ± 38.8	-8.86 ± 8.91	-43.11 ± 25.77	-22.83 ± 16.21	1.85 ± 9.08
130433.16+090706.9	···	L0	2	···	···	···	38.2 ± 7.3	-18.40 ± 12.50	···	···	···
130541.04+204639.8	2MASSI J1305410+204639	L3	2	-59.1 ± 33.1	73.8 ± 22.6	2	20.6 ± 3.9	10.58 ± 8.93	2.39 ± 3.51	7.01 ± 2.67	18.62 ± 8.87
130617.23+382029.6	2MASS J13061727+3820296	L0	2	-158.2 ± 16.5	-21.7 ± 28.5	2	37.2 ± 7.1	-0.99 ± 8.41	-10.70 ± 5.46	-14.09 ± 5.88	8.38 ± 8.31
130831.01+081852.3	···	L0	2	-207.3 ± 29.8	44.5 ± 35.9	2	59.4 ± 11.3	···	···	···	···
131002.88+055404.2	···	L0	2	···	···	···	72.2 ± 13.8	-10.70 ± 10.60	···	···	···
131113.81+240105.0	···	L3	2	-124.3 ± 50.7	-92.8 ± 16.0	2	57.9 ± 11.1	0.40 ± 7.50	-3.21 ± 11.92	-35.47 ± 11.71	8.60 ± 7.55
131207.01+393744.5	2MASS J13120707+3937445	L0:	10	-120.8 ± 17.0	-6.0 ± 7.7	2	25.9 ± 4.9	···	···	···	···
131221.79+290935.0	···	L0	2	208.8 ± 19.7	-91.9 ± 24.1	2	34.9 ± 6.7	-2.30 ± 3.30	46.76 ± 7.87	12.35 ± 4.02	2.42 ± 3.33
131223.12+493126.2	···	L0	2	-41.1 ± 41.2	-28.6 ± 27.1	2	62.1 ± 11.9	-18.30 ± 9.00	7.78 ± 10.95	-14.63 ± 9.99	-5.71 ± 8.92
131448.64+240532.0	···	L3	2	23.9 ± 20.5	1.4 ± 44.3	2	101.3 ± 19.4	3.60 ± 8.40	19.31 ± 14.77	12.24 ± 18.30	9.57 ± 8.48
131543.68+233458.0	···	L1	2	-284.2 ± 36.1	35.7 ± 23.3	2	50.7 ± 9.7	-8.29 ± 5.46	-51.17 ± 13.88	-27.77 ± 9.24	5.74 ± 5.66
131545.55+245407.3	···	L0	2	-47.0 ± 22.7	1.9 ± 18.2	2	51.1 ± 9.8	-42.20 ± 12.70	-3.72 ± 5.60	-2.17 ± 4.97	-33.88 ± 12.65
131614.35+213329.9	···	L0	2	-18.7 ± 29.9	23.4 ± 32.3	2	64.8 ± 12.5	-40.73 ± 4.49	-4.29 ± 9.52	8.51 ± 9.69	-32.08 ± 4.65
131839.06+213043.0	···	L0	2	-149.8 ± 32.1	23.3 ± 18.0	2	58.0 ± 11.1	1.52 ± 8.97	-26.60 ± 10.50	-13.95 ± 7.49	13.49 ± 8.99
132511.10+051704.2	···	L1	2	···	···	···	45.5 ± 8.7	7.30 ± 10.20	···	···	···
132715.21+075937.5	···	L1	2	-150.5 ± 25.6	15.1 ± 55.9	2	38.7 ± 7.4	-7.90 ± 11.70	-15.74 ± 8.73	-7.85 ± 9.19	4.37 ± 11.49
132855.13+211446.0	2MASSW J1328550+211449	L5	8	230.5 ± 26.8	-431.3 ± 16.8	2	26.2 ± 5.1	···	···	···	···
132937.21+035729.6	···	L0	2	···	···	···	49.7 ± 9.5	16.60 ± 12.70	···	···	···
133010.02+141113.3	···	L0	2	-168.4 ± 36.7	17.9 ± 17.5	2	60.3 ± 11.5	-15.20 ± 8.60	-34.58 ± 11.88	-18.40 ± 8.86	0.74 ± 8.65
133132.98+340757.5	2MASS J13313310+3407583	L0	2	-373.1 ± 21.9	-199.7 ± 13.3	2	35.6 ± 6.8	15.40 ± 7.80	-17.66 ± 6.31	-56.25 ± 12.61	35.73 ± 8.11
133148.88-011652.5	···	L7	2	-432.4 ± 29.6	-1073.5 ± 49.2	2	13.2 ± 2.5	···	···	···	···
133228.52+263508.0	2MASSI J1332286+263508	L2	14	-187.5 ± 12.1	4.6 ± 16.9	2	114.0 ± 21.9	···	···	···	···

Table 2.6 (cont'd)

SDSS Designation (SDSS J +)	Other Name	Spectral Type	ST ref	μ_{RA} (mas yr^{-1})	μ_{dec} (mas yr^{-1})	μ ref	distance (pc)	radial velocity (km s^{-1})	U (km s^{-1})	V (km s^{-1})	W (km s^{-1})
133312.79+150956.5	···	L0	2	-144.3 ± 29.0	-73.3 ± 19.3	2	85.3 ± 16.3	-43.50 ± 12.20	-29.75 ± 11.96	-50.60 ± 14.67	-31.78 ± 12.04
133406.17+194035.8	2MASSW J1334062+194034	L1	2	-106.4 ± 13.4	86.2 ± 13.8	2	66.8 ± 12.8	-21.10 ± 14.30	-36.87 ± 9.61	6.50 ± 4.35	-4.38 ± 14.11
133506.46+431725.1	···	L0	2	-25.8 ± 66.9	128.7 ± 12.8	2	50.2 ± 9.6	···	···	···	···
133640.53+374322.6	2MASS J13364062+3743230	L1	2	-221.3 ± 20.1	-90.2 ± 9.4	2	23.7 ± 4.5	···	···	···	···
133731.17+493836.8	2MASS J13373116+4938367	L0	10	30.8 ± 25.0	27.7 ± 10.3	2	20.8 ± 4.0	···	···	···	···
133849.45+043731.2	2MASS J13384944+0437315	L1	2	112.0 ± 14.0	-224.0 ± 13.0	3	31.5 ± 6.0	14.70 ± 5.40	45.65 ± 6.38	-13.37 ± 3.69	4.39 ± 5.81
134148.85+551046.2	···	L1	2	-112.0 ± 16.2	99.5 ± 22.1	2	24.5 ± 4.7	26.60 ± 6.00	-11.28 ± 4.02	16.80 ± 3.44	27.44 ± 5.39
134203.11+134022.2	···	L5.5	1	6.3 ± 23.3	-1.8 ± 62.6	2	32.0 ± 6.9	···	···	···	···
134223.57+175155.6	2MASSW J1342236+175156	L2.5	8	-107.8 ± 18.4	-22.8 ± 47.0	2	55.9 ± 8.9	···	···	···	···
134224.93+603731.5	···	L0	2	···	···	···	105.8 ± 20.4	-43.00 ± 15.60	···	···	···
134228.41-002705.6	···	L0	2	···	···	···	58.7 ± 11.2	-25.30 ± 9.80	···	···	···
134316.54+394509.2	2MASSW J1343167+394508	L5	2	-382.3 ± 21.8	101.1 ± 11.5	2	24.0 ± 4.7	···	···	···	···
134322.50-030100.2	···	L0	2	41.9 ± 58.3	2.7 ± 30.9	2	46.1 ± 8.8	4.80 ± 19.50	18.89 ± 13.58	9.69 ± 10.92	9.51 ± 16.96
134329.01+131226.2	···	L1	2	-265.3 ± 25.8	-80.1 ± 18.7	2	90.3 ± 17.3	···	···	···	···
134338.73-022044.5	···	L1	2	···	···	···	84.9 ± 16.3	1.40 ± 12.40	···	···	···
134515.81-025514.4	···	L0	2	···	···	···	51.8 ± 9.9	8.20 ± 14.60	···	···	···
134544.36+654217.9	···	L1	2	···	···	···	54.5 ± 10.4	6.60 ± 8.70	···	···	···
134607.41+084234.5	···	L2	2	-214.1 ± 35.0	-19.5 ± 52.6	2	50.8 ± 9.7	-17.70 ± 10.60	-32.82 ± 12.30	-28.24 ± 13.08	-0.02 ± 10.89
134845.94+035354.2	2MASS J13484591+0353545	L1	2	207.0 ± 23.0	-356.0 ± 11.0	3	24.4 ± 4.7	0.80 ± 4.30	49.53 ± 7.97	-11.64 ± 3.77	-13.92 ± 5.68
134925.25+504954.5	···	L0	2	5.0 ± 21.0	26.6 ± 12.0	2	32.3 ± 6.2	-12.15 ± 9.06	9.01 ± 2.85	2.90 ± 4.59	-5.63 ± 8.20
135238.65+324002.4	···	L0	2	-53.1 ± 26.7	-40.9 ± 11.6	2	48.4 ± 9.3	-13.10 ± 7.60	5.43 ± 5.02	-12.48 ± 5.41	-2.08 ± 7.54
135439.53+504451.0	···	L1	2	-253.1 ± 12.3	1.3 ± 35.0	2	22.7 ± 4.3	-22.10 ± 17.40	-8.47 ± 4.90	-21.67 ± 8.68	-6.24 ± 15.69
135712.40+142839.8	···	L3	2	90.9 ± 32.3	-2.6 ± 20.7	2	55.5 ± 10.6	-11.30 ± 8.90	24.12 ± 8.37	19.73 ± 7.36	-9.80 ± 8.81
135825.72+423434.4	···	L0	2	-78.7 ± 28.2	41.7 ± 59.3	2	46.9 ± 9.0	···	···	···	···
135955.19+324719.0	···	L0	2	-55.7 ± 15.0	-87.1 ± 16.9	2	34.4 ± 6.6	16.50 ± 8.80	15.27 ± 2.92	-7.44 ± 4.51	26.35 ± 8.52
140023.11+433822.2	···	L7+/-1	1	-246.0 ± 39.4	5.3 ± 16.6	2	23.7 ± 11.1	···	···	···	···
140231.75+014830.2	···	L1	2	-232.0 ± 14.0	8.0 ± 11.0	3	34.8 ± 6.6	10.30 ± 7.50	-13.44 ± 6.76	-20.09 ± 5.05	26.84 ± 6.86
140307.47+201859.3	···	L0	2	···	···	···	48.4 ± 9.3	-41.67 ± 18.08	···	···	···
140347.84+351313.0	···	L0	2	-227.6 ± 56.0	118.5 ± 16.6	2	83.9 ± 16.1	-5.70 ± 5.80	-88.11 ± 25.08	-20.02 ± 15.69	21.14 ± 9.13
140409.90+400214.0	···	L0	2	···	···	···	57.6 ± 11.0	14.30 ± 18.80	···	···	···
140412.19+133922.1	···	L0	2	-48.7 ± 23.7	-25.7 ± 34.0	2	61.3 ± 11.8	47.10 ± 10.10	21.60 ± 8.57	-10.33 ± 9.24	52.88 ± 9.88
140441.67+023550.1	···	L0	2	54.0 ± 17.0	-248.0 ± 13.0	3	59.5 ± 27.9	36.60 ± 16.90	73.80 ± 23.54	-43.92 ± 20.84	5.20 ± 21.55
140442.38-022426.0	···	L0	2	39.5 ± 29.1	30.0 ± 68.2	2	63.4 ± 12.2	-76.40 ± 19.40	-25.28 ± 15.21	36.32 ± 16.91	-54.92 ± 19.06
140444.87+463430.4	2MASS J14044495+4634297	L0	2	-239.2 ± 28.5	169.8 ± 20.0	2	25.6 ± 4.9	-23.60 ± 11.40	-25.01 ± 7.35	-9.70 ± 5.49	-12.58 ± 10.47
140601.48+524930.9	···	L0	2	-9.4 ± 34.3	-11.6 ± 28.6	2	64.4 ± 12.3	-22.50 ± 11.60	12.22 ± 9.69	-9.78 ± 10.19	-10.42 ± 11.12
140633.17+360449.2	···	L0	2	-120.7 ± 12.8	-110.7 ± 49.6	2	44.5 ± 8.5	-31.00 ± 14.30	4.06 ± 7.67	-36.84 ± 10.74	-12.17 ± 13.81
140753.53+124110.1	2MASS J14075361+1241099	L3	2	-335.6 ± 23.4	53.3 ± 32.0	2	22.0 ± 4.2	31.30 ± 20.00	-5.99 ± 9.84	-13.60 ± 4.60	47.48 ± 18.58
140818.89+064954.3	···	L1	2	···	···	···	47.1 ± 9.0	-16.70 ± 6.30	···	···	···
140909.45+432750.0	···	L0	2	7.3 ± 20.9	-13.5 ± 38.2	2	46.2 ± 8.9	48.40 ± 19.40	15.12 ± 6.79	22.59 ± 9.74	51.92 ± 18.07
141117.12+393636.7	2MASSW J1411175+393636	L2	2	-903.7 ± 33.1	160.1 ± 18.1	2	28.8 ± 5.5	-14.00 ± 6.60	-93.47 ± 19.80	-63.90 ± 12.86	27.39 ± 8.99
141133.55+172530.6	···	L1	2	-26.3 ± 29.5	80.7 ± 16.7	2	58.8 ± 11.3	-1.98 ± 9.48	-9.75 ± 8.13	17.37 ± 6.81	11.54 ± 9.33
141224.49+163311.1	2MASSW J1412244+163312	L0.5	14	5.5 ± 13.6	-78.1 ± 48.0	2	32.3 ± 6.1	···	···	···	···
141624.09+134826.7	···	L6	2	17.3 ± 22.8	122.2 ± 58.5	2	5.6 ± 1.1	-43.40 ± 20.00	-9.15 ± 8.15	6.75 ± 1.42	-32.04 ± 18.29
141838.08+145522.3	···	L0	2	-140.2 ± 13.8	-88.5 ± 19.0	2	47.9 ± 9.1	-33.30 ± 18.90	-12.97 ± 8.47	-32.37 ± 7.90	-17.55 ± 17.41
141910.99+484257.0	···	L0	2	68.1 ± 15.9	-2.2 ± 54.3	2	76.8 ± 36.1	12.20 ± 5.50	27.51 ± 17.04	26.18 ± 14.75	9.84 ± 9.02
141942.82+420524.0	···	L0	2	-94.9 ± 13.1	92.8 ± 28.1	2	61.8 ± 11.8	-38.50 ± 12.90	-31.80 ± 9.92	-10.17 ± 7.77	-24.87 ± 12.06
142058.30+213156.6	···	L1	2	-308.0 ± 18.4	189.1 ± 12.9	2	29.7 ± 5.7	18.63 ± 7.19	-30.67 ± 9.49	-0.62 ± 2.84	42.32 ± 7.58
142131.13+182739.7	2MASSW 1421314+182740	L0	4	-739.9 ± 17.8	-174.2 ± 11.5	2	25.1 ± 4.8	···	···	···	···
142227.24+221557.0	···	L6.5+/-2	1	123.2 ± 31.0	-107.5 ± 56.5	2	31.4 ± 6.4	···	···	···	···

Table 2.6 (cont'd)

SDSS Designation (SDSS J +)	Other Name	Spectral Type	ST ref	μ_{RA} (mas yr^{-1})	μ_{dec} (mas yr^{-1})	μ ref	distance (pc)	radial velocity (km s^{-1})	U (km s^{-1})	V (km s^{-1})	W (km s^{-1})
142241.28+234011.8	···	L0	2	0.9 ± 20.5	-6.6 ± 51.9	2	63.8 ± 12.2	···	···	···	···
142257.15+082752.1	···	L2	2	-109.5 ± 37.0	-605.7 ± 28.3	2	52.4 ± 10.	1.10 ± 15.40	76.36 ± 16.30	-126.90 ± 26.39	-32.29 ± 16.04
142806.99+512022.4	···	L0	2	-112.1 ± 56.6	-24.7 ± 22.1	2	78.9 ± 15.1	0.70 ± 2.40	-10.98 ± 15.87	-27.26 ± 15.91	26.12 ± 9.20
142831.28+592335.3	2MASS J14283132+5923354	L5	2	···	···	···	26.1 ± 5.0	-8.80 ± 5.00	···	···	···
142843.13+331036.8	LHS 2924	L0	2	-371.4 ± 30.1	-698.6 ± 13.7	2	10.8 ± 2.1	-42.20 ± 3.30	14.07 ± 2.83	-45.09 ± 7.25	-22.98 ± 3.57
142935.19+383221.4	···	L0	2	-67.8 ± 25.4	44.0 ± 35.3	2	71.4 ± 13.6	-47.90 ± 20.00	-23.19 ± 11.96	-17.87 ± 12.22	-30.66 ± 18.74
143043.51+291541.3	2MASSI J1430435+291540	L2	2	-189.1 ± 13.2	156.7 ± 20.3	2	34.1 ± 6.5	-9.40 ± 6.60	-30.45 ± 7.92	0.53 ± 3.24	9.77 ± 6.55
143130.77+143653.4	2MASS J14313097+1436539	L3	2	-422.2 ± 22.8	-78.2 ± 12.5	2	20.0 ± 3.8	-21.70 ± 20.00	-21.18 ± 9.83	-28.36 ± 6.45	0.85 ± 18.11
143132.79+351300.6	···	L1	2	-35.7 ± 26.5	110.4 ± 32.3	2	51.2 ± 9.8	0.90 ± 11.70	-15.06 ± 8.89	17.78 ± 8.19	8.62 ± 11.08
143147.92+124329.0	···	L0	2	77.0 ± 52.1	37.8 ± 16.0	2	64.5 ± 12.4	-5.40 ± 5.60	15.99 ± 11.26	28.86 ± 12.00	-3.58 ± 7.99
143242.10+345142.7	···	L1	2	-205.0 ± 32.9	-74.9 ± 27.2	2	37.3 ± 7.1	-28.70 ± 6.90	-9.78 ± 5.99	-37.31 ± 8.35	-4.49 ± 7.32
143251.01+363643.6	···	L0	2	-253.5 ± 17.7	-74.2 ± 7.9	2	18.2 ± 3.5	-35.90 ± 5.40	-6.03 ± 2.35	-26.38 ± 4.18	-16.85 ± 5.28
143435.92+220247.2	2MASS J14343616+2202463	L2.5+/-1.5	20	-750.4 ± 18.0	209.5 ± 56.7	2	20.2 ± 3.8	···	···	···	···
143517.20-004612.8	···	L0	2	22.0 ± 9.0	10. ± 6.0	2	80.4 ± 15.4	-25.10 ± 14.10	-1.37 ± 8.80	16.26 ± 3.64	-14.42 ± 11.33
143832.62+572216.8	···	L3	2	116.2 ± 35.3	-5.9 ± 43.8	2	35.5 ± 6.8	19.70 ± 10.80	21.55 ± 7.31	28.73 ± 8.51	15.60 ± 9.72
143911.87+082315.6	···	L0	2	-174.8 ± 49.9	-14.7 ± 26.3	2	41.3 ± 7.9	-48.10 ± 15.70	-35.36 ± 11.38	-20.43 ± 8.87	-21.12 ± 14.25
143925.22+424141.7	···	L0	2	44.1 ± 35.9	95.0 ± 21.4	2	47.0 ± 9.0	-18.80 ± 12.50	-2.08 ± 6.69	16.21 ± 8.94	-18.02 ± 11.76
143933.43+031759.1	···	L3	2	-6.0 ± 21.0	19.0 ± 16.0	3	52.7 ± 10.2	0.70 ± 6.90	7.00 ± 5.61	7.54 ± 4.61	10.12 ± 6.26
143940.91+182637.0	2MASSW J1439409+182637	L1	2	-26.0 ± 24.1	4.3 ± 11.6	2	55.8 ± 10.7	4.84 ± 10.43	6.92 ± 6.35	2.04 ± 5.06	14.33 ± 9.73
144139.88+353809.5	···	L0	2	36.8 ± 21.0	52.8 ± 32.2	2	41.3 ± 7.9	-10.80 ± 8.10	4.53 ± 5.67	12.62 ± 6.17	-6.68 ± 7.60
144430.14+485807.3	···	L0	2	···	···	···	100.8 ± 19.4	-4.60 ± 14.00	···	···	···
144635.65+164337.3	···	L0	2	-78.3 ± 53.3	12.8 ± 22.7	2	57.9 ± 11.2	-18.49 ± 13.66	-13.94 ± 12.05	-9.29 ± 11.11	0.72 ± 13.74
144804.96+060802.2	···	L0	2	···	···	···	36.0 ± 6.9	37.50 ± 10.90	···	···	···
144825.68+103158.8	2MASSW J1448256+103159	L5	2	266.5 ± 42.0	-69.3 ± 28.6	2	16.5 ± 3.1	-17.90 ± 15.40	16.48 ± 8.99	13.48 ± 3.47	-18.87 ± 13.29
144842.76+371932.0	···	L0	2	···	···	···	50.2 ± 9.6	-15.90 ± 9.50	···	···	···
144927.99+205434.1	···	L0	2	-3.7 ± 18.8	38.5 ± 67.2	2	90.5 ± 17.5	-11.32 ± 7.67	-6.85 ± 20.49	13.52 ± 21.62	0.14 ± 8.81
144937.86+235537.8	2MASSW J1449378+235537	L0	2	39.5 ± 16.0	-0.6 ± 24.3	2	52.3 ± 10.	3.20 ± 6.80	17.27 ± 5.62	12.16 ± 5.43	5.54 ± 6.40
145017.31+461739.4	···	L0	2	66.1 ± 22.4	-116.3 ± 38.5	2	50.4 ± 9.6	-44.00 ± 9.10	37.73 ± 10.0	-22.01 ± 7.78	-31.19 ± 8.51
145255.58+272324.4	···	L0	2	-145.6 ± 20.4	-249.8 ± 25.5	2	23.9 ± 4.5	-20.60 ± 7.90	13.49 ± 4.21	-31.43 ± 6.72	-5.42 ± 7.21
145325.89+142041.8	···	L1	2	175.8 ± 29.7	168.0 ± 17.1	2	40.3 ± 7.7	16.20 ± 6.00	18.02 ± 4.97	53.10 ± 9.87	13.78 ± 5.96
145447.76+371823.1	···	L0	2	-106.9 ± 12.0	-66.1 ± 62.3	2	50.6 ± 9.7	5.40 ± 15.70	8.24 ± 12.20	-19.66 ± 12.61	25.06 ± 14.25
145502.92+261919.6	···	L1	2	263.5 ± 20.9	-131.6 ± 27.4	2	40.7 ± 7.8	9.70 ± 7.10	61.93 ± 10.59	23.95 ± 5.84	-9.42 ± 8.12
145658.17+070104.7	···	L3	2	56.6 ± 39.3	-19.5 ± 21.4	2	58.5 ± 11.2	3.40 ± 20.00	24.24 ± 13.94	11.53 ± 8.62	0.53 ± 17.19
150238.47+182539.8	···	L0	2	26.1 ± 13.1	10.1 ± 34.1	2	72.9 ± 14.1	-19.89 ± 14.78	3.34 ± 10.90	9.31 ± 9.65	-13.64 ± 13.03
150240.80+613815.4	···	L0	2	-98.0 ± 10.	36.0 ± 22.0	9	61.1 ± 11.8	-9.10 ± 18.60	-13.67 ± 7.51	-15.76 ± 12.71	9.19 ± 14.52
150309.53+115323.1	···	L2	2	···	···	···	58.5 ± 11.2	-4.20 ± 7.80	···	···	···
150319.64+252522.4	2MASS J15031961+2525196	T6	15	79.2 ± 32.9	546.8 ± 15.4	2	···	···	···	···	···
150844.43+433955.5	···	L0	2	-229.0 ± 24.9	51.6 ± 47.4	2	83.3 ± 16.0	-35.90 ± 12.80	-62.33 ± 20.77	-62.22 ± 16.67	18.37 ± 14.73
151136.24+353511.4	···	L0	2	-1.6 ± 41.7	-49.9 ± 12.7	2	41.9 ± 8.1	-5.70 ± 9.70	16.11 ± 5.80	-3.71 ± 7.20	2.80 ± 9.34
151240.67+340350.1	···	L3	2	230.2 ± 17.6	-9.8 ± 11.5	2	67.3 ± 12.8	-2.10 ± 1.40	51.58 ± 9.08	51.00 ± 9.97	-32.47 ± 7.83
151500.62+484744.8	2MASSW J1515008+484742	L6	2	-954.8 ± 24.0	1473.2 ± 44.4	2	6.9 ± 1.3	···	···	···	···
151506.10+443648.2	···	L7.5+/-1.5	1	82.6 ± 66.1	-26.2 ± 24.6	2	25.2 ± 5.2	···	···	···	···
151527.14+341232.7	···	L1	2	28.5 ± 29.7	-19.8 ± 28.9	2	76.2 ± 14.7	···	···	···	···
151542.28+325543.2	···	L0	2	-90.3 ± 22.6	-60.9 ± 19.7	2	52.1 ± 10.	-8.00 ± 8.20	7.35 ± 5.51	-22.48 ± 7.48	11.99 ± 7.90
151603.96+573907.6	···	L0	2	···	···	···	100.6 ± 19.2	-54.00 ± 15.70	···	···	···
151643.00+305344.3	···	T0.5+/-1	1	-137.5 ± 50.5	9.6 ± 14.8	2	31.7 ± 8.1	···	···	···	···
152039.82+354619.8	···	T0+/-1	1	294.6 ± 36.1	-367.0 ± 26.6	2	···	···	···	···	···
152314.46+105258.9	···	L0	2	-37.9 ± 33.1	-76.7 ± 51.3	2	45.1 ± 8.6	-44.20 ± 16.80	-10.99 ± 12.77	-19.93 ± 10.25	-28.00 ± 14.02
152324.45-021133.8	···	L0	2	···	···	···	65.4 ± 12.5	-32.40 ± 6.30	···	···	···

Table 2.6 (cont'd)

SDSS Designation (SDSS J +)	Other Name	Spectral Type	ST ref	μ_{RA} (mas yr^{-1})	μ_{dec} (mas yr^{-1})	μ ref	distance (pc)	radial velocity (km s^{-1})	U (km s^{-1})	V (km s^{-1})	W (km s^{-1})
152529.74+200407.9	···	L1	2	24.6 ± 26.3	-33.4 ± 22.1	2	40.3 ± 7.7	-5.36 ± 8.11	14.11 ± 5.81	2.16 ± 5.03	-1.15 ± 7.22
152613.92+204339.0	2MASSI J1526140+204341	L7	14	-245.2 ± 21.1	-342.2 ± 22.8	2	15.0 ± 2.9	···	···	···	···
152621.05+280806.9	···	L1	2	34.3 ± 15.2	-105.5 ± 27.4	2	53.7 ± 10.2	11.30 ± 7.80	39.48 ± 8.06	-1.98 ± 6.36	9.49 ± 6.95
153108.87+060111.2	ULAS J153108.89+060111.1	L1	2	28.0 ± 25.0	-48.0 ± 25.0	9	41.1 ± 7.9	-12.70 ± 8.70	9.30 ± 7.04	0.02 ± 5.01	-8.92 ± 7.27
153119.91+262835.2	···	L0	2	···	···	···	43.7 ± 8.4	33.10 ± 9.90	···	···	···
153223.34+261118.8	···	L1	2	-66.0 ± 20.7	-13.2 ± 11.3	2	50.1 ± 9.6	9.20 ± 12.40	8.92 ± 6.39	-3.89 ± 6.46	23.13 ± 10.58
153453.32+121949.2	···	L4+/-1.5	1	158.8 ± 15.9	-54.9 ± 22.1	2	18.3 ± 3.5	···	···	···	···
153721.97+140507.5	···	L0	2	3.9 ± 19.3	-112.5 ± 30.0	2	77.5 ± 14.8	0.85 ± 12.38	38.03 ± 12.05	-23.06 ± 11.03	-4.77 ± 10.99
154009.37+374230.8	···	L9+/-1.5	1	-268.1 ± 75.2	-416.1 ± 46.4	2	19.2 ± 3.9	···	···	···	···
154343.91-014737.2	···	L0	2	-58.1 ± 44.1	15.8 ± 51.0	2	73.4 ± 14.0	22.70 ± 12.50	15.94 ± 14.50	-2.64 ± 16.82	36.36 ± 15.15
154501.09+033714.3	···	L0	2	···	···	···	83.8 ± 39.4	-2.90 ± 8.80	···	···	···
154502.88+061807.8	···	L1	2	···	···	···	44.8 ± 8.6	4.20 ± 6.70	···	···	···
154508.93+355527.3	···	L7.5	1	-187.0 ± 33.9	40.3 ± 51.5	2	34.6 ± 7.3	···	···	···	···
154625.94+160917.9	···	L0	2	77.9 ± 20.1	-192.1 ± 16.7	2	65.6 ± 12.5	18.00 ± 14.40	71.63 ± 13.70	-14.81 ± 8.49	-9.99 ± 12.86
154628.38+253634.3	···	L0	2	-446.7 ± 33.1	138.1 ± 21.0	2	29.7 ± 5.7	-73.80 ± 5.30	-67.32 ± 8.97	-54.54 ± 6.96	-9.02 ± 9.36
154727.23+033636.3	···	L3	2	-63.0 ± 13.0	52.0 ± 17.0	3	104.1 ± 20.0	-15.60 ± 16.10	-28.42 ± 13.87	1.21 ± 7.88	26.46 ± 13.28
154849.01+172235.3	···	L8	2	-293.1 ± 24.1	-112.3 ± 15.5	2	19.7 ± 3.8	-107.50 ± 20.00	-57.29 ± 11.81	-55.01 ± 8.31	-58.48 ± 15.20
154910.11+551203.2	···	L3	2	···	···	···	49.3 ± 9.5	-36.90 ± 20.00	···	···	···
154914.17+502235.8	···	L0	2	···	···	···	91.5 ± 17.6	29.10 ± 13.00	···	···	···
154951.38+490450.1	···	L0	2	···	···	···	65.8 ± 12.6	-16.40 ± 11.80	···	···	···
155008.50+145517.0	2MASS J15500845+1455180	L3	2	116.2 ± 26.0	-168.6 ± 14.0	2	39.2 ± 7.5	-7.00 ± 12.10	35.68 ± 9.77	-4.67 ± 5.34	-20.34 ± 10.27
155120.86+432930.3	···	L3	2	-14.3 ± 27.2	-9.8 ± 19.3	2	40.0 ± 7.6	9.10 ± 6.70	12.55 ± 4.17	7.79 ± 5.53	15.91 ± 6.12
155152.36+094114.6	2MASS J15515237+0941148	L2	4	-81.2 ± 36.7	-64.8 ± 32.0	2	89.3 ± 17.5	···	···	···	···
155215.39+065041.5	···	L0	2	···	···	···	48.9 ± 9.4	-33.90 ± 17.10	···	···	···
155252.32-003501.9	···	L0	2	···	···	···	38.4 ± 7.4	-42.00 ± 14.60	···	···	···
155252.32-003501.9	···	L0	2	···	···	···	50.5 ± 23.7	9.50 ± 3.30	···	···	···
155252.32-003501.9	···	L0	2	···	···	···	39.2 ± 18.4	-9.40 ± 3.50	···	···	···
155252.32-003501.9	···	L0	2	···	···	···	78.8 ± 37.0	-0.50 ± 18.80	···	···	···
155252.32-003501.9	···	L1	2	···	···	···	35.3 ± 16.6	4.80 ± 7.60	···	···	···
155252.32-003501.9	···	L2	2	···	···	···	38.2 ± 18.0	-17.60 ± 16.00	···	···	···
155252.32-003501.9	···	L0	2	···	···	···	57.7 ± 27.1	8.20 ± 10.30	···	···	···
155252.32-003501.9	···	L2	2	···	···	···	54.6 ± 25.6	32.40 ± 11.20	···	···	···
155259.02+294848.3	2MASSW J1552591+294849	L0	2	-193.9 ± 12.4	-76.3 ± 26.8	2	18.6 ± 3.5	-15.30 ± 5.80	1.78 ± 3.18	-17.43 ± 4.28	5.51 ± 4.92
155302.08+153237.8	2MASSI J1553022+153236	T7	7	-436.5 ± 13.5	150.2 ± 22.5	2	···	···	···	···	···
155321.40+210907.8	2MASSW J1553214+210907	L5.5	8	-48.8 ± 20.1	90.2 ± 12.7	2	27.3 ± 5.8	···	···	···	···
155644.35+172308.9	···	L0	2	26.6 ± 26.1	-0.8 ± 13.7	2	33.0 ± 6.3	-4.60 ± 3.10	9.00 ± 2.90	6.04 ± 3.25	0.96 ± 3.53
160005.47+170832.8	2MASSI J1600054+170832	L1.5	14	-14.2 ± 22.4	-1.0 ± 15.2	2	96.8 ± 18.6	···	···	···	···
160140.86+215945.3	···	L1	2	-24.9 ± 26.4	80.8 ± 36.0	2	47.4 ± 9.1	21.40 ± 12.80	6.10 ± 9.97	21.79 ± 8.47	29.84 ± 10.32
160510.15+042152.1	···	L0	2	···	···	···	60.3 ± 11.5	-20.30 ± 12.80	···	···	···
160743.08+345947.3	···	L0	2	-7.0 ± 26.9	65.3 ± 25.3	2	34.0 ± 6.5	-4.90 ± 3.70	-1.22 ± 4.44	6.99 ± 4.17	4.55 ± 4.00
161106.31+002547.0	···	L0	2	···	···	···	86.2 ± 16.9	12.40 ± 12.60	···	···	···
161312.06+472918.2	···	L0	2	···	···	···	56.5 ± 10.8	-19.00 ± 12.80	···	···	···
161349.44+134608.6	···	L0	2	···	···	···	98.9 ± 18.9	-5.69 ± 12.07	···	···	···
161420.49+004643.5	···	L2	2	-57.0 ± 21.0	-31.0 ± 21.0	3	107.7 ± 20.8	-9.20 ± 15.80	0.59 ± 14.19	-27.16 ± 12.43	14.72 ± 12.84
161542.54+495321.2	2MASS J16154255+4953211	L4	10	-23.0 ± 34.0	41.8 ± 45.5	2	71.0 ± 14.5	···	···	···	···
161544.16+355858.4	2MASSW J1615441+355900	L4	2	-29.9 ± 20.9	-516.3 ± 34.0	2	29.7 ± 5.7	-32.10 ± 17.90	59.77 ± 14.14	-52.70 ± 13.20	-16.15 ± 13.06
161611.36+521327.9	···	L0	2	···	···	···	30.5 ± 5.8	6.30 ± 9.80	···	···	···
161626.46+221859.2	···	L5+/-2	16	-89.2 ± 50.3	16.0 ± 26.9	2	37.6 ± 13.6	···	···	···	···
161840.27+202045.6	···	L0	2	37.4 ± 22.0	0.8 ± 35.4	2	39.2 ± 7.5	-19.00 ± 11.90	0.86 ± 8.69	1.19 ± 7.23	-10.64 ± 8.71

Table 2.6 (cont'd)

SDSS Designation (SDSS J +)	Other Name	Spectral Type	ST ref	μ_{RA} (mas yr^{-1})	μ_{dec} (mas yr^{-1})	μ ref	distance (pc)	radial velocity (km s^{-1})	U (km s^{-1})	V (km s^{-1})	W (km s^{-1})
161928.30+005011.7	···	L2	2	74.0 ± 16.0	-88.0 ± 17.0	3	33.5 ± 6.4	-46.40 ± 12.60	-16.75 ± 10.49	-7.37 ± 3.68	-33.21 ± 7.81
162124.66+274702.7	···	L1	2	56.4 ± 59.7	-70.4 ± 27.7	2	77.5 ± 36.4	-15.90 ± 14.80	29.52 ± 18.30	-4.89 ± 16.95	-22.51 ± 20.54
162255.27+115924.0	···	L6+/-1.5	1	-158.8 ± 20.1	30.3 ± 53.4	2	26.1 ± 5.4	···	···	···	···
162307.37+290827.6	···	L1	2	-103.0 ± 47.3	-133.6 ± 46.8	2	48.9 ± 9.4	-8.10 ± 11.50	24.19 ± 11.54	-31.64 ± 12.70	14.11 ± 11.48
162321.84+153039.2	···	L0	2	-41.0 ± 24.1	-27.7 ± 17.3	2	59.2 ± 11.3	5.40 ± 17.20	15.36 ± 12.02	-5.31 ± 8.99	16.31 ± 12.12
162559.01+334705.4	···	L0	2	18.2 ± 27.4	-107.4 ± 23.2	2	44.1 ± 8.4	···	···	···	···
162603.03+211313.0	···	L3	2	31.5 ± 44.5	-81.3 ± 33.3	2	26.8 ± 5.1	-5.90 ± 10.0	15.42 ± 7.12	-1.63 ± 6.47	-2.16 ± 7.84
162834.35+242847.2	···	L1	2	9.6 ± 22.5	-98.1 ± 31.2	2	57.3 ± 10.9	-2.40 ± 13.60	30.28 ± 10.97	-10.29 ± 9.73	-1.79 ± 10.26
162838.35+625945.7	···	L0	2	20.5 ± 12.7	20.7 ± 19.5	2	60.6 ± 11.6	-81.73 ± 8.69	10.59 ± 5.55	-52.92 ± 7.13	-51.26 ± 6.43
162838.40+230822.1	···	T7	1	-345.4 ± 33.6	-340.0 ± 46.1	2	···	···	···	···	···
163041.37+093844.3	2MASS J16304139+0938446	L0	2	-77.9 ± 16.7	-56.2 ± 31.6	2	30.5 ± 5.8	4.95 ± 14.39	15.49 ± 10.98	-6.04 ± 6.57	15.12 ± 8.77
163050.00+005101.3	···	L3	2	-80.0 ± 15.0	-139.0 ± 18.0	3	109.4 ± 21.0	-20.10 ± 12.70	17.61 ± 12.51	-79.33 ± 17.72	-5.56 ± 9.66
163229.25+190440.3	2MASSW J1632291+190441	L8	7	298.4 ± 17.3	-51.2 ± 12.6	2	16.0 ± 3.3	···	···	···	···
163355.23+010027.0	···	L0	2	···	···	···	59.7 ± 28.0	-22.80 ± 5.40	···	···	···
163359.22-064056.6	···	L6	1	-260.8 ± 20.7	-224.8 ± 18.7	2	17.7 ± 3.4	···	···	···	···
163600.79-003452.5	···	L0	2	···	···	···	23.3 ± 4.4	-9.90 ± 14.60	···	···	···
163655.90+002526.3	···	L1	2	···	···	···	···	-6.30 ± 11.80	···	···	···
163817.31+321144.1	···	L0	2	-105.8 ± 41.9	-76.2 ± 38.9	2	41.3 ± 7.9	2.60 ± 8.00	18.70 ± 7.87	-13.75 ± 8.89	22.26 ± 8.52
164230.27+202048.1	···	L1	2	-75.2 ± 22.4	-12.3 ± 14.3	2	104.4 ± 20.0	16.10 ± 15.40	15.70 ± 11.29	-13.54 ± 12.26	43.14 ± 13.61
164438.13+284614.5	···	L2	2	-30.1 ± 45.2	-56.7 ± 40.5	2	46.3 ± 8.9	-10.10 ± 11.30	13.70 ± 9.77	-11.57 ± 10.35	3.48 ± 10.47
164439.66+260013.3	···	L1	2	85.5 ± 26.8	128.9 ± 33.4	2	35.6 ± 6.8	-22.50 ± 13.90	-16.49 ± 9.31	13.27 ± 9.72	-13.43 ± 9.43
164522.06+300406.8	2MASS J16452207+3004071	L3	2	-56.1 ± 51.4	-98.7 ± 45.8	2	51.9 ± 9.9	-8.20 ± 5.70	23.30 ± 10.83	-20.87 ± 11.01	8.39 ± 10.49
164540.16+290744.4	···	L0	2	···	···	···	71.7 ± 13.8	-11.10 ± 9.10	···	···	···
165031.33+352359.5	···	L2	2	···	···	···	72.2 ± 13.8	9.10 ± 9.30	···	···	···
165301.98+413847.5	···	L0	2	···	···	···	71.5 ± 13.8	-40.50 ± 16.70	···	···	···
165309.92+245039.8	···	L0	2	···	···	···	57.3 ± 11.0	5.60 ± 4.70	···	···	···
165329.68+623136.4	···	L2	2	31.0 ± 16.0	-24.0 ± 35.0	9	33.5 ± 6.4	8.90 ± 9.70	14.38 ± 5.55	14.67 ± 7.89	9.27 ± 6.31
165450.79+374714.7	···	L2	2	-128.8 ± 44.8	262.9 ± 30.2	2	37.3 ± 7.1	-20.20 ± 7.50	-44.09 ± 10.58	-3.27 ± 7.41	16.54 ± 8.81
165850.25+182000.5	···	L0	2	-180.7 ± 22.0	131.0 ± 24.3	2	55.1 ± 10.5	-52.20 ± 14.30	-57.85 ± 12.35	-29.05 ± 9.15	26.06 ± 12.87
170219.44+385841.2	···	L1	2	···	···	···	86.0 ± 16.7	-35.50 ± 13.50	···	···	···
170302.52+355824.3	···	L0	2	1.3 ± 31.0	15.6 ± 47.0	2	47.6 ± 9.1	-37.10 ± 9.80	-8.39 ± 10.41	-18.91 ± 9.10	-14.88 ± 8.18
170733.24+430130.1	2MASSI J1707333+430130	L0.5	17	-210.5 ± 8.8	-54.4 ± 20.0	2	25.5 ± 4.9	···	···	···	···
171113.51+232633.2	2MASS J17111353+2326333	L0	2	-59.5 ± 19.1	-28.3 ± 14.1	2	26.0 ± 4.9	-20.90 ± 8.60	-0.79 ± 5.37	-13.69 ± 5.55	0.95 ± 5.02
171145.71+223204.3	2MASSI J1711457+223204	L6.5	14	-49.0 ± 23.2	-18.7 ± 34.7	2	37.2 ± 7.8	···	···	···	···
171147.17+233130.5	···	L3.5+/-1.5	1	13.4 ± 47.9	-90.6 ± 29.2	2	85.0 ± 19.3	···	···	···	···
172244.28+632947.0	···	L0	2	13.0 ± 12.0	-38.0 ± 27.0	9	44.0 ± 8.4	38.30 ± 14.60	16.42 ± 5.85	38.16 ± 12.18	26.91 ± 8.43
172543.84+532534.8	···	L1	2	75.9 ± 28.7	42.9 ± 53.9	2	43.0 ± 20.2	-17.10 ± 8.20	0.28 ± 11.47	0.91 ± 8.94	-15.29 ± 8.96
172822.17+584509.7	···	L2	2	24.0 ± 13.0	102.0 ± 12.0	3	57.1 ± 11.1	1.90 ± 13.00	-17.03 ± 6.21	12.06 ± 11.04	1.73 ± 7.87
175023.82+422237.6	···	T2	7	-101.9 ± 47.5	103.3 ± 27.0	2	···	···	···	···	···
175805.46+463311.9	···	T6.5	7	31.4 ± 67.3	603.8 ± 68.3	2	···	···	···	···	···
191709.94+775600.1	2MASS J19170993+7755597	L0:	4	7.2 ± 6.6	115.9 ± 24.4	2	28.6 ± 5.5	···	···	···	···
205435.83+151903.7	2MASSI J2054358+151904	L1:	14	-66.0 ± 50.1	-135.9 ± 51.2	2	111.5 ± 21.6	···	···	···	···
205715.39+171515.7	2MASSI J2057153+171515	L1.5	14	35.9 ± 40.6	77.6 ± 32.3	2	86.8 ± 16.7	···	···	···	···
205755.92-005006.7	···	L0	2	-37.2 ± 19.2	-30.1 ± 26.9	2	30.8 ± 5.9	5.30 ± 10.10	18.77 ± 6.61	4.91 ± 7.27	6.63 ± 5.54
214046.53+011259.2	···	L4	2	-78.0 ± 20.0	-164.0 ± 22.0	3	35.3 ± 6.9	0.80 ± 10.80	33.68 ± 7.29	-13.50 ± 8.62	2.25 ± 7.01
214527.82-073434.1	···	L0	2	192.6 ± 55.4	-50.6 ± 31.7	2	63.2 ± 12.1	-34.90 ± 19.90	-44.71 ± 17.97	-32.45 ± 14.06	-12.59 ± 19.25
215125.93-000200.7	···	L0	2	4.8 ± 34.8	-88.5 ± 54.8	2	65.6 ± 12.5	-65.80 ± 18.90	-5.38 ± 14.31	-58.82 ± 18.23	34.94 ± 15.96
221743.53+000253.8	···	L1	2	···	···	···	···	-5.10 ± 15.40	···	···	···
222000.97+121436.5	···	L0	2	···	···	···	41.3 ± 7.9	4.00 ± 11.90	···	···	···

Table 2.6 (cont'd)

SDSS Designation (SDSS J +)	Other Name	Spectral Type	ST ref	μ_{RA} (mas yr^{-1})	μ_{dec} (mas yr^{-1})	μ ref	distance (pc)	radial velocity (km s^{-1})	U (km s^{-1})	V (km s^{-1})	W (km s^{-1})
223550.14+122737.3	···	L0	2	3.3 ± 25.5	-113.6 ± 18.0	2	63.5 ± 12.1	-24.10 ± 6.90	23.61 ± 7.83	-34.10 ± 7.56	0.84 ± 7.75
225529.07-003434.0	···	L0	2	51.7 ± 50.0	-181.5 ± 37.8	2	39.1 ± 7.5	-23.30 ± 18.50	13.50 ± 9.46	-36.88 ± 13.54	6.04 ± 15.78
233358.42+005012.1	···	L0	2	···	···	···	39.9 ± 7.6	-2.10 ± 6.70	···	···	···
233526.42+081721.3	···	L0	2	55.8 ± 26.0	-14.2 ± 12.6	2	48.4 ± 9.2	-18.14 ± 10.79	0.94 ± 5.72	-13.78 ± 7.66	15.33 ± 8.68
234034.42-001351.6	···	L1	2	···	···	···	65.5 ± 12.7	-34.40 ± 10.60	···	···	···
234406.88+011515.6	···	L3	2	···	···	···	87.2 ± 16.9	-7.80 ± 6.80	···	···	···

References. — (1) Chiu et al. (2006); (2) this paper; (3) Jameson et al. (2008a); (4) Reid et al. (2008); (5) Kirkpatrick et al. (2010); (6) H02; (7) Burgasser et al. (2006); (8) Kirkpatrick et al. (1999); (9) Faherty et al. (2009); (10) Cruz et al. (2007); (11) Schneider et al. (2002); (12) Cruz et al. (2009); (13) unpublished?; (14) Kirkpatrick et al. (2000); (15) Burgasser et al. (2003a); (16) Knapp et al. (2004); (17) Cruz et al. (2003); (18) Gizis (2002); (19) Looper et al. (2007); (20) Sheppard & Cushing (2009)

Table 2.7. New L Dwarfs Within 30 pc

SDSS Designation	ST	$J - K_S$	δ_{J-K}	distance (pc) $i - z$ vs. M_i	distance (pc) $i - J$ vs. M_i	distance (pc) ST vs. M_J	distance (pc) mean
SDSS J141624.09+134826.7	L6	1.03 ± 0.03	-2.68	5.6 ± 1.1	5.2 ± 0.8	6.7 ± 3.2	6.2 ± 2.0
SDSS J092308.70+234013.7	L1	1.04 ± 0.03	-1.55	13.7 ± 2.6	20.7 ± 3.2	23.5 ± 11.0	21.4 ± 7.4
SDSS J090023.68+253934.3	L7	1.77 ± 0.14	0.00	18.6 ± 3.6	28.7 ± 4.8	25.1 ± 11.8	24.8 ± 8.2
SDSS J135439.54+504451.0	L1	1.20 ± 0.05	-0.75	22.7 ± 4.3	28.4 ± 4.4	29.6 ± 13.9	28.0 ± 9.0
SDSS J093113.23+280227.1	L3	1.25 ± 0.05	-1.62	31.0 ± 5.9	23.9 ± 3.7	29.0 ± 13.6	28.7 ± 9.1

Table 2.8. Means and Dispersions of Kinematic Components

Velocity Vector	Component	Mean (km s^{-1})	σ (km s^{-1})
U	cold	4.5 ± 0.1	27.2 ± 0.1
U	hot	−7.4 ± 0.4	72.3 ± 0.5
V	cold	−10.5 ± 0.1	24.5 ± 0.1
V	hot	−24.4 ± 0.3	49.3 ± 0.4
W	cold	1.2 ± 0.1	18.2 ± 0.1
W	hot	−7.2 ± 0.4	60.1 ± 0.4

Chapter 3

RADIAL VELOCITIES FROM TRIPLESPEC DATA

As part of my goal to examine the kinematics of nearby L dwarfs, I joined the Brown Dwarf Kinematics Program (BDKP; Faherty et al. 2009), a collaboration (led by J. Faherty) to measure six dimensional kinematics (positions and space velocities) of late-M, L, and T dwarfs within 20pc of the Sun. In Fall 2008, I initiated a program to measure radial velocities for nearby L dwarfs from infrared spectra taken with TripleSpec on the ARC 3.5-m telescope at APO. During 23 half-nights over the course of 3 years, I obtained 145 observations of 116 L dwarfs. I began data reductions in early 2009, and have since used six different software packages but have been unable to produce spectra of sufficient quality for radial velocity measurements. This chapter describes the project and targets, the attempted reduction methods, and characterizes the reduced spectra.

3.1 BDKP: Goals and Progress

As discussed in Chapter 1 the ages of ultracool dwarfs are particularly interesting due to the inclusion of disk-age stars and young brown dwarfs in the same spectral classes. One of the most reliable methods for determining the ages of ultracool dwarfs are velocities and velocity dispersions. The kinematics for hundreds of stars and brown dwarfs can characterize both the underlying age distribution of ultracool dwarfs and identify interesting kinematic outliers (young moving group members, old halo dwarfs, and common proper motion binaries). Proper motion and parallax programs have been carried out by J. Faherty (Faherty et al. 2009, 2010, 2012), and radial velocity measurements for late-M and T dwarfs are currently in progress by other members of the BDKP collaboration. This chapter describes the status of my current efforts to measure the radial velocities of the 20pc volume limited sample of L dwarfs.

3.1.1 Proper Motions and Parallaxes

BDKP paper I (Faherty et al. 2009) reported new measurements of 427 proper motions for ultracool dwarfs and analyzed all 841 available ultracool dwarf proper motions. Using these proper motions, Faherty et al. investigated the kinematics of late-M, L, and T dwarfs compared to other disk stars and found the kinematics to be statistically equivalent. They also first explored correlations between $J - K_S$ color and age using kinematic arguments, finding that dwarfs with bluer $J-K_S$ colors had larger mean velocities and dispersions. The proper motions are not only useful in their own right, but are essential to the measurement of the complete space velocities once radial velocity measurements have been completed.

BDKP paper II presented and discussed nine wide binaries found through a search for proper motion companions to the BDKP proper motion sample (Faherty et al. 2010). These binaries, each containing both an ultracool dwarf and higher mass star, are useful benchmark objects, allowing calibration of age and metallicity for the lower mass objects through their high mass counterparts. These wide companion systems also test the limits of binding energy required for a binary to remain gravitationally bound.

BDKP paper III includes new parallax measurements for 70 ultracool dwarfs (Faherty et al. 2012). One motivation for a large sample of ultracool dwarf parallaxes is to examine trends in M_{JHK} as a function of color and spectral type to test evolutionary models. Additionally, these parallax measurements are essential in providing an updated calibration of photometric and spectrophotometric distances. It is typically impossible to measure the parallax of every star in a kinematic sample, so well-calibrated spectrophotometric distances will result in more precise and reliable three-dimensional kinematics.

3.1.2 Radial Velocities of L Dwarfs

My contribution to BDKP is to measure radial velocities for every known L dwarf within 20pc. These velocities, when combined with previously measured proper motions, will produce three-dimensional velocities for a volume-limited sample of L dwarfs. The BDKP collaboration will use these velocities to analyze the kinematic ages of a complete sample of nearby L dwarf population and select objects with peculiar space motions. To perform

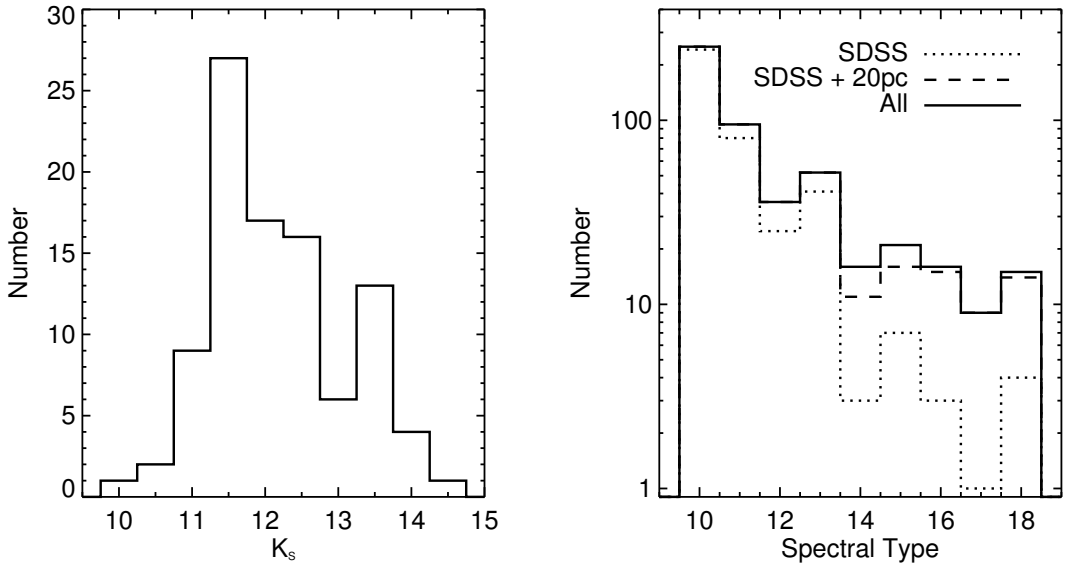

Figure 3.1 Left: The distribution of K_S magnitudes for the L dwarfs within 20pc in the northern hemisphere. Right: Spectral type distribution of SDSS L dwarfs with radial velocities, the 20pc sample, and the additional late-L dwarfs observed with TripleSpec.

the planned analyses, we require velocities with a precision of 10-15 km s^{-1}. The initial list of L dwarfs was based on a query from DwarfArchives.org, including 116 dwarfs within 20pc based on the spectral type/M_J distances relation from Cruz et al. (2003). Of the 116 L dwarfs, 101 are accessible from the northern hemisphere with a range of K_S magnitudes from 10.5 to 14.7 (Figure 3.1). Estimated exposure times to obtain spectra with S/N$\sim$15 per pixel range from 5 minutes to two hours, with a total estimated observing time of $\sim$100 hours.

The clear advantage of working with a volume limited sample is its balance of early- and late-L dwarfs, especially compared to the SDSS L dwarf sample (Figure 3.1). Analysis of the SDSS L dwarfs (which included mostly early-L dwarfs) showed no kinematic bias from the inclusion of both young brown dwarfs and a disk age stellar sample, but a larger sample of mid- to late-L dwarfs could show a bias towards younger ages due to the inclusion of a significant number of young brown dwarfs. As observations progressed, I began observing some additional L4-L9 dwarfs that fell just outside the 20pc boundary (and so were still

relatively bright). While analysis of the kinematics of these objects will be treated separately from those of the 20pc sample, they are included in this chapter because the focus is primarily on data reduction techniques. Their inclusion increases the number of L dwarfs observed to 116 objects.

At the outset of the project, 17 of the 116 objects on our list were considered radial velocity standards, with high precision radial velocities from Mohanty & Basri (2003); Bailer-Jones (2004); Blake et al. (2007) and Zapatero Osorio et al. (2007). Over the course of the next three years of observations, the number of standard stars with published radial velocities grew to 58 with velocities from Blake et al. (2010) and Seifahrt et al. (2010). The large number of published radial velocities is an advantage for increasing the number of radial velocity templates and comparison objects.

Upon the completion of the observing program in early 2011, I had obtained 145 observations of 116 L dwarfs with TripleSpec. Table 3.1 lists these targets, previously observed radial velocities, and characterizes the exposure times and sky conditions of each observation.

Table 3.1. L Dwarf Radial Velocity Targets

Name	R.A.	Decl.	ST	J	K_S	RV (km s^{-1})	RV Ref.	Date Observed	N_{exp}[1]	ET[1] (s)	airmass	conditions	20pc?
SDSS J000112.18+153535.5	00 01 12.1	+15 35 35.5	L4	15.52 ± 0.06	13.71 ± 0.04	···	···	UT100929	12	180	1.1	clear	n
								UT101029	12	180	1.05	clear	n
2MASSWJ0015447+351603	00 15 44.76	+35 16 02.6	L2	13.88 ± 0.03	12.26 ± 0.02	−37.4 ± 0.2	1	UT090803	8	120	1.03	partly cloudy	y
								UT100822	12	90	1.08	partly cloudy	
2MASS J00332386−1521309	00 33 23.8	−15 21 30.9	L4	15.29 ± 0.06	13.41 ± 0.04	···	···	UT101029	8	200	1.5	clear	y
2MASSWJ0036159+182110	00 36 16.17	+18 21 10.4	L3.5	12.41 ± 0.06	11.09 ± 0.06	19.2 ± 1.4	1,2,3	UT100723	4	100	1.03	partly cloudy	y
2MASSWJ0045214+163445	00 45 21.43	+16 34 44.6	L3.5	13.06 ± 0.02	11.37 ± 0.02	3.3 ± 0.2	1	UT081017	4	120	1.29	clear	y
								UT100929	4	60	1.14	clear	
SDSSp J010752.33+004156.1	01 07 52.42	+00 41 56.3	L8	15.82 ± 0.06	13.71 ± 0.04	···	···	UT091107	12	180	2.18	partly cloudy	y
2MASS J01311838+3801554	01 31 18.3	+38 01 55.4	L4	14.68 ± 0.03	13.05 ± 0.03	···	···	UT100929	8	150	1.11	clear	y
								UT101029	4	150	1.04	clear	
2MASSJ01443536−0716142	01 44 35.36	−07 16 14.2	L5	14.19 ± 0.03	12.27 ± 0.02	24.7 ± 0.1	1	UT080907	8	150	1.31	mstly clr, humid	y
								UT100929	4	130	1.3	clear	
DENIS−P J0205.4−1159	02 05 29.40	−11 59 29.6	L7	14.59 ± 0.03	13.00 ± 0.03	7 ± 2	4	UT081017	4	150	2	clear	y
2MASSW J0208236+273740	02 08 23.6	+27 37 40.0	L5	15.71 ± 0.06	13.87 ± 0.05	···	···	UT100929	12	180	1.1	clear	n
								UT101026	12	200	1.01	clear, humid	
2MASSIJ0213288+444445	02 13 28.80	+44 44 45.3	L1.5	13.49 ± 0.03	12.21 ± 0.02	−23.5 ± 0.1	1	UT090803	4	200	1.18	mstly clr	y
2MASSIJ0251148−035245	02 51 14.90	−03 52 45.9	L3	13.06 ± 0.03	11.66 ± 0.02	1.3 ± 0.1	1	UT080907	4	150	1.26	mstly clr, humid	y
2MASSJ02572581−3105523	02 57 25.81	−31 05 52.3	L8	14.67 ± 0.04	12.88 ± 0.03	···	···	UT091207	8	140	2.84	mstly clr	y
2MASSWJ0310599+164816	03 10 59.86	+16 48 15.5	L8	16.03 ± 0.08	14.31 ± 0.07	···	···	UT100929	16	200	1.13	clear	y
								UT101029	8	200	1.12	clear	
2MASSJ03140344+1603056	03 14 03.44	+16 03 05.6	L0	12.53 ± 0.02	11.24 ± 0.02	−7.4 ± 1	3,5	UT100929	4	60	1.33	clear	y
								UT101026	4	60	1.1	clear, humid	
2MASSJ03185403−3421292	03 18 54.03	−34 21 29.2	L7	15.57 ± 0.06	13.51 ± 0.04	···	···	UT100822	12	180	2.61	mstly clr	y
2MASSWJ0320284−044636	03 20 28.39	−04 46 35.8	L0.5	13.26 ± 0.02	12.13 ± 0.03	···	···	UT080907	4	200	1.27	mstly clr, humid	y
2MASSJ03521086+0210479	03 52 10.86	+02 10 47.9	L0	13.08 ± 0.03	11.96 ± 0.02	···	···	UT080907	4	150	1.16	mstly clr, humid	y
2MASSJ03552337+1133437	03 55 23.37	+11 33 43.7	L6	14.05 ± 0.02	11.53 ± 0.02	11.8 ± 0.4	1,5	UT081019	4	150	1.09	clear	n
SDSSp J042348.57−041403.5	04 23 48.58	−04 14 03.5	L7.5	14.47 ± 0.03	12.93 ± 0.03	···	···	UT091107	16	200	1.47	partly cloudy	n
2MASSIJ0439010−235308	04 39 01.01	−23 53 08.3	L6.5	14.41 ± 0.03	12.82 ± 0.02	···	···	UT091107	8	180	1.9	partly cloudy	y
2MASSIJ0445538−304820	04 45 53.87	−30 48 20.4	L2	13.39 ± 0.03	11.98 ± 0.02	···	···	UT091207	8	120	2.27	mstly clr	y
2MASSJ05002100+0330501	05 00 21.00	+03 30 50.1	L4	13.67 ± 0.02	12.06 ± 0.02	12.3 ± 0.2	1	UT081019	4	200	1.15	clear	y
2MASSIJ0523382−140302	05 23 38.22	−14 03 02.2	L2.5	13.08 ± 0.02	11.64 ± 0.03	11.8 ± 0.5	1,3,5	UT081017	4	120	1.47	clear	y
SDSSp J053951.99−005902.0	05 39 52.00	−00 59 01.9	L5	14.03 ± 0.03	12.53 ± 0.02	12.7 ± 1.8	1,2	UT081019	4	200	1.21	clear	y
LSR 0602+3910	06 02 30.45	+39 10 59.2	L1	12.30 ± 0.02	10.87 ± 0.02	7.5 ± 0.6	1,3	UT081017	4	90	1.05	clear	y
								UT090303	4	60	1.02	partly cloudy	
DENIS−P J0615493−010041	06 15 49.34	−01 00 41.5	L2	13.75 ± 0.03	12.54 ± 0.03	···	···	UT081019	4	200	1.22	clear	y
DENIS−P J0652197−253450	06 52 19.77	−25 34 50.5	L0	12.76 ± 0.02	11.52 ± 0.02	···	···	UT081019	4	150	1.98	clear	y
2MASSIJ0652307+471034	06 52 30.73	+47 10 34.8	L4.5	13.51 ± 0.02	11.69 ± 0.02	−7 ± 0.1	1	UT081019	4	150	1.04	clear	y
SDSS J065405.63+652805.4	06 54 05.6	+65 28 05.1	L6	16.14 ± 0.09	14.6 ± 0.08	···	···	UT110323	20	200	1.24	clear	y
2MASSJ07003664+3157266	07 00 36.64	+31 57 26.6	L3.5	12.92 ± 0.02	11.32 ± 0.02	−43 ± 1.5	1,3	UT090304	4	120	1.06	mostly cloudy	y
2MASSWJ0717163+570543	07 17 16.26	+57 05 43.0	L6.5	14.64 ± 0.03	12.95 ± 0.03	−16.3 ± 0.2	1	UT081017	4	200	1.11	clear	y

Table 3.1 (cont'd)

Name	R.A.	Decl.	ST	J	K_S	RV (km s^{-1})	RV Ref.	Date Observed	N_{exp}[1]	ET[1] (s)	airmass	conditions	20pc?
2MASSIJ0746425+200032	07 46 42.56	+20 00 32.1	L0.5	11.76 ± 0.02	10.47 ± 0.02	53.2 ± 0.8	1,3,6	UT080324	10	120	···	clear	y
								UT090303	8	60	1.03	partly cloudy	
DENIS−P J0751164−253043	07 51 16.45	−25 30 43.2	L2.5	13.16 ± 0.02	11.99 ± 0.02	···	···	UT090303	4	150	1.91	partly cloudy	y
SDSS J080531.84+481233.0	08 05 31.8	+48 12 33.1	L4	14.73 ± 0.03	13.44 ± 0.04	···	···	UT110323	12	150	1.07	clear	y
DENIS−P J0812316−244442	08 12 31.70	−24 44 42.3	L2.5	13.82 ± 0.03	12.39 ± 0.02	···	···	UT090303	4	300	1.87	partly cloudy	n
2MASSIJ0825196+211552	08 25 19.68	+21 15 52.1	L7.5	15.10 ± 0.03	13.03 ± 0.03	20.5 ± 2	6	UT081019	4	240	1.08	clear	y
DENIS−P J0828343−130919	08 28 34.19	−13 09 19.8	L1	12.80 ± 0.03	11.30 ± 0.02	···	···	UT090303	4	90	1.44	mstly clr	y
SSSPM J0829−1309	08 28 34.19	−13 09 19.8	L2	12.80 ± 0.03	11.30 ± 0.02	26 ± 0.6	1,3	UT090304	8	90	1.52	mostly cloudy	y
SDSSp J083008.12+482847.4	08 30 08.25	+48 28 48.2	L8	15.44 ± 0.05	13.68 ± 0.04	···	···	UT081019	8	150	1.12	clear	y
2MASSIJ0835425−081923	08 35 42.56	−08 19 23.7	L5	13.17 ± 0.02	11.14 ± 0.02	27.4 ± 1.5	1,3,5	UT081017	4	120	1.45	clear	y
								UT090303	4	90	1.33	mostly clear	
2MASSIJ0847287−153237	08 47 28.72	−15 32 37.2	L2	13.51 ± 0.03	12.06 ± 0.02	2 ± 0.1	1	UT090303	8	90	1.51	mstly clr	y
SDSS J085234.90+472035.0	08 52 34.90	+47 20 35.9	L9.5	16.30 ± 0.06	14.61 ± 0.06	···	···	UT100127	20	200	1.09	clear	y
SDSSp J085758.45+570851.4	08 57 58.49	+57 08 51.4	L8	15.04 ± 0.04	12.96 ± 0.03	−123.5 ± 10	7	UT091107	8	200	1.17	partly cloudy	y
2MASSIJ0859254−194926	08 59 25.47	−19 49 26.8	L6	15.53 ± 0.05	13.75 ± 0.06	···	···	UT090304	8	300	1.7	mostly cloudy	y
2MASS J09054654+5623117	09 05 46.5	+56 23 11.7	L5	15.40 ± 0.05	13.73 ± 0.04	···	···	UT110413	16	180	1.1	clear	y
								UT110522	12	200	1.45	clear	
2MASSIJ0908380+503208	09 08 38.03	+50 32 08.8	L5	14.53 ± 0.06	12.93 ± 0.06	−33.2 ± 10	7	UT090304	8	200	1.05	mostly cloudy	y
2MASSJ09111297+7401081	09 11 12.97	+74 01 08.1	L0	12.92 ± 0.03	11.75 ± 0.03	−4.1 ± 0.2	1	UT081017	4	120	1.51	clear	y
2MASSJ09153413+0422045	09 15 34.13	+04 22 04.5	L7	14.55 ± 0.03	13.01 ± 0.04	···	···	UT090303	8	250	1.14	partly cloudy	y
2MASSWJ0920122+351742	09 20 12.23	+35 17 42.9	L6.5	15.63 ± 0.06	13.98 ± 0.06	···	···	UT091107	4	200	1.09	partly cloudy	y
								UT100303	12	140	1.11	clear	
2MASSJ09211410−2104446	09 21 14.10	−21 04 44.6	L2	12.78 ± 0.02	11.69 ± 0.02	80.3 ± 0.7	1,3	UT090506	8	90	2	mstly clr	y
SDSS 09230870+23401365	09 23 08.70	+23 40 13.65	L1	13.85 ± 0.02	12.81 ± 0.02	−29.9 ± 10	7	UT091107	8	200	1.07	partly cloudy	y
2MASSWJ1004392−333518	10 04 39.29	−33 35 18.9	L4	14.48 ± 0.04	12.92 ± 0.02	···	···	UT100127	8	140	2.62	clear	y
2MASSIJ1010148−040649	10 10 14.80	−04 06 49.9	L6	15.51 ± 0.06	13.62 ± 0.05	···	···	UT090506	8	250	1.4	mstly clr	y
2MASSJ10224821+5825453	10 22 48.21	+58 25 45.3	L1	13.50 ± 0.03	12.16 ± 0.03	19.5 ± 0.7	1,3	UT081017	4	200	1.51	clear	y
								UT090303	4	200	1.11	mostly clear	
2MASSWJ1036530−344138	10 36 53.05	−34 41 38.0	L6	15.62 ± 0.05	13.80 ± 0.04	···	···	UT100127	12	200	2.86	mstly clr	y
								UT110413	16	200	2.68	clear	
2MASSJ10430758+2225236	10 43 07.58	+22 25 23.6	L8	15.97 ± 0.07	13.99 ± 0.04	7 ± 1.1	3	UT090508	8	300	1.07	clear	y
								UT091107	12	200	1.12	partly cloudy	
2MASSIJ1045240−014957	10 45 24.00	−01 49 57.6	L1	13.16 ± 0.02	11.78 ± 0.02	6.3 ± 0.1	1,5	UT090303	4	150	1.25	partly cloudy	y
								UT110321	8	70	1.67	partly cloudy	
SDSS J104842.84+011158.5	10 48 42.81	+01 11 58.0	L1	12.92 ± 0.02	11.62 ± 0.02	24 ± 0.6	3,5	UT090303	4	150	1.19	mstly clr	y
								UT110321	8	60	1.72	partly cloudy	
2MASSJ10511900+5613086	10 51 19.00	+56 13 08.6	L2	13.24 ± 0.03	11.91 ± 0.02	−16.4 ± 3.8	7	UT090304	4	150	1.1	mostly cloudy	y
DENIS−P J1058.7−1548	10 58 47.87	−15 48 17.2	L3	14.16 ± 0.04	12.53 ± 0.03	19 ± 2	4	UT090508	8	200	1.52	clear	y
2MASSIJ1104012+195921	11 04 01.27	+19 59 21.7	L4	14.38 ± 0.03	12.95 ± 0.03	−8.7 ± 6.6	7	UT090506	8	150	1.13	clear	n
2MASSWJ1108307+683017	11 08 30.81	+68 30 16.9	L1	13.12 ± 0.02	11.58 ± 0.02	−9.8 ± 0.1	1	UT090304	4	150	1.24	mostly cloudy	y
SDSS J115553.86+055957.5	11 55 53.89	+05 59 57.7	L7.5	15.78 ± 0.06	14.11 ± 0.06	136.8 ± 10	7	UT100303	12	200	1.13	clear	y

Table 3.1 (cont'd)

Name	R.A.	Decl.	ST	J	K_S	RV (km s^{-1})	RV Ref.	Date Observed	N_{exp}[1]	ET[1] (s)	airmass	conditions	20pc?
								UT110413	8	200	1.13	clear	
SDSSp J120358.19+001550.3	12 03 58.12	+00 15 50.0	L3	14.01 ± 0.03	12.48 ± 0.02	−1.5 ± 1.5	1,3,6	UT090506	4	180	1.19	mstly clr	y
								UT110321	8	150	1.5	partly cloudy	
SDSS J120747.17+024424.8	12 07 47.17	+02 44 24.9	L8	15.53 ± 0.06	14.17 ± 0.06	−41.8 ± 10	7	UT100127	16	200	1.18	partly cloudy	n
								UT110413	8	180	1.22	clear	
2MASSIJ1213033−043243	12 13 03.36	−04 32 43.7	L5	14.68 ± 0.04	13.01 ± 0.03	···	···	UT090508	8	150	1.27	clear	y
SDSS J121951.45+312849.4	12 19 51.56	+31 28 49.7	L8	16.00 ± 0.06	14.31 ± 0.06	···	···	UT100127	16	200	1.15	partly cloudy	n
2MASSJ12212770+0257198	12 21 27.70	+02 57 19.8	L0	13.17 ± 0.02	11.95 ± 0.03	−10.1 ± 2.2	1,3,7	UT090508	4	110	1.17	clear	y
2MASSWJ1239272+551537	12 39 27.27	+55 15 37.1	L5	14.71 ± 0.03	12.79 ± 0.03	−17.8 ± 10	7	UT100127	8	120	1.09	partly cloudy	n
2MASSWJ1300425+191235	13 00 42.55	+19 12 35.4	L1	12.72 ± 0.02	11.62 ± 0.02	−17.7 ± 0.6	1,3	UT100303	4	60	1.03	clear	n
Kelu−1	13 05 40.19	−25 41 05.9	L2	13.41 ± 0.03	11.75 ± 0.02	9.5 ± 3.2	1,3,4	UT090506	2	90	1.92	mostly clear	y
2MASSIJ1315309−264951	13 15 30.94	−26 49 51.3	L5.5	15.20 ± 0.05	13.46 ± 0.04	···	···	UT090508	8	220	1.99	clear	y
SDSS J141624.08+134826.7	14 16 24.09	+13 48 26.74	L6	13.15 ± 0.02	12.11 ± 0.02	−43.4 ± 10	7	UT100127	4	130	1.07	partly cloudy	y
								UT110321	8	100	1.09	partly cloudy	
2MASSW1421314+182740	14 21 31.45	+18 27 40.7	L0	13.23 ± 0.02	11.94 ± 0.02	···	···	UT090508	4	110	1.04	clear	y
DENIS−P J142527.97−365023.4	14 25 27.98	−36 50 22.9	L5	13.75 ± 0.03	11.81 ± 0.03	5.4 ± 0.3	1	UT100505	8	130	3.17	clear	y
2MASSWJ1439284+192915	14 39 28.36	+19 29 14.9	L1	12.76 ± 0.02	11.55 ± 0.02	−27.2 ± 0.9	1,3,4,6	UT100303	4	60	1.12	clear	y
								UT110321	16	60	1.06	partly cloudy	
2MASSWJ1506544+132106	15 06 54.41	+13 21 06.0	L3	13.37 ± 0.02	11.74 ± 0.02	−0.8 ± 0.7	1,3	UT090508	4	90	1.1	clear	y
2MASSWJ1507476−162738	15 07 47.69	−16 27 38.6	L5	12.83 ± 0.03	11.31 ± 0.03	−36.5 ± 2.7	1,3,6	UT080322	6	300	···	clear	n
2MASSWJ1515008+484742	15 15 00.83	+48 47 41.6	L6	14.11 ± 0.03	12.50 ± 0.02	···	···	UT090508	4	180	1.04	clear	y
Gl 584C	15 23 22.63	+30 14 56.2	L8	16.06 ± 0.10	14.35 ± 0.07	···	···	UT100303	10	200	1.01	clear	y
2MASSIJ1526140+204341	15 26 14.05	+20 43 41.4	L7	15.59 ± 0.06	13.92 ± 0.05	···	···	UT090508	8	220	1.04	clear	y
DENIS−P J153941.96−052042.4	15 39 41.89	−05 20 42.8	L4	13.92 ± 0.03	12.58 ± 0.03	27.3 ± 0.2	1	UT090506	4	200	1.32	clear	y
								UT110321	12	150	1.3	partly cloudy	
2MASSWJ1552591+294849	15 52 59.06	+29 48 48.5	L1	13.48 ± 0.03	12.02 ± 0.03	−16.9 ± 4	1,7	UT100303	4	80	1.01	clear	y
2MASSWJ1555157−095605	15 55 15.73	−09 56 05.5	L1	12.56 ± 0.02	11.44 ± 0.02	14.7 ± 0.7	1,3	UT090506	4	75	1.42	clear	y
								UT110321	16	50	1.4	partly cloudy	
2MASSWJ1645221−131951	16 45 22.11	−13 19 51.6	L1.5	12.45 ± 0.03	11.15 ± 0.03	26.5 ± 0.6	1,3	UT110321	12	40	1.45	partly cloudy	n
2MASSWJ1658037+702701	16 58 03.80	+70 27 01.5	L1	13.29 ± 0.02	11.92 ± 0.02	−25.6 ± 0.1	1	UT100303	4	60	1.29	clear	n
DENIS−P J170548.38−051645.7	17 05 48.34	−05 16 46.2	L4	13.31 ± 0.03	12.03 ± 0.02	12.2 ± 0.6	1,3	UT100303	8	70	1.33	clear	n
2MASSJ17072343−0558249B	17 07 23.43	−05 58 24.9	L3	13.96 ± 0.11	12.20 ± 0.08	···	···	UT100303	4	90	1.37	clear	y
SDSS J171714.10+652622.2	17 17 14.0	+65 26 22.1	L4	14.95 ± 0.04	13.18 ± 0.03	···	···	UT100723	8	160	1.45	mstly clr	y
2MASSIJ1721039+334415	17 21 03.90	+33 44 16.0	L3	13.63 ± 0.02	12.49 ± 0.02	···	···	UT090803	8	125	1.57	mstly clr	y
2MASSJ17312974+2721233	17 31 29.74	+27 21 23.3	L0	12.09 ± 0.03	10.91 ± 0.02	−30.1 ± 0.8	1,3	UT090803	6	60	1.43	clear	y
DENIS−P J1745346−164053	17 45 34.66	−16 40 53.8	L1.5	13.65 ± 0.03	12.40 ± 0.02	···	···	UT100303	8	70	1.69	clear	y
								UT100505	8	120	1.73	clear	
2MASS J17461199+5034036	17 46 11.9	+50 34 03.6	L5	15.1 ± 0.06	13.53 ± 0.04	···	···	UT101029	8	200	1.32	clear	y
2MASSJ17502484−0016151	17 50 24.84	−00 16 15.1	L5.5	13.29 ± 0.02	11.85 ± 0.02	···	···	UT100303	4	60	1.27	clear	y
2MASSIJ1807159+501531	18 07 15.93	+50 15 31.6	L1.5	12.93 ± 0.02	11.60 ± 0.03	−1.2 ± 2.2	1,3	UT100723	8	60	1.17	mstly clr	y
								UT110522	12	60	1.55	clear	

The observing procedure typically consisted of the following steps. Targets were placed on the spectrograph slit using a guide camera with a roughly K band filter. The slit was oriented without reference to the parallactic angle. Once the target was centered on the slit, an observing script was run that shuffled the target from its initial position to a position on the other side of the slit, forming an ABBA nod pattern. The data for each exposure was read out using a Fowler sampling of 8. Each individual exposure ranged from 10 seconds (long enough for the required fowler sampling readouts) to 200 seconds (where the sky background in K band begins to dominate). The number of exposures and individual exposure times are given in Table 3.1.

An A0 standard star spectrum was taken before or after each target star to provide telluric correction. The A0 standards were also observed using an ABBA nod pattern, with notably shorter exposure times. Each night, a series of 10 flat field spectra (Quartz lamp) were taken; no arc lamp exposures were taken because the assumed method of calibration was the telluric emission lines, and no darks were taken because the assumed calibration involved pair subtraction (which subtracts the dark and thermal currents).

3.2 Overview of the TripleSpec Instrument

TripleSpec (Wilson et al. 2004) is a mid-resolution (R$\sim$3500) infrared (0.95 μm to 2.5 μm) spectrograph. The TripleSpec instrument was designed to be easily reproduced, and was initially planned for three telescopes, resulting in the "Triple" portion of the instrument name. As of the publication of this dissertation, one TripleSpec is a facility instrument at the Palomar 200-in telescope and a second is a facility instrument at the Astrophysical Research Consortium (ARC) 3.5-m telescope at Apache Point Observatory (APO). ARC TripleSpec was commissioned in March 2008 and was available for all APO users as of Q4 2008.

TripleSpec is unusual for its wide wavelength coverage and medium resolution, distinguishing it from other infrared spectrographs with lower-resolution, but covering a similar wavelength range (e.g. SpeX on IRTF; Rayner et al. 2003) and higher-resolution instruments covering only a portion of the infrared spectrum (e.g. NIRSPEC on Keck; McLean et al. 1998). This combination of resolution and wavelength coverage has only been sur-

Table 3.1 (cont'd)

Name	R.A.	Decl.	ST	J	K_S	RV (km s^{-1})	RV Ref.	Date Observed	N_{exp}[1]	ET[1] (s)	airmass	conditions	20pc?
2MASS J18212815+1414010	18 21 28.15	'+14 14 01.0	L4.5	13.43 ± 0.03	11.65 ± 0.03	9.8 ± 0.2	1	UT100505	4	160	1.16	clear	y
2MASSJ20025073−0521524	20 02 50.73	−05 21 52.4	L6	15.32 ± 0.05	13.42 ± 0.04	···	···	UT100505	16	200	1.56	clear	y
2MASSJ20360316+1051295	20 36 03.16	+10 51 29.5	L3	13.95 ± 0.03	12.45 ± 0.03	19.7 ± 0.5	1	UT100505	8	140	1.3	clear	y
2MASSIJ2057540−025230	20 57 54.09	−02 52 30.2	L1.5	13.12 ± 0.02	11.72 ± 0.03	−24.8 ± 1.7	1,3	UT091001	8	140	1.24	mostly cloudy	y
2MASSIJ2104149−103736	21 04 14.91	−10 37 36.9	L3	13.84 ± 0.03	12.37 ± 0.02	−20.8 ± 1.3	1,3	UT100929	4	150	1.38	clear	y
2MASS J21321145+1341584	21 32 11.5	+13 41 58.4	L6	15.80 ± 0.06	13.84 ± 0.06	···	···	UT100723	12	200	1.08	mostly clear	y
2MASS J21373742+0808463	21 37 37.4	+08 08 46.3	L5	14.77 ± 0.03	13.02 ± 0.03	···	···	UT100723	8	150	1.16	mostly clear	y
								UT101029	8	150	1.16	clear	
2MASS J21481628+4003593	21 48 16.28	+40 03 59.3	L6	14.15 ± 0.04	11.77 ± 0.04	···	···	UT100505	4	150	1.3	clear	y
2MASSJ21522609+0937575	21 52 26.09	+09 37 57.5	L6	15.19 ± 0.03	13.34 ± 0.03	···	···	UT090803	8	180	1.09	mostly clear	y
								UT100929	8	180	1.09	clear	
2MASS J21580457−1550098	21 58 04.5	−15 50 09.8	L4	15.04 ± 0.04	13.19 ± 0.04	···	···	UT100822	8	180	1.62	mostly clear	y
								UT100929	8	180	1.54	clear	
								UT101029	8	150	1.52	clear	
2MASSWJ2224438−015852	22 24 43.81	−01 58 52.1	L4.5	14.02 ± 0.06	12.02 ± 0.06	−37.9 ± 1.1	1,3,6	UT090803	4	175	1.22	mostly clear	y
2MASS J22490917+3205489	22 49 09.1	+32 05 48.9	L5	15.48 ± 0.06	13.59 ± 0.05	···	···	UT101029	8	200	1.02	clear	y
DENIS−P J225210.73−173013.4	22 52 10.73	−17 30 13.4	L7.5	14.31 ± 0.03	12.90 ± 0.02	···	···	UT100723	8	120	1.7	mostly clear	y
2MASS J23254530+4251488	23 25 45.3	+42 51 48.8	L8	15.49 ± 0.05	13.76 ± 0.05	···	···	UT100723	12	200	1.02	partly cloudy	y
2MASSJ23440624−0733282	23 44 06.24	−07 33 28.2	L4.5	14.80 ± 0.04	13.23 ± 0.03	···	···	UT090803	8	160	1.32	mostly clear	y

References. — (1) Blake et al. (2010), (2) Zapatero Osorio et al. (2007), (3) Seifahrt et al. (2010), (4) Mohanty & Basri (2003), (5) Blake et al. (2007), (6) Bailer-Jones (2004), (7) Schmidt et al. (2010b)

[1]The ET given is for individual exposures; total exposure time is $N_{exp} \times$ ET.

passed with commissioning of X-shooter on the VLT in September 2008 (Vernet et al. 2011) and FIRE on Magellan in March 2010 (Simcoe et al. 2010).

To achieve the combination of wide wavelength coverage and medium resolution, light from the telescope is cross-dispersed, resulting in 5 orders which are captured on a 1024x 2048 detector. Each order is curved with respect to the x,y coordinates of the detector, and lines of constant wavelength are tilted with respect to each order. These effects are shown in full frame images of a flat field and a target + sky (Figure 3.3) and a detail image of a portion of the target + sky (Figure 3.4). Extracting useful data from raw images like these involves fitting both the curved order and the tilt of lines of constant wavelength across the slit.

Our observations exclusively used the 1.1" (2.1 pixel) slit, resulting in an average resolution of R$\sim$3500, but the resolution of TripleSpec varies over the length of each order and between the orders themselves. Figure 3.2 shows both $\Delta\lambda$ and Δv as a function of wavelength for all five TripleSpec orders when the 1.1" slit is in use. The $\Delta\lambda$ of each pixel varies from 1.2Å in the 7th order to 3.0Å in the 3rd order, while the Δv varies from 34 km s^{-1} to 47 km s^{-1} within each order.

Most reduction software packages begin by identifying and fitting the curved orders. Following that fit, the orders were either interpolated onto a straightened grid (which effectively smooths the spectrum, resulting in a loss of information) or the fit to each order was used in conjunction with additional fits to derive a two-dimensional wavelength solution (which must account for some tilt). While the tilt is small (1-4 pixels over an order width of 90-110 pixels), correctly fitting it across all orders is essential for radial velocity work and for faint stars where the precise sky subtraction is important.

3.3 Reduction Codes

While obtaining the observations described in Section 3.1.2, I was reducing data with the APO SpexTool, which is described in detail in Section 3.3.2. As it became clear that the APO SpexTool reductions were not producing velocities wither either accuracy (as measured from comparison to literature values) or the needed accuracy (10-15 km s^{-1}), I briefly attempted four different reduction codes before moving to the Firehose reduction

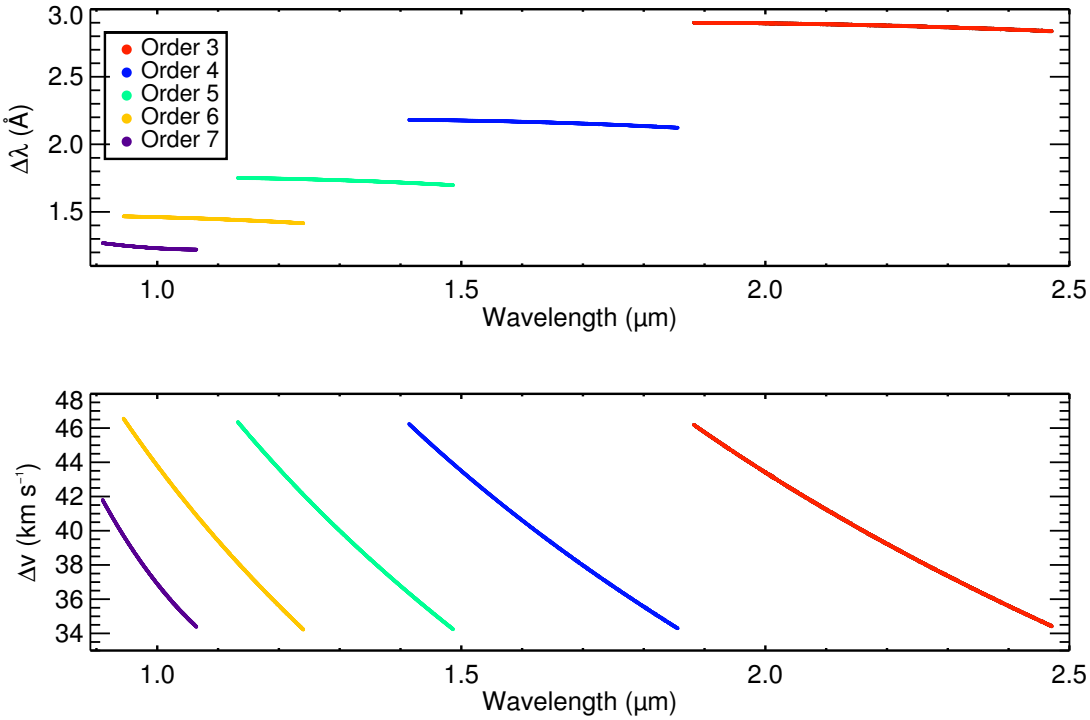

Figure 3.2 Pixel ($\Delta\lambda$) and velocity (Δv) resolution of TripleSpec as a function of wavelength. Each order is shown in a different color. The resolution varies both between the orders and throughout each order from 1.2 to 3.0Å per pixel and from 34 to 47 km s^{-1}.

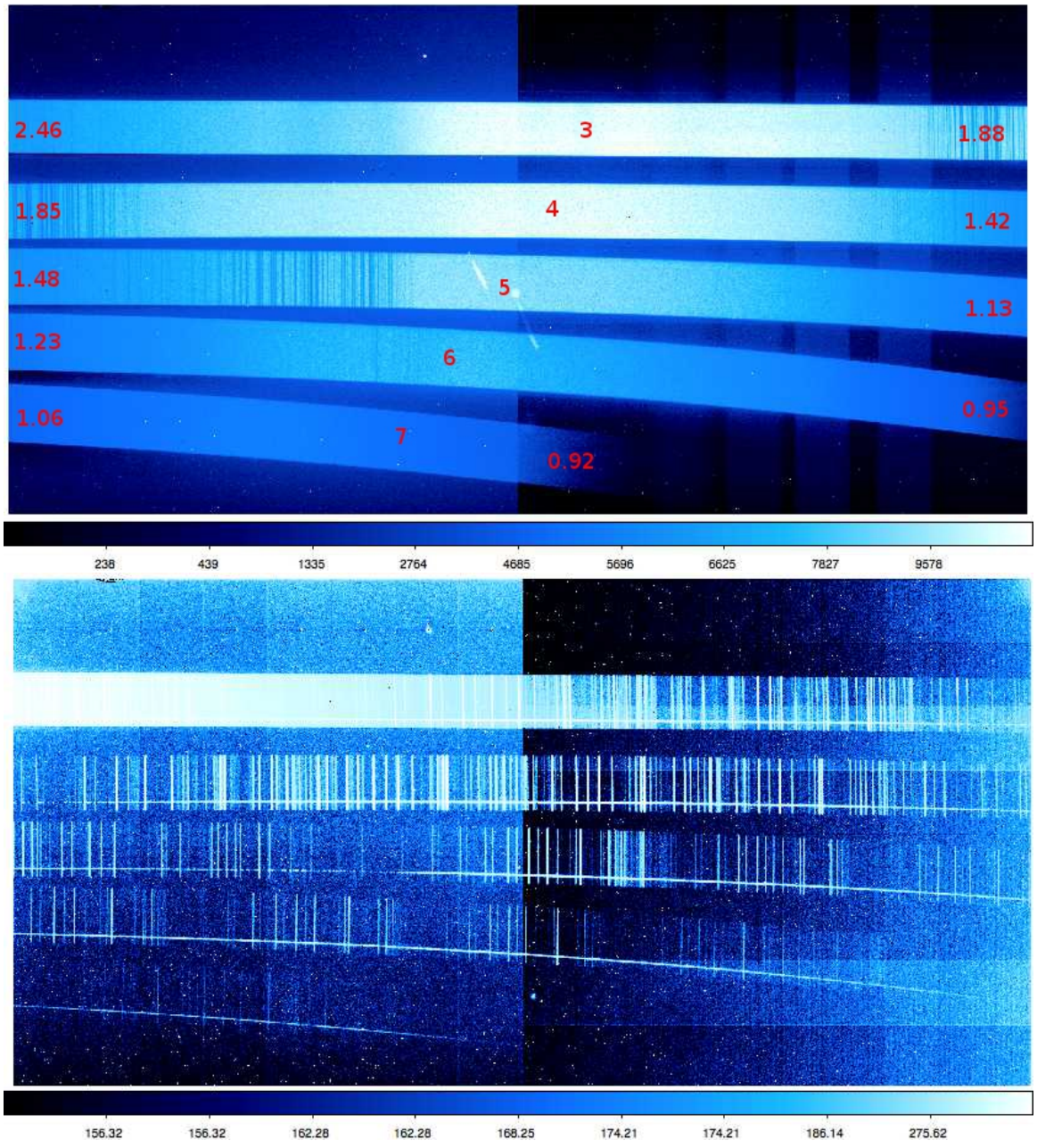

Figure 3.3 Top Panel: A 60 second exposure of bright quartz lamp taken on UT 2010 March 3. The orders are numbered in the center, and the approximate wavelength of the end of each order is given in microns. Bottom Panel: A raw 60 second exposure of 2MASSW J1300425+191235, an L1 dwarf also taken on UT 2010 March 3. In both panels, the shading corresponds to the number of counts in each pixel.

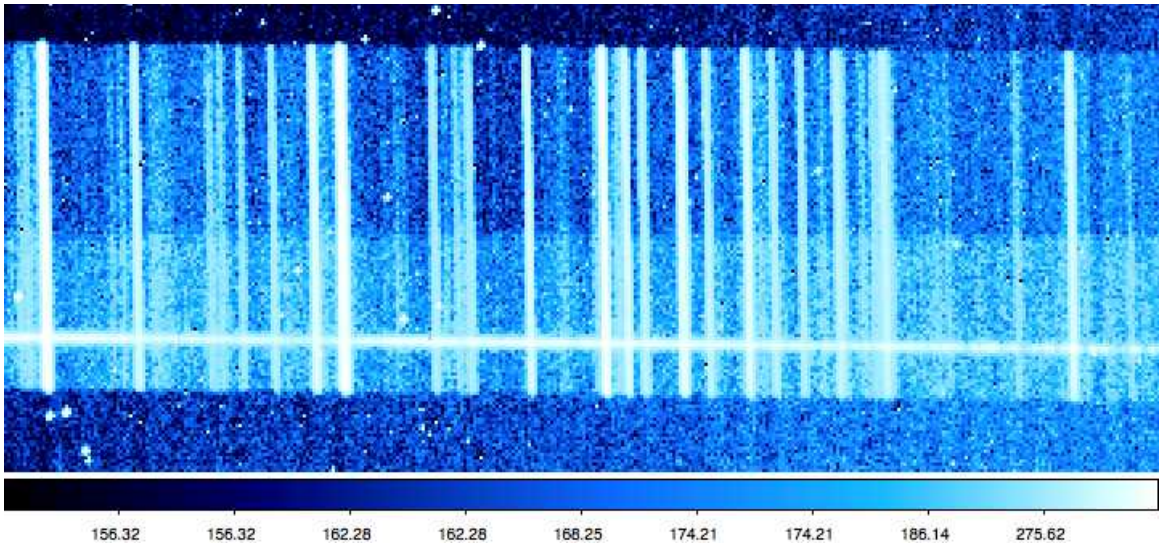

Figure 3.4 A portion of the 3rd spectral order near 2.1 microns from the 60 second exposure of 2MASSW J1300425+191235 shown in the bottom panel of Figure 3.3. This is not a region of large order curvature, but the lines show a tilt of ∼4 pixels across the order of ∼104 pixels.

code (Section 3.3.3). A description of the reduction attempted with each of the codes is described below.

3.3.1 Attempted Reduction Codes

NIRSPEC reduction code

NIRSPEC is an R∼25,000 cross-dispersed infrared spectrograph which is a facility instrument at Keck II (McLean et al. 1998). The NIRSPEC reduction code, REDSPEC[1], is an IDL-based code which has been adapted to reduce data from other instruments as well. REDSPEC begins by measuring the curve and tilt of each order in a single input science image. The curve is measured through the object trace, then the order is rectified in the spatial direction and saved as an output. The user then identifies sky lines in the spatially rectified image, and the tilt of those sky lines is measured and used to rectify the image in the spectral direction.

[1]http://www2.keck.hawaii.edu/inst/nirspec/redspec.html

After putting a few test images through the rectification procedure, the output spectra were found to still have residual tilts of 0.5-1 pixel (over a 100 pixel order; $\sim$0.57°) , and residual curvature of 1-5 pixels (over 2048 pixels; $\sim$0.14°). These residuals did not disappear for any iteration of selected sky lines (there are at least 10 in each order) or polynomial order to fit the curvature. When combined with the unavoidable smoothing that would result from interpolating the input data twice, these residuals (of at least 1 pixel, or >30 km s^{-1}) were deemed unacceptable. A reinvestigation of the NIRSPEC code using sub-images may be warranted if the TripleSpec data remains unreduced by other methods.

Palomar TripleSpec Reduction Code

The TripleSpec instrument at Palomar was commissioned before the APO TripleSpec, and Phillip Muirhead wrote a custom IDL code to rectify raw data and prepare it for further reductions. The file format of data from Palomar TripleSpec has a surprisingly large number of differences from the APO TripleSpec, so the code was not simple to adapt to the L dwarf data. After a brief attempt to use the software, I instead used it to inform my later attempts at writing my own code.

IRAF Echelle Reduction

IRAF contains an echelle reduction package which performs many of the order finding and flat fielding strategies used in the other reduction codes discussed. The routines are designed to handle the curved orders and object traces which are often part of echelle data. Additionally, a parameter can be set to extract the arc from the wavelength calibration image at the same location as the science aperture, minimizing the effects of tilt. Unfortunately, there is no IRAF parameter to handle the tilts of the lines, resulting in very poor sky subtraction. Additionally, the tilt proved to be significant over the spatial extent of the aperture, resulting in a "smoothed" wavelength resolution in the extracted spectrum.

Custom IDL Code

I also made a brief attempt to write reduction code in IDL, hoping that a combination of my own parameters and fitting, combined with functions from other codes, would produce a better solution. The solution I chose was to measure order curvature using a flat field image, then flat field and rectify each order of each science image. Then I would measure tilts from the positions of sky lines and further rectify each image before using IRAF extraction techniques. This produced an image with residual tilts and curvature that was only marginally less than the NIRSPEC code. This lack of success convinced me that the proper reduction code would fit curvature and tilts with more complex functions to produce adequate spectra.

3.3.2 Spextool As a Reduction Tool for APO TripleSpec

Spextool is an IDL-based reduction code written for the Spex instrument on IRTF (Vacca et al. 2003; Cushing et al. 2004). Spex includes both a low-resolution mode at R$\sim$1000-2000 and a prism mode at R$\sim$100. Following the commissioning of TripleSpec, M. Cushing adapted Spextool to reduce TripleSpec data using the code written for the low-resolution mode. The APO Spextool reduction pipeline is described fully in Cushing et al. (2004), but I will also summarize the main features of the pipeline here.

The APO Spextool Reduction Pipeline

Flat field: The flat fielding process begins with the identification and median combination of all images of the bright quartz lamp (usually the recommended 10 exposures at 60s). The edges of each of the five orders are found on the master flat; the reduction package relies on input guesses for the edge of each order, then finds the real edge by locating a high and low point nearby with a flux change of 75%. Once the positions are located, a set of fourth order polynomial coefficients are stored in the header of the final flat field image for use in the next steps.

Wavelength Calibration: The current iteration of APO Spextool relies on sky emission lines for wavelength calibration. The user inputs a group of wavelength calibration

images, usually a number of target exposures with relatively bright sky lines. The pipeline then creates a sky image from a median combination of the input images and extracts an aperture from the center of each order for wavelength calibration. The lines are found by fitting a gaussian to the area around each of a list of guessed positions. A third order polynomial is then fit to the lines, and the resulting wavelengths per pixel are stored for application to the extracted spectrum. The residuals for the wavelength fit performed by APO Spextool were typically 0.1-0.3Å for orders 3 and 4, and 0.8-1.5Å for orders 5, 6, and 7.

Pairwise Sky Subtraction: The primary extraction mode in APO Spextool is pairwise subtraction, where the data are taken in pairs of A and B exposures with equal exposure times. As described in Section 3.1.2, the target is moved from one side of the slit (the "A" position) to the other (the "B" position) between two images. Since the B image is taken immediately after the A image, the sky conditions should remain relatively constant between images. Subtracting A−B images should result in a pairwise subtracted image with little or no residual sky lines. The subtraction also removes any thermal or dark current background, which are roughly equal in the two images. In practice, sky lines often remain after subtraction (as shown in Figure 3.5) likely due to changing conditions over short timescales.

Aperture Extraction The apertures are extracted in pairs from the A−B images. To find the apertures, each column (or wavelength) of the order is shifted by its polynomial offset and added together to construct a spatial profile image. The profile image shows the A and B apertures in their positions across the slit. The user can select the center of each aperture, or an automated process will find the aperture center based on a gaussian fit to the aperture profile. The user can then select the aperture width in addition to a region for sky subtraction along each order. The aperture is then extracted along each order. Additional sky subtraction is performed during the extraction with a polynomial fit to the sky on either side of both apertures.

Telluric Correction: All of the exposures of each target are median combined, then flux calibrated and telluric corrected using the method described in detail in Vacca et al. (2003). Briefly, the calibration uses an A0 star standard that was taken at a similar airmass,

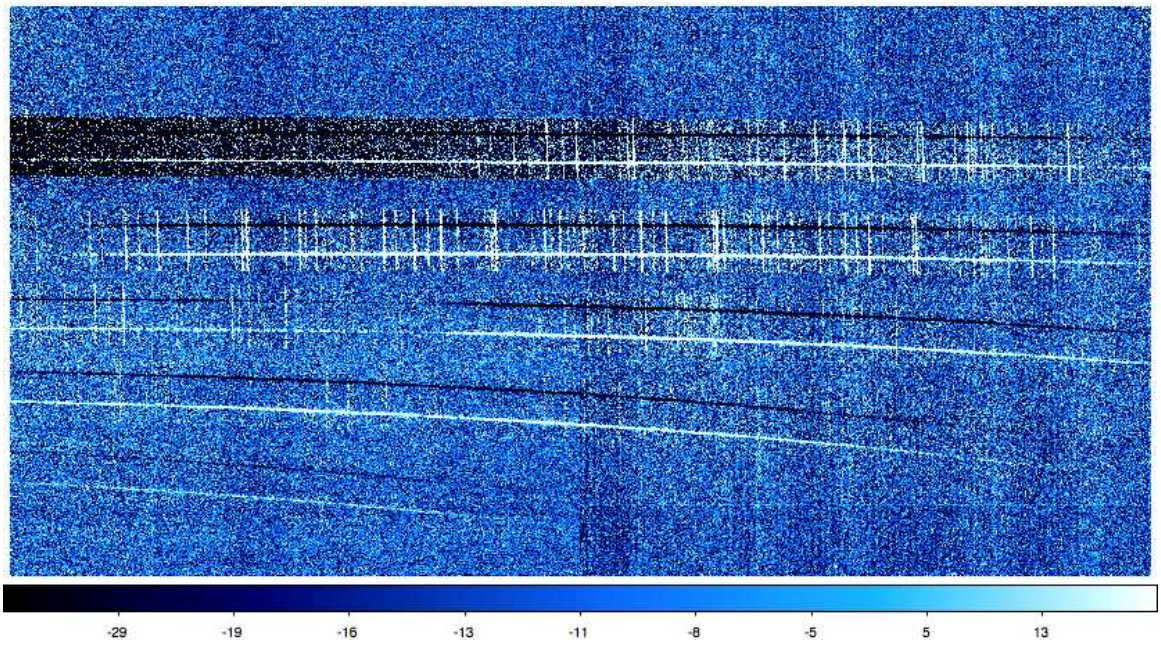

Figure 3.5 Flat fielded and pair subtracted spectra of L2.5 dwarf D081224 taken on 2009 March 3. Note the residual sky lines, still strong compared to the spectrum even when equal-length exposures are subtracted.

hour angle, time, and region of the sky to the science target. The spectrum of this standard star (as extracted) is then de-reddened (using published B and V magnitudes) and shifted to approximately zero radial velocity to match the model spectrum. The A0 standard spectrum is then divided by a model spectrum of Vega[2] with hydrogen absorption lines (the main spectral feature) modified to match the strength and the broadening measured from a fit of the 1.00494μm Paschen δ line in the sixth spectral order. The resulting telluric calibration spectrum contains both telluric lines and the relation between counts detected and absolute flux for the whole spectrum. The final science target spectrum is calculated by dividing the extracted, combined spectrum by the telluric correction spectrum.

[2]from http://kurucz.harvard.edu/stars.html

Spectra Reduced With APO Spextool

An example spectrum of L2.5 dwarf DENIS-PJ0812316-244442 (hereafter D081224) reduced using SpexTool is shown in Figure 3.6. For comparison, a similar type L dwarf spectrum and the positions of the telluric OH lines are shown. The emission/absorption features which correspond to the OH lines exemplify the two main problems with SpexTool reductions of TripleSpec spectra. The sky lines are imperfectly subtracted - leaving an excess in emission for the A or B exposure and effectively an absorption line for the other object in the pair. The wavelength solution is also derived from a fit to the middle of the order[3], which results in an offset between spectra taken at different sides of the slit due to the tilt across the order.

The spectrum shown in Figure 3.6 is not representative of the *appearance* of the entire sample of spectra. The reduction of this spectrum is particularly bad, though the cause of the particularly poor sky subtraction is unknown. D081224 is of an average brightness (K_S = 12.39) compared to the rest of the L dwarfs and the spectrum was taken during "grey" time (50% moon illumination during that portion of the night) and in clear conditions with low humidity. The airmass of the observations was relatively high (1.8), but as is discussed further in Section 3.5, no obvious factor seems to determine the quality of the final spectrum.

Even if other spectra have reductions which appear better, with weaker residual sky lines, the primary issue is that the wavelength solution is offset by 1-4 pixels between the A and B exposures in every order (which would have a corresponding effect of at least ∼30 - 120 km s^{-1} in the final spectrum). It is possible that this effect would be sufficiently corrected by an offset calculated from comparison of sky lines extracted from the A and B apertures, but the corrected spectra would still be subject to smoothing from the assumption that pixel = wavelength within the aperture. This solution was not attempted.

[3]A further updated version of SpexTool was released in beta by M. Cushing in March 2011, which constructed a more sophisticated wavelength solution without the assumption of that wavelength is constant across the order. Extensive tests showed that this update still produced qualitatively similar results for my spectra. The version of the code which I discuss is most similar to the current publicly available version of APOSpexTool and the version of Spextool described in Cushing et al. (2004)

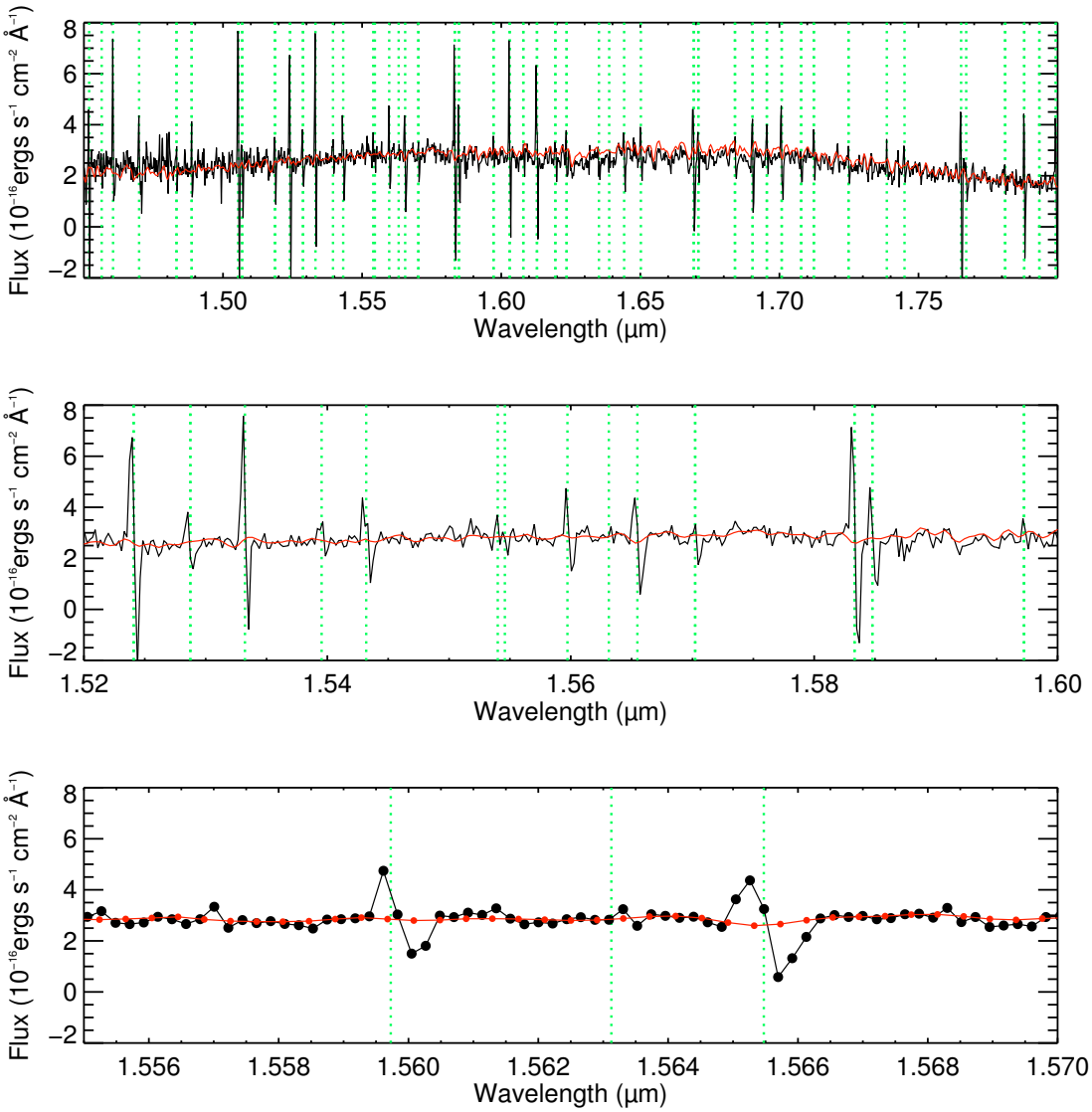

Figure 3.6 Spectrum of L2.5 dwarf D081224 (also shown in Figure 3.5), extracted using the standard Spextool reduction pipeline. The spectrum of L1 dwarf 2MASS J14392836+1929149 from Cushing et al. (2005, red line) and the wavelengths of strong telluric OH lines (green dotted) are also shown; the residual sky features are aligned with the OH lines, while the real L dwarf features (mostly FeH absorption) are present in the spectrum of 2MASS J14392836+1929149 as well.

3.3.3 Adapting Firehose to TripleSpec

The FIRE (Folded-port InfraRed Echellette) spectrograph was built for the Magellan telescope and was commissioned there in March 2010 (Simcoe et al. 2010). Reduction software for FIRE should be a good match to TripleSpec because the instruments are similar; FIRE has a slightly larger wavelength coverage than TripleSpec (0.82-2.51 microns), and a higher resolution (R$\sim$6000). The raw data are cross-dispersed over twenty-one orders, which are both curved and tilted. The FIRE reduction code, named Firehose, is written in IDL and based on MASE, a spectral reduction code written for the Magellan Echellette Spectrograph (Bochanski et al. 2009). The MASE code is in turn based heavily on the IDL routines written to reduce the SDSS spectra (the SDSS spectro2d pipeline[4]; and XIDL routines[5]). I worked with John Bochanski to adapt the Firehose code to TripleSpec data.

Description of the Firehose Pipeline

Order Edges: On a single flat field image, the pipeline locates the edges of the orders using a sawtooth technique. Each row in the image is shifted by one spatial pixel and then subtracted from the original row. The edges of the order then stand out as peaks and troughs, which are identified using the x_fndpeaks IDL routine. The locations of the edges of each order are saved in a file which is accessed in subsequent steps.

Flat Fields: The Firehose pipeline constructs two flat fields - an illumination flat (which corrects for the scattered light on an image due to using an in-dome calibration for an on-sky observation) and a pixel flat (which is the typical flat used to quantify the detector response). Before either of these flat fields are constructed, an estimate of the tilt of each line is calculated from the positions of the sky lines. No input sky line positions are used; peaks are found in each x (spatial) row parallel to the order edge.

The illumination flat is constructed from a set of median combined on-sky images. Before the illumination flat is created, each order is rectified in both dimensions using the order edges and the slit tilts. The illumination flat is then created by fitting the average change in

[4]http://spectro.princeton.edu/

[5]http://www.ucolick.org/xavier/IDL/index.html

flux over the spatial direction of the order. Large deviations from the median value in the spatial direction are ignored. Using an image of a target star, the illumination flat produced shows a very small (∼1%) gradient over the detector.

The pixel flat is constructed without rectifying the flat field images. A median filter is applied to each image to remove large scale variations, then the group of filtered images is median combined. Pixels outside the boundaries of each order are set to unity.

Fire Structure: The remainder of the code depends on a fits table named the "fire structure". The fire structure contains a list of all the observations and the user classifies each object as "science," "telluric," "lamp" or "unknown." Each group of science observations is assigned a single ID and final name. Additionally, each science observation is matched to one or more telluric observations. Lamp exposures are assigned to data without strong sky lines; for our observations, the telluric observations are assigned a science image as a wavelength calibration reference.

Extraction Pipeline: Once the above steps are completed, the extraction pipeline is run on each group of science exposures which re-measures tilts, finds sky lines and calculates a wavelength solution, generates and subtracts a sky model, extracts apertures, and interpolates the aperture extracted from each order onto a wavelength grid.

Wavelength Solution: The initial wavelength solution is derived from lines identified and labeled in an interactive procedure. This initial solution used 6th order polynomials to determine a wavelength solution, and had average resulting RMS values of 0.2Å.

During the reduction pipeline, the wavelength calibration begins with a new measurement of the tilts in the image based on the locations of the sky lines; peaks are found in every row across the spatial dimension and the change in location of the peaks is calculated to rectify the image. The image is then rectified, and a master arc is constructed by a median combine of all the rows. OH lines are located by looking for peaks near the locations of lines in a stored arc with identified lines, and the wavelength solution is determined by a polynomial fit to the locations of those lines. The fits typically produced RMS values of 0.5Å. The wavelength solution is then translated to a wavelength image, which assigns a wavelength value to each pixel in the original image.

Sky Subtraction: The sky subtraction is performed by a fit to the sky in each science

image. The aperture of the target is first crudely traced and extracted, then an initial sky trace is taken along the spatial center of the slit. The sky trace is fit with a B-spline (Kelson 2003). A B-spline is a functional fit defined by the order and separation of a series of piece-wise polynomials. This initial fit is propagated along the slit in the spatial direction using the tilt found in the wavelength solution process. Note that this sky subtraction procedure does not include any assumption of the location and width of the sky lines, but fits a function to the background sky as it is measured in the image. The B-spline fit to the sky is then used as an initial sky subtraction image and fed into the aperture extraction routines.

Aperture Extraction: After a rough spectrum is extracted from each order, the spectra are then extracted using optimal extraction techniques (e.g., Mukai 1990). In optimal extraction, each pixel is weighted by the fraction of total flux it contains, determined by a collapsed trace of the entire order in wavelength space. After the weights are determined, the image is fit by two sets of B-spline functions, one for the aperture and one for the sky background. Outliers from the B-spline fits (usually cosmic rays) are rejected, and the B-splines are re-fit, producing an aperture and a final sky background image.

An example of a final sky subtracted image is shown in Figure 3.7. The sky subtraction was very good for orders 5-7, but consistently failed for orders 3 and 4. Within both of those orders, the residuals show that the sky model did not match the tilt of the real data; there is an over-subtracted line offset from the sky line in the data. These poorly subtracted features was present in every reduced spectrum. We mainly attempted to address the problem through adjusting the B-spline spacing, using values from 0.05 to 1 pixel and the B-spline order from 3 to 7 (other parameters had no effect on the subtraction problem). Due to these issues with sky subtraction, orders 3 and 4 (H and K band) were deemed unusable for velocities.

To assign wavelengths, an identical aperture is extracted from the wavelength image, and the extracted apertures in flux and wavelength are interpolated onto a wavelength array generated for each order.

Telluric Correction and Combination: The Telluric standards are extracted in a similar fashion to the science objects, but done with a science image with strong telluric lines.

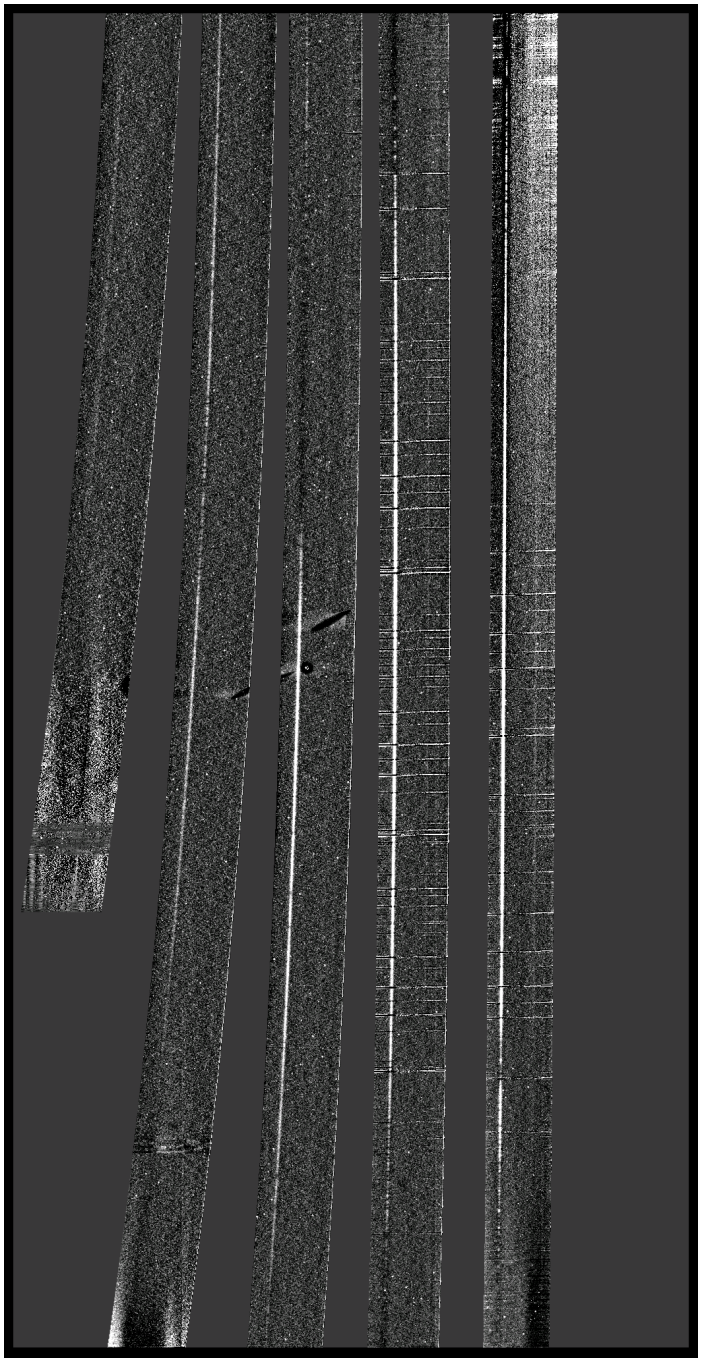

Figure 3.7 The final sky subtracted image from Firehose reduction. While the sky subtraction looks good for order 5-7, there is a residual tilt between the modeled lines and the real lines in orders 3 and 4. These residuals remained for every value of B-spline spacing between 0.1 and 1.

The telluric calibration routines from the Spextool reduction package (Vacca et al. 2003) are also used for Firehose. A description of those routines can be found in Section 3.3.2. The only difference in telluric correction is that Firehose runs telluric calibration before combining the spectra, while Spextool runs telluric calibration afterwards.

Spectra Reduced With Firehose

An example spectrum of L2.5 dwarf D081224 reduced using Firehose is shown in Figure 3.8, again with a comparison L dwarf spectrum and the positions of the telluric OH lines. There are many residual absorption features at the position of many of the OH lines, again emphasizing (as shown in Figure 3.7) that the sky model which was fit to this order overestimated the strength of the sky lines. The reduction of this object is atypically poor (as was the case for its reduction with Spextool), but similar residuals are apparent in most spectra reduced using Firehose, as is discussed in the description above.

While Firehose reduction produced, on average, better reductions for the TripleSpec L dwarfs, the software failed to find tilts and/or apertures for 34 of the 145 observations. These are preferentially (though not exclusively) data with individual exposures of 60 seconds or shorter, indicating that the problem is likely caused by weaker sky lines in short exposures. In a further updated version of the code, I will implement a co-adding feature to produce stronger lines for the reductions. Using the current version of the software, there were sufficient spectra to examine the wavelength and velocity fidelity of the sample without solving this issue.

Figure 3.9 shows a portion of the spectrum of DENIS-PJ0812316-244442 in the J band, constructed from the 5th and 6th spectral orders, again with a comparison spectrum and OH lines (though those shown for the J band are on average 5 times weaker than those shown for the H band). Because the sky subtraction appears to be adequate in this portion of the spectrum, this is the region of the spectrum that is most suitable for velocity measurement. The next few sections focus on this region of the spectrum extracted using the Firehose pipeline.

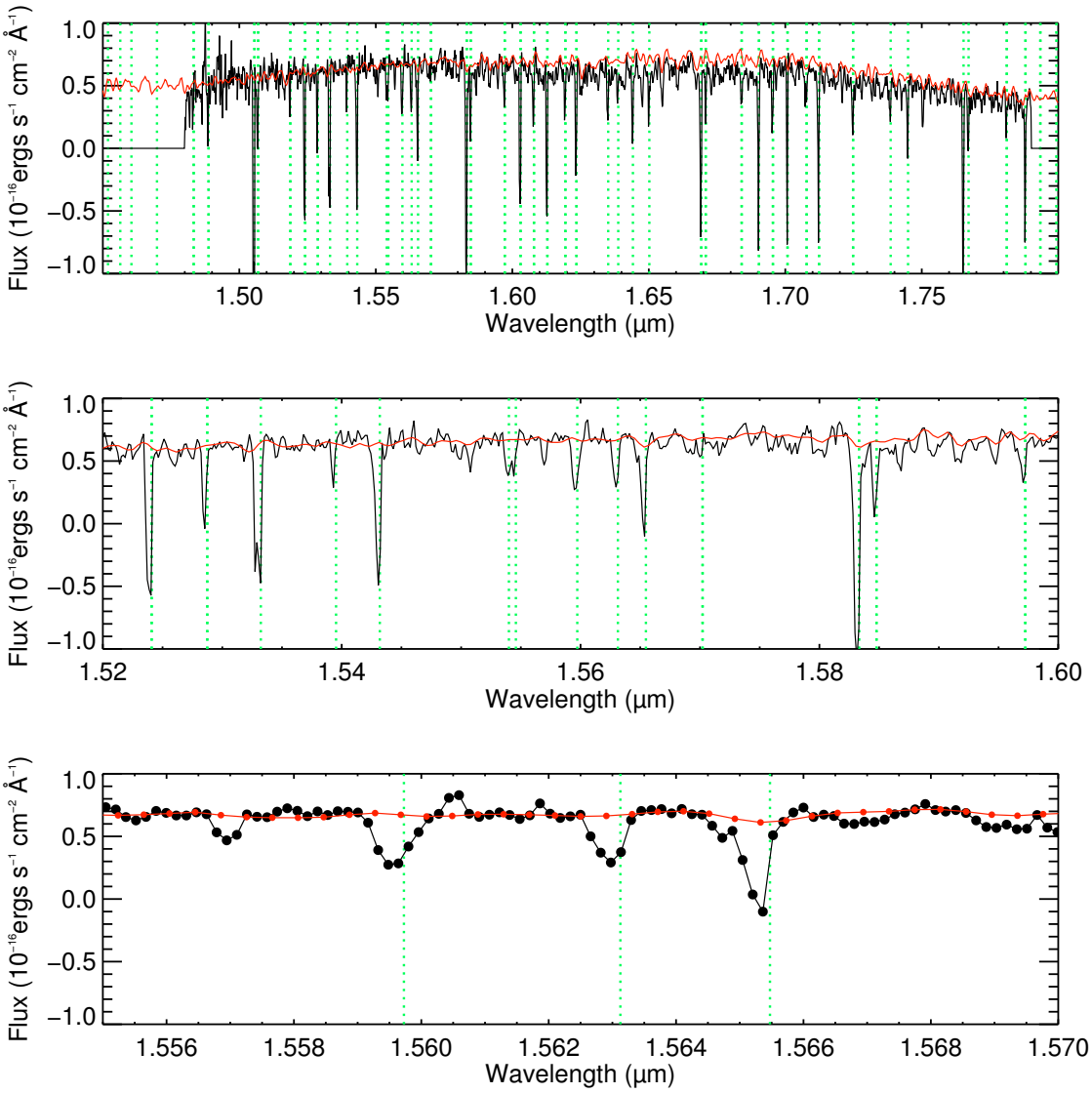

Figure 3.8 Spectrum of L2.5 dwarf D081224, extracted using the Firehose pipeline. The spectrum of L1 dwarf 2MASS J14392836+1929149 from Cushing et al. (2005, red) and the wavelengths of strong telluric OH lines (green dotted) are shown. The residual sky features are aligned with the OH lines, while the real L dwarf features (mostly FeH absorption) are present in the spectrum of 2MASS J14392836+1929149 as well. A heliocentric correction of -11 km s^{-1} was applied to the data, which may account for the shift between the sky lines and their rest wavlengths.

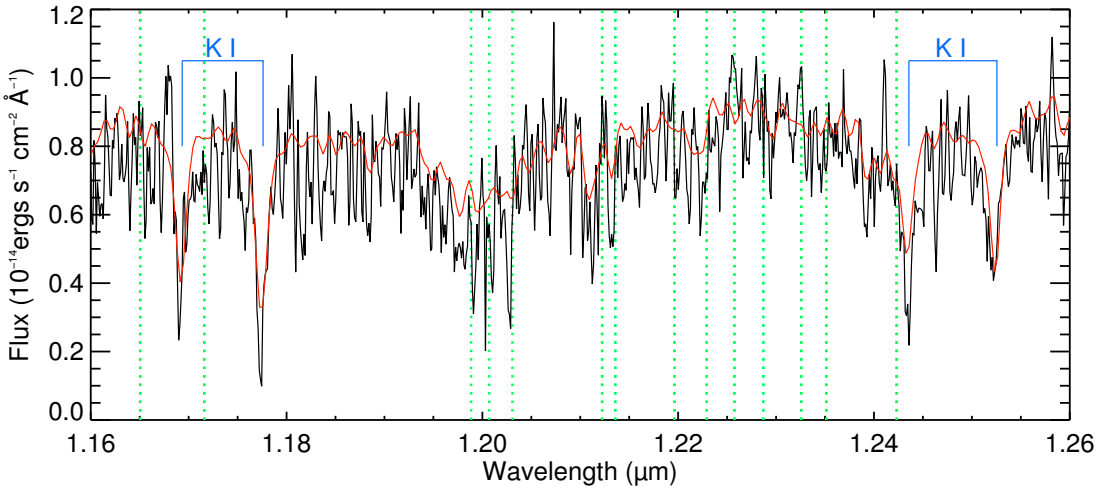

Figure 3.9 Same as Figure 3.8, but for the region of the J band which is most promising for wavelength determination. Despite the prominent sky residuals in the H band of the same spectrum (Figure 3.8), the data in this region is mostly free of OH lines; those shown here are on average 5 times weaker than the OH lines shown in Figure 3.8

3.4 Examining Wavelength Fidelity In The J Band

Two L dwarfs observed with TripleSpec and successfully reduced with Firehose also have publicly available high resolution (R∼20,000) spectra in the J band from NIRSPEC (McLean et al. 2007). Figures 3.10 and 3.11 show TripleSpec spectra of the L2 dwarf Kelu-1 ($J = 13.4$) and the L7 dwarf DENIS J020529−115930 ($J = 14.6$; hereafter D0205011) compared to NIRSPEC spectra which have been interpolated onto the same wavelength array. The agreement between each of the spectra seems reasonable, considering the lower resolution of TripleSpec and the lower S/N of the TripleSpec spectrum of D0205011. to check the wavelength agreement, I performed a cross-correlation of the NIRSPEC spectra with the TripleSpec spectra for both of these dwarfs.

Tables 3.2 and 3.3 show the result of cross correlating 8 different spectral orders with the TripleSpec data. Ideally, the match between the spectra would result in pixel and velocity shifts near zero. For velocities from these spectra to be useful for the study of L dwarfs as a kinematic population, our wavelength calibration should be accurate to at least 15-20

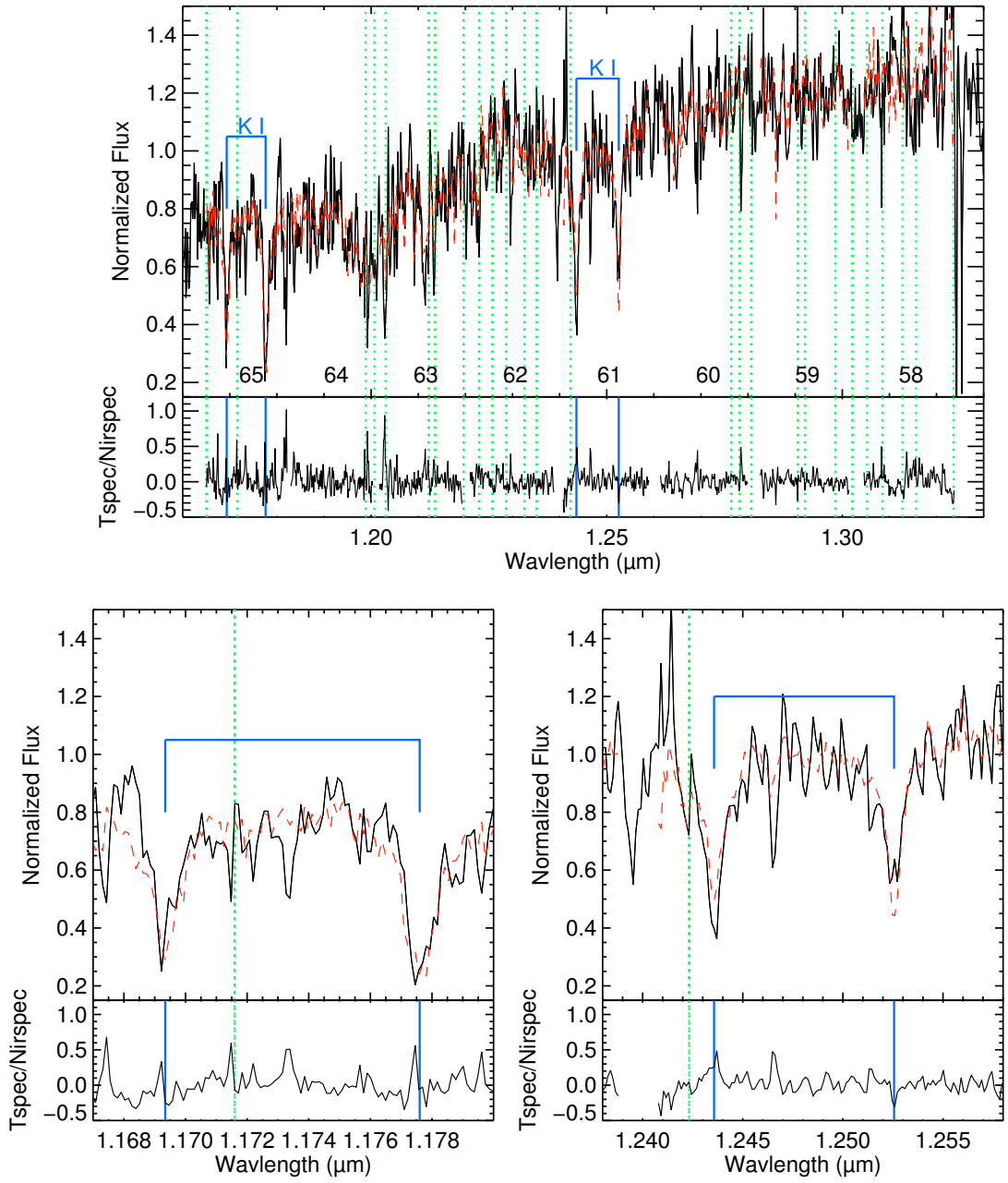

Figure 3.10 Spectrum of L2 dwarf Kelu-1, taken on 2009 May 6 with TripleSpec, compared to a NIRSPEC spectrum of Kelu-1 (red dashed line). The NIRSPEC spectrum has been interpolated onto the TripleSpec wavelength array to better compare the two spectra. The telluric lines are shown (green dotted lines) and the KI doublets are identified and labelled (blue). The numbers of each NIRSPEC order are also shown.

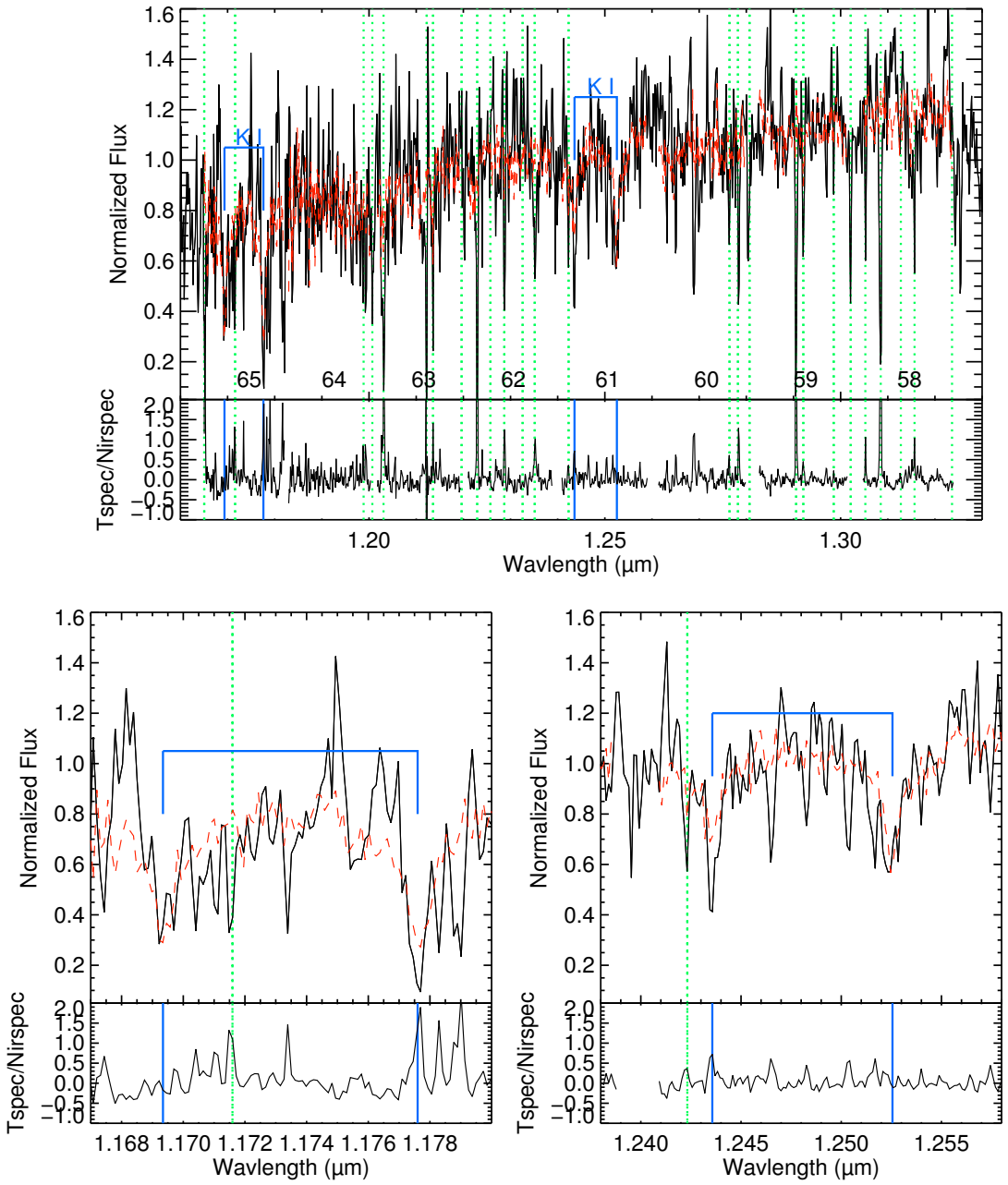

Figure 3.11 Same as Figure 3.10 but for L7 dwarf DENIS J020529−115930 taken on 2008 November 17.

Table 3.2. Cross Correlation For Kelu-1

NIRSPEC Order	Wavelenth (microns)	Shift (pixels)	Velocity (km s^{-1})
58	1.305 - 1.324	-6.66	-203.0
59	1.283 - 1.301	0.90	27.5
60	1.261 - 1.280	-0.05	-1.5
61	1.241 - 1.259	0.25	7.6
62	1.221 - 1.239	0.52	15.9
63	1.202 - 1.219	0.29	8.8
64	1.183 - 1.200	0.46	14.0
65	1.165 - 1.182	0.83	25.3

km s^{-1}, which corresponds to $\sim$0.5 pixel in the J band. For both Kelu-1 and D020511, the cross-correlation fails catastrophically (shifts of over five pixels) for the 58th order. This is likely because of the large amounts of noise in the TripleSpec spectra, as it is on the edge of a telluric absorption band.

Compared to the NIRSPEC spectrum, the TripleSpec spectrum of Kelu-1 appears to have a relatively good wavelength calibration, with NIRSPEC orders 60-64 (corresponding with wavelengths of 1.183-1.28 microns) showing reasonably good agreement. This is true even for orders 62 and 63, which overlap with a relatively large number of sky lines. While the agreement is in general good, orders 61-64 are all offset in the same direction, possibly indicating a systematic wavelength error of $\sim$10 km s^{-1}. With this spectrum alone, it is impossible to draw strong conclusions about the wavelength fidelity of TripleSpec spectra as reduced by Firehose.

The cross correlation results indicate that D020511 is a particularly poor match for the NIRSPEC spectrum, with only the 59th, 63rd, and the 64th order matching even within one pixel. These offsets appear to be due to combination of noise and sky line residuals in the TripleSpec spectrum rather than an offset between the two spectra. If this is the case, spectra with poor S/N should have systematically poor matches between their measured

Table 3.3. Cross Correlation For D020511

NIRSPEC Order	Wavelenth (microns)	Shift (pixels)	Velocity (km s^{-1})
58	1.305 - 1.324	10.28	313.7
59	1.283 - 1.301	0.54	16.5
60	1.261 - 1.280	4.16	126.9
61	1.241 - 1.259	1.45	44.3
62	1.221 - 1.239	8.88	270.8
63	1.202 - 1.219	0.75	22.9
64	1.183 - 1.200	-0.94	-28.7
65	1.165 - 1.182	2.11	64.4

velocities and previously published velocities. It is also possible that the wavelength solution is poor, though if that was the only problem with this spectrum, we might expect systematic offsets in the cross-correlation results.

The agreement between the NIRSPEC spectra and the TripleSpec spectra for these two objects is not particularly encouraging. The spectrum of Kelu-1 is nearly a good match, while the noisy spectrum of D020511 is a poor match, mostly due to its low S/N in the J band. Further testing is needed to determine (A) if there is a systematic effect where low S/N dwarfs have poor velocities or (B) these results are typical of the results for our L dwarf velocity standards. Because there are no other high resolution spectra available for this comparison, I investigate these issues by comparing velocities measured from TripleSpec data to published velocities.

3.5 Examining Velocity Fidelity

Fifty-two L dwarfs have both TripleSpec data and velocities measured in Chapter 2, Mohanty et al. (2002); Bailer-Jones (2004); Blake et al. (2007); Zapatero Osorio et al. (2007) or Blake et al. (2010); these velocities are given in Table 3.1. In this section, I compare velocities measured using three different methods with radial velocities from literature for

these objects. The first method fits K I lines with gaussian functions and compares the measured values are compared to their laboratory values to calculate velocities. The second and third methods use cross correlation. The second cross correlates the data against 9 standard spectra that showed good matches to their literature velocities from K I lines, and the third correlates velocities with spectroscopic models.

3.5.1 Velocities From K I Lines

The K I lines are some of the most prominent features in the J band spectra of L dwarfs. While they are subject to some pressure broadening, they are suitable for a first look at the velocities that can be measured from TripleSpec data. To find the centers of the K I lines, we use the IDL "mpfitfun" procedure with a custom input gaussian function that includes a linear component to fit the surrounding continuum. Figure 3.12 shows the velocities measured from the line centers as a function of the velocities measured from the literature.

The first look at the velocities measured from the K I lines shows that they do not fall on (or indeed, necessarily near) the line of equality with literature values. One possibility is that the velocities which are poor matches with literature values are subject to some systematic effect based on their properties (e..g, brightness, spectral type) or observations (e.g., airmass, sky conditions). To compare velocities which seem to be good with those that are poor, we define an object whose velocity is a "good match" as one that meets three criteria:

- $abs(v_{meas} - v_{lit}) \leq 20$ km s^{-1}
- $\frac{abs(v_{meas} - v_{lit})}{\sqrt{\sigma^2_{meas} + \sigma^2_{lit}}} \leq 1$
- $\sigma_{meas} \leq 40$ km s $^{-1}$

Where v_{meas} is the mean line center radial velocity measured from TripleSpec, v_{lit} is the radial velocity from literature, and σ_{meas} is the uncertainty in the TripleSpec velocity based on the range of values measured from each of the lines, and σ_{lit} is the quoted uncertainty on the literature values. This set of criteria was designed to require both relatively good

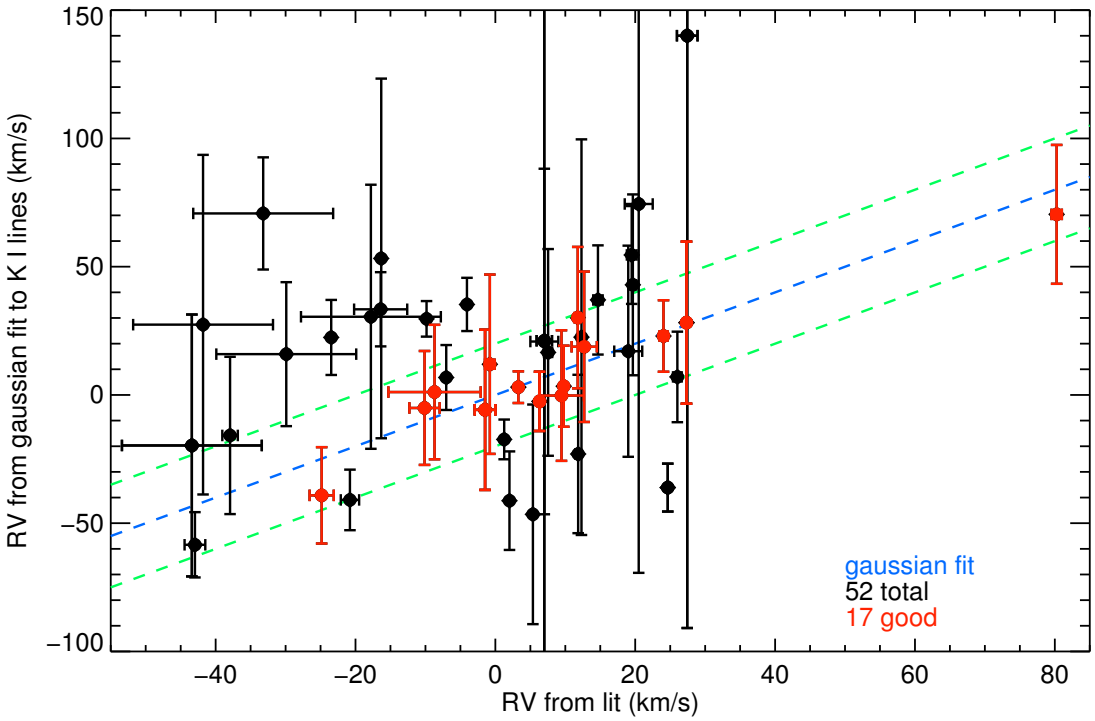

Figure 3.12 Radial velocities from literature as a function of velocities measured from a gaussian fit to the K I lines. A one to one correspondence line is shown (blue dashed) in addition to a line showing a 20 km s^{-1} offset from equality (green dashed). Objects meeting the criteria for "good match" are shown in red. For velocities determined from the K I line maxima, 17 of the 52 velocity standards are classified as a "good match."

agreement and reasonable uncertainties. Applying these criteria to the velocities measured using the K I lines measured from gaussian fits, 17 of the 52 standards are a "good match."

Figure 3.13 shows "good match" objects distinguished from the poor match objects in terms of J magnitude, spectra S/N per pixel in the J band, K I EW, spectral type, air temperature minus dewpoint (a proxy for humidity), sky conditions, airmass, and date of observation. There is little evidence of any correlation between any of those properties and the chance of measuring a good (or poor) velocity. The one notable exception is the lack of good velocities for the brightest objects (J<12.5). When combined with the failure of the code to determine tilts for objects with shorter exposure times, this indicates that fainter sky lines can interfere with the reduction pipeline. While this problem must be addressed, it is not likely the only problem, as many longer exposure objects fail as well.

The lack of correlation between good matches and any specific property indicates that there is no one sure way of separating data which will produce good radial velocities from data which will not. This could, however, be an issue with the radial velocity measurement itself; these results should be confirmed with cross-correlation.

3.5.2 Velocities From Cross Correlation

Velocities measured from cross correlation are often more reliable that velocities measured by lines centers due to the ability to use a larger range of the spectrum, which could include both molecular bands and atomic lines. Before measuring radial velocities from cross correlation of data with templates and models, I first test the effect of S/N on the cross correlation method and examine spectra for the ideal cross-correlation range.

Testing the Effect of S/N Using Models

To test the quality of cross correlation in spectra with poor S/N, I cross correlate a model spectrum (1700K AMES Dusty model; Allard et al. 2001) with that same model spectrum plus a noise array. To quantify the effects of random noise, I ran 1000 iterations with each noise level, then took the mean and standard deviation. The mean and standard deviation for each generated S/N are shown in Figure 3.14. For S/N $<$ 3, the resulting

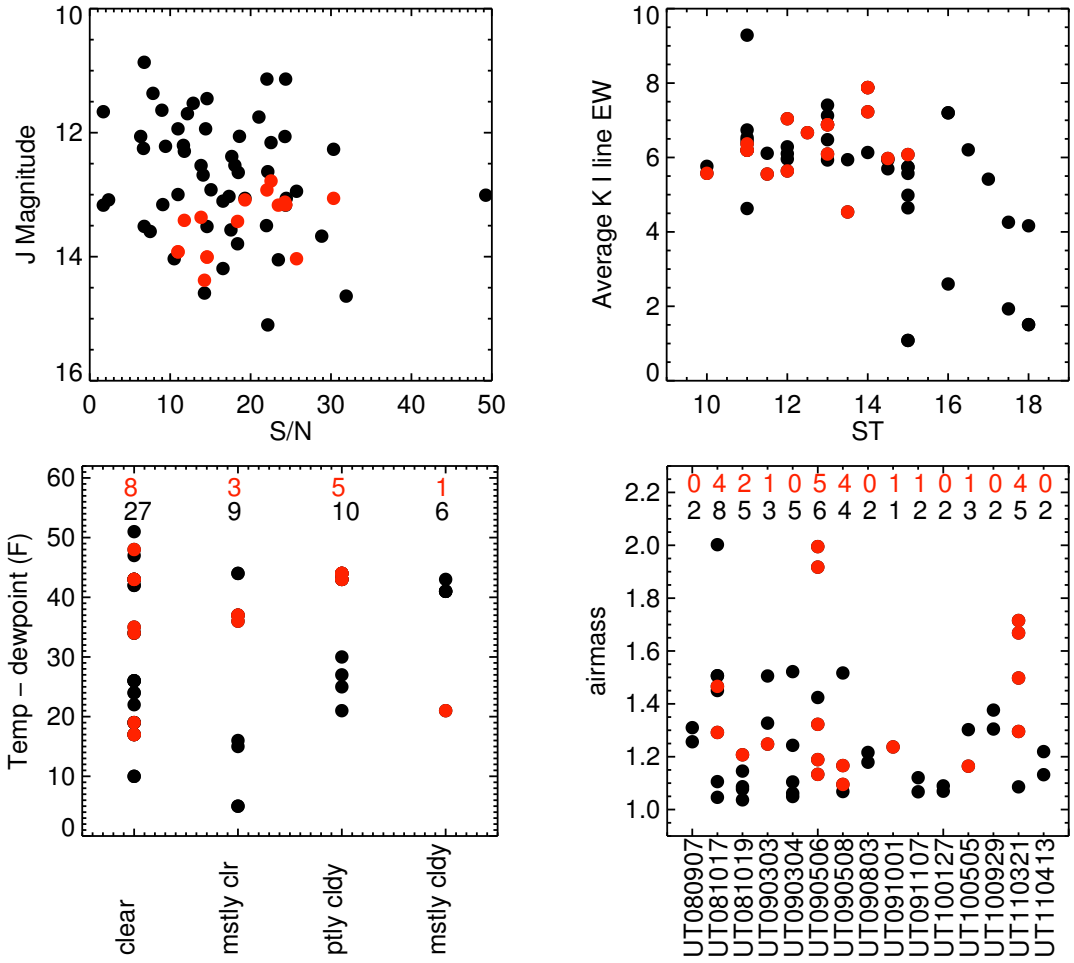

Figure 3.13 Good match objects compared to poorer match objects in terms of J magnitude as a function of S/N in the J band region (top left), average K I line EW as a function of spectral type (top right), air temperature minus dewpoint as a function of cloud cover (bottom left), and airmass as a function of night of observation (bottom right). In each panel, the "good match" objects as measured with a gaussian fit to the K I lines are shown in red. In the bottom two panels, the number of good objects in each bin is given in red, while the total number of objects in each bin is in black.

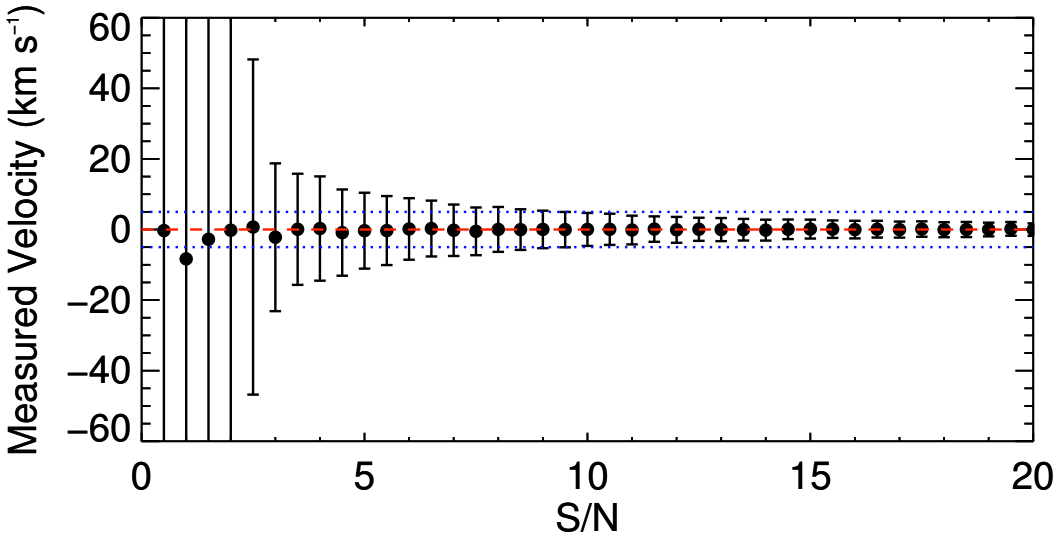

Figure 3.14 The velocity measured from cross-correlating a model spectrum with the same model spectrum with noise added. The velocities were measured from 1000 trials adding the same magnitude of random noise to the spectrum; the mean is shown with associated standard deviations. Zero velocity is shown (red dashed line) in addition to ±5 km s^{-1} (blue dotted line).

measured velocities have standard deviations over 10 km s^{-1}, indicating the S/N is too low for accurate measurement of radial velocities. The standard deviation continues to decline, reaching 5 km s^{-1} at S/N =10. Spectra with S/N >10 are of sufficient quality for radial velocity measurement (with 3σ uncertainties $<$ 15 km s^{-1}), while those with 3<S/N<10 are likely sufficient, but with larger uncertainties.

Selecting a Cross Correlation Region From Data

For cross correlation templates, I selected 9 spectra spanning the entire range of spectral types which were classified as "good match" using K I line velocity technique. Velocities were measured from cross correlation of the object spectrum to each of the 9 templates, and a final velocity was calculated from a sigma clipped median of those 9 values.

To determine the best spectral range to measure velocities, I performed cross correlation

Table 3.4. Wavelength Regions for Cross Correlation

Range (microns)	v diff (km s^{-1})
1.15 - 1.25	26.1
1.2 - 1.3	26.9
1.25 - 1.35	29.9
1.3 - 1.4	29.2
1.175 - 1.197	31.9
1.247 - 1.275	30.5

on 6 different regions of the J band and compared the median difference between the resulting velocities and the velocities from literature for each region. Four regions were selected to span the J band, and the final 2 were selected to avoid OH lines. Table 3.4 shows the results for each range; I selected 1.15 to 1.25 microns for cross correlation.

3.5.3 Cross Correlation of Data With Data

For the first attempt at cross correlation, I used the 9 spectra from the previous section as templates and cross correlated each spectrum with all 9 templates in the 1.15 to 1.25 micron range of the spectrum. The cross correlation functions were each examined, and functions without strong minima were rejected. The typical width of the cross correlation function had a FWHM $\sim$ 4 pixels, corresponding to roughly 120 km s^{-1}. The median velocity was adopted and the uncertainties were the standard deviation of the 9 or less (if some were rejected due to poor cross-correlation functions) measurements.

Figure 3.15 compares the velocity results from cross correlation of the TripleSpec spectra to radial velocities from literature. There are 20 "good match" objects out of a total of 52 standards, 17 of which overlap with those measured using K I lines. Figure 3.16 compares the "good match" objects to the poorer match in terms of observational and object properties. The velocities show the same patterns (or lack thereof) as those measured with K I line centers. These results further confirm that there may be some underlying issues with the

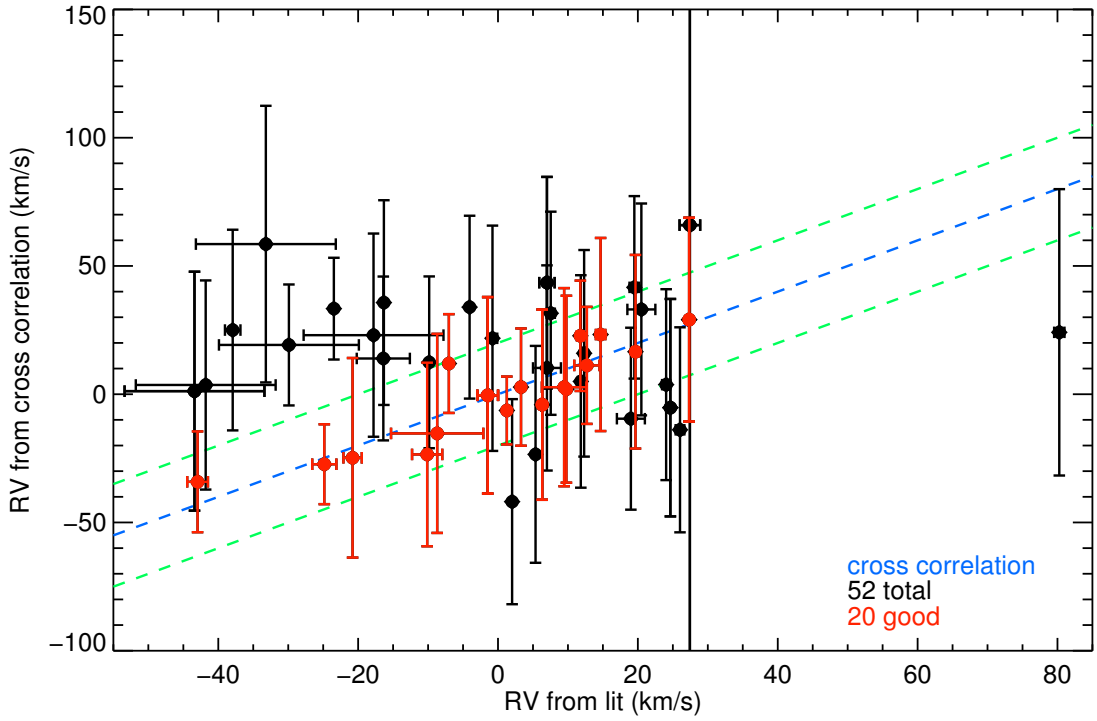

Figure 3.15 Same as Figure 3.12 but for velocities measured from cross correlation from 1.15 to 1.25 microns. For this velocity measuring method, 20 of the 52 standard observations are classified as a good velocity match.

data or reductions which are not well correlated with the observational properties.

3.5.4 Velocities From Cross-Correlation of Data With Models

Spectroscopic models have two distinct advantages over data; they are set at zero velocity, and they are not subject to telluric emission and absorption. The final set of tests on the wavelength fidelity were run by cross-correlation of AMES Dusty models (Allard et al. 2001) with the TripleSpec data. Models were selected for each object based on their T_{eff} and the spectral subtype of the L dwarf. Again, cross correlation functions were examined and those without strong minima were rejected. The velocities were assigned uncertainties based on the simulation data shown in Figure 3.14 and their S/N.

I tested both the 1.15 to 1.25 micron region and a K band region from 2.3 to 2.4 microns.

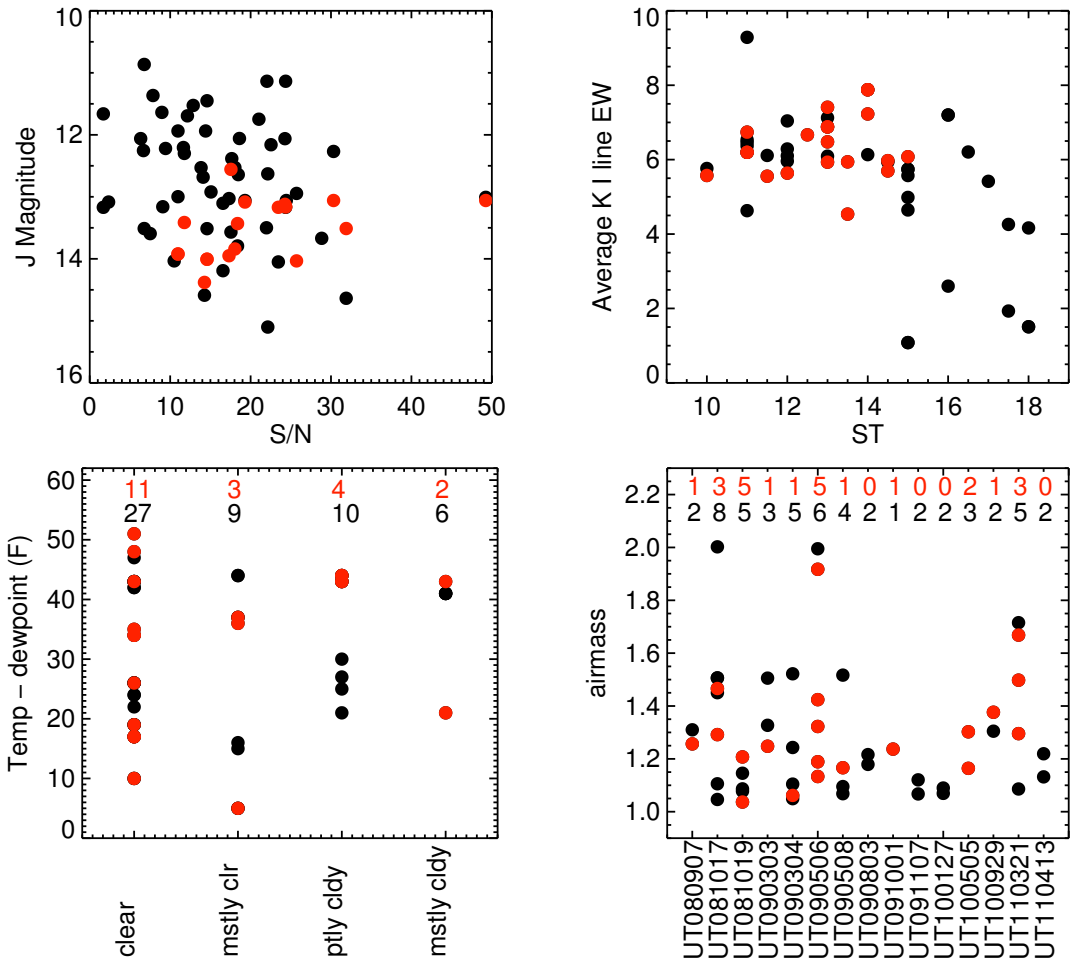

Figure 3.16 Same as Figure 3.13 but with "good objects" from velocities measured with cross correlation from 1.15 to 1.25 microns.

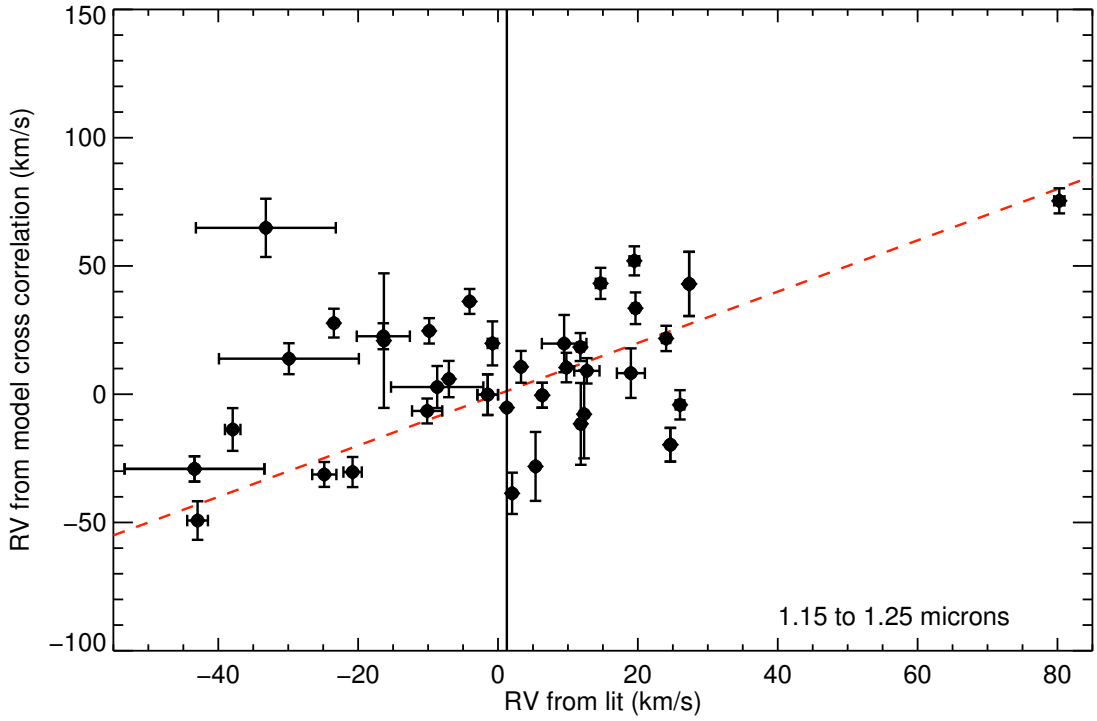

Figure 3.17 Radial velocities measured from a cross correlation of TripleSepc data and spectroscopic models between 1.15 and 1.25 microns. A line of equality is shown for reference.

The K band has been avoided in previous sections due to relatively poor sky subtraction. This effect should be less important when cross-correlation is performed with models, which have no sky emission or absorption. Figure 3.17 shows the velocities measured from cross correlation in the 1.15 to 1.25 region and Figure 3.18 shows velocities from the 2.3 to 2.4 micron region.

The results from cross-correlation with model spectra show no better matches than the previous results. Due to lower assigned uncertainties, only 4 observations meet the strict "good match" criteria defined above, but approximately 20 fall within 20 km s^{-1} of the literature values. It seems that either some spectra were reduced and wavelength calibrated properly and others weren't, or none were properly calibrated and there are no more matches beyond those resulting from random scatter. The failure to measure radial velocities points

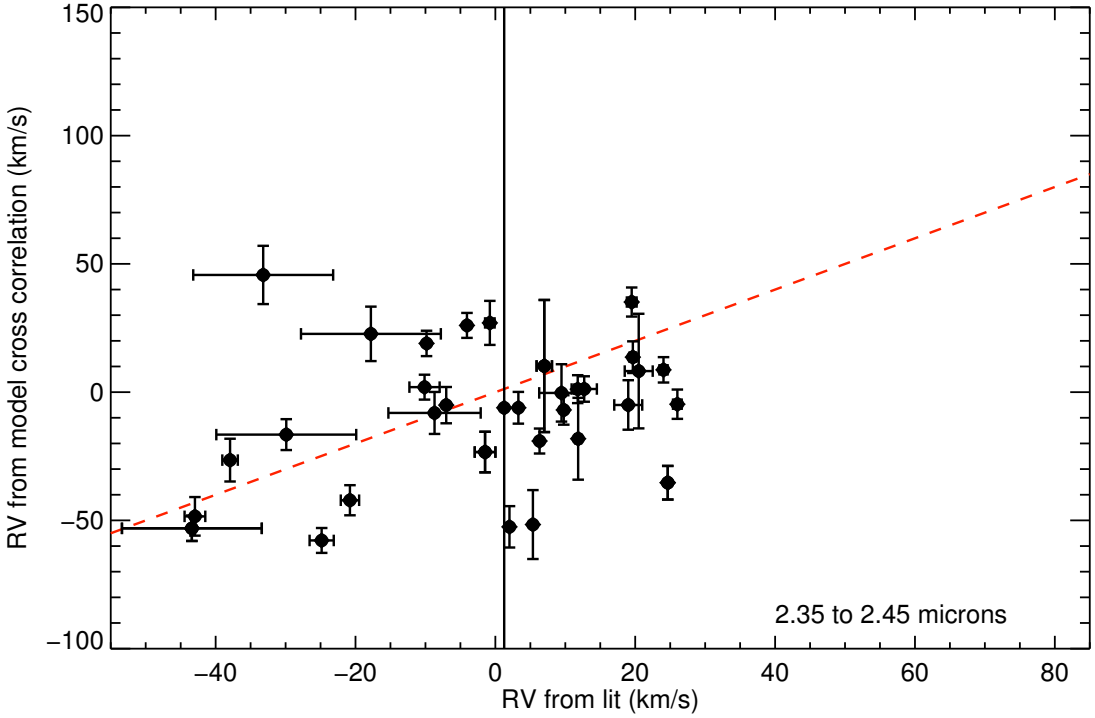

Figure 3.18 Radial velocities measured from a cross correlation of TripleSepc data and spectroscopic models between 2.3 and 3.4 microns. A line of equality is shown for reference.

to an issue with wavelength fidelity in the reduced data, an issue that needs to be addressed in detail in future work.

3.6 Summary

While there have been important advances in kinematics already from the BDKP, radial velocities are necessary for analysis of the complete space motions of the late-M, L, and T dwarfs within 20pc. So far, the current data set and attempted methods at reduction using a variety of software have not yielded radial velocities of sufficient quality for the 20pc sample of L dwarfs.

The different reduction packages suffered from at least one of three problems: (a) an assumption that pixel = wavelength across the aperture, resulting in a smoothing of up to 1/2 pixel (b) a difficulty in a simultaneous fit to the tilts and curvature across every order or (c) a poor wavelength solution. The first problem has been well solved by both the NIRSPEC reduction routines and the Firehose pipeline, which give them an advantage over other pipelines. The second may be mitigated by using co-added sky images to produce brighter sky lines in short exposures, but neither code produces perfect solution for objects with brighter sky lines so that may not entirely solve the problem. The second and third issues are also likely related; the full wavelength solution relies on extrapolating a one-dimensional fit into two dimensions, fitting a curvature and a tilt which are also poorly fit during sky subtraction.

This chapter described attempts to tweak polynomial fits and B-spline parameters to fit the data, all of which were unsuccessful. The next planned avenues for investigation are a careful re-examination of the wavelength solution in Firehose, an implementation of a sky co-add between multiple exposures of the same target, and an attempt to reduce spectra in sub-images, which would require fitting tilts and curves over a smaller range of each order. With the proper reduction of the TripleSpec data, I can then begin a thorough analysis of the three-dimensional kinematics of the 20pc sample of L dwarfs. While those reductions progress, I can begin examining the J band spectral features (e.g., K I line EW) of this large sample of L dwarfs.

Chapter 4

COLORS AND KINEMATICS OF ULTRACOOL DWARFS

Upon the completion of Chapter 2, my collaborators and I identified a need for additional data to investigate the kinematics of both late-M and late-L dwarfs for comparison to the SDSS sample of mostly early-L dwarfs. Due to the faint magnitudes of late-L dwarfs, additional velocities can only be measured through targeted observing programs like the one described in Chapter 3, but the multi-fiber spectrograph of SDSS is well suited to obtain large numbers of spectra for the brighter late-M dwarfs.

In late 2008, the SDSS-III Baryon Oscillation Sky Survey (BOSS) project put out a call for ancillary proposals to fill spare spectroscopic fibers during their survey observations (spanning 2009-2015). I submitted a proposal (in collaboration with S. Hawley, J. Bochanski, and A. West) to obtain 10,000 spectra of late-M and L dwarf candidates, with the goal of targeting every L dwarf within the SDSS footprint and increasing the number of late-M dwarfs with SDSS spectra.

This chapter introduces the BOSS Ultracool Dwarfs (BUD) sample, which greatly expands on the previous SDSS late-M and L dwarf samples by including new objects discovered in the first half of BOSS observations (with all data taken before 15 March 2012) as well as photometry from the Wide-Field Infrared Survey Explorer (WISE; Wright et al. 2010) all-sky release (made available on 14 March 2012). In this chapter I will discuss sample selection, characterize colors, and examine initial kinematic results.

4.1 Introduction

The combination of photometry and spectroscopy from the seventh data release (DR7; Abazajian et al. 2009) of the Sloan Digital Sky Survey (SDSS; York et al. 2000) has been an essential resource for cool and ultracool dwarfs (Schmidt et al. 2010b,a; Bochanski et al. 2011; West et al. 2011). This chapter expands upon those results with the inclusion of

data selected from the Baryon Oscillation Sky Survey (BOSS; Ross et al. 2011); these data combine serendipitous ultracool dwarfs targeted by the main survey with those selected as part of our ancillary program. The combined BOSS Ultracool Dwarf (BUD) sample includes late-M and L dwarfs from both DR7 and BOSS and represents the largest spectroscopic sample of M7 and later dwarfs yet assembled. This Chapter discusses the selection, colors, and kinematics of the BUD data.

A well-defined color locus for ultracool dwarfs is essential to the selection and classification of these objects (e.g., Chapter 2). Color-spectral type relations can also be used to provide an initial spectral type estimate, indicating useful targets for further follow-up observations (e.g., Zhang et al. 2009; Castro & Gizis 2012). While the combination of SDSS and 2MASS colors provides a broad color space to examine late-M and L dwarfs, the recent release of all-sky data from the Wide-Field Infrared Sky Explorer (WISE; Wright et al. 2010) has expanded the available color space for ultracool dwarfs. Other initial efforts to examine WISE colors have focused on earlier-type main sequence stars (Davenport 2012, in prep.) or cooler brown dwarfs (Kirkpatrick et al. 2011), so the BUD sample fills important gaps in WISE color sequences.

SDSS data have already proven a useful resource for the kinematics of M dwarfs. Using data from SDSS DR5 (Adelman-McCarthy et al. 2007), Bochanski et al. (2007a) investigated the kinematics of M dwarfs as a tracer for galactic structure. The means and dispersions of the M dwarf velocities were in broad agreement with most predictions of Galactic models (e.g., Robin et al. 2003), but the models failed to produce sufficiently large σ_W. The velocities of M dwarfs have also been useful for investigating correlations between activity, metallicity and age (e.g., West et al. 2004, 2006, 2008). In Chapter 2, we first examined the kinematics of L dwarfs from SDSS, finding first evidence for a hot (thick) disk kinematic component in the local population of L dwarfs. But comparing L dwarfs with the more massive late-M dwarfs has proven difficult due to the small fraction of proper motions available for late-M dwarfs in the Munn et al. (2004) catalog, which was used in previous SDSS M dwarf studies. By calculating new proper motions from SDSS–2MASS–WISE positions for known M dwarfs, we increase the number of late-M dwarfs with UVW velocities by an order of magnitude.

In Section 4.2, I discuss the selection of our sample and properties measured from the spectra. Section 4.3 describes the selection of photometry and Section 4.4 shows SDSS/2MASS/WISE colors for late-M and early-L dwarfs. The kinematics are discussed in Sections 4.5 and 4.6.

4.2 Sample Selection and Spectra

The BOSS Ultracool Dwarf (BUD) sample is the combination of data from three different components of SDSS: M7-M9 dwarfs selected from the DR7 M dwarf sample described by West et al. (2011, hereafter W11), L dwarfs from the DR7 L dwarf sample described by Schmidt et al. (2010b, hereafter S10), and late-M and L dwarfs selected from BOSS data. This section describes the spectroscopic data included from each sample.

4.2.1 Late-M Dwarfs From DR7

The largest component of our sample is a subset of the M dwarfs selected from the seventh data release (DR7) of SDSS. The main selection criteria were a color cut ($r - i > 0.42$ and $i - z > 0.24$) and a signal-to-noise cut (S/N >3 at ∼8300Å). Over 100,000 spectra were assigned types by eye, resulting in 70,841 M dwarfs. From the W11 sample, we selected M7-M9 dwarfs which were not flagged as white-dwarf-M-dwarf pairs, resulting in 8971 late-M dwarfs.

We adopted spectral types, radial velocities, and Hα equivalent widths (EW) directly from the values measured in W11. The radial velocities were not assigned uncertainties, so (following W11) we adopt a characteristic uncertainty of 7 km s^{-1} for the measured radial velocities (Bochanski et al. 2007a). While the uncertainty is likely a function of spectral S/N, that issue was not addressed in W11 so we regard 7 km s^{-1} as a reasonable lower limit. We did not directly adopt the photometry (or the photometric distances) from the W11 catalog. Instead we re-queried the SDSS and 2MASS catalogs to insure the entire BUD sample photometry contained uniform flag and uncertainty cuts. We also did not adopt the proper motions which were obtained via a cross-match to the USNO-B/SDSS catalog (available for 1127 of the 8971 late-M dwarfs; Munn et al. 2004), but use them to check our updated proper motions in Section 4.5.2.

4.2.2 L Dwarfs From DR7

Our sample also includes the 484 L dwarfs from S10, discussed in Chapter 2. Briefly, they were selected by requiring a single color cut of $i-z > 1.4$ and sufficient S/N to assign a type by eye (no specific S/N cut was made; spectra that were too noisy to match spectral template were rejected). We adopt the spectra types, Hα EW, and radial velocities measured by S10 for that sample. We also measured a S/N at $\sim$8000Å to identify a subsample of 128 dwarfs which would meet the criteria for the selection of the DR7 M dwarfs. Again, we did not adopt the photometry, distances, or proper motions of the S10 sample.

4.2.3 Color Selection of the BOSS Ancillary Targets

Our 10,000 fibers were assigned with different densities in two different regions of the sky. In Stripe82, a 270 deg^2 region of the sky pointed towards the south galactic pole, we were awarded $\sim$4 fibers per plate. in the rest of the legacy footprint ($\sim$2,500deg^2 towards the northern galactic pole), we were awarded $\sim$1 fiber per plate. The primary goal of our target selection was to obtain spectra for every L dwarf candidate in the SDSS footprint. Our selection criterion was based on the properties of the W11 and S10 samples.

In the S10 sample, we found 97.5% of the L dwarfs had matches with good quality 2MASS photometry, so we began our target selection with a list of objects with SDSS colors of $i-z > 1.0$ cross-matched within 5" of 2MASS sources. The first cuts selected were in $i-J$ and $z-J$; those cuts excluded objects which fell far off the late-M and L dwarf color locus (see, e.g., Figures 2.2 and 2.4). The limiting i magnitudes were selected based on the estimates of S/N$\sim$5 per pixel for $i = 21$ (Eisenstein et al. 2011). These magnitude limits ($i < 21$ for Stripe 82 and $i < 20.5$ for the remaining SDSS footprint) include early L dwarfs out to $\sim$100pc, and late-L dwarfs out to $\sim$15pc (see Figure 4.5 for the final distance distribution).

The $i-z$ color cut for the main SDSS footprint was selected to include all L dwarfs; it is located four standard deviations bluer than the L0 dwarf median color at $i-z = 1.85$ (S10). A bluer limit was placed on the Stripe 82 dwarfs, in part to test the color criteria for the main survey, and in part to include a significant portion of M8 and M9 dwarfs. The

Table 4.1. Cuts Made For Ancillary Target List

Color/Magnitude	Stripe82 cut	rest of SDSS cut
$i-z$	>1.14	>1.14
i	<21	<20.5
$i-J$	>3.7	>3.7
$z-J$	$1.9<z-J<4$	$1.9<z-J<4$

color criteria are summarized in Table 4.1.

Hess diagrams of the BOSS sample compared to the DR7 sample are shown in Figure 4.1. While the above selection criteria do affect the color distribution of our final sample, the DR7 sample has even stronger selection effects due to the color criteria for choosing quasars in that sample.

4.2.4 Selecting Ultracool Dwarfs From BOSS Data

The selection of ultracool dwarfs from BOSS is intended to expand the already existing DR7 samples of late-M and L dwarfs (discussed in Sections 4.2.1 and 4.2.2), resulting in a combination of the two sets of criteria for both M and L dwarfs. To include the largest possible sample, I selected BOSS spectra without any reference to their inclusion in my ancillary program. The targets either meet the criteria for M dwarfs ($r-i>0.42$ and $i-z>0.24$) or L dwarfs ($i-z>1.4$). These color criteria resulted in a total of 27,967 candidates in all plates observed as of 14 March 2012.

I spectral typed each object by eye using the Hammer spectral typing software (Covey et al. 2007). Of the initial list, 23,377 were identified as M or L dwarfs (the rejected 4,590 objects include spectra too noisy to type, A-K stars, easily identified binaries, and extragalactic sources). The sample of M7 and later dwarfs includes a total of 3735 objects . No objects were excluded when a color cut was applied to exclude white-dwarf-M-dwarf binaries (Smolčić et al. 2004). For the M7-M9 dwarfs, I performed a cut to include only spectra with S/N>3 at ∼8000Å, excluding 334 dwarfs for a total of 2540 M7-M9 dwarfs. I include all 188 L dwarfs, 47 of which are flagged as having S/N< 3.

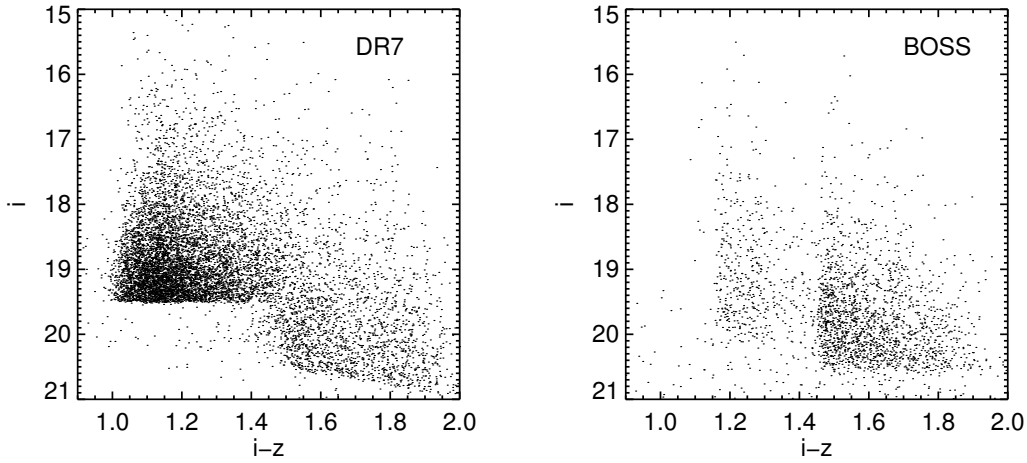

Figure 4.1 Hess diagrams for the DR7 M and L dwarf samples (from W11 and S10; left) and the BOSS sample (right). The blue limit of the DR7 sample reflects the spectral type cut at M7, while the color and magnitude cuts represent the criteria applied to select low and high redshift quasars (Schneider et al. 2010). The artifacts at $i - z = 1.14$ and $i - z = 1.44$ are due to the color cuts applied to the S82 and the remainder of the legacy survey, respectively (see Section 4.2.3).

4.2.5 Radial Velocities and Spectral Features

Radial velocities for each of the 2,638 BOSS ultracool dwarfs were measured from cross-correlation of each spectrum to a spectroscopic template of the same spectral type from Bochanski et al. (2007b) or Schmidt (2012, in prep.). Each cross-correlation function was examined and those without well-defined minima or showing strong asymmetries were excluded. Uncertainties were assigned based on the range of radial velocities measured from a cross-correlation with templates ± 1 spectral type. Measurements with radial velocity uncertainties of greater than 20 km s^{-1} were also excluded, resulting in 2,463 objects with measured radial velocities.

Each spectrum with a measured velocity was shifted to zero radial velocity before measuring the Hα EW using the routine included in the HAMMER spectral typing suite (Covey et al. 2007).

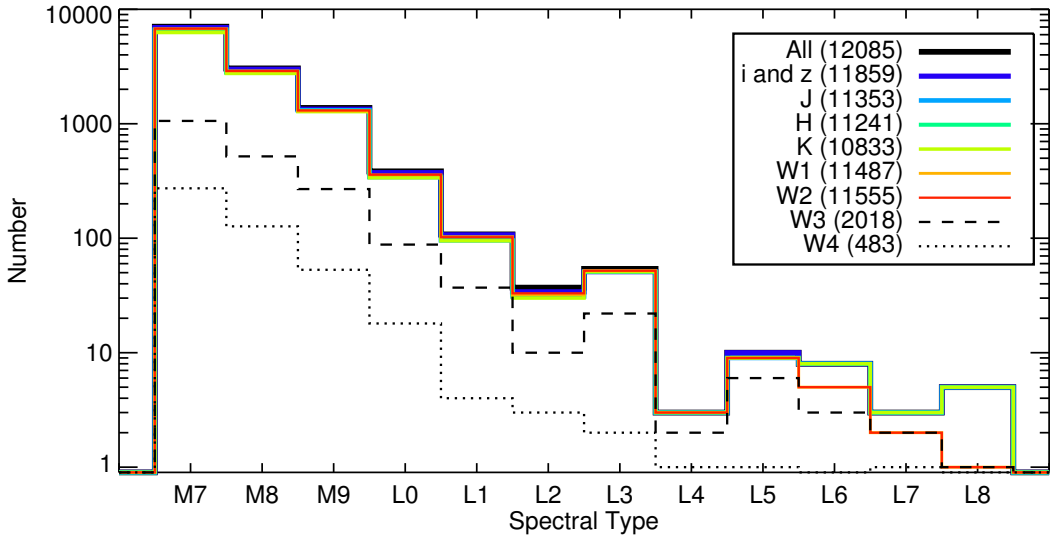

Figure 4.2 Number of dwarfs as a function of spectral type. The entire spectroscopic sample is shown (black solid line) in addition to the number of dwarfs with good photometry in each of the SDSS, 2MASS, and WISE bands (detailed in legend).

4.3 BUD Data from SDSS, 2MASS, and WISE

The combination of the three samples discussed in Section 4.2 resulted in a total of 12,085 ultracool dwarfs included in the BUD sample. Its spectral type distribution is shown in Figure 4.2. Similar to the L dwarf sample in Chapter 2, a larger number of dwarfs with earlier spectral types are included due to their greater intrinsic luminosities and larger densities (e.g., Cruz et al. 2007). The entire sample has only 29 dwarfs with spectral types L4-L8, so the majority of the analysis is based on M7-L3 dwarfs.

4.3.1 SDSS Photometry

While the S10 and W11 samples already include SDSS photometry, we retrieved photometry for the entire combined sample from the DR7 database to obtain a sample with consistent flag cuts and sufficient information to use SDSS positions to calculate proper motions. Our

Table 4.2. Flag Cuts on SDSS Photometry

Flag	excluded in i	excluded in z
SATURATED	2	0
BAD_COUNTS_ERROR	0	0
INTERP_CENTER	29	55
PSF_FLUX_INTERP	28	39
NODEBLEND	90[1]	90[1]

[1]The NODEBLEND flag was set in both i and z for all 90 objects.

photometry was retrieved based on an RA, decl. match within 0'.1[1] of the coordinates associated with the spectroscopic observations[2]. We excluded objects with the SATURATED, BAD_COUNTS_ERROR, INTERP_CENTER, PSF_FLUX_INTERP, or NODEBLEND flags set in either the i or the z band. Table 4.2 gives a brief summary of the number of objects excluded in each flag cut. A total of 226 objects were excluded (due to interpolation around bad pixels or poor deblending affecting the quality of photometry) resulting in 11,859 dwarfs with SDSS photometry.

The photometry has not been corrected for extinction due to the proximity of the BOSS ultracool dwarfs to the Sun; the median galactic height of the BUD sample is 100pc. The extinction corrections typically used by SDSS are calculated for extragalactic objects (Schlegel et al. 1998). The scale height of the dust disk has been measured at 120 to 150pc (Kalberla & Kerp 2009; Jones et al. 2011), but local dust data suggests that the Sun is located in a bubble with a radius of 150pc and a dust density at 40% of normal values (Jones et al. 2011). Based on the complex local structure of dust, it is likely that extinction corrections would artificially de-redden the majority of the BUD sample.

[1]SDSS spectra have a guaranteed best match in the photometric database, so the matching radius is not important.

[2]specobjID was not available for the BOSS spectra, which are still in a pre-public release platefile format

4.3.2 2MASS Photometry

We obtained photometry from 2MASS based on a match to the closest source within 5" of the SDSS coordinates, which returned a total of 11,444 matches. The 641 dwarfs which did not match 2MASS sources were significantly fainter than the sources which returned matches; the reason for mismatches is likely due to the faint magnitude limit of 2MASS. Flag cuts were performed on each band individually (instead of cutting all three bands if one was poor) to include the largest possible sample of good photometry; we required rd_flg = 2, cc_flg=0, and ph_qual=ABCD for each magnitude. The number and spectral type distribution of sources with photometry that passed quality cuts in each band is shown in Figure 4.2.

4.3.3 WISE Photometry

WISE photometry for each dwarf is based on a match to the closest source within 5" of the SDSS coordinates. We included only WISE matches with ext_flg $\neq$ 2 and nb = 1 to minimize the effects of blending on WISE coordinates, producing a total of 11,756 matches. The 341 dwarfs not found in WISE photometry have no clear bias in color or magnitude. A by-eye review of SDSS images shows that objects not found in WISE are more likely to have an additional point sources within ∼5-10". The lack of matches could be due to blending effects from the larger psf of WISE photometry (6"; Wright et al. 2010)

As a check on our matching, we compared the 2MASS magnitudes associated with WISE to those from our 2MASS cross-match. All but seven sources (0.05% of the total) had identical magnitudes in both our selected samples. Those seven dwarfs appear to be mismatches between the two datasets. No effort was made to remove them in either set of data, instead we use them to estimate an overall mismatch rate of <0.1%.

We again made cuts on each band of photometry individually, requiring cc_flg = 0, ph_qual=ABC, and a real (not null) uncertainty. The numbers and spectral type distribution of each band are shown in Figure 4.2. The number of sources with W1 and W2 photometry is comparable to the number of 2MASS sources with photometry, but there are only a few matches for late-L dwarfs and only a small fraction of sources that have good W3

(17%) and W4 (4%) photometry. The lack of WISE photometry for these sources is due to the survey depth, which has brighter limits compared to the 2MASS and SDSS photometry for these objects (e.g., Wright et al. 2010).

Due to the orbital pattern of the WISE satellite, the number of exposures on each region of the sky varied from 1 to 3000. The current all-sky release does not include the time-variable data from each of these exposures, but instead includes a variable flag in each band. The values include "n" (not enough exposures to detect variability) and 0-9, with 0-5 showing little or no variability, 6-9 indicating the source is increasingly likely to be variable (6 and 7 are prone to false positives). Seven of our dwarfs were flagged 6-9 in the W1 or W2 bands (none were flagged in W3 or W4). Variability data are shown in Table 4.3.

4.4 Colors

4.4.1 Color Trends With Spectral Type

Median colors as a function of spectral type are given in Table 4.4 and shown in Figure 4.3. In addition to the flag cuts described in Section 4.3, I applied additional cuts on the uncertainties of each band to ensure good quality median colors ($\sigma_i = 0.04$, $\sigma_z = 0.05$, $\sigma_J = 0.15$, $\sigma_H = 0.19$, $\sigma_K = 0.22$, $\sigma_{W1} = 0.05$, $\sigma_{W2} = 0.1$, $\sigma_{W3} = 0.2$, $\sigma_{W4} = 0.4$). For most colors, these uncertainty cuts were selected to exclude the low quality tail of the uncertainty distribution. A large number of objects had W3 photometry with relatively large uncertainties. To select the cut for W3, I iteratively increased the uncertainty limit until the W2$-$W3 median colors remained constant.

The SDSS/2MASS colors show good agreement with the colors given in W11 and S10, but the larger sample size has resulted in larger dispersions in many colors. The $i-z$ color is a strong function of spectral type for both late-M and mid-L dwarfs, but remains essentially constant for L0-L3 dwarfs. The dispersion in $i-z$ at each spectral type is relatively small ($\sigma = 0.11$ to 0.16; two to three times the typical uncertainties), indicating that it is a useful color in distinguishing late-M dwarfs from mid-L dwarfs. The $z-J$ color strongly increases with spectral type for M7-L2 dwarfs, showing a weaker rise for late-L dwarfs. The $J-H$ and $H-K_S$ colors show similar patterns, but with smaller changes relative to the dispersion

Table 4.3. Variable WISE Sources

Designation (SDSS J+)	ST	Hα EW (Å)	W1 mag	W1 Flag	W1 #	W1 t (days)	W2 mag	W2 Flag	W2 #	W2 t (days)	ref.
021248.5+221822.0	L0	···	15.45±0.04	8	26	192.6	15.16±0.13	1	4	186.9	1
024352.6+004816.0	M8	···	15.89±0.05	0	22	192.4	15.47±0.13	6	4	192.4	2[1]
025223.0−011046.4	M7	2.28±0.60	15.46±0.04	2	33	193.1	14.78±0.06	7	17	193.1	new
083848.1+163156.1	M7	3.70±1.07	15.26±0.05	1	13	3.1	15.00±0.14	8	5	1.0	3, 4[2], 5, 6[3]
132737.6+551126.6	M7	···	14.84±0.03	9	24	1.7	14.61±0.06	0	18	1.7	3
151022.2−022119.1	M7	···	15.63±0.05	1	23	181.5	15.02±0.08	7	10	181.5	3
155057.6+401255.2	M9	···	15.31±0.04	9	30	181.5	15.16±0.07	6	13	181.5	3

References. — (1) S10 (2) Zhang et al. (2010) (3) W11 (4) Kraus & Hillenbrand (2007) (5) Silvestri et al. (2007) (6) Rebassa-Mansergas et al. (2010)

[1]Reference only includes proper motion.

[2]This dwarf has a 69% probability of membership in Praesepe according to [4]

[3]Identified as a possible white-dwarf-M-dwarf binary in [5] due to a slightly elevated blue flux, [6] listed the source as a single M dwarf without a companion.

Table 4.4. Median Colors

	$i-z$			$z-J$			$J-H$			$H-K_S$			K−W1			W1−W2			W2−W3		
st	#	med	σ	#	med	σ	#	med	σ	#	med	σ	#	med	σ	#	med	σ	#	med	σ
M7	6713	1.17	0.12	6178	1.72	0.14	5929	0.61	0.13	5516	0.35	0.16	5182	0.19	0.14	5018	0.20	0.08	107	0.30	0.97
M8	2586	1.50	0.14	2526	1.96	0.16	2425	0.64	0.13	2346	0.39	0.15	2246	0.21	0.14	2176	0.22	0.08	40	0.34	0.81
M9	1054	1.67	0.13	1160	2.15	0.17	1143	0.68	0.14	1148	0.43	0.15	1089	0.25	0.14	1071	0.23	0.08	36	0.41	0.86
L0	198	1.81	0.10	295	2.37	0.16	296	0.74	0.15	306	0.46	0.15	298	0.33	0.14	310	0.27	0.08	15	0.56	0.56
L1	62	1.89	0.09	87	2.49	0.16	92	0.79	0.14	93	0.51	0.16	89	0.38	0.13	92	0.26	0.06	3	0.42	0.50
L2	18	1.85	0.07	24	2.55	0.13	27	0.89	0.14	29	0.55	0.12	25	0.41	0.11	30	0.27	0.08	3	0.63	0.13
L3	27	1.86	0.11	41	2.62	0.18	48	0.91	0.16	49	0.63	0.15	49	0.41	0.15	50	0.30	0.07	4	0.57	0.22
L4	0	···	···	3	2.76	0.24	3	0.91	0.23	3	0.58	0.27	3	0.54	0.14	3	0.25	0.03	0	···	···
L5	5	2.09	0.06	8	2.78	0.10	8	1.12	0.16	9	0.60	0.09	8	0.64	0.14	9	0.30	0.13	3	0.59	0.07
L6	0	-	···	8	2.79	0.08	8	0.96	0.13	8	0.59	0.15	5	0.82	0.15	5	0.35	0.06	0	···	···

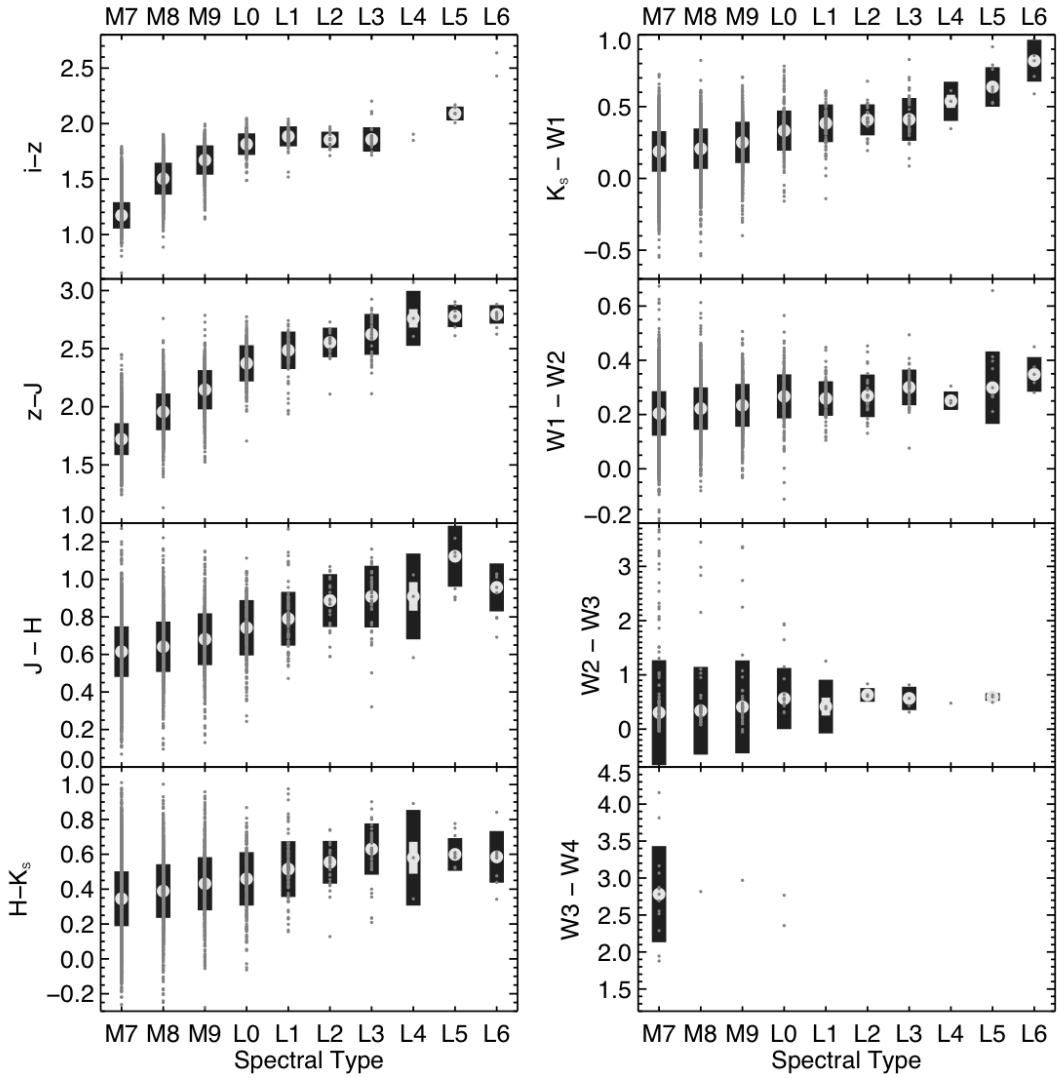

Figure 4.3 Median colors as a function of spectral type. In each panel, individual objects are shown (small dark grey circles) in addition to the median (large light grey circles) and standard deviations (black bars). The median and standard deviation values are given in Table 4.4 and each panel is discussed in Section 4.4.1

at each spectral type.

The K_S-W1 color shows a slight increase with spectral type until L3, where the increase becomes more dramatic, showing a similar pattern to the K_S-W2 color favored by Kirkpatrick et al. (2011) to distinguish L and T dwarfs. The W1−W2 color shows a slight increase with spectral type and a relatively large amount of scatter. For late-M and early-L dwarfs, W1−W2 color does not sample a portion of the spectral energy distribution which is sensitive to changes in T_{eff}. The W1−W2 also shows less scatter in each spectral type ($\sim$0.08) than the other colors, indicating that it is also not strongly affected by metallicity or clouds.

The W2−W3 color shows a slight increase with an extremely large scatter. While the values are comparable to the end of the Davenport (2012, in prep.) locus and the M dwarfs shown in Kirkpatrick et al. (2011), the color dispersions are likely not representative of the true color dispersion due to the sharp cut off in color at W2−W3$\sim$0. There are also a relatively large number of late-M dwarfs with W2−W3$>$1. These color outliers are unremarkable in other colors and also have velocity dispersions consistent with values for the rest of the late-M dwarf sample. Much of the BUD photometry in W3 is near the detectability limits of WISE, which may be the primary difficulty in determining WISE colors.

The uncertainty cuts necessary to remove bad photometry leave only a few dwarfs with W3−W4 colors, which are shown in Figure 4.3 but not included in Table 4.4 due to their small numbers. The W2−W3 and W3−W4 colors of late-M dwarfs should be investigated in more detail using a nearby sample of stars (e.g., PMSU; Hawley et al. 1996).

4.4.2 SDSS–2MASS–WISE Ultracool Dwarf Locus

The SDSS–2MASS stellar locus, defined by Covey et al. (2007), has proven important both in identifying the colors of main sequence stars and in identifying peculiar or non-stellar objects due to their distances from the colors defined in the locus. Davenport (2012, in prep.) is in the process of expanding the stellar locus defined in Covey et al. (2007) to cover the entire SDSS–2MASS–WISE color space. Because the color locus is defined in terms

of $g-i$ color, ultracool dwarfs (which are typically too faint to be detected in g) are not included in the stellar locus.

We measured the ultracool dwarf locus from the BUD sample in steps of $\delta(i-J)=0.1$, and applying the the uncertainty cuts described in Section 4.4.1 to each color. The number of objects in each $\delta(i-J)$ bin varies, ranging from 100-1000 per bin for the $i-z$ and $z-J$ colors to $\sim$10 per bin for the $W2-W3$ color. The ultracool dwarf locus for 7 adjacent colors (from $i-z$ to $W2-W3$) is given in Table 4.5. The ultracool dwarf locus is shown compared to the stellar locus in six of the seven colors (excluding $H-K$) in Figure 4.4.

While both the $i-z$ and $z-J$ colors vary strongly over the range of $i-J$ color covered by the BUD sample, their variation in the redder colors is much weaker. In $J-H$ color, ultracool dwarfs have the same colors as stars with $i-J\sim1.5$, and in K_s-W1 and $W1-W2$ colors there is essentially no variation in color for ultracool dwarfs bluer than $i-J=3.7$. Beyond $i-J=4$, the K_S-W1 color shows a strong upturn, but with large dispersion.

The color relationships from Figure 4.3 and 4.4 show that there is no one color that is ideal for assigning spectral type across the M7-L6 range. The $i-z$ color is strongly dependent on spectral type from M7-L0, but remains constant for early-L dwarfs. The $z-J$ color shows a stronger dependence on spectral type from M7-L4, but then saturates for mid-L dwarfs. While the $J-H$ and $H-K_S$ colors also show an increase with spectral type, they often depend more strongly on clouds than on $T_{\rm eff}$ (e.g., Burgasser et al. 2008; Cruz et al. 2009) so are not ideal for spectral typing. For L5 and later dwarfs, 2MASS-WISE colors are better discriminants of spectral type (here K_S-W1, but also $J-$W1 and K_S-W2; Kirkpatrick et al. 2011).

4.5 Proper Motions and Distances

4.5.1 Distances

There is currently no photometric distance relation that spans the entire range of M7 to L8 dwarf in SDSS colors. For the ultracool dwarfs with bluer $i-z$ colors ($1.0<i-z<1.8$), I calculated distances based on the M_r, $(i-z)$ relation from Bochanski et al. (2011, requiring

Table 4.5. The SDSS–2MASS–WISE Utracool Dwarf Locus

$i-J$	$i-z$		$z-J$		$J-H$		$H-K_s$		K_s-W1		$W1-W2$		$W2-W3$	
	mean	σ	mean	σ	mean	σ	mean	σ	mean	σ	mean	σ	mean	σ
2.800	1.167	0.060	1.693	0.061	0.610	0.124	0.336	0.148	0.188	0.131	0.202	0.076	0.222	0.538
2.900	1.218	0.069	1.730	0.067	0.603	0.129	0.341	0.157	0.191	0.129	0.205	0.081	0.258	0.928
3.000	1.273	0.074	1.777	0.068	0.606	0.135	0.354	0.146	0.200	0.140	0.209	0.075	0.204	0.596
3.100	1.343	0.077	1.808	0.071	0.617	0.129	0.359	0.143	0.208	0.128	0.214	0.075	0.507	0.950
3.200	1.414	0.082	1.842	0.075	0.621	0.130	0.376	0.150	0.207	0.133	0.214	0.075	0.237	0.537
3.300	1.473	0.067	1.877	0.069	0.645	0.140	0.382	0.157	0.208	0.137	0.213	0.078	0.287	1.076
3.400	1.502	0.064	1.935	0.066	0.647	0.124	0.397	0.153	0.210	0.139	0.218	0.077	0.223	0.727
3.500	1.550	0.067	1.994	0.066	0.659	0.137	0.399	0.152	0.210	0.143	0.217	0.078	0.394	0.067
3.600	1.601	0.070	2.046	0.072	0.661	0.141	0.411	0.146	0.227	0.155	0.224	0.074	0.374	0.947
3.700	1.658	0.073	2.095	0.075	0.672	0.143	0.430	0.160	0.223	0.146	0.230	0.077	0.343	0.366
3.800	1.708	0.075	2.132	0.078	0.668	0.151	0.445	0.160	0.260	0.167	0.241	0.082	0.396	0.214
3.900	1.754	0.068	2.188	0.076	0.693	0.150	0.445	0.139	0.292	0.130	0.249	0.079	0.406	0.367
4.000	1.773	0.070	2.277	0.075	0.685	0.160	0.469	0.146	0.278	0.135	0.250	0.078	0.403	0.572
4.100	1.816	0.062	2.325	0.079	0.703	0.138	0.478	0.131	0.327	0.120	0.272	0.085	0.500	0.646
4.200	1.845	0.066	2.394	0.072	0.750	0.144	0.501	0.127	0.353	0.125	0.261	0.077	0.429	0.616
4.300	1.852	0.131	2.474	0.113	0.765	0.133	0.485	0.148	0.363	0.129	0.262	0.061	···	···
4.400	1.854	0.061	2.575	0.067	0.780	0.164	0.555	0.175	0.404	0.115	0.290	0.067	0.728	1.010
4.500	1.939	0.102	2.604	0.098	0.767	0.158	0.579	0.137	0.430	0.114	0.302	0.064	···	···
4.600	···	···	2.751	0.302	0.862	0.261	0.592	0.240	0.481	0.109	0.305	0.119	···	···
4.900	···	···	2.756	0.165	1.021	0.121	0.679	0.106	0.620	0.145	0.307	0.051	···	···

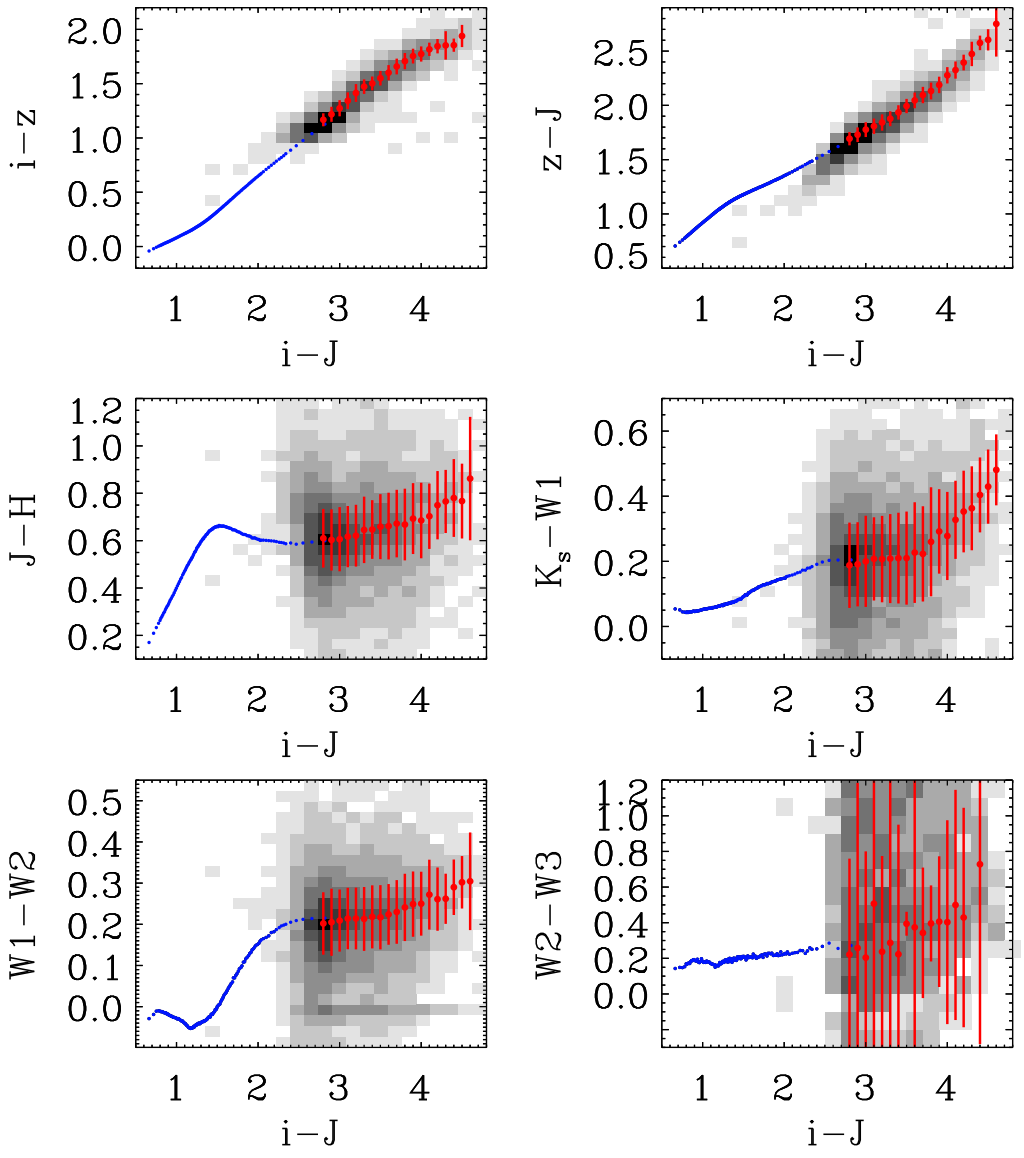

Figure 4.4 Values for the color locus defined in term of $i-J$ color. In each panel, the stellar locus from Davenport (2012, in prep.) is shown (blue points) in addition to the density of BUD stars (greyscale pixels) and the mean and dispersion of the ultracool dwarf locus (red points).

$\sigma < 0.5$ in r, i, and z). For the ultracool dwarfs with redder $i-z$ colors ($1.8 \geq i-z < 3.2$), I used the M_i, $(i-z)$ relation from S10 (requiring $\sigma < 0.5$ in i, and z). Only 565 dwarfs failed to meet one of these two criteria, resulting in distances for 11,510 dwarfs.

Figure 4.5 shows the distribution of distances as a function of spectral type, emphasizing the differences in distance between the earlier and later spectral types of our sample. The changing limits in distance are caused both by the magnitude limits which are an artifact of target selection, shown in Figure 4.1, and the required flux to assign a spectral type. As a result, the median distances of the M7-M9 dwarfs fall at or outside 100pc, the median distances of early-L dwarfs are closer to ∼50pc, and the mid-to late-L dwarfs are mostly within 30pc.

While the majority of the dwarfs found in SDSS are at the largest distances permitted by the effective magnitude limits, some nearby dwarfs are also detected in the BUD sample. Because many different efforts are focused on understanding the solar neighborhood, (e.g., RECONS; Henry et al. 2006), in Table 4.6 we list 24 ultracool dwarfs within 30pc that are new to the SDSS sample. Nine of them (including three L dwarfs) are entirely new detections, and six (including two L dwarfs) are the first spectroscopic confirmation of ultracool dwarf candidates selected from proper motions and photometry.

4.5.2 Proper Motions

One of the largest advantages of selecting data from three different photometric surveys is the ability to measure positions in at least three epochs, which greatly increases the fidelity of the proper motion measurements. The combination of SDSS, 2MASS, and WISE is especially advantageous due to the dates of observation, shown in Figure 4.6. The 2MASS and WISE data are separated by 9-13 years, and the SDSS data often add an epoch between the two. Of our total sample of 12085 objects, 11010 had photometry in all three bands, while another 962 objects had two epochs. Only 113 dwarfs had matches in one or no photometric database.

The WISE data are based on a series of exposures taken over the course of a year and a half. In the main all-sky catalog, these observations are averaged into a single set of

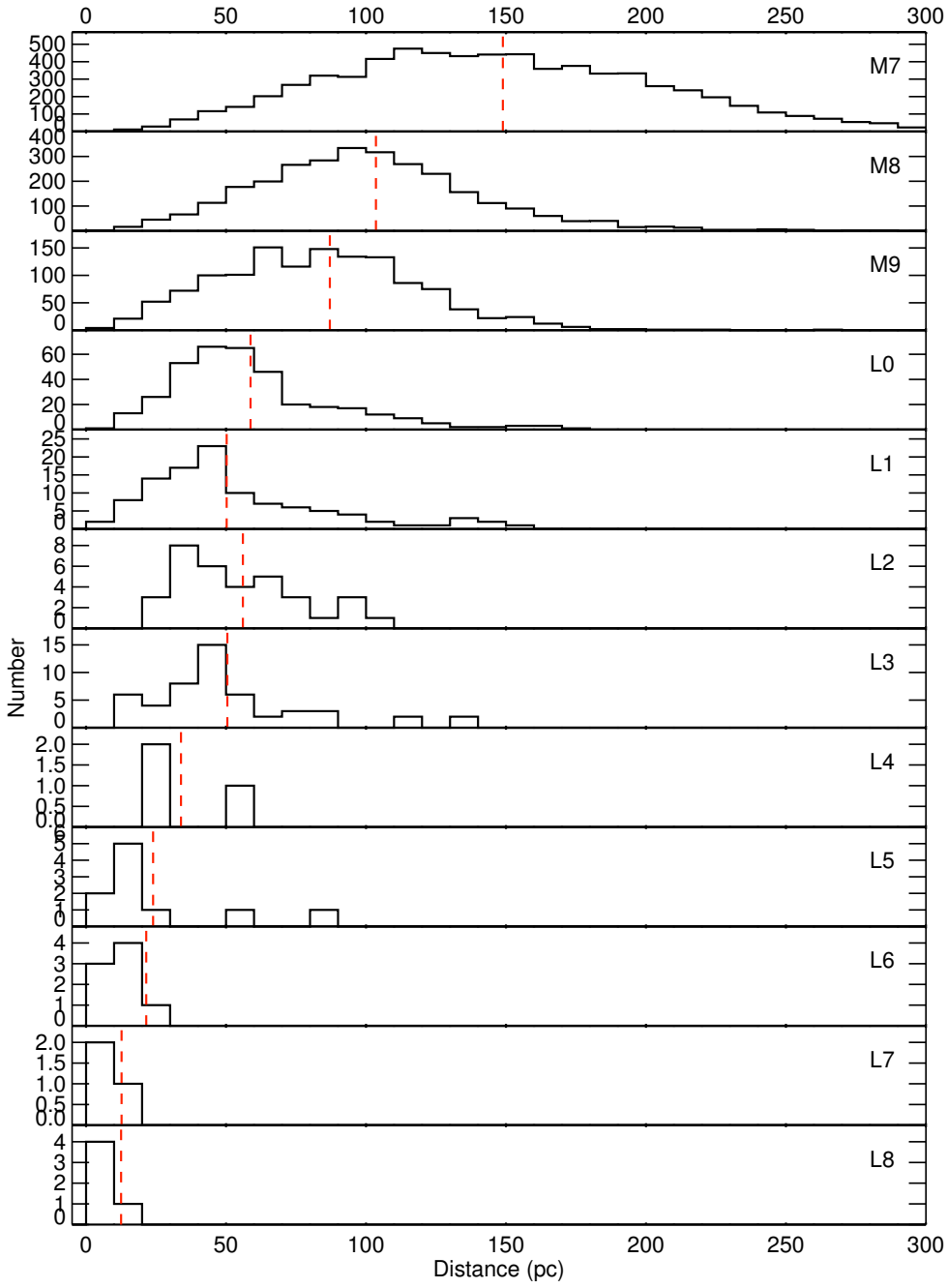

Figure 4.5 Number of objects as a function of distance for M7 to L8 dwarfs. The median distance is shown (red dashed line) over each histogram. The median distance shows a dramatic decrease from M7 to L8, showing that different median distances are being sampled at each spectral type. The maximum distance shown is 300pc; 79 M7, 12 M8, and 1 M9 are farther than 300pc and not shown.

Table 4.6. BOSS Ultracool Dwarfs Within 30pc

Name	RA	decl.	ST	distance	$i-z$	$J-K$	ref.
081110.3+185527.9	08 11 10.3	+18 55 27.9	L1	24.5±0.3	1.89±0.02	1.29±0.04	new
081945.9+165853.6	08 19 45.9	+16 58 53.6	M9	16.0±0.2	1.90±0.03	1.17±0.03	1
083523.6+102931.0	08 35 23.6	+10 29 31.0	M9	25.1±0.3	1.66±0.02	1.09±0.03	2
083557.3+431831.1	08 35 57.3	+43 18 31.1	M8	25.8±0.4	1.50±0.02	1.08±0.03	2
084457.3+120825.4	08 44 57.3	+12 08 25.4	M9	27.5±0.5	1.91±0.03	1.23±0.06	new
084900.5+022015.5	08 49 00.5	+02 20 15.5	M8	22.8±0.2	1.50±0.02	1.03±0.03	new
095246.2+062041.0	09 52 46.2	+06 20 41.0	M8[1]	19.1±0.3	1.54±0.02	0.99±0.03	3
105145.1+071732.4	10 51 45.1	+07 17 32.4	M8	28.4±0.7	1.54±0.04	1.02±0.03	new
112301.2+040041.1	11 23 01.2	+04 00 41.1	M8	22.4±0.2	1.75±0.02	1.03±0.04	new
112329.3+015404.0	11 23 29.3	+01 54 04.0	M7[1]	17.0±0.3	1.53±0.03	1.01±0.04	3
113911.0+084112.0	11 39 11.0	+08 41 12.0	M8	23.8±0.4	1.71±0.03	1.09±0.03	2
114247.1-003021.7	11 42 47.1	−00 30 21.7	M8[1]	28.4±0.4	1.55±0.02	1.01±0.04	4
115833.4+395306.4	11 58 33.4	+39 53 06.4	M8[1]	24.9±0.7	1.51±0.04	1.01±0.03	3
131142.1+362923.9	13 11 42.1	+36 29 23.9	L6[1]	22.5±0.6	2.19±0.05	1.40±0.07	5
140222.3+064847.9	14 02 22.3	+06 48 47.9	M8	20.1±0.3	1.85±0.02	1.21±0.03	2
153453.3+121949.4	15 34 53.3	+12 19 49.4	L6	17.6±0.4	2.29±0.05	1.51±0.06	6
154455.1+330145.2	15 44 55.1	+33 01 45.2	L6[1]	21.5±0.5	2.21±0.06	1.61±0.07	5
155526.5+095413.4	15 55 26.5	+09 54 13.4	M8	20.1±3.6	2.57±0.46	0.73±0.03	new
155732.8+175238.2	15 57 32.8	+17 52 38.2	M8	29.5±0.4	1.63±0.02	1.06±0.03	7
160312.7+263029.0	16 03 12.7	+26 30 29.0	M7	24.6±0.3	1.49±0.02	0.92±0.03	new
161345.5+170827.4	16 13 45.5	+17 08 27.4	M9	29.5±0.3	1.75±0.02	1.28±0.03	7
163256.1+350507.3	16 32 56.1	+35 05 07.3	L1	23.6±0.3	1.93±0.03	1.35±0.04	new
165950.9+351508.0	16 59 50.9	+35 15 08.0	L0	20.1±0.6	1.95±0.06	1.23±0.04	new
234539.0+005513.4	23 45 39.0	+00 55 13.4	M9	22.6±0.4	1.82±0.03	1.19±0.04	2

References. — (1) Cruz et al. (2003); (2) Reid et al. (2008); (3) Lepine 2005 AJ 129,1483; (4) Liebert 2006 PASP 118, 659; (5) Zheng 2009 A&A 497, 619; (6) Chiu et al. (2006); (7) Cruz et al. (2007)

[1]Reference provided only a list of photometric candidates, these data are the first spectroscopic confirmation.

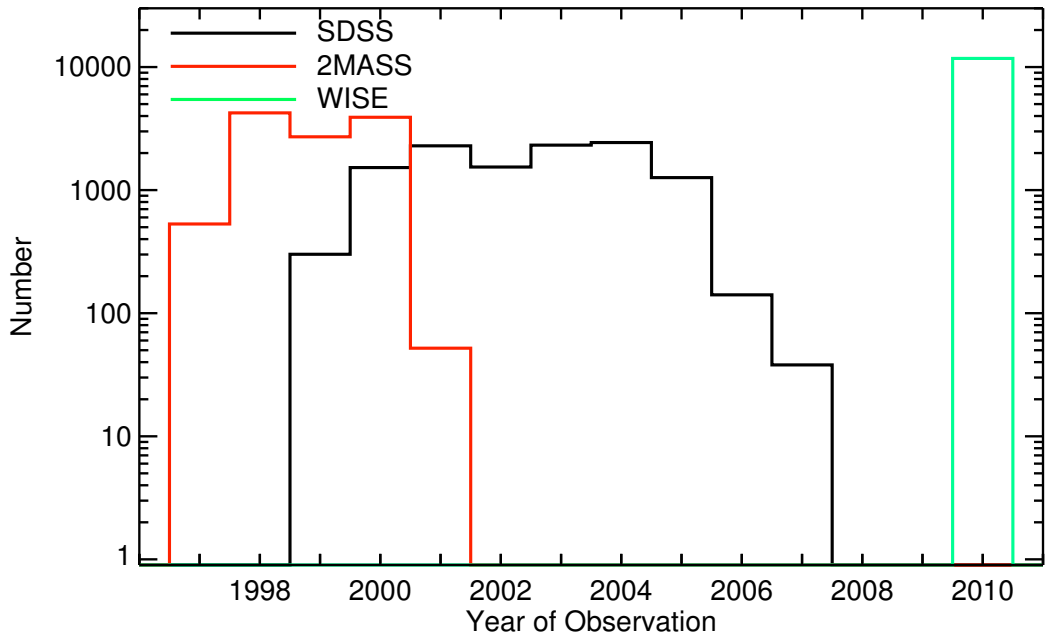

Figure 4.6 The distribution of observation year for the BUD sample in the SDSS, 2MASS, and WISE surveys. The baseline for proper motion measurements varied from nine to thirteen years. For many objects, the SDSS measurement provided an epoch between the 2MASS and WISE surveys, ensuring a more accurate proper motion measurement.

photometry and coordinates with an average mjd. Upon examination of the time-resolved database, we found that ∼3000 of our objects have two sets of 5-20 WISE observations taken approximately 6 months apart. For these objects, we calculated two distinct positions and MJDs from an average of each set of observations. The uncertainties in R.A. and Decl. were propagated from the published uncertainties in the WISE time-resolved catalog.

Before calculating proper motions, we applied a parallax correction based on the photometric distances (described in Section 4.5.1). For objects with two epochs, the proper motions are simply the difference in coordinates over the change in time, with uncertainties based on the uncertainties in each of the coordinates. For dwarfs with three or four epochs, the proper motions in RA (μ_{RA}) and decl. (μ_{dec}) are the slope of a line fit to the points in time and position. The uncertainties of these proper motions are a combination of the uncertainty in the slope of the linear fit (calculated without uncertainties on each point) and the uncertainties in the coordinates.

For our final proper motion sample, we make a cut of the total error in proper motion $\sigma_{tot} > 0.06$"/yr. As is described more fully in Section 4.6, a cut in the ratio of of the total uncertainty to the total proper motion (σ_{tot}/μ_{tot}) results in a bias towards higher proper motions. I flag objects with $\sigma_{tot}/\mu_{tot} > 1$ as uncertain, but they are included in our sample of velocities. These cuts resulted in 10,213 proper motions, which is nearly 85% of our entire spectroscopic sample. As the result of other cuts, the minimum total baseline for the proper motion measurements is just over 2 years.

To check our proper motions against previously measured values, we compare our proper motions to the USNO-B proper motions (Munn et al. 2004) which were cross-matched to the W11 sample. Figure 4.7 shows both the proper motions plotted against each other and a histogram of the differences between the old and new proper motions. Only 64 objects have different proper motions by more than 0.12"yr in either R.A. or decl.

Because these M7-M9 dwarfs are on the faint end of the USNO-B sample, it is possible that the majority of the objects showing poor agreement are mismatches in the USNO-B catalog, where the automated software could not detect another epoch of the faint M dwarf and instead matched it with a nearby star. The new proper motions, based on infrared detections in 2MASS and WISE, should be correct.

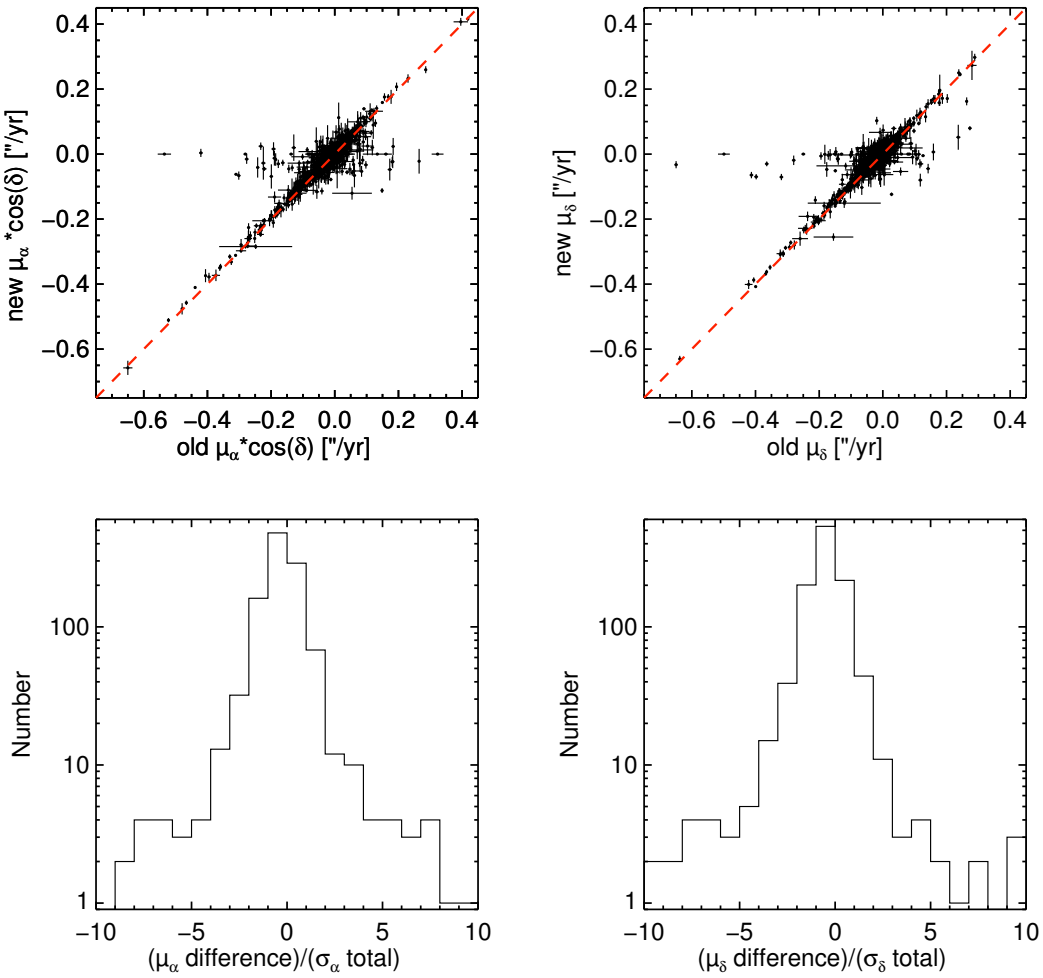

Figure 4.7 New proper motions as a function of old proper motions (from Munn et al. 2004) in R.A. (top left) and decl. (top right). The red dashed line shows proper motion equality. The difference between old and new proper motions in R.A. and Decl. divided by the total of the old and new uncertainties are shown on the bottom left and bottom right, respectively. The majority (750 of 1127) of proper motions match within uncertainties, with most (1050 of 1127) matching within three times the uncertainties. Most proper motions that show poor agreement have new proper motions which are much smaller, which implies that the old proper motions could be mismatches in the USNO-B catalog.

4.6 Three Dimensional Kinematics

A total of 9,442 late-M and L dwarfs in the BUD sample have measured proper motions, distances, and radial velocities. Using these values, we calculated U, V, and W velocities and their uncertainties using the method outlined in Johnson & Soderblom (1987). These velocities were calculated with respect to the local standard of rest assuming $UVW_{\odot}$ = (−10, 5, 7) km s^{-1} (Dehnen & Binney 1998, with positive U defined toward the Galactic center).

While there are uncertainties associated with each velocity, we use the jackknife re-sampling method to estimate velocity dispersion uncertainties (Efron 1982). If a value is calculated from a sample of n data points, the uncertainty is determined by calculating that value n times, each time excluding a different data point.

4.6.1 Testing For a Correlation Between Age and Spectral Type

As described in Section 4.1, an increasing contribution of young brown dwarfs with later spectral type should skew the mean age of each spectral type bin, with later spectral types showing younger ages and cooler kinematics. To test if this effect is apparent in the BUD sample, we examine the UVW velocity dispersion as a function of spectral type, shown in Figure 4.8. The BUD data are supplemented by M4-M6 dwarfs from the W11 DR7 sample. To minimize the effect of differing distributions in distance and galactic height, we excluded stars with distances greater than 100pc.

If the ages of early-L dwarfs were systematically younger due to a contribution from young brown dwarfs, the velocity distributions would show a net decrease with spectral type. The velocity dispersions, while showing small variations, are relatively constant with respect to spectral type. There is a net increase in the W velocity from 20 km s^{-1} to 30 km s^{-1}, but the increase is not likely to indicate an increase in ages because it is not accompanied by an increase in the U and V bands. The other notable deviation from a constant velocity dispersion is the L2 bin. Out of 14 L2 dwarfs with UVW kinematics, three are high velocity objects, with total velocities of over 100 km s^{-1}.

To further investigate age as a function of spectral type, we calculated ages for each

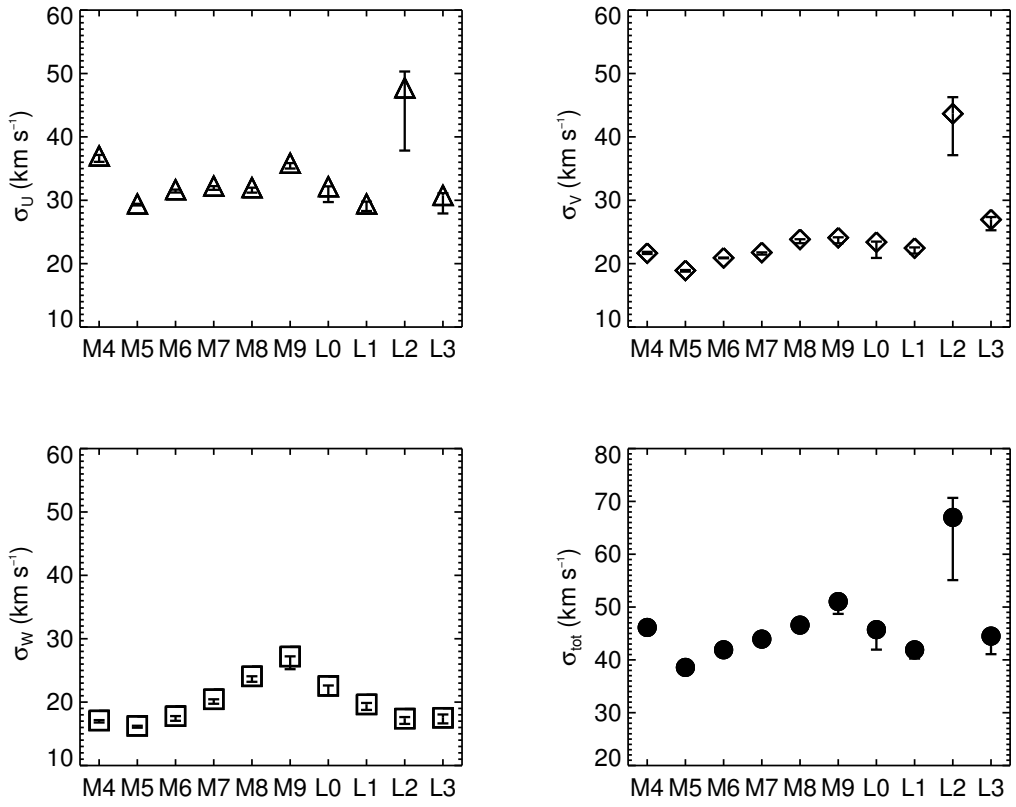

Figure 4.8 UVW and total velocity dispersions of the cold component (for bins with >100 stars) or the full distribution of dwarfs in each spectral type bin. The uncertainties are based on jackknife resampling, where the dispersion is calculated with each individual point successively removed (see Section 4.6) . The shown bars indicate the entire range of dispersions with each point removed. Note that the U velocity dispersions are larger than those in V and W; this is simply a consequence of the increased strength of scattering interactions parallel to the Galactic plane but perpendicular to the direction of rotation (often referred to as asymmetric drift; Strömberg 1922; Lindblad 1925).

Table 4.7. Ages For Each Spectral Type

ST	Number	Component used	σ_{tot} (km s^{-1})	Age estimate (Gyr)
M4	100	cold	$46.1^{+0.3}_{-1.0}$	$3.9^{+0.1}_{-0.2}$
M5	272	cold	$38.6^{+0.1}_{-0.4}$	$2.6^{+0.0}_{-0.1}$
M6	419	cold	$41.9^{+0.1}_{-0.9}$	$3.2^{+0.0}_{-0.1}$
M7	1200	cold	$43.9^{+0.0}_{-1.0}$	$3.5^{+0.0}_{-0.2}$
M8	1196	cold	$46.6^{+0.0}_{-1.3}$	$4.0^{+0.0}_{-0.2}$
M9	615	cold	$51.0^{+0.1}_{-2.3}$	$4.8^{+0.0}_{-0.4}$
L0	206	cold	$45.7^{+0.1}_{-3.8}$	$3.8^{+0.0}_{-0.7}$
L1	64	cold	$41.9^{+0.5}_{-1.7}$	$3.2^{+0.1}_{-0.3}$
L2	21	all	$67.0^{+3.7}_{-11.9}$	$7.7^{+0.6}_{-2.1}$
L3	35	cold	$44.5^{+0.7}_{-3.4}$	$3.6^{+0.1}_{-0.6}$

spectral type bin using the total velocity dispersion , $\sigma_{tot} = \sqrt{\sigma_U^2 + \sigma_V^2 + \sigma_W^2}$, combined with the relationship between σ_{tot} and τ from Wielen (1977)[3]:

$$\sigma_{tot}^3 = \sigma_{tot,0}^3 + \frac{3}{2}\gamma_{v,p} T_\gamma (e^{\tau/T_\gamma} - 1) \tag{4.1}$$

where $\sigma_{tot,0}$ =10.0 km s^{-1}, $\gamma_{v,p} = 1.4 \times 10^{-5}$ (km s^{-1})^3 yr^{-1}, and $T_\gamma = 5 \times 10^9$ yr. The total velocity dispersions and ages of M4-L3 dwarfs are show in Table 4.7. The ages of the M4-L3 dwarfs are all above 2 Gyr, consistent with disk age stars instead of a young population. The age of the L2 dwarfs is notably larger than that of the other dwarfs, but it includes dwarfs which are likely part of a hotter kinematic component. The ages of the L0-L3 dwarfs show no bias towards younger dwarfs, expected if there is a large contribution from the young brown dwarfs.

4.6.2 Activity and Kinematics

Kinematics are a useful tool for investigating the relationships between activity and age. Using galactic height as a proxy for age, West et al. (2006, 2008) showed that the distribution of galactic heights for active and inactive M0-M7 dwarfs is consistent with an activity lifetime

[3]Schmidt et al. (2007) and Faherty et al. (2009) make use of equation 13, which Wielen (1977) notes is only accurate to ages of 3×10^9 years. The equation presented here is equation 16, which should be valid over the entire calibrated range of ages.

which increases with spectral type from 0.8 Gyr for M0 dwarfs to 8.0 Gyr for M7 dwarfs. The longer activity lifetimes of late-M dwarfs correspond with higher active fractions, and a greater probability of detections of active dwarfs at significant galactic heights. We test if this trend continues through M7-L dwarfs by examining the activity fraction of M7, M8, M9 and L dwarfs as a function of galactic height, shown in Figure 4.9.

The M7 dwarfs show a similar pattern to previous results (West et al. 2006, 2008), and the M8 and M9 dwarfs show higher overall fractions and a similar decline to the M7 dwarfs. These results suggest that the activity lifetime continues to increase throughout the M spectral type. The L dwarfs (which include results from L0-L4 dwarfs) have been observed only within a distance of 100pc, leading to a smaller range of galactic heights. The two distance bins suggest that L dwarfs follow the same activity lifetime patterns as the late-M dwarfs. More L dwarf data are needed to more thoroughly investigate their activity lifetimes.

Ongoing BOSS observations will increase the total number of L dwarfs in the BUD sample, but the mean L dwarf distance is unlikely to increase due to their faint absolute magnitudes. To investigate the activity lifetimes of L dwarfs, it may be important to examine the velocity dispersions of active and inactive L dwarfs. Figure 4.10 shows UVW velocity dispersions for active and inactive M7, M8, M9, and L dwarfs within 100pc of the Sun. For the late-M dwarfs, there is a clear separation of the active and inactive dwarfs, with the inactive dwarfs showing much hotter (older) kinematics. The active L dwarfs show similar U and V dispersions to the inactive L dwarfs and a larger W dispersions (though with large uncertainties). There are currently only 4 inactive L dwarfs with full UVW velocities, so an expanded sample may provide a more distinct kinematic difference between active and inactive L dwarfs.

4.7 Summary

This chapter outlined the selection of the BUD sample, 12,085 M and L dwarfs drawn from the spectroscopic data taken as part of SDSS DR7 and BOSS. The majority of these ultracool dwarfs have photometric data from SDSS, 2MASS, and WISE, enabling a full investigation of their colors. As discussed in Chapter 2, $i - z$ and $z - J$ show the most

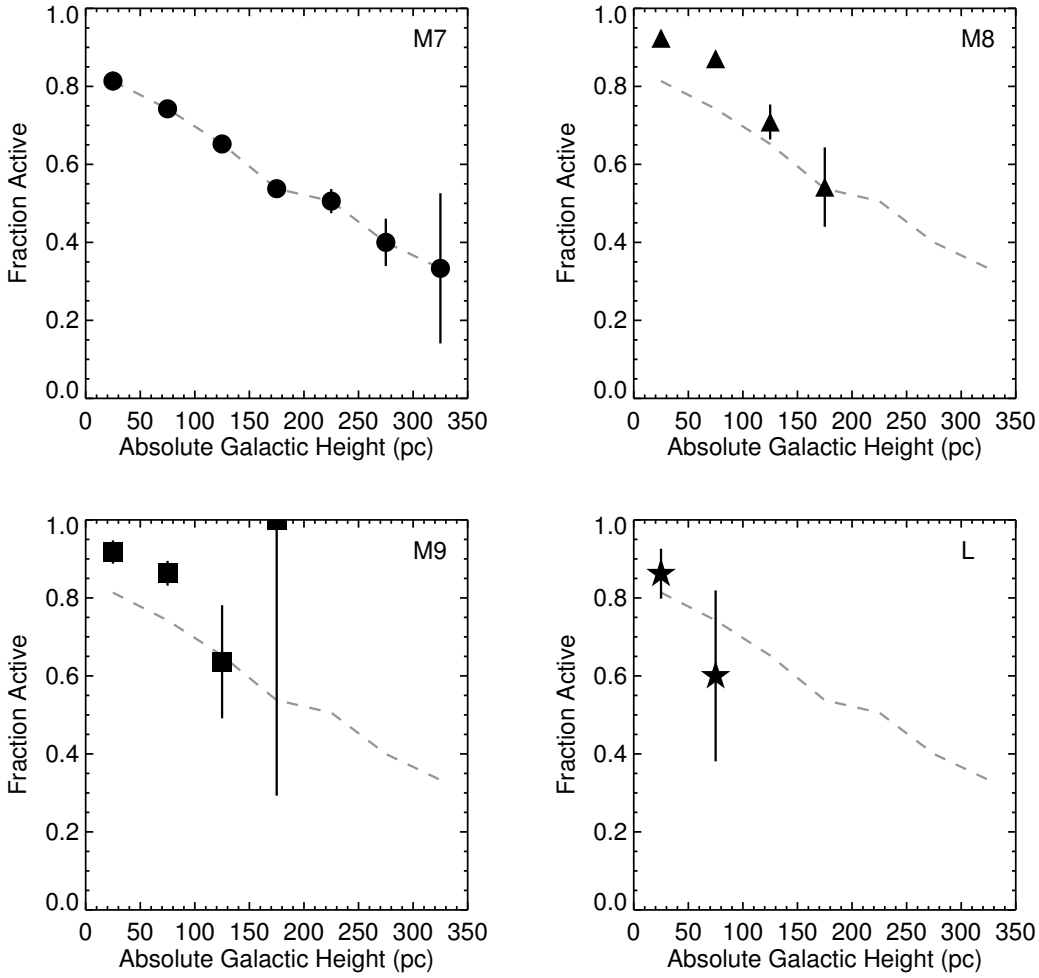

Figure 4.9 Fraction of active stars, as measured by the presence of Hα emission, as a function of absolute galactic height for M7, M8, M9, and L dwarfs. The fraction for M7 dwarfs is shown (dashed grey line) for reference in each panel.

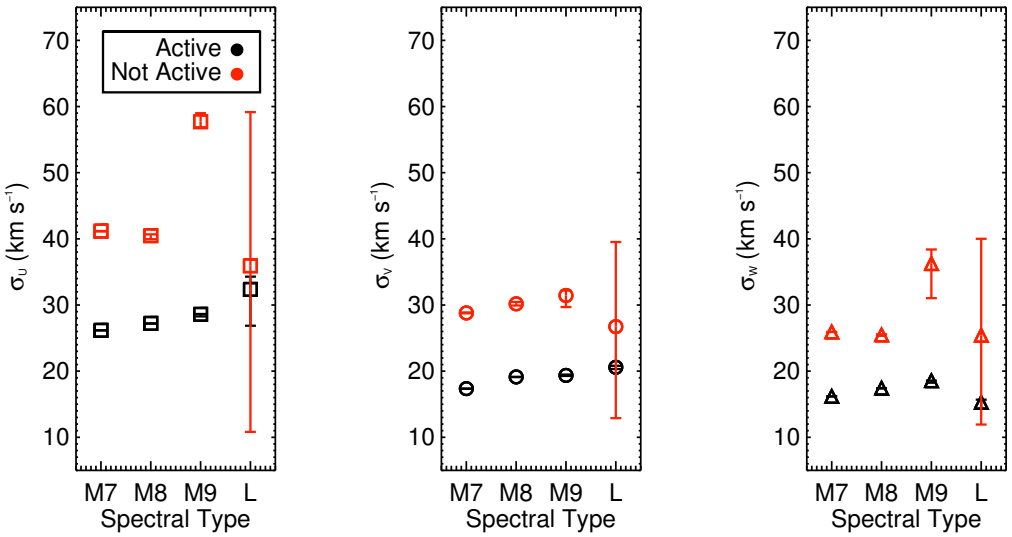

Figure 4.10 UVW velocity dispersions as a function of spectral type for active and inactive late-M and L dwarfs. The uncertainties in dispersion were calculated using jackknife resampling.

clear relations with spectral type (T_{eff}) for late-M and early-L dwarfs. 2MASS and WISE colors have a weaker dependence on spectral type for these late-M and early-L dwarfs. A full investigation of WISE colors in the further infrared bands should take advantage of a nearby, bright, sample of late-M and L dwarfs.

Photometric distances, calculated from $i-z$ vs. M_r or M_i relations, show that the BUD sample includes primarily late-M dwarfs at 100 and more parsecs, early-L dwarfs around 50 pc, and late-L dwarfs closer than 20 pc. The BOSS data add 24 ultracool dwarfs within 30pc to the SDSS samples, nine of which are entirely new discoveries. Proper motions were measured from a combination of SDSS, 2MASS, and WISE astrometry, and radial velocities adopted from W11 and S10 or measured from new BOSS spectra. We measured proper motions for 10,213 dwarfs and obtained radial velocities for 11,436 dwarfs in the BUD sample.

We calculated UVW velocities for 9,442 ultracool dwarfs and used them to investigate ages as a function of spectral type. We find that there is no correlation between age and spectral type, indicating that young brown dwarfs are not a major kinematic contribution

to the early-L dwarf population. We also examine trends between activity and kinematics, finding that late-M and L dwarfs should follow a similar relationship between activity and age as the early- to mid-M dwarfs.

4.8 Future Work

The BUD sample is ripe for additional analysis. The kinematic analysis presented here focused on correlations with activity and spectral type; a full analysis would examine relationships between color and kinematics in addition to kinematics as a function of galactic height. Additionally, the kinematic outliers should be further investigated to search for possible members of young moving groups and fast moving halo objects. A search for proper motion companions will also be initiated in the near future.

Chapter 5

THE CHROMOSPHERES OF COOL AND ULTRACOOL DWARFS

One of the motivations for using BOSS spectroscopic fibers to observe late-M and L dwarfs was to enlarge our understanding of magnetic activity in cool and ultracool dwarfs. SDSS spectra include the Hα emission line, often used as an indicator of chromospheric activity (e.g., Hawley et al. 1996) Activity is another tracer of age in solar-type stars (Skumanich 1972), and enhancing our understanding of the generation and sustenance of magnetic fields in M and L dwarfs could lead to a firm determination of ages for these low mass stars (e.g., West et al. 2008).

Hα detections from the BOSS Ultracool Dwarf (BUD; described in Chapter 4) sample are instrumental in obtaining a coherent picture of magnetic activity over the full range of M0-L8 dwarfs. In this chapter, I will characterize the chromospheric activity detected in BUD spectra and use RH, a non local thermodynamic equilibrium (NLTE) radiative transfer code (Uitenbroek 2001), to explore the chromospheric temperature structures and surface filling factors that are consistent with observed activity levels. These parameters can be used to determine how the structure of the chromosphere changes with spectral type/effective temperature. This chapter contains a first look at chromospheric structure over the entire M and L spectral sequence.

5.1 Introduction

Chromospheric activity, which is ubiquitous in mid- to late-M dwarfs, is often classified based on the presence and strength of Hα emission (e.g., Hawley et al. 1996; Liebert et al. 2003; West et al. 2006). The strength of Hα, frequently parameterized as the ratio of the luminosity in the Hα line to the bolometric luminosity ($\log(L_{H\alpha}/L_{bol})$; e.g., Hawley et al. 1996), has an average value that remains constant for early-M dwarfs, albiet with a large dispersion, then shows a steady decline through early-L spectral types (Gizis et al. 2000;

Schmidt et al. 2007; Reiners & Basri 2008; West et al. 2008).

The fraction of cool and ultracool dwarfs showing detectable Hα emission, however, increases from M0 through late-M spectral types and has been shown to decline into early-L dwarfs (Kirkpatrick et al. 1999, 2000; Gizis et al. 2000; West et al. 2004). The detection of a peak and decline at late-M spectral types has more recently been attributed to the difficulty of detecting relatively weak Hα emission in the fainter late-M and L spectral types (e.g., Schmidt et al. 2007; Reiners & Basri 2008; West et al. 2008). Using BUD data, we show that there is no evidence of a decline in the fraction of late-M and L dwarfs showing Hα emission.

This result is supported by other measurements of magnetic activity in late-M and L dwarfs. Strong radio detections of ultracool dwarfs indicate that they are still capable of generating and sustaining strong magnetic fields (Stelzer et al. 2006; Berger et al. 2010). These strong magnetic fields have also been confirmed by measurements of Zeeman broadening of FeH bands in late-M dwarfs (Reiners & Basri 2007). There is no evidence to indicate that the magnetic fields are weaker or missing in L dwarfs; their typically fast rotational velocities (e.g., Reiners & Basri 2008) are possible evidence that L dwarfs maintain strong magnetic fields over long timescales due to an inefficient magnetic breaking mechanism.

A surface magnetic field is a necessary, but not sufficient, condition for chromospheric activity; the chromosphere must also be heated by interaction of charged particles with the magnetic field. The decline in the strength of Hα emission with later spectral type is primarily the result of increasingly cool photospheres with higher magnetic resistivities due to a low ionization fraction (e.g., Mohanty et al. 2002). In the cool, dusty atmospheres of L dwarfs, the chromosphere may instead be heated by the interaction of the magnetic field with charge cascades in the upper atmosphere (Helling et al. 2011b,a). To better understand the mechanism for magnetic heating in the atmospheres of ultracool dwarfs, an important first step is to characterize the chromospheric filling factors and temperature structures consistent with observations of Hα emission on M and L dwarfs.

In Section 5.2, I describe current results for Hα emission in the cool and ultracool dwarfs using SDSS data supplemented by previously reported Hα detections in mid-L dwarfs. Section 5.3 describes a suite of tests on one-dimensional atmospheres designed to select

which parameters of pervious atmosphere models (e.g., Short & Doyle 1998a; Fuhrmeister et al. 2005) are suitable to reproduce the observations. Section 5.4 makes extensive use of the NLTE radiative transfer code, RH (Uitenbroek 2001), to constrain the ranges of chromospheric temperature and filling factor which match the data. In Section 5.5, I discuss the results in the context of current knowledge about the chromospheres of cool and ultracool dwarfs.

5.2 Properties of Activity in M and L dwarfs

M dwarf activity has been investigated in detail using SDSS spectra for early- to mid-M dwarfs (e.g., West et al. 2006, 2008) but the relatively small numbers of cooler objects have prevented an extension of these results to late-M and L dwarfs. The selection of new dwarfs from the BOSS spectroscopic database as part of the BOSS Ultracool Dwarf (BUD) sample (described in Chapter 4) has increased the number of late-M and L dwarf spectra by ∼2500 (20%). BUD is ideal for determining the characteristics of Hα emission in M7-L1 dwarfs due to these increased numbers, but to place these results in the context of activity over the entire M and L spectral sequence, additional data are needed for both earlier and later dwarfs. For early- and mid-M dwarfs, I include the the spectra from SDSS DR7 (West et al. 2011, hereafter W11); for L2 and later dwarfs, I combine data from the BUD sample with additional data from the literature.

5.2.1 Hα Emission in the BUD Sample

The selection of the BUD sample and its properties are described in detail in Section 4.2.3 of Chapter 4. Briefly, the sample is a combination of the M7-M9 dwarfs from W11, L dwarfs from Schmidt et al. (2010b), and the new sample of 2,638 ultracool dwarfs selected from BOSS data. Each of the 12,085 M7-L8 dwarfs in the sample have SDSS spectroscopy.

When radial velocities were available, the spectra were first velocity-corrected to 0 km s^{-1}. The equivalent widths (EW) of Hα emission lines were measured using the Hammer spectral typing software (Covey et al. 2007). The Hammer first measures the EW of Hα using a range of 6557.61Å to 6571.61Å for the line and 6500Å to 6550Å and 6575Å to

6625Å for the surrounding continuum. These ranges are shown in Figure 5.1. The uncertainties on the Hα EW were calculated including both the formal uncertainties on the flux and the standard deviation of the continuum ranges.

To define each dwarf as either active or inactive, we required a S/N>3 in the continuum ranges surrounding the Hα line. This S/N cut limits the BUD activity sample to 5934 M7-L3 dwarfs. Each active dwarf was required to have an Hα detection greater than its uncertainty and a measured Hα EW greater than a detection threshold of EW = 0.75Å. This threshold was selected in part to conform with the lower limit of activity selected in W11, and additionally because examination of the BOSS spectra confirms that EW=0.75Å is a suitable balance between including active dwarfs with small EW and excluding false positives.

Figure 5.1 shows the spectra of M7 dwarfs surrounding the EW = 0.75Å threshold, with a range of 0.72Å<EW<0.81 and range of 3<S/N<6. In the lower S/N objects, the detections of Hα is slightly ambiguous, but the spectra above the detection threshold have a noticeable excess of flux at the Hα line. As can be seen in some of the higher S/N spectra, the activity threshold does exclude some Hα emission that can be relatively clearly observed.

Figure 5.2 shows the fraction of active objects as a function of spectral type for BUD data compared to the entire M dwarf sample from W11. For spectral types M7-M9, the BUD active fraction is higher than the DR7 fraction due to less restrictive selection criteria; DR7 dwarfs were also required to have good photometry to be included in the activity fraction, while the BUD spectra were only required to have S/N> 3. The same minimum activity threshold of EW=0.75Å has been applied to both samples.

The fraction of active dwarfs continues to increase as a function of spectral type past the late-M dwarfs, with the L0 and L1 dwarfs both having fractions >90% - only two dwarfs out of 28 with S/N>3 failed to show emission. The activity fraction for the L2 and L3 dwarfs is still undetermined; five of eight L2/L3 dwarfs show Hα emission, and the activity fractions have large uncertainties. Previous data have shown a decrease in the activity fraction from late-M dwarfs to early-L dwarfs, though it was noted that the observed decline could be due to the effect of observational biases caused by poor or variable S/N and resolution (e.g., Schmidt et al. 2007; Reiners & Basri 2008). The possible decline found in the BUD

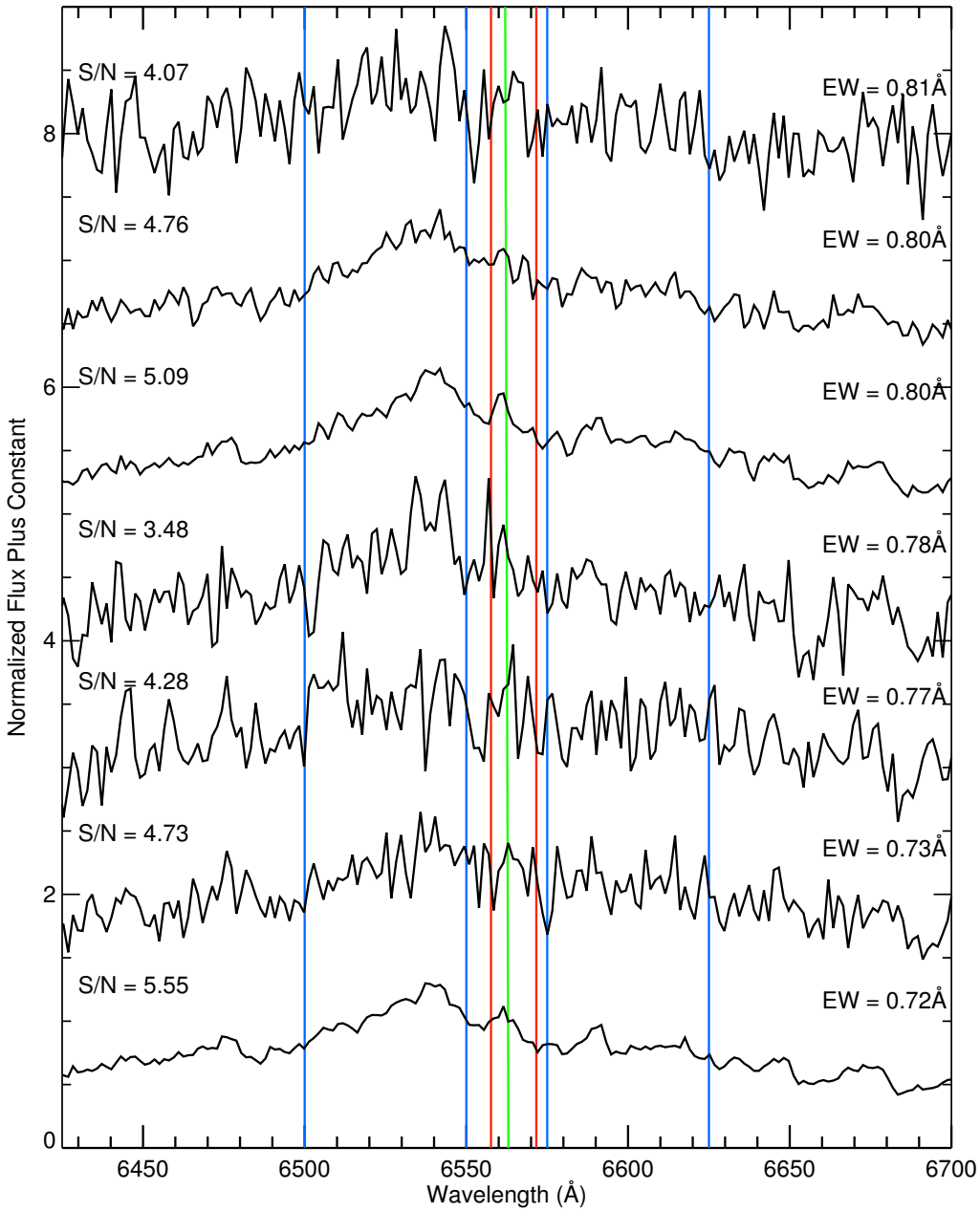

Figure 5.1 Normalized flux as a function of wavelength for M7 spectra with a variety of S/N near Hα and a small range of measured EW. The wavelength of Hα is shown (green) in addition to the wavelength ranges used to measure the line (red) and continuum (blue). These spectra were selected because they surround the active/inactive threshold of EW=0.75Å.

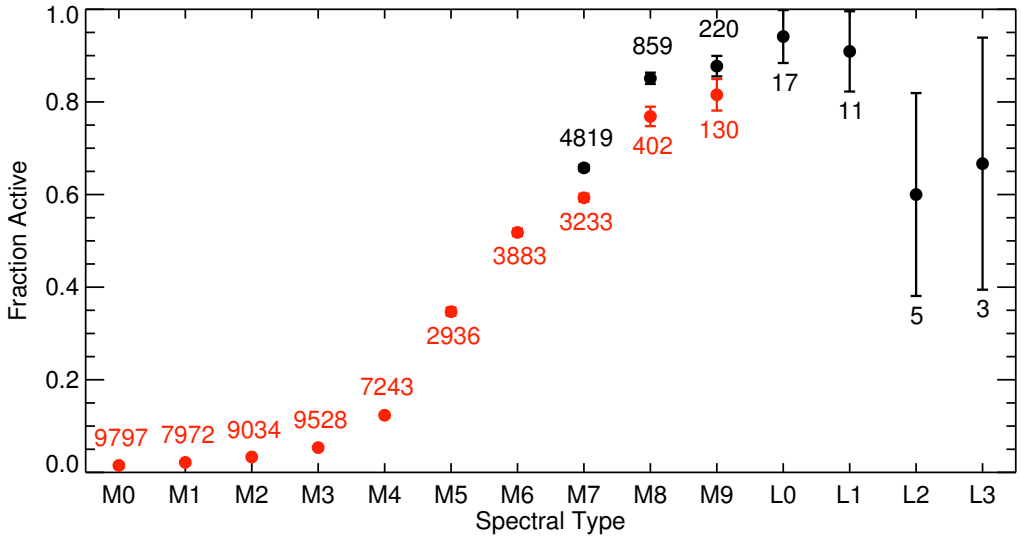

Figure 5.2 Fraction of active stars (as determined by the presence of Hα emission) as a function of spectral type. Fractions computed from the W11 sample using their criteria (red) are compared to fractions computed from the BUD sample using the criteria described in Section 5.2. The total number of objects used to compute the fraction (active and inactive) are shown above or below the data in corresponding colors.

sample from the L0/L1 dwarfs to L2/L3 could also be biased by small numbers; additional observations with consistent S/N and spectral resolution are needed to determine the active fractions of L2/L3 dwarfs with more certainty.

The strength of activity has often been quantified by the ratio of luminosity in the Hα line to bolometric luminosity, or $L_{H\alpha}/L_{bol}$ (e.g., Hawley et al. 1996). This ratio removes the dependence of the measured EW on the surrounding continuum so it is better suited to comparing emission strength across a range of spectral type and T_{eff}. To convert EW to $L_{H\alpha}/L_{bol}$, I use the relation between χ and spectral type from West & Hawley (2008) for M7-M9 dwarfs and the relation between χ and T_{eff} from Reiners & Basri (2008) combined with the relation between T_{eff} and spectral type from Stephens et al. (2009) for L0 and later dwarfs.

Figure 5.3 shows the distribution of Hα emission strength, as measured by $\log(L_{H\alpha}/L_{bol})$, for each spectral type from M7-L3. Activity strength remains relatively constant across the

M7-M9 spectral types, then appears to make a steady decline with later spectral type into the L dwarfs. For each spectral type, there appears to be a wide range of activity strength, with the activity in M7-M9 dwarfs spanning a full range of 2.0 in $\log(L_{H\alpha}/L_{bol})$ and the more sparsely sampled L dwarfs showing ranges of 0.5 to 1.0.

For M7-M9 dwarfs, the lower limit of detectable emission is near (but not below) the tail of the distribution, and for L0-L3 dwarfs the lower limit is well below the detected Hα emission. A similar effect is apparent for the DR7 M dwarf sample (shown in Figure 5 of West et al. 2004). In each case, the activity threshold is well below the median activity strength, but this undoubtedly has at least a small effect on the fraction of M dwarfs with Hα detections. The effect of this overestimate is also likely to change with spectral type, as the EW threshold corresponds to lower values of $L_{H\alpha}/L_{bol}$ for later spectral types. The overall shape of the fraction (low for early-M, rising with later spectral type) is not likely to drastically change with the selection of a different activity threshold.

5.2.2 Observations of Activity in M0-L8 Dwarfs

To place these results in a broader context, additional observations are needed for L2-L8 dwarfs. Table 5.1 summarizes the $\log(L_{H\alpha}/L_{bol})$ determined for L2-L5 dwarfs from the BUD sample and published values (for references see Table 5.1; no L6-L8 dwarfs have yet shown observable Hα emission). Much of the literature includes upper limits on $\log(L_{H\alpha}/L_{bol})$ that range from -5.8 to -8.2 and are not included.

Figure 5.3 shows $\log(L_{H\alpha}/L_{bol})$ as a function of spectral type for active dwarfs from W11, BUD, and Table 5.1. Because the M0-L1 dwarfs from W11 and BUD were selected using a homogeneous sample and consistent criteria, they are represented by the minimum, maximum, median, and interquartile range for each spectral type. The values for L2-L5 dwarfs are inhomogeneous and much more sparsely sampled, so each individual determination is shown.

The L5 dwarfs show high levels of activity compared even to the L0 dwarfs. 2MASS 01443536−0716142 was observed to be active only during a short series of observations classified as a flare (the value given is the minimum measured value from that flare; Liebert

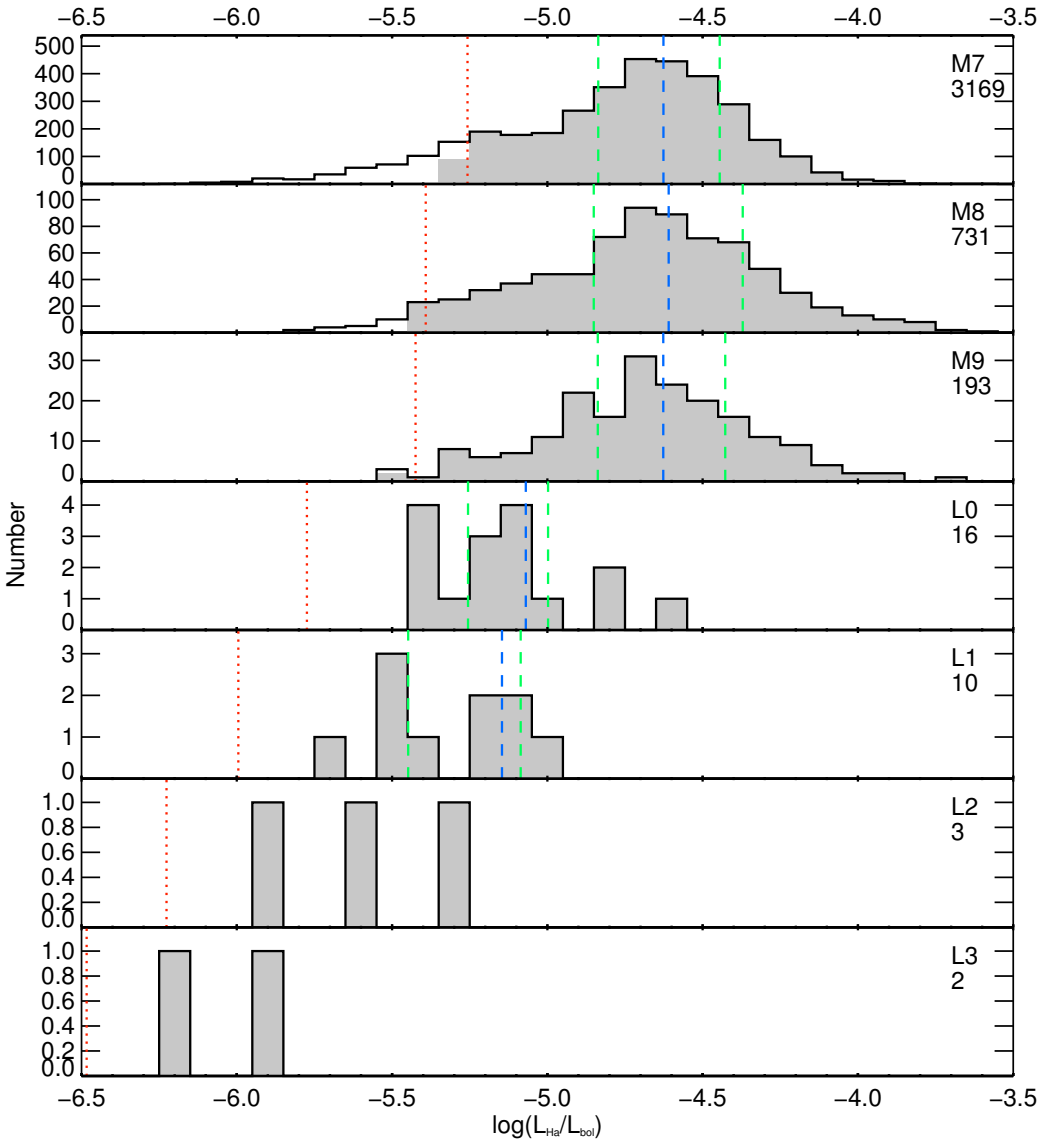

Figure 5.3 For each spectral type (given along the right side) number of dwarfs as a function of $\log(L_{H\alpha}/L_{bol})$. All dwarfs with H$\alpha$ EW greater than their uncertainty in Hα EW are shown; those defined as active are shown in the shaded histogram. For each spectral type, the effective lower limit of detection is shown (based on the 0.75Å active threshold; red dotted) and for spectral types M7-L1, the median (blue dashed) and first and third quartiles (green dashed) of active dwarfs are shown.

Table 5.1. Hα Emission Strength in L2 and Later Dwarfs

Name	Spectral Type	$\log(L_{H\alpha}/L_{bol})$	Hα Ref.	Other Ref.
2MASS J11553952−3727350	L2.0	−5.96	1	
Kelu-1	L2:	−5.50	2	1
SDSS J101707.5+130839.3	L2	−5.24	3	
SDSS J161928.3+005011.7	L2	−5.83	3	
SDSS J165329.6+623136.4	L2	−5.55	3	
2MASS J05233822−1403022	L2.5	−6.52	1	4
SDSS J102921.8+162649.8	L3	−5.80	3	1
SDSS J114634.5+223053.0	L3	−6.14	3	
DENIS P J1058.7−1548	L3	−5.67	2	
2MASS J15065441+1321060	L3	−6.32	1	
2MASS J2224438−015852	L4.5	−6.14	2	
LHS 102B/GJ 1001B	L5	−5.87	2	
2MASS J13153094−2649513	L5	−4.18[1]	5	6, 7
2MASS 01443536−0716142	L5	−5.10[2]	8	

References. — (1) Reiners & Basri (2008); (2) Schmidt et al. (2007); (3) this thesis; (4) Berger et al. (2010); (5) Burgasser et al. (2011) (6) Hall (2002) (7) Gizis (2002) (8) Liebert et al. (2003)

[1]This source is variable; the quoted flux is from Burgasser et al. (2011) and represents a rough median.

[2]The adopted value is the lowest in a series of observations classified as a part of a flare.

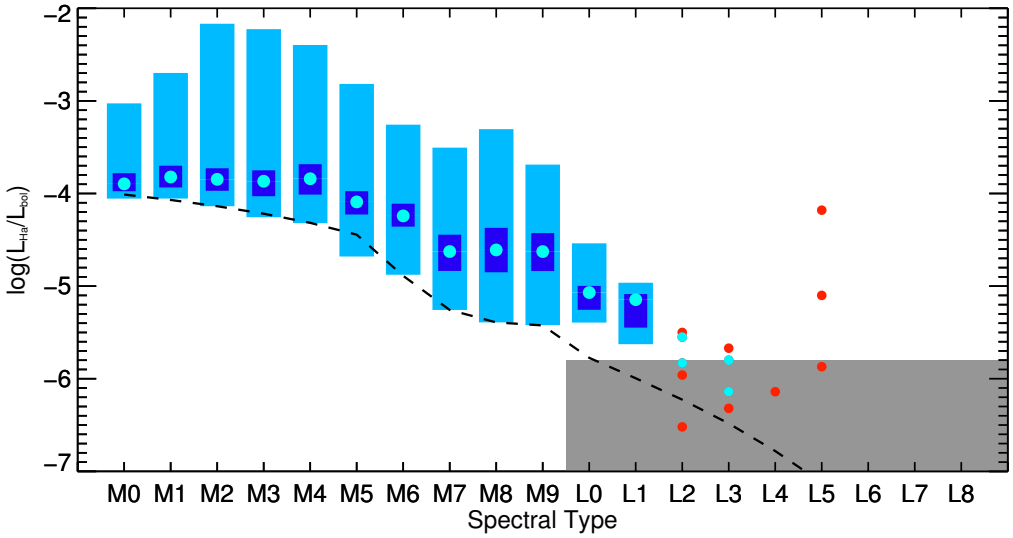

Figure 5.4 Activity strength as a function of spectral type for DR7 and BUD data for M0-L1 dwarfs, and for BUD and literature values (given in Table 5.1) for L2 and later dwarfs. For the M0-L1 dwarfs, the minimum and maximum (medium blue bar), the interquartile range (dark blue bar) and median values (large light blue circle) are shown. For L2-L5 dwarfs, the SDSS data are shown in light blue circles, and the literature values are shown in red circles. The shaded region shows characteristic upper limits from literature non-detections, and the dashed black line shows the effective lower limit of detection for SDSS data (based on the 0.75Å active threshold).

et al. 2003), and the high level of activity in 2MASS J1315−2649 has been repeatedly discussed (Gizis 2002; Hall 2002; Burgasser et al. 2011). LHS 102B shows weaker emission than the other two L5 dwarfs; it is not a noted variable or flare star.

5.3 The Temperature Structure of a Quiet Chromosphere

To understand the changes in the presence and strength of chromospheric emission over the M and L spectral sequence, it is important to characterize the properties of the chromospheres which give rise to the observed Hα emission. For this first effort at characterizing the chromospheres of ultracool dwarfs, I adopt the one-dimensional atmosphere approach used in similar work investigating the chromospheres of earlier M dwarfs (e.g., Hawley et al. 2003; Fuhrmeister et al. 2005; Walkowicz & Hawley 2009). This one-dimensional approach can provide constraints on the possible range of temperature structures and filling factors of cool and ultracool dwarf atmospheres.

This use of one-dimensional stellar atmospheres includes two main assumptions: (1) the temperatures in the outer atmosphere are either low (photospheric) or high (chromospheric) and (2) the chromosphere is well modeled by a single temperature distribution. The first assumption is likely to be true due to stellar bifurcation (Ayres 1981), the principle that any material not heated to chromospheric temperatures will quickly cool to photospheric temperatures. The second assumption is likely untrue, but the strengths of multiple atomic emission lines are needed to place constraints on a chromosphere that contains more than one temperature distribution over its spatial extent (e.g., Walkowicz 2008).

For the photosphere, I use the Bt-Settl models of Allard et al. (2011). The Bt-Settl models were generated with the LTE radiative transfer code Phoenix (Hauschildt et al. 1999). These models include a treatment of mixing and convection due to the sedimentation of dust clouds, which are common in L dwarf atmospheres. The BT-Settl grid covers 100,000K>T_{eff} >400K, 5.5>log(g)> −0.5, and 0.5>[M/H]> −1.5. For simplicity, we assume a single log(g) = 5.0 and [M/H] = 0.0 for each dwarf.

5.3.1 A Short Description of RH

The models presented here and in Chapter 6 were calculated using the RH radiative transfer code, which is described in detail by Uitenbroek (2001). For completeness, a summary is also provided here. RH is a radiative transfer code based on the Multilevel Accelerated Lambda Iteration (MALI) formalism of Rybicki & Hummer (1991). Lambda Iteration is a method of treating non-LTE (local thermal equilibrium) effects by iteratively calculating the radiation field (based on local populations) and the local populations (which in turn depend upon the radiation field). This process is repeated until there is little change in either the populations or the output radiation between successive iterations.

To calculate the radiation field, RH relies upon the formalism of Partial Redistribution (PRD), which allows the optically thick cores of lines to be in LTE, but treats the NLTE effects of coherent scattering in the optically thin line wings. PRD has been demonstrated to greatly speed to convergence of MALI on a final solution (e.g. Paletou 1995). During the calculations, one atom is solved in detail, while the rest are treated as background opacity. RH was implemented with one-, two- and three- dimensional geometries, with the complexities of multidimensional modeling made possible by the speed of PRD iterations. In this chapter, I use one-dimensional geometry and a six level hydrogen atom.

5.3.2 Constructing Model Atmospheres

Before modeling activity on the full range of M and L dwarfs, I explore the effects of varying different parameters that characterize the chromospheric temperature structure on the modeled Hα flux using a $T_{\rm eff}$ = 2400K photosphere (shown in Figure 5.5). I adopt a chromospheric temperature structure that consists of two different components, both of which have a linear increase in temperature with the log of column mass (log(col mass)). The slopes of the two components are characterized by the positions of the start of the chromospheric temperature rise, the chromosphere break[1], and the start of the transition

[1]In this chapter, the chromosphere break is used as a convenient parameter to characterize the chromospheric temperature structure. The motivation for the two different temperature slopes with respect to column mass can be found in detailed models of the Sun's chromosphere (e.g. Vernazza et al. 1981). The lower chromosphere cannot cool efficiently so the temperature rises steeply as a function of column mass, while the upper chromosphere cools via hydrogen emission resulting in a more shallow temperature slope.

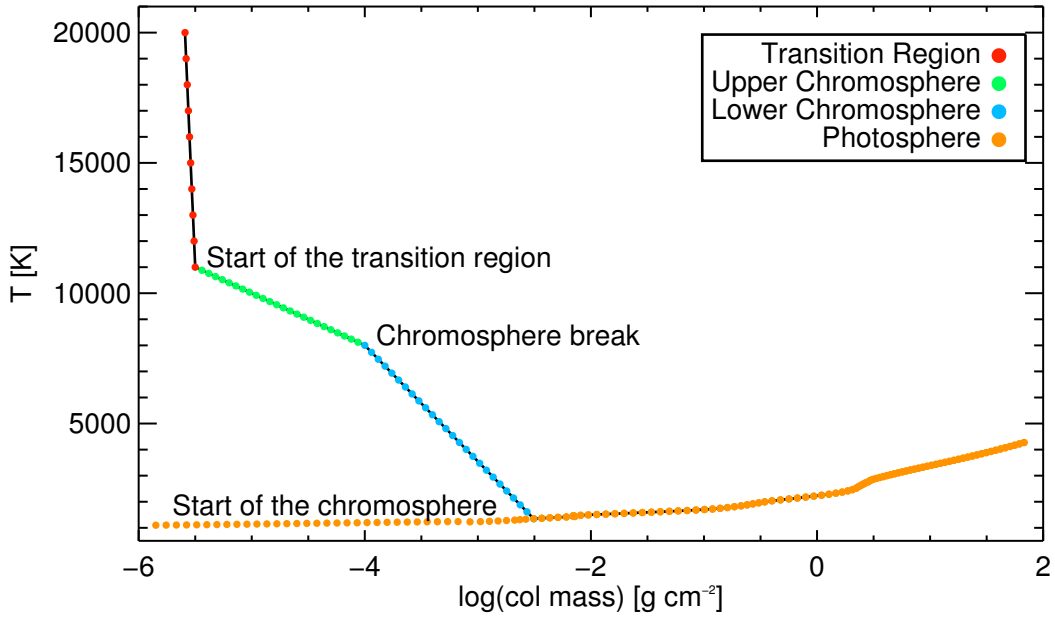

Figure 5.5 Model atmosphere of T_{eff} = 2400K with the an added two component chromospheric temperature structure. The different regions of the atmosphere are shown in different colored circles, each one showing a single value in the atmosphere. The features that are discussed throughout Section 5.3.2 are labeled.

region, which are labeled in Figure 5.5.

The slope of the transition region can be constrained using measurements of the UV flux, but there are no observations of ultracool dwarfs at these wavelengths. For the transition region I follow the prescription of Fuhrmeister et al. (2005); Walkowicz (2008) for a steep linear rise of temperature with respect to log(col mass). This chromospheric temperature structure includes a rise of 9000 K between log(col mass) = −5.5 and −5.6 as an approximation of the beginning of the transition region.

To test the dependence of Hα flux on chromospheric properties I ran a series of models exploring the effect of varying each of the five parameters which characterize the chromospheric temperature structure[2]. For each model, I calculated the $\log(L_{H\alpha}/L_{bol})$ using the method detailed in Section 5.3.4 and a chromospheric filling factor of 0.01. The range of

[2]Note that the temperature at the start of the chromosphere is given by the temperature of the photosphere model at the selected value of log(col mass).

Table 5.2. The Effect of Chromospheric Changes on Hα Emission

Parameter	Range	Δ log($L_{H\alpha}/L_{bol}$)
starting log(col mass) of the chromosphere	-1.5 to 0.5 g cm^{-2}	0.04
log(col mass) of the chromosphere break	-4.5 to -3.5 g cm^{-2}	1.62
log(col mass) of the transition region start	-6.5 to -4.5 g cm^{-2}	0.12
temperature of the chromosphere break	6000 to 10000 K	2.01
temperature of the transition region start	9000 to 13000 K	0.07

each parameter and resulting range in Δ(log($L_{H\alpha}/L_{bol}$) are given in Table 5.2 and illustrated in Figure 5.6.

The primary cause of changes in Hα emission in this series of models is the amount of hot (T>8000K) material located at larger log(col mass) (> -4.5). The position of the base of the chromospheric temperature rise (starting log(col mass)) has no effect on the Hα emission because the material is too cold, while the temperature and log(col mass) at the transition region start have only a small effect because they primarily control the amount of relatively diffuse material at log(col mass) < -5.

As shown in Table 5.2, variations in both the temperature and the log(col mass) of the chromosphere break have a relatively large effect on the strength of Hα emission. To construct models that represent the chromospheres of a range of cool and ultracool dwarfs, I will vary the position of the chromosphere break in log(col mass). While the models presented in Figure 5.6 show that the temperature at the chromosphere break causes a larger range of activity strengths, the change in temperature affects the slope of the chromospheric temperature rise, which in turn affects the location where the temperature exceeds 8000K. The density of material at 8000K is the most important factor in determining the amount of flux generated. Controlling the position of the chromosphere break in log(col mass) has a more direct effect on the Hα flux.

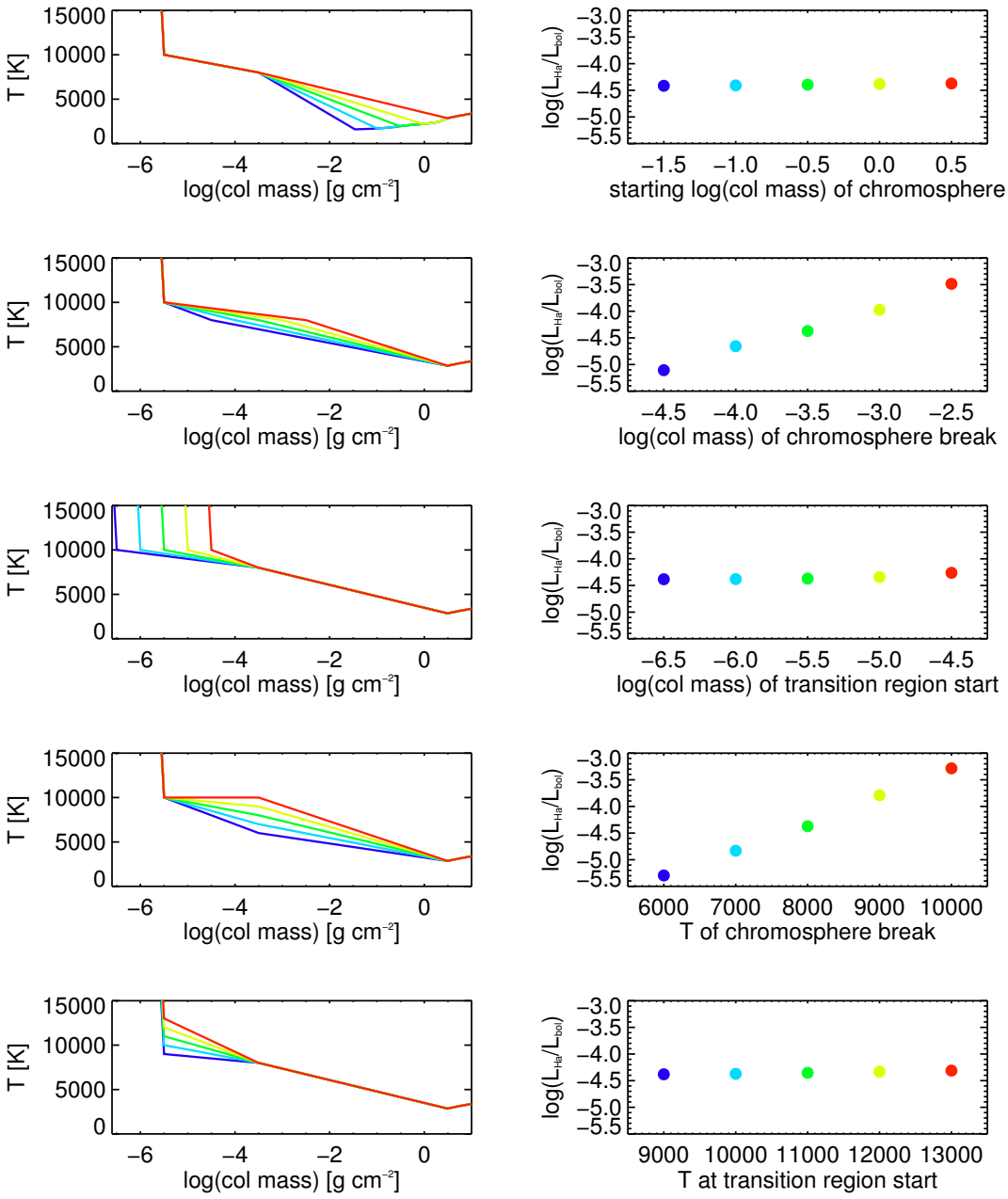

Figure 5.6 Model atmospheres (left) and resulting $\log(L_{H\alpha}/L_{bol})$ (right) for five values of each of five different parameters. The colors of each atmosphere in the left panels correspond with colors of the generated emission in the right panels.

5.3.3 A Grid of Model Chromospheres

I generated a grid of model chromospheres for five different representative effective temperatures, with T_{eff} = 1400, 1900, 2400, 2900, and 3400K roughly corresponding to L7, L3, M8, M4, and M0 dwarfs. Each model photosphere has a set of chromospheric temperature structures attached at log(col mass) = 0.5, rising to a chromosphere break at T=8000K and 13 different positions from log(col mass) = -2 to -5. The chromospheric temperatures then rise to 10,000K at log(col mass) = -5.5. For the transition regions, I include the same increase of 9000 K between log(col mass) = -5.5 and -5.6. While the shape of these chromospheric temperature structures is based on previous M dwarf work (e.g., Fuhrmeister et al. 2005; Walkowicz 2008) which are analogs of solar chromosphere models (e.g., Vernazza et al. 1981), these particular values were adjusted to produce the observed range of Hα emission from M and L dwarfs.

For each output model spectrum, I measured the corresponding Hα line flux by integrating the flux (minus continuum flux) from 6540Å to 6586Å. This relatively large range was required by the hottest model chromospheres, where the resulting emission lines were very broad. The set of model atmospheres and the resulting Hα line flux are shown in Figure 5.7.

In Section 5.3.2 I found that the relative amount of emission depends primarily on the position of the chromosphere break, not the slope of the lower chromospheric temperature rise. This is true for the line flux generated from models with different photospheric temperatures, with the exception of the models at the hottest T_{eff}. The slight decrease in flux is due to an Hα absorption core component that increases in strength with hotter T_{eff}. This core is formed ein the lower chromosphere, where hydrogen can be more easily excited into the n=2 state (where it can absorb a Hα photon) than to higher states associated with Hα emission. The temperatures in the lower chromosphes are much hotter for the T=3400K model than the T=1400K model.

5.3.4 Converting Modeled Quantities to Observed Values

Line flux at the stellar surface (the model output of RH) is not a directly observable quantity, so it is not immediately useful for comparison to observed Hα emission; the emitted line flux

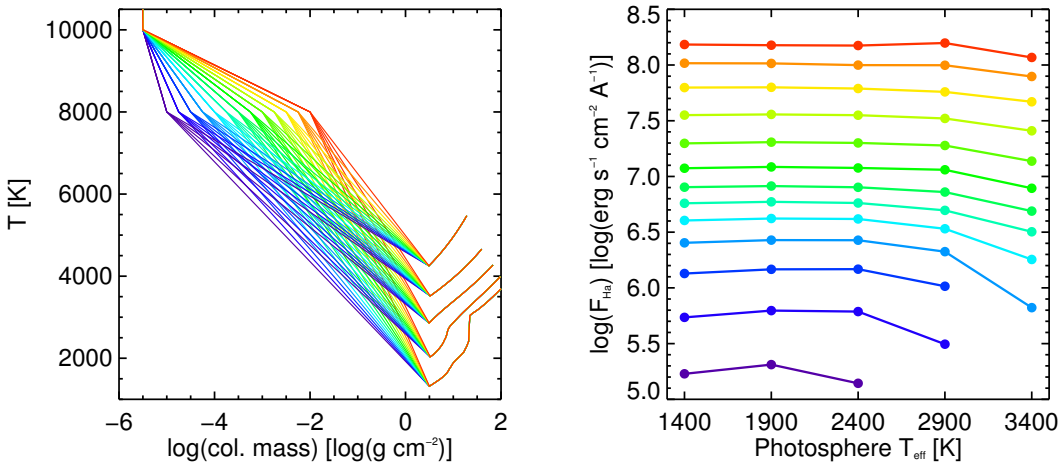

Figure 5.7 Left panel: Grid of model atmospheres used to generate Hα emission. Each chromosphere break is shown in a different color. Right panel: The log of Hα line flux as a function of photosphere $T_{\rm eff}$, with results from chromosphere break shown in the same color as in the left panel. Line fluxes that were in absorption were not shown

must be converted to observed line flux, EW, or activity strength. Calculating any of these quantities requires an estimate of the chromospheric filling factor, or the surface coverage of the chromosphere with the modeled temperature structure. Additional quantities are needed for each of those three observed quantities.

Calculating an observed line flux also requires a distance, but the comparison data must be precisely flux calibrated. Calculating an EW from line flux requires the superposition of the line onto an M dwarf spectrum, but there are no high S/N quiet spectra for late-M dwarfs. Calculating activity strength, or $\log(L_{H\alpha}/L_{bol})$, requires an estimate of the bolometric luminosity, which can be estimated with relative precision. For comparison to data, the model output will be converted to activity strength.

$L_{H\alpha}/L_{bol}$ can be calculated from model parameters using:

$$\frac{L_{H\alpha}}{L_{bol}} = \frac{F_{H\alpha} \times f \times 4\pi R^2}{L_{bol}} \tag{5.1}$$

where $L_{H\alpha}$ is the luminosity in the Hα line, L_{bol} is the bolometric luminosity, $F_{H\alpha}$ is the flux in the Hα line, f is the chromospheric filling factor and R is the stellar radius.

Radii and bolometric luminosities are particularly poorly known for M and L dwarfs,

especially over a range of magnetic activity (e.g., Kraus et al. 2011). These two quantities are not independent of each other, however, because:

$$L_{bol} \approx L_{thermal} = 4\pi R^2 \sigma T_{eff}^4 \tag{5.2}$$

where σ is the Stephan-Boltzmann constant. This makes the assumption that non-thermal contributions to the luminosity are negligible. To test this assumption and estimate the maximum non-thermal contribution, I will assume that the non-thermal flux can be estimated by adding up the contrition from the luminosity of Hα, the radio luminosity, and the x-ray luminosity:

$$L_{nonthermal} \approx L_{H\alpha} + L_{rad} + L_x \tag{5.3}$$

and adopt characteristic values for each of these based on detections from Berger et al. (2010, and references therein) of $L_{H\alpha} = L_{bol} \times 10^{-4}$, $L_{rad} = L_{bol} \times 10^{-6}$, and $L_x = L_{bol} \times 10^{-4}$. This results in an upper limit of

$$L_{nonthermal} \approx L_{bol} \times 10^{-4} + L_{bol} \times 10^{-6} + L_{bol} \times 10^{-4} = 0.000201 \times L_{bol} \tag{5.4}$$

which is a 0.02% non-thermal contribution to the bolometric luminosity. This indicates that $L_{bol} \approx L_{thermal}$ is a reasonably accurate assumption, so I can calculate the strength of Hα using T_{eff} instead of explicitly estimating R or L_{bol}:

$$\frac{L_{H\alpha}}{L_{bol}} = \frac{F_{H\alpha} \times f}{\sigma T_{eff}^4} \tag{5.5}$$

Using T_{eff} is preferable because each photospheric model is generated for a specific T_{eff}, and because it is more straightforward to explore the effects of varying a single parameter rather than both radius and luminosity. The uncertainties in the final calculation are characterized by varying T_{eff} by $\pm$200K; this is greater than the 1% uncertainty from the non-thermal contribution to the bolometric luminosity and also characteristic of the uncertainty on the correlation of spectral type and T_{eff}.

The $\log(L_{H\alpha}/L_{bol})$ for each T_{eff}, chromosphere break, and a range of chromospheric filling factors from 0.3×10^{-6} to 1.0 is shown in Figure 5.8. The resulting emission strength declines with cooler chromospheric temperatures and smaller filling factors. A more subtle effect is the decline in the strength of emission produced at the same chromosphere break

and chromospheric filling factor for hotter effective temperatures. For example, the hottest atmosphere with a chromospheric filling factor of 0.01 produces $\log(L_{H\alpha}/L_{bol}) \sim -2$ for $T_{eff} = 1400$K and $\log(L_{H\alpha}/L_{bol}) \sim -4$ for $T_{eff} = 3400$K. As the line flux remains nearly constant for the different values of T_{eff} (see Figure 5.7), this effect is entirely due to the change in radius and bolometric luminosity in the cooler objects. The ratio between the line luminosity and the total luminosity increases rather sharply for these cool objects.

5.4 Results

Section 5.2 illustrated the observed properties of activity as function of spectral type, and Section 5.3 described a grid of model atmospheres assembled to characterize those observations. I can combine the observations and model atmospheres to determine the range of chromospheric filling factors and chromosphere break heights which are consistent with Hα observations of M and L dwarfs.

I adopt the minima, maxima, and interquartile ranges from data for M0, M4, M8, and L3 dwarfs (shown in Figure 5.3) corresponding to 3400, 2900, 2400, and 1900K atmospheres. For each spectral type, I compare these statistics to the range of modeled values for the corresponding temperature. Figure 5.9 shows the comparison of values for the 2900K model and the M8 data and the resulting ranges of chromospheric filling factor and log(col mass) of the chromosphere break. I have chosen to illustrate the entire range of observed values with smaller dots and the interquartile range with larger dots to show simultaneously the entire range of the population and values close to the median for each spectral type.

The chromospheric temperature structures and filling factors that correspond to the ranges of $\log(L_{H\alpha}/L_{bol})$ observed in SDSS data are shown in Figure 5.10. To generate the observed Hα strength, the warmest dwarfs (3400K and 2900K; M0 and M4) need to have significantly higher chromospheric filling factors than the cooler dwarfs (2400K and 1900K; M8 and L0). Even using the hottest model chromosphere, the filling factors of the early- and mid-M dwarfs range from 0.01 to 0.1, a significant fraction of the stellar surface. Additionally, the warmest active dwarfs are limited to models with the hottest chromospheric temperature structures, requiring a minimum chromospheric break of -4.0 and -4.75, respectively.

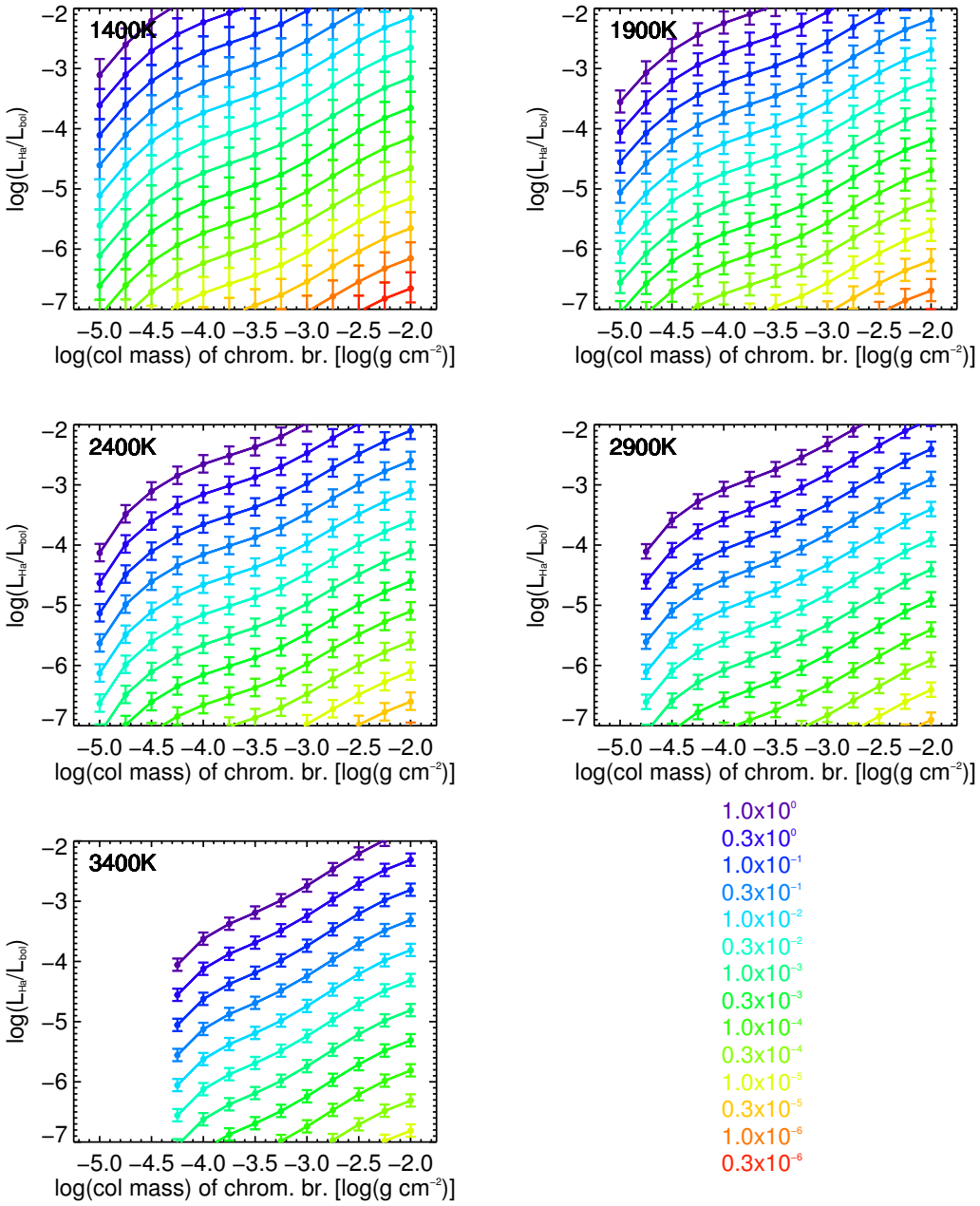

Figure 5.8 For each photosphere $T_{\rm eff}$, $\log(L_{H\alpha}/L_{bol})$ as a function of chromosphere break for a range of chromospheric filling factors (each shown in a color given in the bottom right). The uncertainties in $\log(L_{H\alpha}/L_{bol})$ are based on varying $T_{\rm eff}$ by $\pm$200K, as discussed in Section 5.3.4.

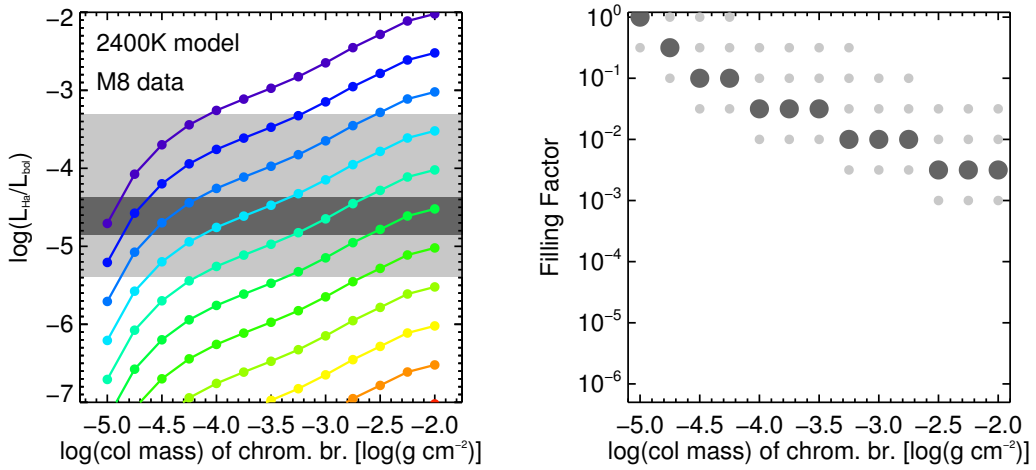

Figure 5.9 Left panel: $\log(L_{H\alpha}/L_{bol})$ as a function of log(col mass) of the chromosphere break for the 2900K set of models. The colored lines show the same chromospheric filling factors as in Figure 5.8. The light grey shading shows the entire range of observed $\log(L_{H\alpha}/L_{bol})$ for M8 dwarfs, and the dark grey shading shows the interquartile range. Right panel: Filling factor as a function of log(col mass) of the chromosphere break. Values that correspond to models that fall in the range of observations for M8 dwarfs are shown as small light grey circles, and values in the interquartile range are shown as large dark grey circles.

While the observed level of activity remains relatively constant for M0-M4 dwarfs, there is a decline in the height of the chromosphere break and chromospheric filling factor between the 3400K and 2900K atmospheres. Figure 5.11 demonstrates the effect of the changing bolometric luminosities on a constant value of $\log(L_{H\alpha}/L_{bol})$. The same activity strength may be produced on a cooler dwarf with a cooler chromospheric temperatures. If an M0 dwarf had a chromospheric temperature structure characterized by a break of at log(col mass) -4, that a chromosphere with that structure would have to cover 10% - 30% of its surface to produce $-5 < \log(L_{H\alpha}/L_{bol}) < -4$. An L8 dwarf with the same chromospheric temperature structure would only need a filling factor of 0.1% to 0.3%.

5.4.1 Extrapolating to Cooler Dwarfs

While there are few Hα detections for L3 dwarfs and none for L7 dwarfs (corresponding to the 1900K and 1400K model atmospheres), we can adopt a range of possible values,

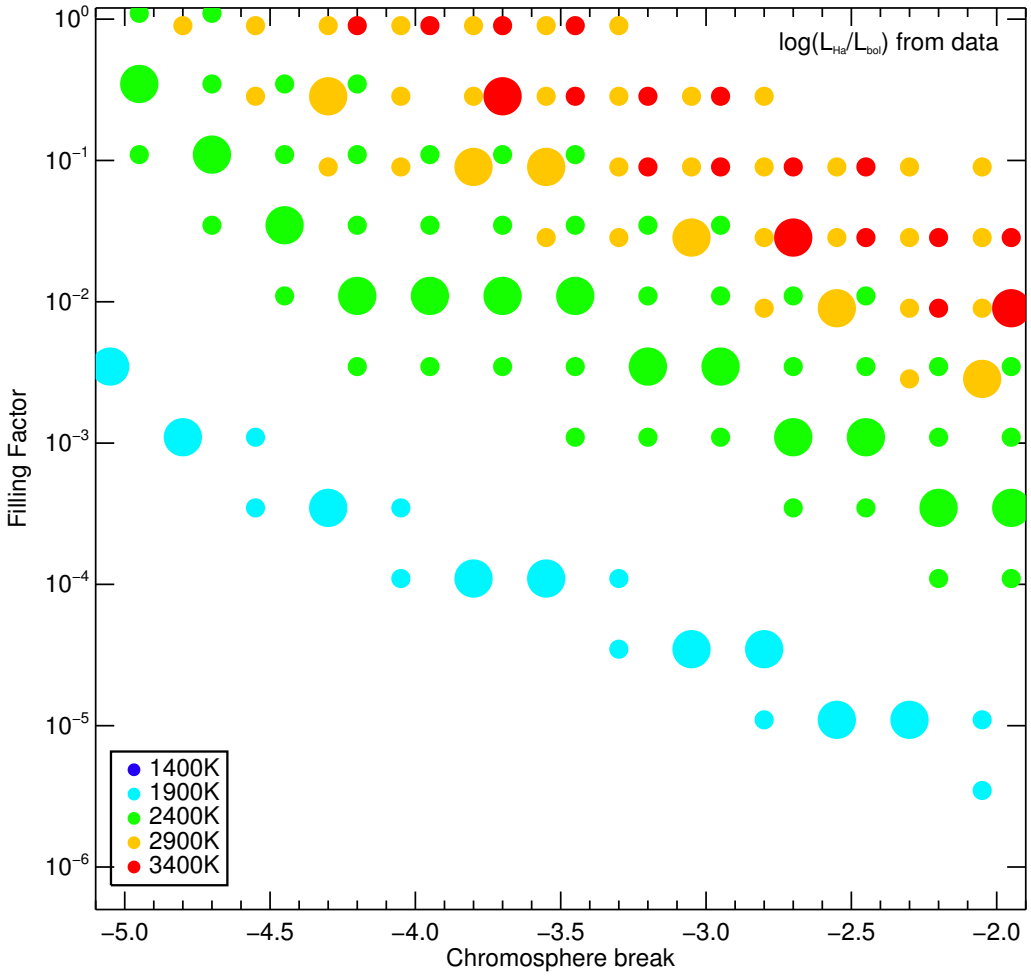

Figure 5.10 Chromosphere break as a function of chromospheric filling factor for models that match the ranges of $\log(L_{H\alpha}/L_{bol})$ for each T_{eff}/Spectral Type shown in Figure 5.12. For each T_{eff}, the large circles are values that match the inner quartile range of observed values, while the smaller circles show matches with the entire range of values. Circles are slightly offset from their exact values for clarity. This set of chromosphere breaks and chromospheric filling factors is based on the data shown in Figure 5.3.

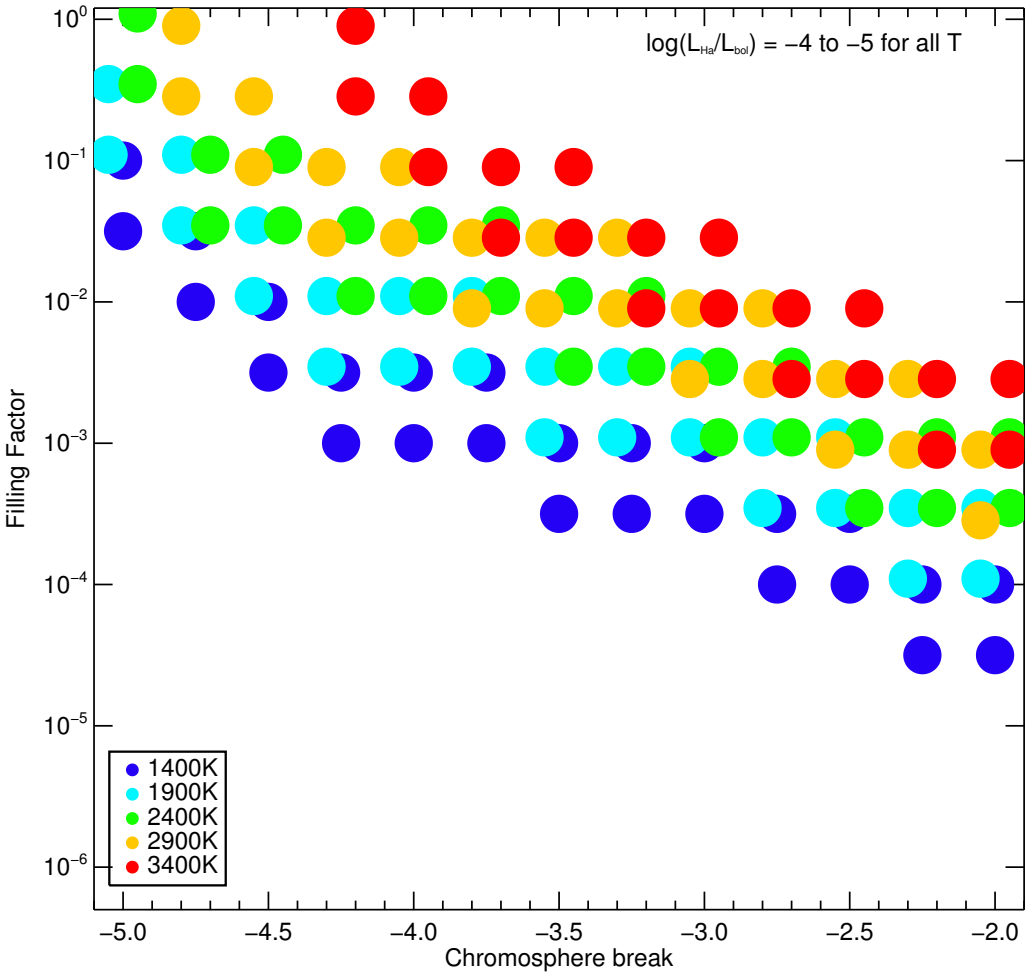

Figure 5.11 Chromosphere break as a function of chromospheric filling factor for models that match the ranges of $\log(L_{H\alpha}/L_{bol})$ for each T_{eff}/Spectral Type shown in Figure 5.12. For each T_{eff}, the circles show models that produce $-4.5 < \log(L_{H\alpha}/L_{bol}) < -5.5$. The circles are slightly offset from their exact values for viewing clarity.

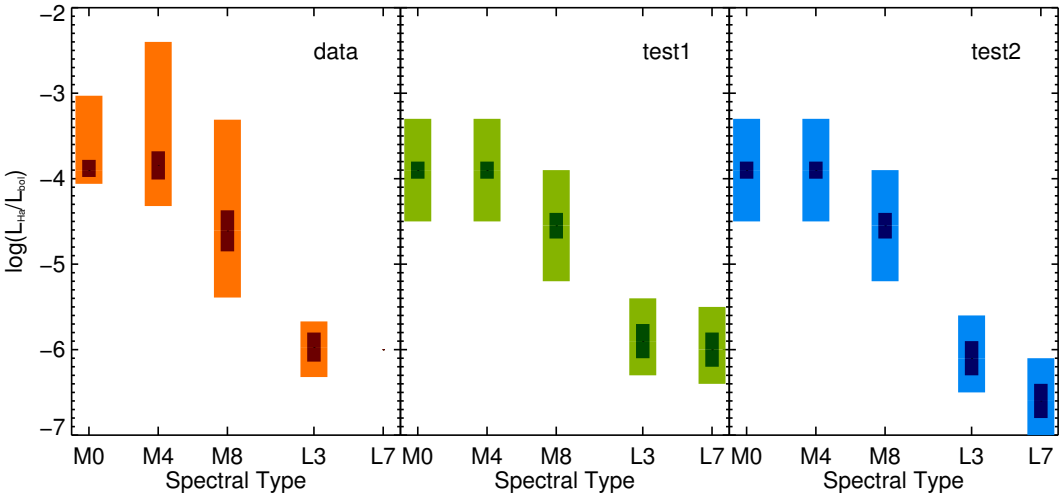

Figure 5.12 Values of $\log(L_{H\alpha}/L_{bol})$ as a function of spectral type. The inner shaded box represents the interquartile range, while the outer shaded box represents the entire range. The data from the W11 sample is shown (red/orange) in addition to two sets of values adopted to approximate the data and extrapolate out to late-L dwarfs (test1 in green, test2 in blue).

consistent with sparse activity strength data and observed upper limits, to characterize upper limits on the possible chromospheric temperatures of L dwarfs. Figure 5.12 shows two sets of minima, maxima, and interquartile ranges adopted for the five different photospheric temperatures compared to those statistics based on the data in Figure 5.3.

The two different sets of values assume different characteristics of late-L dwarfs. The higher values, labeled test1, assume the Hα emission from mid- to late-L dwarfs does not dramatically decrease from that of early-L dwarfs ($-6.4 < \log(L_{H\alpha}/L_{bol} < -5.5$). This implies that observed upper limits more often correspond with non-detections than weak emission. The lower set of values, labeled test2, were adopted to characterize a weaker mean Hα emission level ($-7.0 < \log(L_{H\alpha}/L_{bol} < -6.1$). The corresponding implication is that upper limits on Hα are often undetected weak emission.

Both test1 and test2 adopt slightly different values for M dwarfs. To select these values, I assumed that the dwarfs with the largest $\log(L_{H\alpha}/L_{bol})$ were observed during flares (and thus do not represent quiet chromospheres), and that the lower limits do exclude a small

number of dwarfs showing emission. The results for test1 and test2 are shown in Figures 5.13 and 5.14.

The results for M dwarfs did not change significantly with our "smoothed" values and still show the same general trend. If there is a low level of chromospheric activity on late-L dwarfs, the chromosphere producing that activity has a surface coverage of three to six orders of magnitude less than the characteristic chromospheres of early-M dwarfs. If the chromospheric filling factors are instead similar, the very coolest of our models would be used for the L7 dwarf and the hottest for the M0. Either way, these differences indicate that a dramatic shift occurs between the characteristic chromospheres of active M0 and L7 dwarfs - in temperature structure, surface coverage, or both.

5.5 Discussion

The chromospheric temperature structure and filling factor required to produce observed values of Hα emission is a strong function of T_{eff}. The strength of $\log(L_{H\alpha}/L_{bol})$ observed in early- to mid-M dwarfs can only be generated by a relatively hot chromosphere covering 0.01 to 1.0 of the observed surface. It is important to note, however, that the results for early-M dwarfs are sampling only a subset of the entire early-M dwarf population. According to the activity fraction calculated using our EW = 0.75Å criteria for inactive vs. active (Figure 5.2), <1% of M0 dwarfs are active and <15% of M4 dwarfs are active. The temperature structures and chromosphere breaks for M0 to M4 dwarfs represent 1 to 15% of the population; the majority of the early-M dwarf population either lacks a chromosphere entirely, or has some combination of lower temperature chromospheres (which in some cases show Hα in absorption) and smaller filling factors.

For late-M and early-L dwarfs, a cooler chromospheric temperature structure and/or a smaller filling factor is required to produce the range of observed emission strengths. These dramatically cooler (or less extended) chromospheres are not likely to be due to a decline in magnetic field strength (current measurements show that late-M dwarfs typically have strong fields), but rather due either to a decrease in the amount of coupling between the atmosphere and the field, or simply the difficulty of heating material on the surfaces of these cool dwarfs to chromospheric temperatures. These results are relatively representative of

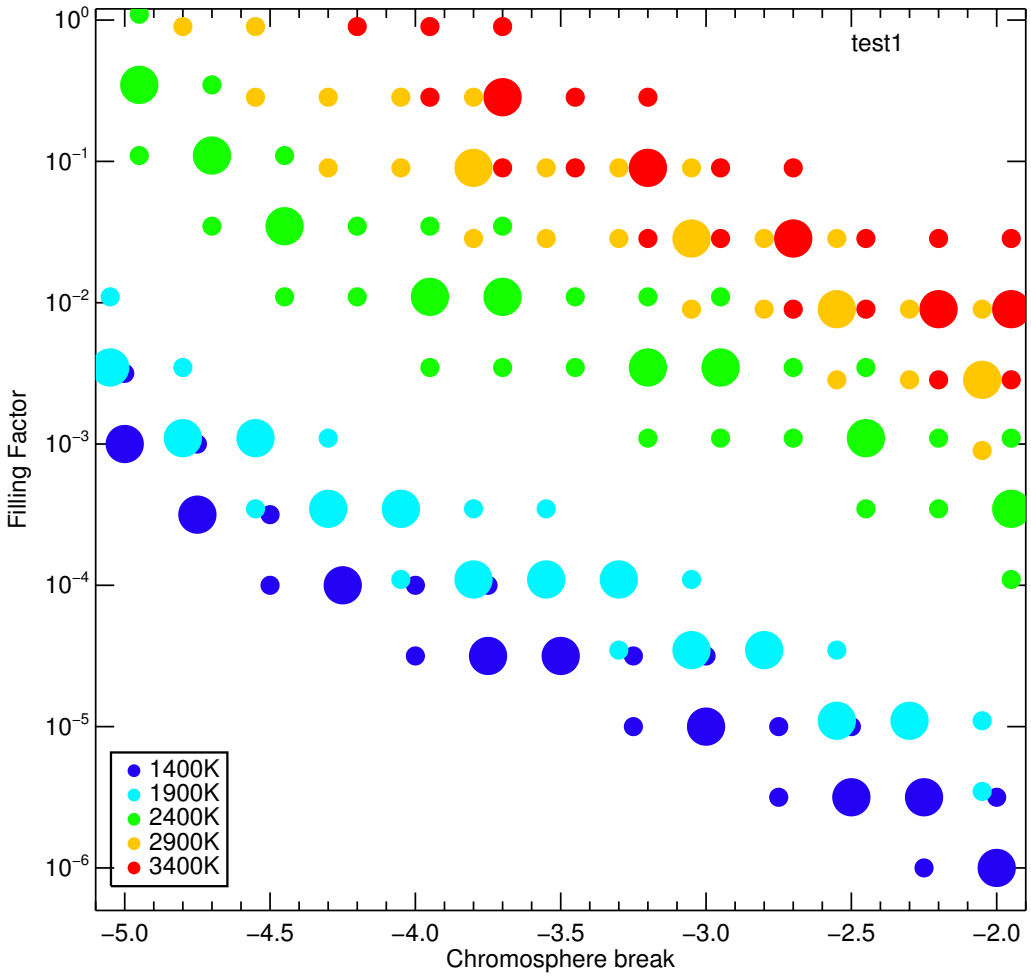

Figure 5.13 Chromosphere break as a function of chromospheric filling factor for models that match the ranges of $\log(L_{H\alpha}/L_{bol})$ for each T_{eff}/Spectral Type shown in Figure 5.12. For each T_{eff}, the large circles show matches to the inner quartile range, while the smaller circles show matches to the entire range of values. Circles are slightly offset from their exact values for viewing clarity. This set of chromosphere breaks and chromospheric filling factors is based on a smoothed interpolation of the data and an extrapolation to later spectral types, assuming relatively strong emission at later spectral types.

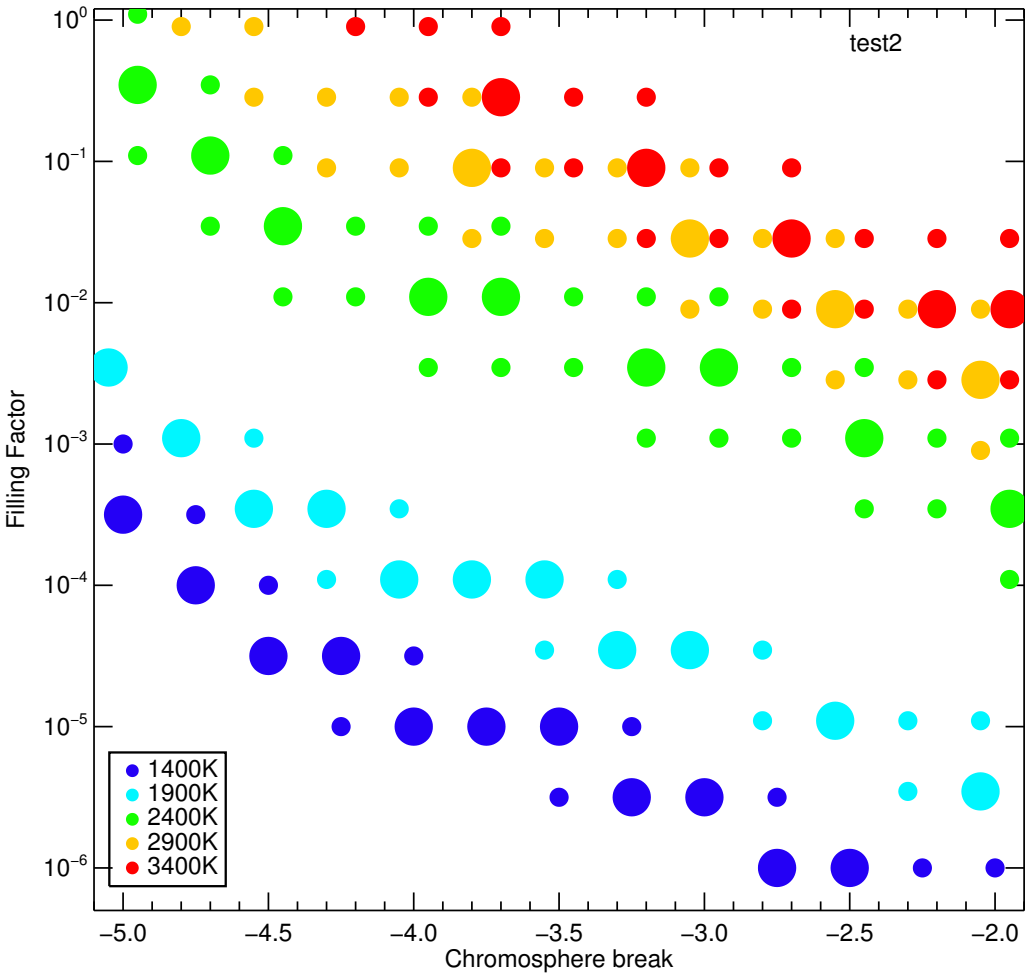

Figure 5.14 Chromosphere break as a function of chromospheric filling factor for models that match the ranges of $\log(L_{H\alpha}/L_{bol})$ for each T_{eff}/Spectral Type shown in Figure 5.12. For each T_{eff}, the large circles show matches to the inner quartile range, while the smaller circles show matches to the entire range of values. Circles are slightly offset from their values for viewing clarity. This set of chromosphere breaks and filling factors is based on a smoothed interpolation of the data and an extrapolation to later spectral types, assuming relatively weak emission at later spectral types.

the local ultracool dwarf population. Over 80% of late-M and L dwarfs are active, so the calculated decline in chromospheric temperature and/or filling factor shows real change between the chromospheres generated on late-M and early-L dwarfs.

While there are only a few detections of Hα for mid- to late-L dwarfs, the range of possible and detected activity strengths are consistent only with chromospheres that cover a very small area of the observable surface ($<$0.003) or have an even cooler temperature structure than those modeled here. The two L5 dwarfs with strong Hα also have cool chromospheres compared to early-M dwarfs, the ranges of chromospheric filling factor and chromosphere break which produce their reported emission strengths most closely resemble those of late-M dwarfs.

It is unclear whether or not most mid- to late-L dwarfs posses chromospheres, but observations of Hα emission in these dwarfs are difficult due to their faint bolometric luminosities. Even cooler dwarfs are capable of sustaining Hα emission; one T dwarf has shown consistently strong Hα emission at a level of $\log(L_{H\alpha}/L_{bol}) = -4.3$ (Burgasser et al. 2002a; Liebert & Burgasser 2007) without any confirmed cause other than chromospheric activity (e.g., accretion, low mass interacting binary companion, flares). If some brown dwarfs can emit strong Hα, then a large fraction of them may emit weaker Hα.

Chapter 6

PROBING THE FLARE ATMOSPHERES OF M DWARFS USING INFRARED EMISSION LINES

Observations of a variety of emission lines are essential to understanding the atmospheric structure during flares. Typically, these lines are found in the optical or ultraviolet region of the spectrum, which is rich with hydrogen Balmer series, Ca II H&K, Mg II, Fe II, etc. Despite the larger number of emission lines, these observations can become difficult on cooler or fainter dwarfs, where the surrounding continuum is low. The near-infrared region of the spectrum ($\lambda = 0.95$ to 2.5μm) has a brighter underlying continuum and contains hydrogen Paschen and Brackett series emission lines, in addition to He 1 λ10830. We initiated a monitoring campaign in order to observe these lines during M dwarf flares.

Another motivation to obtain near-infrared spectra of flares was an effort to locate tracers of quiescent activity at infrared wavelengths. As discussed in Chapter 5, observations of Hα emission become increasingly difficult with later spectral type. The spectral energy distribution of L dwarfs peak in the near-infrared, so an activity indicator at those wavelengths would be ideal for examining activity in ultracool dwarfs.

This chapter was originally published in collaboration with Adam F. Kowalski, Suzanne L. Hawley, Eric J. Hilton, John P. Wisniewski, and Benjamin M. Tofflemire in the January edition of the Astrophysical Journal (Schmidt et al. 2011, ApJ, Vol. 745, pp. 14-23, © 2012 by the American Astronomical Society) and is reproduced below with permission of the American Astronomical Society.

6.1 Introduction

M dwarfs are notorious for dramatic flares, presumably caused by magnetic reconnection in their atmospheres. Weaker analogs of these flares are present on the Sun, where the surface magnetic field is thought to be powered by the rotationally induced shear between the radiative and convective layers of the Sun (Parker 1955). For fully convective M dwarfs

(spectral types M3 and later; Chabrier & Baraffe 1997), strong magnetic fields are created and sustained solely through turbulence and rotation within the star (e.g., Browning 2008). The dynamo powering the magnetic fields which result in flares on these M dwarfs is not fully understood, but additional observations constraining the chromospheric heating are essential to a coherent picture relating stellar magnetic fields to flares.

The atmospheric heating during a flare results in emission from many wavelength regimes, and flares have been well observed in the X-ray (e.g., Osten et al. 2010), ultraviolet (e.g., Robinson et al. 2005; Hawley et al. 2007), optical (e.g., Kowalski et al. 2009; Walkowicz et al. 2011), and radio (e.g., Stepanov et al. 2001; Osten & Bastian 2008). The combination of observations at these different wavelengths, especially when obtained as part of multi-wavelength flare monitoring campaigns, has informed our interpretation of the physics underlying these dramatic emission events (e.g., Hawley et al. 2003; Osten et al. 2005). However, to date there have been no concerted efforts to observe infrared emission lines from flaring stars. Quiescent M dwarfs are particularly bright in the near-infrared portion of the spectrum, so emission from the hydrogen Paschen and Brackett series and the He 1 λ10830 transition are both easily observable and essential to probing different atmospheric heights. These infrared emission lines are particularly useful for examining accretion in T Tauri stars (e.g. Bary et al. 2008; Vacca & Sandell 2011).

In quiescent (not flaring) active M stars, high resolution ($R > 20{,}000$) spectra have shown weak absorption from Pβ in AU Mic (Short & Doyle 1998b); Pϵ was also seen in absorption in six out of ten active M dwarfs (Houdebine et al. 2009). Emission from higher-order Paschen lines has only been detected in a few serendipitous observations at the far red end of optical spectra. The first occurred during a survey to classify photometrically selected late-M and L dwarfs. Liebert et al. (1999) observed Paschen emission (Pδ – P11) between 8800 Å and 10500 Å in a $R \sim 4300$ spectrum of the M9.5 dwarf 2MASSW J0149090+295613. The flare also showed a variety of optical emission lines, but had no evidence of continuum emission. Schmidt et al. (2007) subsequently observed Paschen emission lines in a $R \sim 2000$ spectrum of the M7 dwarf 2MASS J1028404−143843. The flaring spectrum included strong continuum enhancement of the entire spectrum blueward of 9200 Å in addition to many emission lines. Pδ – P11 were again identified, with equivalent widths (EWs) of 2-5 Å. For

both of these observations, there was no corresponding photometry, which prohibited the characterization of the overall strength and duration of the flare.

Fuhrmeister et al. (2008) observed Pδ – P11 on the M5.5 dwarf CN Leo during a large-amplitude flare with a total duration of about 45 minutes. Their data included $R \sim 40,000$ spectra over the range 3000–10500 Å. Line strengths were not given for the Paschen lines, but inspection of the three consecutive 100 s exposures near the peak of the flare shows a decay in line strength. Fuhrmeister et al. (2010) used one-dimensional atmosphere models to examine the emission from the flare, finding that a single model can reproduce most, but not all, flare emission lines.

An unexplored region of the spectrum during M dwarf flares, both in observations and modeling, is the 1.0–2.5 μm range, which contains the lower-order Paschen lines, higher-order Brackett and Pfund lines, and He 1 λ10830. We report on the results of our campaign to observe active M dwarfs in this wavelength regime with simultaneous photometric monitoring. The data include three flares with infrared line emission; observations of the strongest flare also include blue optical spectra. Using these data, we quantify the duty cycle for infrared flare line emission and examine the relative line strengths during the evolution of each of the three flares. Congruent with previous studies (e.g., Hawley & Fisher 1992; Walkowicz et al. 2008; Fuhrmeister et al. 2010), we use one-dimensional atmospheres and the static NLTE radiative transfer code RH (Uitenbroek 2001) to model the line flux ratios of the largest flare.

In Section 6.2, we discuss our targets and observations and in Section 6.3 we describe our methods for flare identification. Individual flares are examined in Section 6.4 together with our duty cycle estimate. Empirical atmospheric models that produce infrared line emission are discussed in Section 6.5.

6.2 Observations

Our targets include three well-known mid-M flare stars: AD Leo, EV Lac, and YZ CMi, in addition to one active late-M dwarf, VB 8. Magnitudes, coordinates, and the duration of our observations for each target are given in Table 6.1. To both detect IR emission and characterize a flare, we need at least infrared spectra and one band of optical photometry,

Table 6.1. Flare Star Observations

Name	ST	J	K	$t_{\rm obs}$ (h:m)	$N_{\rm flares}$	$t_{\rm flare}$ (h:m)	$N_{\rm flares}$ IR	$t_{\rm flare}$ IR (h:m)	$\rm Frac_{IR}$
YZ CMi	M4.5	6.58±0.02	5.70±0.02	16:36	8	1:55	1	0:08	0.008
AD Leo	M3	5.45±0.02	4.59±0.02	12:18	1	0:31	0	0:00	0
EV Lac	M3.5	6.11±0.03	5.30±0.02	15:21	6	3:56	2	1:14	0.081
VB 8	M7	9.78±0.03	8.82±0.02	4:37	1	0:15	0	0:00	0
M3-M4.5				44:15	15	6:22	3	1.37	0.031
Total				48:52	16	6:38	3	1.37	0.028

Note. — The total time observed is given in Column 5 ($t_{\rm obs}$), the total time each object spent in flare is given in Column 7 ($t_{\rm flare}$), and the time with observed infrared line emission is given in Column 9 ($t_{\rm obs}$; see Figures 6.3, 6.5, and 6.6). The last column gives the fraction of time each object spent with infrared line emission.

but some nights include additional data. The targets, times observed, and instruments used each night are detailed in Table 6.2.

6.2.1 Flare-cam on the ARCSAT 0.5 m

Photometry for all of the nights was obtained using Flare-cam on the Astrophysical Research Consortium Small Aperture Telescope (ARCSAT). ARCSAT was formerly used as the photometric calibrating telescope for the Sloan Digital Sky Survey (York et al. 2000; Tucker et al. 2006). Its location at Apache Point Observatory (APO) makes it an ideal telescope for obtaining simultaneous data with the ARC 3.5 m telescope, which we used for our infrared spectroscopy (see Section 6.2.3). Flare-cam is equipped with *ugri* filters, and the CCD is optimized for observing flare stars because of its good blue response and fast readout (Hilton 2011). Exposure times and filters are given in Table 6.2.

The data were reduced using standard IRAF routines combined with a custom python code that tracked the change in each star's position over the course of the night. The magnitudes were calibrated using differential photometry with respect to the brightest stars in the image. See Hilton (2011) for more details on the photometric reductions.

6.2.2 NMSU 1 m

For four of the eleven nights of observations listed in Table 6.2, we also obtained U-band photometry using the NMSU 1 m, a robotically operated telescope located at APO (Holtz-

Table 6.2. List of Observations

UT Date	Target	Telescope/Instrument	Filter[1]	ET (s)	UT Time (h:m)	Time (h:m)	$t_{\rm obs}$ (h:m)	$N_{\rm flares}$
2009 Feb 4	YZ CMi	APO TripleSpec[2]		4	3:20 to 7:10	3:50	1:42	1
2009 Feb 4	YZ CMi	ARCSAT flare-cam	*u*, *g*	7, 2	5:30 to 7:12	1:42		
2009 Feb 4	AD Leo	APO TripleSpec		2	7:14 to 13:46	6:32	5:20	1
2009 Feb 4	AD Leo	ARCSAT flare-cam	*u*, *g*	5, 1	7:18 to 12:38	5:20		
2009 Apr 14	AD Leo	APO TripleSpec		2–5	2:54 to 7:44	4:50	1:18	0
2009 Apr 14	AD Leo	ARCSAT flare-cam	*g*	10–100	2:28 to 4:12	1:44		
2009 Oct 24	EV Lac	APO TripleSpec		8	1:41 to 6:51	5:10	3:35	1
2009 Oct 24	EV Lac	ARCSAT flare-cam	*u*, g	10, 1	1:06 to 5:05	3:59		
2009 Oct 24	EV Lac	DAO Spectrograph[3]		60–300	2:26 to 9:05	6:39		
2009 Oct 24	EV Lac	NMSU 1 m camera	*U*	4	1:26 to 9:30	8:04		
2009 Oct 27	EV Lac	APO TripleSpec		8	1:04 to 6:53	5:49	5:19	3
2009 Oct 27	EV Lac	ARCSAT flare-cam	*u*, *g*	5, 1	1:34 to 9:13	7:49		
2009 Oct 27	EV Lac	DAO Spectrograph		200–420	2:02 to 6:18	4:16		
2009 Oct 27	EV Lac	NMSU 1 m camera	*U*	4	1:12 to 9:18	8:06		
2010 Apr 25	VB 8	APO TripleSpec		60	7:24 to 11:07	3:43	3:12	0
2010 Apr 25	VB 8	ARCSAT flare-cam	*g*	120	7:57 to 11:06	2:33		
2010 May 26	VB 8	APO TripleSpec		30	7:28 to 8:53	1:25	1:25	1
2010 May 26	VB 8	ARCSAT flare-cam	*g*	60	6:22 to 8:54	2:32		
2010 May 26	EV Lac	APO TripleSpec		8	9:01 to 11:39	2:38	1:50	1
2010 May 26	EV Lac	ARCSAT flare-cam	*u*, *g*	10, 2	9:10 to 11:00	1:50		
2010 Nov 27	EV Lac	APO TripleSpec		5	0:24 to 5:14	4:50	4:37	1
2010 Nov 27	EV Lac	ARCSAT flare-cam	*u*, *g*, *r*	5, 1, 1	0:37 to 5:17	4:40		
2011 Feb 14	YZ CMi	APO TripleSpec		4	2:07 to 6:08	4:01	4:01	4
2011 Feb 14	YZ CMi	ARCSAT flare-cam	*g*, *r*, *i*	1, 1, 1	1:24 to 4:30	3:06		
2011 Feb 14	YZ CMi	NMSU 1 m camera	*U*	10	2:07 to 7:20	5:13		
2011 Feb 15	AD Leo	APO TripleSpec		2	9:35 to 12:28	2:53	2:36	0
2011 Feb 15	AD Leo	ARCSAT flare-cam	*g*, *r*, *i*	1, 1, 1	9:26 to 10:36	1:10		
2011 Feb 15	AD Leo	NMSU 1 m camera	*U*	4	9:52 to 13:09	3:17		
2011 Feb 15	YZ CMi	APO TripleSpec		4	1:16 to 3:08	1:52	1:07	2
2011 Feb 15	YZ CMi	ARCSAT flare-cam	*g*, *r*, *i*	1, 1, 1	1:26 to 3:56	2:30		
2011 Feb 15	YZ CMi	APO TripleSpec		4	4:49 to 9:34	4:45	4:45	
2011 Feb 15	YZ CMi	ARCSAT flare-cam	*g*, *r*, *i*	1, 1, 1	4:50 to 5:27	1:37		
2011 Feb 15	YZ CMi	NMSU 1 m camera	*U*	10	1:59 to 9:41	7:42		
2011 Feb 21	AD Leo	APO TripleSpec		2	8:41 to 12:16	3:35	3:04	0
2011 Feb 21	AD Leo	ARCSAT flare-cam	*u*, *g*, *r*	5, 1, 1	6:07 to 11:45	5:38		
2011 Feb 22	YZ CMi	APO TripleSpec		4	2:08 to 7:09	5:01	5:01	1
2011 Feb 22	YZ CMi	ARCSAT flare-cam	*u*, *g*, *r*, *i*	6, 1, 1, 1	1:49 to 7:40	5:51		

Note. — Column 7 (Time) refers to the total duration of observations for each instrument, while Column 8 ($t_{\rm obs}$) gives the duration of observations that overlap for the photometry and infrared spectroscopy. Column 9 ($N_{\rm flares}$) gives the number of flares found from the photometry using the process described in Section 6.3.

[a]The filter in bold was used to identify flares for those observations.

[b]R ∼3500; $\lambda \sim 0.95$ to 2.45μm; see Section 6.2.3.

[c]R ∼750; $\lambda \sim$ 3540 to 4710 Å; see Section 6.2.4.

man et al. 2010). Typical exposure times were 4 –10 s, and readout was 10 s. The reductions were performed using an automated pipeline which measured the magnitude of the flare star with respect to several background stars.

6.2.3 TripleSpec on the ARC 3.5 m

Infrared spectra were obtained with the TripleSpec instrument on the ARC 3.5 m telescope at APO. TripleSpec is a cross-dispersed near-infrared spectrograph that covers 0.95–2.45 μm (Wilson et al. 2004). We used the 1″.1 slit, resulting in a resolution of R$\sim$3500. All data were obtained using an A/B nod pattern, shifting the star along the slit in order to perform sky subtraction. We obtained data for an A0 calibrator star every $\sim$40 minutes in order to correct for the changing telluric absorption over the course of the night. Our typical exposure times were 2–4 s for AD Leo, EV Lac, and YZ CMi, and 30 s for VB 8.

The data were reduced using a version of SpexTool modified to work with ARC 3.5 m TripleSpec data (Cushing et al. 2004). We constructed telluric correction spectra from our A0 standards using the routine included in SpexTool (Vacca et al. 2003), but modified the remaining post-processing r outines to automatically process each spectrum instead of using the provided GUI interface. Although the formal residuals of our wavelength solution were 0.5–1 pixel, the curved, tilted orders of the spectra impose additional systematic effects in the wavelength calibration.

We detected Pβ, Pδ, Pγ, Brγ, and He 1 λ10830 during the most energetic flare observed. No higher-order Brackett or Pfund emission was detected in any of our spectra. We measured the EWs using regions defined individually for each line in order to include all observed flux; for Pβ, Pδ, Pγ, and He 1 λ10830 these were 10–20 Å wide (6–12 pixels; 0.001–0.002 μm) and for Brγ the line region was 40 Å wide (14 pixels; 0.004 μm). Continuum regions were defined as $\pm$0.01 μm on either side of each line. Quiet and flare profiles for the five lines are shown with the regions used for line measurements in Figure 6.1. The spectrum surrounding and underlying each of the emission lines contains many other molecular and atomic features so the EWs of the emission lines are not zero even in quiescence. The EW measured in the quiescent spectrum is subtracted from each flare measurement.

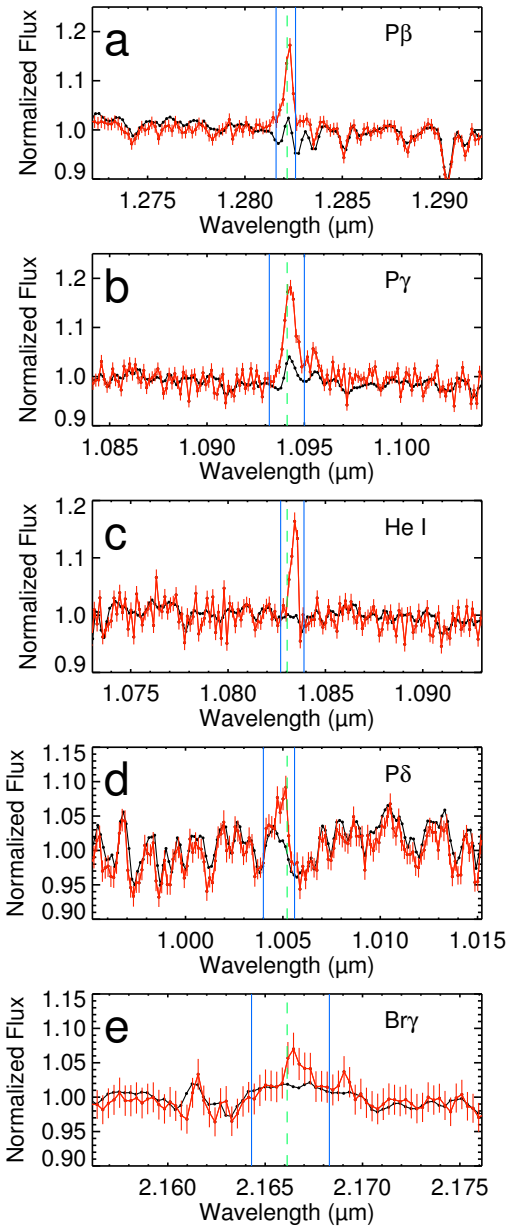

Figure 6.1 Spectra of EV Lac during quiescence (black) co-added from ∼2 hr of exposure during UT 2009 October 24, and from eight co-added spectra with exposure times of 8 s each during the flare peak on UT 2009 October 27 (red). The emission lines are labeled and their central wavelengths are shown (dashed green lines). The regions used to measure the EW of each line are also shown (solid blue lines). The shifts of some lines from the nominal central wavelengths are likely due to small (1–2 pixel) systematic errors in the wavelength solution (see the text).

We could not determine absolute line fluxes directly from individual TripleSpec spectra because the observed flux in each spectrum varies due to the movement of the star on and off the slit during the nod pattern. We used a method similar to the χ factor of Walkowicz et al. (2004) to calculate absolute line flux by multiplying measured EWs (which do not depend on the continuum level) by a calibrated continuum flux. Continuum fluxes were obtained from a quiet, co-added, high signal-to-noise spectrum of each star normalized to Two Micron All Sky Survey (2MASS) photometry using 2MASS filter curves (Cohen et al. 2003; Skrutskie et al. 2006). While this method would not be feasible in the UV and optical due to white-light emission, continuum enhancement during flares is negligible in the JHK_S passbands. Davenport et al. (2012) use a flare continuum model on an M3 star to predict that a flare with $\Delta u = 4$ mag would produce a $\Delta J < 10$ mmag peak, and Tofflemire et al. (2012) report no broadband (J, H, K_S) continuum enhancements above a level of 5–8 mmag during flares having similar total energy as reported here. The variations detected by Tofflemire et al. (2012) and Davenport et al. (2012) are smaller than the formal uncertainty quoted with the 2MASS magnitudes (20–30 mmag), so we assume that the variation between the published 2MASS magnitudes and the magnitudes of the M dwarfs during our observing was negligible.

6.2.4 DAO 1.8 m

For two nights, we used the DAO 1.8 m telescope with the SITe5 CCD and spectrograph to observe EV Lac during a coordinated campaign with the telescopes at APO. Our setup resulted in a spectral resolution of $R \sim 750$ and wavelength coverage from 3550 Å to 4700 Å. We measured Ca 2 K, He 1 λ4471, and the hydrogen Balmer series Hγ and Hδ. Exposure times for EV Lac ranged from 60 to 420 s. Due to these relatively long integration times, additional cosmic-ray cleaning was performed with the LACOSMIC utility (van Dokkum 2001).

The spectra were wavelength-calibrated with an FeAr lamp and flux-calibrated using data from the standard star G191B2B, then spectrophotometrically calibrated by normalizing to the simultaneous U-band data. EWs are not useful for blue flare spectra because

of the changes in the surrounding continuum flux during the flare. Instead, we measured absolute line fluxes directly from the data. The values we use during the flare have the quiet line flux subtracted.

6.3 Identifying Flares

Flares are most easily seen at blue and ultraviolet wavelengths, where the hot, white-light continuum emission from the flare is in high contrast to the small amount of flux emitted from cool M dwarf photospheres (Lacy et al. 1976; Hawley & Pettersen 1991). To identify as many flares as possible, we used the bluest band of photometry available. This was typically u, but for some nights only U was available, and VB 8 was too faint to observe in U or u, so we used g-band data. The band used to identify flares for each set of observations is given in Table 6.2.

Photometrically, flares are observed as excursions above the mean quiescent value of the star's flux, which can be any size or shape. Realistically, flare detection must take into account small variations in the continuum caused by observational effects and so a minimum duration and energy above the observed quiescent value is required. To identify individual flares, we used the custom IDL code discussed in Hilton (2011), which selects peaks that have at least three consecutive epochs more than three standard deviations above the local quiescent light curve. At least one of those epochs must be 5σ above quiescence. We reviewed each flare by eye to confirm that the deviations from the mean were not caused by bad photometry. Over the course of 48.9 hr of observations on four different stars, we observed a total of 16 flares, which are listed per star in Table 6.1 and per night in Table 6.2. Figure 6.2 shows the energy and peak magnitude of each flare.

To identify flares which had associated IR line emission, we examined the measured EWs of Pβ and He 1 λ10830 as a function of time during the flare. We found that the three most energetic flares, which occurred on EV Lac on UT 2009 October 27 and UT 2010 November 27, and on YZ CMi on UT 2011 February 14, each showed infrared emission lines. These flares are discussed in detail in Section 6.4.1.

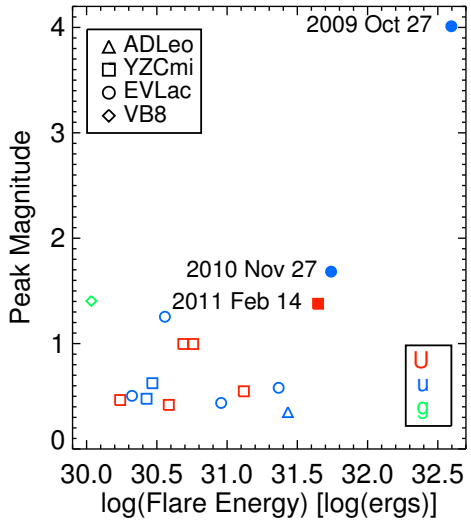

Figure 6.2 Peak magnitude in U , u , or g bands as a function of total flare energy in those bands. The flares from AD Leo (triangles), YZ CMi (squares), EV Lac (circles), and VB 8 (diamonds) observed in U (red), u (blue), and g (green) bands are shown. The flares where IR line emission was observed are distinguished (solid symbols) and labeled with their dates. The flares with accompanying IR line emission have the largest total flare energy and relatively high peak magnitudes.

6.4 Characterizing Infrared Flares

6.4.1 Individual Flares

2009 October 27 flare on EV Lac. We were observing with all four instruments during the most energetic event, a $\Delta u = 4.02$[2] mag flare on EV Lac on UT 2009 October 27. The light curves for our observations are shown in Figure 6.3. The photometry (in U, u, and g bands) exhibits a typical flare light curve with a fast rise and exponential decay. The u-band flare emission lasted 1.68 hr and released a total energy of 3.9 $\times 10^{32}$ erg.

The combination of optical (DAO) and infrared (TripleSpec) spectroscopy allows us to examine a total of nine emission lines–Hγ, Hδ, He 1 λ4471, and Ca 2 K in the UV/blue part of the spectrum, and Pβ, Pγ, Pδ, Brγ, and He 1 λ10830 in the infrared. Figure 6.4 shows the light curve of each emission line normalized to its value at $t = 4.97$ hr (the peak of u-band emission), and the ratio of each line to Hγ for comparison of their evolution during the flare.

The light curves for Hγ, Hδ, and He 1 λ4471 have a fast-rise exponential-decay shape similar to the photometry. Pγ and Pδ show a similar fast rise, but their decay is slower than the Balmer series lines. The Pβ and Ca 2 K emission both peak after the other Paschen and Balmer series lines, and exhibit an even slower decay after their late peaks. Brγ is similar to Pβ and Ca 2 K in its late peak, but seems to decay faster than any other line. This may be an observational effect, as it is by far the weakest line detected. Without a stronger detection, we assume that its ratio to the Paschen lines is constant throughout the flare. The He 1 λ10830 emission shows a shape distinct from the rest of the lines–it remains nearly at its peak flux for 0.8 hr, approximately half of the duration of the flare in u band.

The slow decay during the gradual phase is a well-known property of Ca 2 K (e.g., Bopp & Moffett 1973; Hawley & Pettersen 1991; Fuhrmeister et al. 2008), but in this flare, He 1 λ10830 emission traces a region that remains heated for an even longer portion of the gradual phase than Ca 2 K. This could be due to the Neupert effect, where the line responds to the total cumulative flare heating for which the time integral of the U band (white-light

[2]Although the Δu represents a negative change in magnitude (corresponding with an increase in flux) we adopt a convention of $\Delta u = |u_{\rm flare} - u_{\rm quiet}|$ throughout.

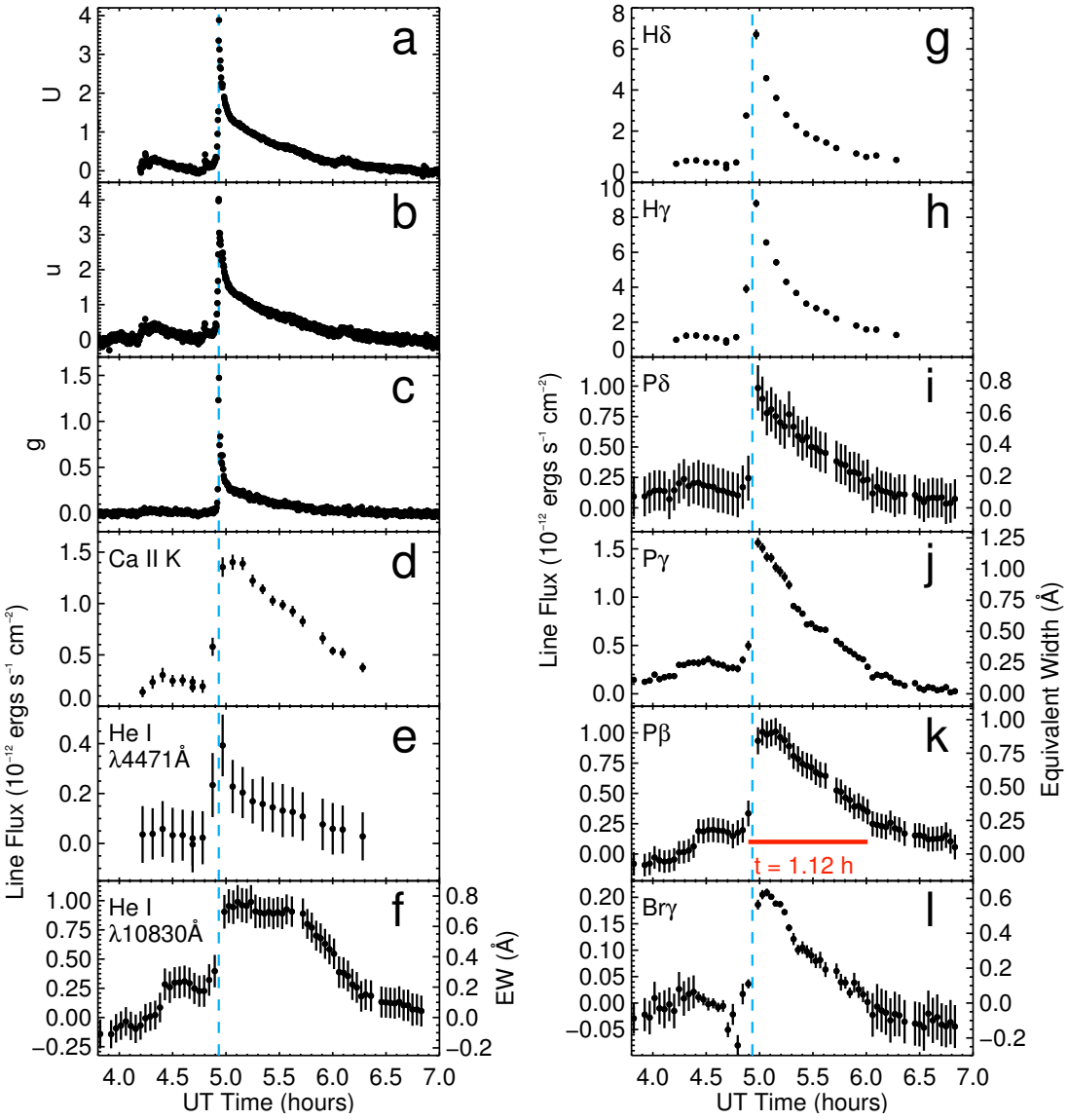

Figure 6.3 Data from the UT 2009 October 27 flare observed on EV Lac. Panels (a), (b), and (c) show U-, u-, and g-band light curves during the flare. The panels (d)–(l) show the variations in the optical and infrared lines. The flaring line flux (with a quiescent value subtracted) is shown along the left y-axis, and for the infrared data equivalent width is shown along the right y-axis. Panel (k) shows the time used as the flare duration in Table 6.1 (red line). The time of the peak u-band flux is shown in each panel (blue dashed line). the infrared emission line fluxes are averaged over 8 exposures of 8 s each. The total exposure time for each point is 64 s, but including instrumental overhead and time to execute the nod pattern, the average cadence is 2.5 minutes. Small gaps in the infrared line data are due to standard star observations.

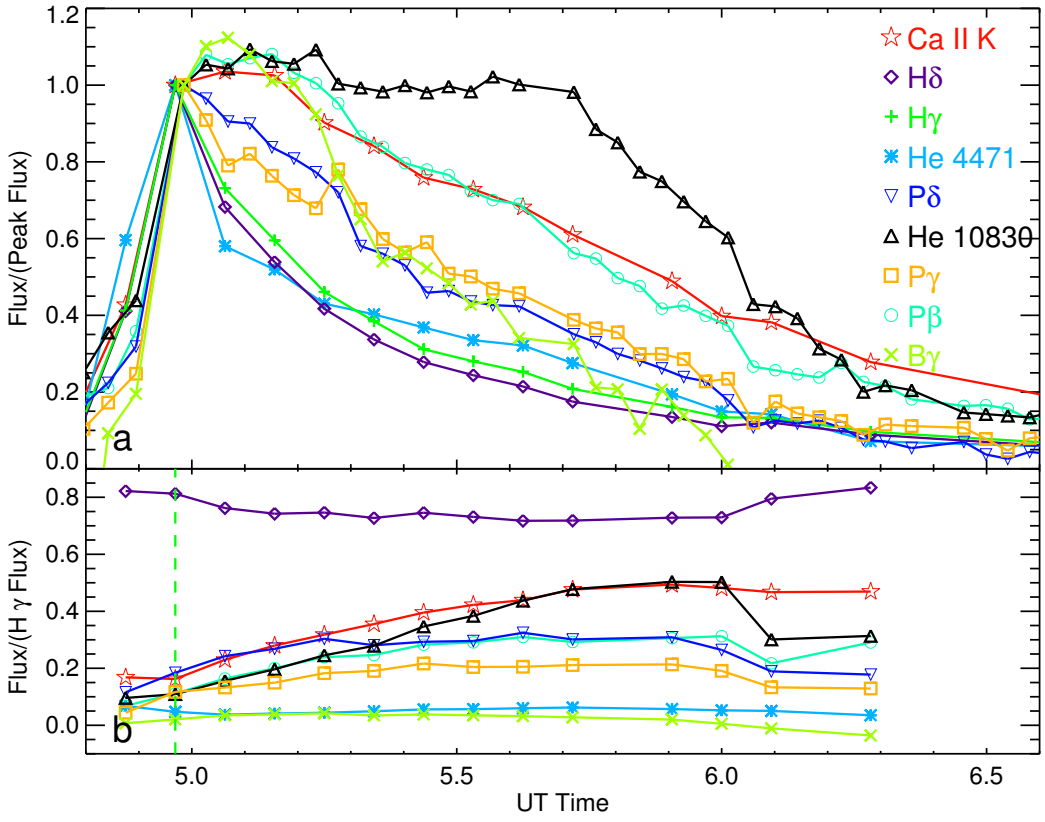

Figure 6.4 Line fluxes for the nine optical and infrared emission lines detected during the UT 2009 October 27 flare observed on EV Lac. In panel (a), the line fluxes are normalized to their flux at the time of peak emission for Hγ (t = 4.97 hr). The normalization emphasizes the different decay patterns. Panel (b) shows the ratios of the other eight emission lines to the Hγ flux. the iR lines were binned to the same time resolution as the optical lines. The vertical green dashed line shows the location of the flare peak in Hγ.

emission) is often used as a proxy (Hawley et al. 1995; Osten et al. 2005). Section 6.5 describes our efforts to model the emission lines from this flare.

2010 November 27 Flare on EV Lac. We observed another flare with infrared line emission on EV Lac on UT 2010 November 27. The flare peaked at $\Delta u = 1.68$, and over the course of $t = 1.30$ hr it emitted 5.5 $\times 10^{31}$ erg in the u band. We observed with both ARCSAT and TripleSpec during the flare, and have photometry in g and r band in addition to the u-band data. The photometry and the line flux lightcurves for Pβ, Pγ, and He 1 λ10830 are shown in Figure 6.5. There was no discernible emission in Pδ and Brγ.

This peculiarly shaped flare contains three separate peaks in the u-band photometry. After the first and third peak, the flux seems to decay exponentially, but after the middle peak there is a gentle rise in the u-band flux. TripleSpec was taking observations of a standard star during the first peak of the flare, so it is unknown if the emission lines showed the same fast rise exponential decay as the first photometric peak. The rise in Pβ and Pγ line emission before and after the standard star gap suggests that those lines showed some emission between the first and second peaks of the flare. An observed increase in infrared line emission occurred $\sim$0.2 hr after the second peak in the u-band photometry, tracing a gentle rise and decay.

The shape of this flare is very different than that of the UT 2009 October 27 flare on EV Lac, and the relative line strengths are also different. In the previous flare, Pβ, Pγ, and He 1 λ10830 emitted nearly the same peak flux. In this flare, He 1 λ10830 peaked at twice the strength of the Pβ and Pγ lines, indicating a different pattern of atmospheric heating during the two flares.

2011 February 14 flare on YZ CMi. On UT 2011 February 14, we observed a $\Delta U = 1.38$ flare on YZ CMi with the NMSU 1 m, ARCSAT, and TripleSpec. The flare lasted for $t = 0.5$ hr and released a total U-band energy of 4.4 $\times 10^{31}$ ergs. Figure 6.6 shows the U, g, and r-band light curves (i band was also observed but showed no change during the flare) and line fluxes from Pβ, Pγ, and He 1 λ10803 Å. This is the lowest energy flare with any evidence of IR line emission, and the measured EWs were small (0.05–0.2 Å), which provides a lower limit on the observability of IR line emission. With these small EWs, it is difficult to compare the strengths of the emission lines; they are all the same strength

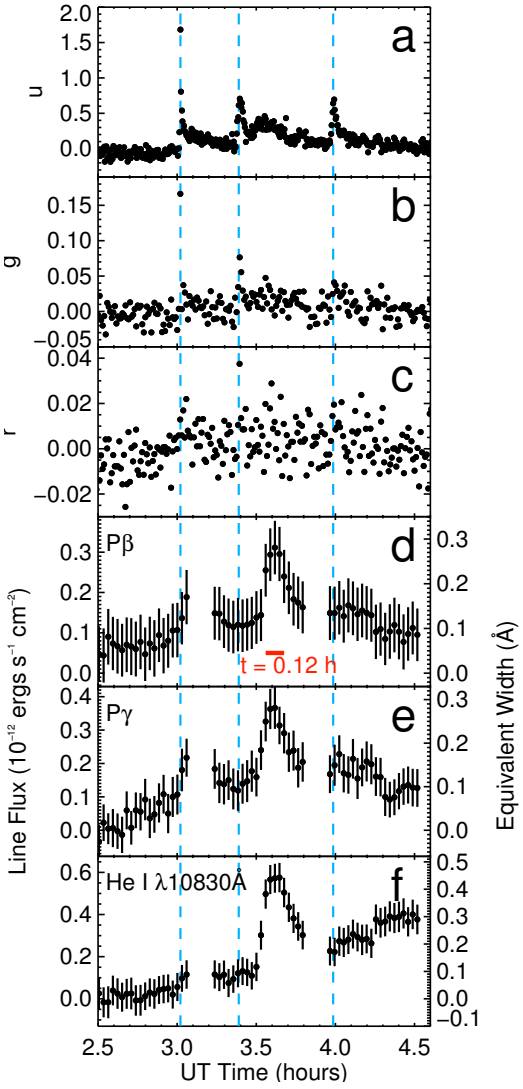

Figure 6.5 Data from the UT 2010 November 27 flare observed on EV Lac. Panels (a), (b), and (c) show the change in u , g , and r bands during the flare, and panels (d), (e), and (f) show the flux (left axis) and EW (right axis) of the infrared emission lines detected during the flare. Panel (d) shows the time used as the flare duration in Table 6.1 (red line). The three dashed blue lines show the times when the three flare peaks occurred in the u band. the infrared emission line fluxes are averaged over eight exposures of 5 s each. The total exposure time for each point is 40 s; the average cadence is 1.7 minutes. The gaps in the infrared line data are due to standard star observations.

within the uncertainties.

The U-band light curve shows a fast-rise exponential-decay shape with a precursor event 0.1 hr before the main peak. the iR emission does not show the precursor or the initial rise of the photometry. However, the co-added infrared measurements have an effective time resolution of 2.5 minutes (due to the inclusion of time spent executing the nod pattern and readout), which is insufficient to resolve those features.

6.4.2 How Often Does IR Line Emission Occur?

In order to determine the expected rate, or duty cycle, of infrared line emission, we first defined detectable emission as approximately 1σ above the mean quiescent level. The length of time with detectable emission is shown for each flare as the red horizontal line on the Pβ light curve in Figures 6.3, 6.5 and 6.6 and given in Table 6.1. The total time spent in emission for all three flares observed is 1.4 hr (out of 48.9 possible hr), which corresponds to an IR flare emission duty cycle of 2.8%. Excluding VB 8, we calculate an IR flare emission duty cycle of 3.1% (of 44.3 hr) for active mid-M dwarfs.

We can also place a limit on the duty cycle using the flare frequency distributions from Hilton (2011), which give the number of u-band flares per unit time for each flare energy. The u and U-band energies of the flares with accompanying infrared emission are all above 3×10^{31} erg, corresponding to a flare frequency <0.1 hr^{-1}. Multiplying this emission time per flare by the flares per hour gives a duty cycle of $<4.6\%$, in agreement with our independent estimate. A duty cycle of 2.8%–4.6% represents an upper limit on detectable emission at this signal-to-noise and resolution, as our criterion requires only a small detection in the brightest line.

6.5 Atmospheric Structure

We used the static NLTE radiative transfer code RH (Uitenbroek 2001) to generate model spectra to compare with the emission lines observed in the UT 2009 October 27 flare on EV Lac. We calculated model spectra based on one-dimensional atmospheres, using a 20-level hydrogen atom, a 20-level calcium atom, and a 25-level helium atom. The multi-level atoms were required to generate the lines observed, while the simplification to a one-dimensional

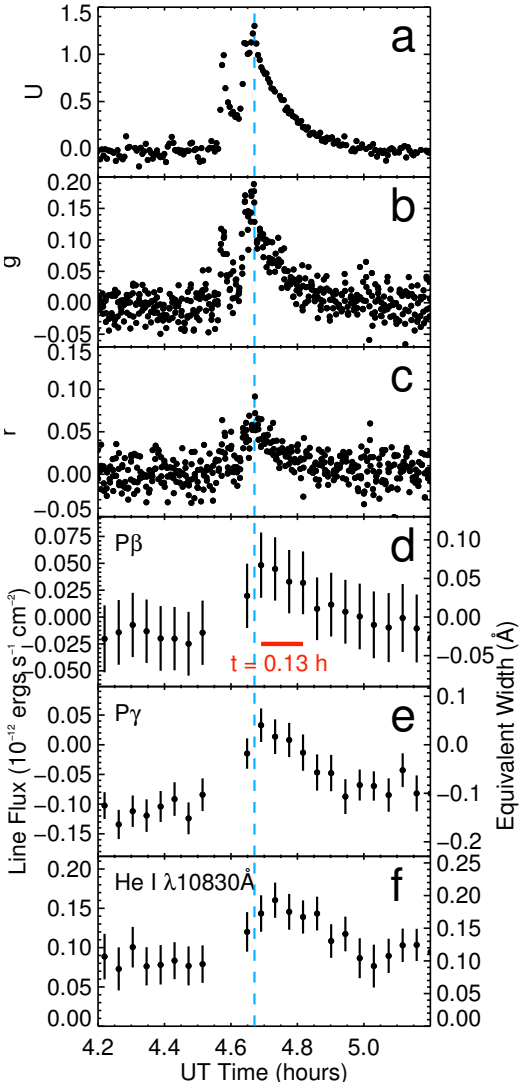

Figure 6.6 Data from the UT 2011 February 14 flare on YZ CMi. Panels (a), (b), and (c) show the change in U , g , and r bands during the flare, and panels (d), (e), and (f) show the flux (left axis) and EW (right axis) of the infrared emission lines detected during the flare. Panel (d) shows the time used as the flare duration in Table 6.1 (red line). The time of the peak u-band flux is shown in each panel (blue dashed line). the infrared emission line fluxes are averaged over 16 exposures of 4 s each. The total exposure time for each point is 64 s; the average cadence is 2.5 minutes. The gap in the infrared line data is due to standard star observation.

atmosphere allowed us to examine a larger range of chromospheric structures without the computationally intensive calculations required by a detailed treatment of flare physics (e.g., Allred et al. 2006).

For a starting atmosphere, we used a Nextgen photospheric model from a $T = 3200$ K solar metallicity dwarf (Hauschildt et al. 1999) and the corona of the pre-flare M dwarf atmosphere model of Allred et al. (2006). Similar to Hawley & Fisher (1992), Christian et al. (2003) and Fuhrmeister et al. (2010), we used chromospheres with a linear temperature rise in log column mass (log(col mass)) to connect the photosphere and corona. The linear temperature rise is a simplification of the actual chromospheric structure during a flare, but it is useful for an initial investigation of the temperatures required to generate emission lines at each atmospheric height. To produce a suite of model atmospheres, we varied the column mass of the transition region ($\log(\text{col mass})_{\rm TR}$), the column mass of the temperature minimum region ($\log(\text{col mass})_{T\rm min}$), and the temperature of the chromosphere at the bottom of the transition region ($T_{\rm TR}$). Figure 6.7 shows the temperature structure of a representative subset of the resulting atmospheres and illustrates the three quantities we varied.

Following Walkowicz (2008), we adopted our initial ranges for $T_{\rm TR}$, $\log(\text{col mass})_{\rm TR}$, and $\log(\text{col mass})_{T\rm min}$ from previous quiescent and flaring M dwarf chromosphere models (Hawley & Fisher 1992; Mauas & Falchi 1994; Houdebine & Stempels 1997; Short & Doyle 1998a; Walkowicz et al. 2008; Fuhrmeister et al. 2010). Table 6.3 shows the range of parameters adopted for each of these three quantities, which differ from previous parameter ranges only in $\rm T_{\mathit{TR}}$. Previous model atmospheres have relatively constant $\rm T_{TR} \sim 10{,}000$ K, but our initial models with a range of $T_{\rm TR} = 10{,}000$ K to 20,000 K underproduced Paschen emission relative to Balmer emission, and showed a trend of increasing Paschen emission with greater $T_{\rm TR}$. We increased the temperature of our hottest models to $T_{\rm TR} = 30{,}000$ K in order to generate relatively more Paschen emission. Although $T_{\rm TR}$ extends to hotter temperatures, it is consistent with results from the radiative-hydrodynamic simulations from Allred et al. (2006), which show that material at the base of the transition region can be heated up to $T = 10^6$ K.

Comparing the strengths of the modeled lines to each other provides strong constraints

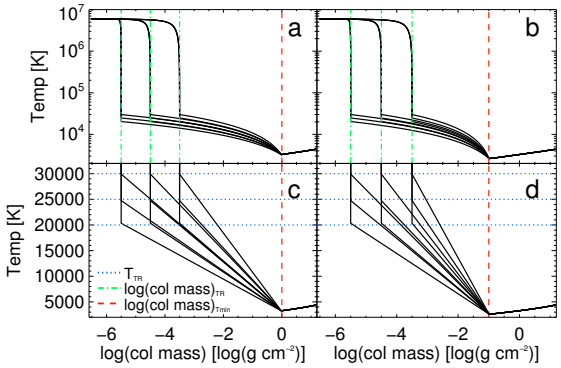

Figure 6.7 Atmospheric temperature structure as a function of log(col mass) for a subset of the atmospheres generated. Panels (a) and (b) show the entire atmosphere, while panels (c) and (d) focus on the chromosphere. The panels (a) and (c) show the models generated with a $\log(\text{col mass})_{T\text{min}} = 0$ and panels (b) and (d) show $\log(\text{col mass})_{T\text{min}} = -1$. Each panel shows nine models, with a range of $\log(\text{col mass})_{\text{TR}} = -3.5$ to -5.5 (blue dot-dashed lines) and a range of T_{TR} =20,000 K to 30,000 K (dotted green lines). Line fluxes ratios for the spectra generated from these models are shown in Figure 6.8.

Table 6.3. Model Atmosphere Parameters

Parameter	Range	Best
$\log(\text{col mass})_{\text{TR}}$	-5.5 to -3.5	-5.5 to -4.5
$\log(\text{col mass})_{T\text{min}}$	-3 to 0	0
T_{TR}	10,000 K to 30,000 K	25,000 K to 30,000 K
T_{min}	2229 K to 3264 K	3264 K

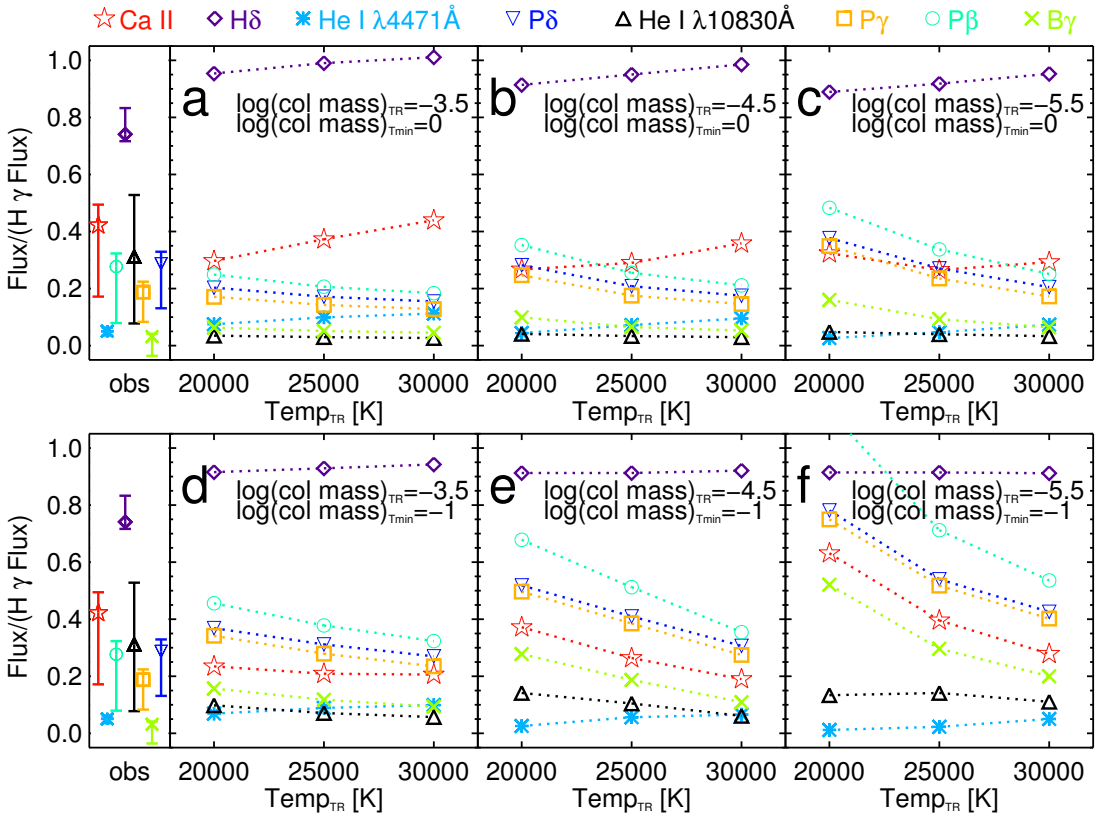

Figure 6.8 Line flux ratio to Hγ flux as a function of transition region temperature generated from the models shown in Figure 6.7. Each line flux ratio is shown in a different color and symbol, which is detailed at the top. The two rows show the line flux ratios from models with different log(col mass)$_{T\mathrm{min}}$. For comparison, the observed median and range of each line flux ratio are shown to the left of both rows. Each panel (a)–(f) shows models with a different log(col mass)$_{\mathrm{TR}}$ and three values of $\mathrm{T_{TR}}$. The dotted lines connecting the model line fluxes are shown only to clarify the positions of crowded points. The models that best represent the data are found in panels (a) and (b), with $\mathrm{T_{TR}}$ = 25,000 K and 30,000 K.

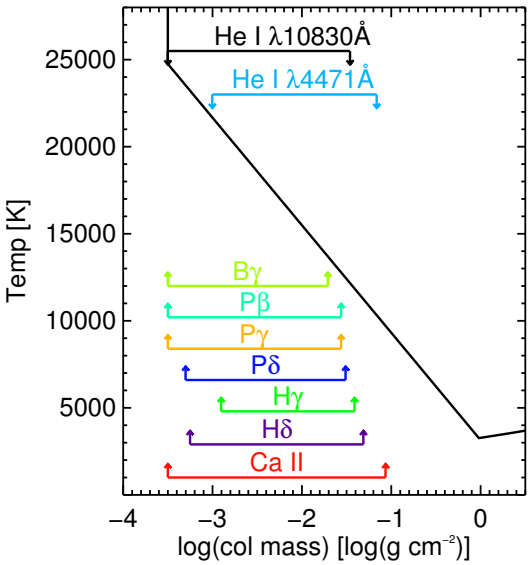

Figure 6.9 Atmospheric temperature structure as a function of log(col mass) for the best fit model ($\log(\text{col mass})_{T\text{min}} = 0$, $\log(\text{col mass})_{\text{TR}} = -3.5$, T_{TR} =25,000 K). The range of formation depth is shown for each of the emission lines; the lines are grouped by type and offset in Temperature for clarity.

on our suite of model atmospheres. The line flux ratios with respect to the Hγ line flux for the best models are shown compared to the median and range of observed line flux ratios in Figure 6.8. In general, a deeper T_{min} (at log(col mass) = 0 or -1), a deeper transition region (at log(col mass) = -3.5 or -4.5), and a hotter chromosphere (with T_{TR} = 25,000 K or 30,000 K) better reproduce the line flux ratios observed during the flare. The line formation regions (where the contribution function for each line is greater than 25% of its peak value) for one model are shown in Figure 6.9.

Most of the lines are produced over regions that include the outer portion of the chromosphere, at log(col mass) = -3.5 and T = 25,000 K. Hγ, the strongest emission line we observed, is formed over the smallest portion of the chromosphere, with its highest temperature at T = 20,000 K. He 1 λ4471 and He 1 λ10830 form over slightly different regions of the atmosphere, with He 1 λ10830 tracing slightly higher temperatures.

During the flare observations, the ratio of Hδ to Hγ is relatively constant. Hδ is slightly

overproduced in the models compared to observations, but is similar in each of the models. He 1 λ4471 emission is weak (with a ratio to Hγ of $\sim$ 0.1–0.3) in both the models and the observations. The ratios of the Paschen series lines and Brackett γ to each other are relatively constant throughout the flare, and those ratios are well produced in every atmospheric structure. The ratio of the Paschen lines and Brγ to Hγ, however, is matched only in the models with a log(col mass)$_{T\mathrm{min}} = 0$. Because these lines are sensitive to the hottest regions of the chromosphere, the advantage of the log(col mass)$_{T\mathrm{min}} = 0$ is likely an increased amount of material at temperatures near T = 20,000 K due to a shallower slope in the chromosphere.

The ratio of Ca 2 K to Hγ and to the other hydrogen series lines is best produced in the models with the deepest T_{min}, a deep transition region (log(col mass)$_{\mathrm{TR}} = -3.5$ or -4.5), and a hot T_{TR} = 25,000 K or 30,000 K. In all other models, Ca 2 K is underproduced relative to the Paschen series lines. As shown in Figure 6.9, the Ca 2 K emission in the best-fit model is formed over a larger range of log(col mass) than any other line. The production of Ca 2 K in a region that includes the upper chromosphere is unusual compared to previous results; typically, Ca 2 K emission during a flare is thought to last longer because it is a lower temperature line (Houdebine 2003; Crespo-Chacón et al. 2006). Our cooler atmospheres, where Ca 2 K emission is formed only in lower temperature regions, do not produce enough Ca 2 K emission relative to Paschen series emission to match our observations.

He 1 λ10830 is underproduced in nearly every model. During the flare, its observed ratio compared to Hγ increases from 0.1 to 0.5, while all our models show line flux ratios of 0.1 or less. This mismatch is apparently worse in one of the other two flares observed; as discussed in Section 6.4, He 1 λ10830 is stronger compared to Pβ and Pγ (the two other lines observed) in the UT 2010 November 27 flare on EV Lac. Simply raising the T_{TR} in our models produces too much Ca 2 K but no additional He 1 λ10830. In the Sun and similar stars, He 1 λ10830 emission is produced in the upper chromosphere during flares as a result of helium ionization via backwarming from coronal UV flux (Mauas et al. 2005; Sanz-Forcada & Dupree 2008). A similar process could be leading to the He 1 λ10830 emission during M dwarf flares, but the details of backwarming from coronal emission are not yet fully implemented in the RH atmosphere code.

While one-dimensional atmosphere models can match the line flux ratios of most of the lines as a sequence of static snapshots, they cannot reproduce the time evolution of the flare. In our observations, Ca 2 K, the Paschen lines, Brγ, and He 1 λ10380 Å all rise relative to Hγ during the decay phase of the flare. The best fitting models in our suite of atmospheres indicate that an increase in Ca 2 K is always coupled with a decrease of the Paschen and Brackett lines. The time evolution of flares may involve different atmospheric components covering the surface of the star with changing filling factors (e.g., Kowalski et al. 2010). It is possible that a linear combination of two or three different one-dimensional atmospheres with changing filling factors would reproduce the time-evolution of this flare.

6.6 Summary

During nearly 50 hr of simultaneous photometric and spectroscopic observations on 4 active M dwarfs, we saw 16 total flares, 3 of them with accompanying infrared emission lines. The strongest flare ($\Delta u = 4.02$) occurred on EV Lac on UT 2009 October 27. It showed emission from Hγ, Hδ, He 1 λ4471, Ca 2 K, Pβ, Pγ, Pδ, Brγ, and He 1 λ10830. A weaker flare (Δu = 1.68) on EV Lac on UT 2010 November 27 showed only emission from Pβ, Pγ, and He 1 λ10830. Remarkably, the He 1 λ10830 emission was twice as strong compared to Pβ and Pγ as it was in the $\Delta u = 4.02$ flare. The weakest flare with infrared emission ($\Delta U = 1.38$) occurred on YZ CMi on UT 2011 February 14; Pβ, Pγ, and He 1 λ10830 were just above their detection limits. We estimate a duty cycle of 2.8%–4.6% for observing the strongest infrared emission line (Pβ) during flares on active mid-M dwarfs. These observations confirm that flares are detectable in the infrared portion of M dwarf spectra, which is much brighter in quiescence than the bluer portions of M dwarf spectra which are typically used to detect flares.

Using a hotter chromosphere than previous one-dimensional static flare models (e.g., Christian et al. 2003; Fuhrmeister et al. 2010), the ratios of Ca 2 K, He 1 λ4471, Hδ, the Paschen lines, and Brγ to Hγ can be relatively well reproduced. The generation of Ca 2 K in the hot, upper portion of the atmosphere is distinct from previous results, and is necessary to produce more Ca 2 K than Paschen series emission, which is observed during our strongest flare. This result confirms that infrared emission is a useful constraint on the

atmospheric heating during M dwarf atmospheres.

The strength of emission from He 1 λ10830 is not predicted from our one-dimensional model, but including a detailed treatment of backwarming from the corona (e.g., Allred et al. 2006) may be warranted, based on solar results. Modeling He 1 λ10830 is also complicated by its different emission strengths compared to Pβ and Pγ in the two flares on EV Lac, but these differences show that He 1 λ10830 has potential to constrain different backwarming scenarios during a variety of flares. The time evolution of the largest flare is not reproduced by our one-dimensional models, but a combination of multiple models with different filling factors (e.g., Walkowicz 2008; Kowalski et al. 2010) or detailed radiative hydrodynamic modeling with non-thermal beam heating (e.g. Allred et al. 2006) may provide a better match to the flare emission.

Chapter 7

CONCLUSIONS

The goals of this dissertation were to: (a) use kinematics as a tool to understand the ages of stars and brown dwarfs and (b) explore the chromospheric temperature structure of M and L dwarfs using atomic emission lines. Each chapter described a distinct project with the ultimate aim of reaching these goals, and here I will attempt to synthesize the main results. In this chapter I will summarize the main points of each chapter, provide broad conclusions that span several of the chapters, and highlight some areas that are particularly ripe for additional work.

7.1 Summary

In Chapter 2, I presented a sample of L dwarfs spectroscopically selected from SDSS DR7. Using a combination of data from SDSS and 2MASS, I calculated three dimensional space velocities and examined a variety of L dwarf colors. Because this sample of L dwarfs was selected based on SDSS $i - z$ colors, I uncovered a bias in previous samples of L dwarfs towards objects with redder $J - K_S$ colors and discovered a nearby blue L dwarf within 10pc of the Sun. These data also indicated that early-L dwarfs are not dynamically distinct from disk stars, and an examination of L dwarf kinematics revealed both thin and thick disk components. The kinematics of the early-L dwarfs presented in this chapter did not reveal a young brown dwarf component included with the older disk stars.

The findings from the SDSS L dwarfs indicated that a complete sample of mid- to late-L dwarfs that were not observed by SDSS in large numbers, might show that kinematic signature we expect from young brown dwarfs. In Chapter 3, I described a project to obtain radial velocities for a volume-limited sample of L dwarfs. Over the course of 3 years and 23 half nights, I observed 116 L dwarfs with TripleSpec, a near infrared spectrograph at APO. These data proved difficult to reduce, and despite attempts with six different reduction

packages, the reduced spectra are not yet of sufficient quality for the measurement of radial velocities. The curved, tilted orders of the raw data have proven difficult to fit, and the poor fits to curvature and tilt interfere both with the wavelength solution and sky subtraction. I identify some areas where modifications are needed to Firehose to possibly produce sufficient quality spectra.

In Chapter 4, I described the BOSS Ultracool Dwarf Sample, which includes 12,085 late-M and L dwarfs from a combination of SDSS DR7 and BOSS data. I presented initial WISE colors for a large sample of late-M and early-L dwarfs; similar to colors using 2MASS JHK_S bands, the WISE colors of these dwarfs were not a strong function of spectral type. The combination of WISE, 2MASS, and SDSS data resulted in three epochs of astrometry that enabled the measurement of proper motions for the majority of the BUD sample. i combined these proper motions with radial velocities from SDSS spectra to calculate three dimensional kinematics. The velocity dispersions of the BUD sample show no significant variation as a function of spectral type, indicating a lack of young brown dwarfs in the sample. The correlations between activity and kinematics show that age/activity relationships extend to L spectral types.

The Hα detections in the BUD sample also proved ideal for exploring the chromospheres of ultracool dwarfs. Chapter 5 presented the activity strengths and fractions for late-M and L dwarfs. To place constraints on the chromospheres needed to produce the observed trends from those and other data, I simulated a range of chromospheric structures and filling factors using the NLTE radiative transfer code RH (Uitenbroek 2001). I found that the chromospheres of early-M dwarfs are much hotter and cover a larger fraction of the surface than those of late-M and L dwarfs.

In Chapter 6, I presented the first detection of infrared line emission during an M dwarf flare as part of a campaign to monitor active early- and mid-M dwarfs. The observing campaign resulted in a total of 16 flares found from 50 hours of observing, with emission in He I 10830Å and Paschen series lines observed during the three largest flares. Using RH, I modeled the atmosphere of EV Lac during the strongest flare. Based on the ratios of Paschen to Balmer lines, I found that a very hot chromosphere is needed to reproduce the ratios of the infrared line strengths to Ca II emission in the optical.

7.2 Concluding Themes

SDSS data are an important resource for discovery and analysis of late-M and L dwarfs. The SDSS $i-z$ color is better correlated with spectral type than the 2MASS $J-K_S$ color, resulting in a less biased color selection. The large number of spectra taken as a part of SDSS are essential to a complete sample of L dwarfs, as the large number of spectra taken don't require strict color cuts to exclude late-M dwarfs.

The dispersions presented in both Chapter 2 and Chapter 4 are evidence that late-M dwarfs and early-L dwarfs are dynamically indistinct populations; young brown dwarfs are not sufficiently numerous to dominate the kinematics of L0-L3 dwarfs. The effect may become more important for mid-L dwarfs, where the expected numbers of brown dwarfs are larger.

The age activity relationship that holds for early- and mid- M dwarfs (and is an adaptation of that of solar-type stars) appears to extend certainly to the end of the M spectral class (M7-M9) and may extend to L spectral types as well. Activity is very common in L dwarfs, with the activity fraction presented in Chapter 5 showing they are perhaps more frequently active than late-M dwarfs. This high fraction is consistent with evidence of strong magnetic fields in ultracool dwarfs. Hα emission on L dwarfs is weak, however, and produced by a cool, compact chromosphere.

The temperature structure needed to produce Paschen series emission observed during flares is much hotter than that needed to produce Hα. This does not bode well for attempts to observe Paschen emission from quiescent late-M and L dwarfs. No infrared emission lines were found during the observations for Chapter 3, indicating that the Paschen emission is weak or not present for dwarfs in quiescence.

The observed duty cycle for infrared line emission ($\sim$3%) in active early- to mid-M dwarfs is not very high, but the lines did prove useful for constraining the chromospheric temperature structure. While there are many lines in the optical and ultraviolet that provide similarly strong constraints, the infrared lines provide a complementary set of constrains and have the advantage of being relatively easy to observe due to the brightness of cool and ultracool dwarfs in the infrared.

7.3 Additional Areas for Exploration

The most pressing question not addressed in this dissertation concerns the kinematics of mid- to late-L dwarfs. Do they show a bias towards younger brown dwarfs? Or are the velocities of these young objects simply not a significant contribution to the kinematics of the entire population? Additional observations, including perhaps the successful reduction of the spectra presented in Chapter 3, are needed to address these questions.

The characteristics of Hα on mid- and late-L dwarfs is another area that should be addressed with future observations. Does weak activity exist on most of these dwarfs, or is the coupling between the magnetic field and the atmosphere entirely quenched? If there is Hα emission, indicating the presence of a chromosphere, on late-L dwarfs, is there a spectral type past which the atmosphere is too cool to sustain a chromosphere?

This dissertation presented the assembly and some initial results for the BUD sample, but there are many other properties to analyze and results to examine. The correlation between age and $J - K_S$ color presented in Chapter 2 has not yet been explored in late-M dwarfs, and other colors may have similar correlations. Additionally, the sample should be investigated for young moving group members, old halo stars, and common-proper motion binaries.

The bias in many of the known L dwarfs towards bluer objects and the discovery of the peculiarly blue L dwarf within SDSS indicates that the current luminosity function of L dwarfs underestimates the true density of these objects by $\sim$5%, but the effect could be larger. As the BUD sample is expanded through BOSS observations during the next two and a half years, it will become an excellent sample for determination of the luminosity function of L dwarfs.

BIBLIOGRAPHY

Abazajian, K., et al. 2003, AJ, 126, 2081

—. 2004, AJ, 128, 502

Abazajian, K. N., et al. 2009, ApJS, 182, 543

Adelman-McCarthy, J. K., et al. 2007, ApJS, 172, 634

Aihara, H., et al. 2011, ApJS, 193, 29

Allard, F. 1998, in Astronomical Society of the Pacific Conference Series, Vol. 134, Brown Dwarfs and Extrasolar Planets, ed. R. Rebolo, E. L. Martin, & M. R. Zapatero Osorio, 370

Allard, F., Hauschildt, P. H., Alexander, D. R., Tamanai, A., & Schweitzer, A. 2001, ApJ, 556, 357

Allard, F., Homeier, D., & Freytag, B. 2011, in Astronomical Society of the Pacific Conference Series, Vol. 448, Astronomical Society of the Pacific Conference Series, ed. C. Johns-Krull, M. K. Browning, & A. A. West, 91

Allers, K. N., et al. 2007, ApJ, 657, 511

Allred, J. C., Hawley, S. L., Abbett, W. P., & Carlsson, M. 2006, ApJ, 644, 484

Audard, M., Osten, R. A., Brown, A., Briggs, K. R., Güdel, M., Hodges-Kluck, E., & Gizis, J. E. 2007, A&A, 471, L63

Aumer, M., & Binney, J. J. 2009, MNRAS, 397, 1286

Ayres, T. R. 1981, ApJ, 244, 1064

Bailer-Jones, C. A. L. 2004, A&A, 419, 703

Bannister, N. P., & Jameson, R. F. 2007, MNRAS, 378, L24

Bary, J. S., Matt, S. P., Skrutskie, M. F., Wilson, J. C., Peterson, D. E., & Nelson, M. J. 2008, ApJ, 687, 376

Basri, G., Mohanty, S., Allard, F., Hauschildt, P. H., Delfosse, X., Martín, E. L., Forveille, T., & Goldman, B. 2000, ApJ, 538, 363

Becklin, E. E., & Zuckerman, B. 1988, Nature, 336, 656

Berger, E., et al. 2009, ApJ, 695, 310

—. 2010, ApJ, 709, 332

Bessell, M. S. 1991, AJ, 101, 662

Bidelman, W. P. 1954, ApJS, 1, 175

Bihain, G., Rebolo, R., Béjar, V. J. S., Caballero, J. A., Bailer-Jones, C. A. L., Mundt, R., Acosta-Pulido, J. A., & Manchado Torres, A. 2006, A&A, 458, 805

Blake, C. H., Charbonneau, D., & White, R. J. 2010, ApJ, 723, 684

Blake, C. H., Charbonneau, D., White, R. J., Marley, M. S., & Saumon, D. 2007, ApJ, 666, 1198

Bochanski, J. J., Hawley, S. L., & West, A. A. 2011, AJ, 141, 98

Bochanski, J. J., Munn, J. A., Hawley, S. L., West, A. A., Covey, K. R., & Schneider, D. P. 2007a, AJ, 134, 2418

Bochanski, J. J., West, A. A., Hawley, S. L., & Covey, K. R. 2007b, AJ, 133, 531

Bochanski, J. J., et al. 2009, PASP, 121, 1409

Boeshaar, P. C. 1976, PhD thesis, Ohio State University, Columbus.

Bopp, B. W., & Moffett, T. J. 1973, ApJ, 185, 239

Bowler, B. P., Liu, M. C., & Dupuy, T. J. 2010, ApJ, 710, 45

Box, G. E. P., & Muller, M. E. 1958, Annals of Mathematical Statistics, 29, 610

Browning, M. K. 2008, ApJ, 676, 1262

Burgasser, A. J. 2004, ApJ, 614, L73

Burgasser, A. J., Geballe, T. R., Leggett, S. K., Kirkpatrick, J. D., & Golimowski, D. A. 2006, ApJ, 637, 1067

Burgasser, A. J., Kirkpatrick, J. D., Liebert, J., & Burrows, A. 2003a, ApJ, 594, 510

Burgasser, A. J., Liebert, J., Kirkpatrick, J. D., & Gizis, J. E. 2002a, AJ, 123, 2744

Burgasser, A. J., Looper, D. L., Kirkpatrick, J. D., Cruz, K. L., & Swift, B. J. 2008, ApJ, 674, 451

Burgasser, A. J., Sitarski, B. N., Gelino, C. R., Logsdon, S. E., & Perrin, M. D. 2011, ApJ, 739, 49

Burgasser, A. J., Witte, S., Helling, C., Sanderson, R. E., Bochanski, J. J., & Hauschildt, P. H. 2009, ApJ, 697, 148

Burgasser, A. J., et al. 2002b, ApJ, 564, 421

—. 2003b, ApJ, 592, 1186

Burrows, A., Hubbard, W. B., Lunine, J. I., & Liebert, J. 2001, Reviews of Modern Physics, 73, 719

Burrows, A., Hubbard, W. B., Saumon, D., & Lunine, J. I. 1993, ApJ, 406, 158

Burrows, A., Sudarsky, D., & Hubeny, I. 2006, ApJ, 640, 1063

Burrows, A., et al. 1997, ApJ, 491, 856

Cannon, A. J., & Pickering, E. C. 1924, Henry Draper (HD) catalog and HD extension

Casagrande, L., Flynn, C., & Bessell, M. 2008, MNRAS, 389, 585

Castro, P. J., & Gizis, J. E. 2012, ApJ, 746, 3

Chabrier, G., & Baraffe, I. 1997, A&A, 327, 1039

—. 2000, ARA&A, 38, 337

Chabrier, G., & Küker, M. 2006, A&A, 446, 1027

Chiu, K., Fan, X., Leggett, S. K., Golimowski, D. A., Zheng, W., Geballe, T. R., Schneider, D. P., & Brinkmann, J. 2006, AJ, 131, 2722

Christian, D. J., Mathioudakis, M., Jevremović, D., Dupuis, J., Vennes, S., & Kawka, A. 2003, ApJ, 593, L105

Cohen, M., Wheaton, W. A., & Megeath, S. T. 2003, AJ, 126, 1090

Covey, K. R., et al. 2007, AJ, 134, 2398

Cram, L. E., & Giampapa, M. S. 1987, ApJ, 323, 316

Cram, L. E., & Woods, D. T. 1982, ApJ, 257, 269

Crespo-Chacón, I., Montes, D., García-Alvarez, D., Fernández-Figueroa, M. J., López-Santiago, J., & Foing, B. H. 2006, A&A, 452, 987

Cruz, K. L., Kirkpatrick, J. D., & Burgasser, A. J. 2009, AJ, 137, 3345

Cruz, K. L., Reid, I. N., Liebert, J., Kirkpatrick, J. D., & Lowrance, P. J. 2003, AJ, 126, 2421

Cruz, K. L., et al. 2007, AJ, 133, 439

Cuddeford, P., & Binney, J. 1994, MNRAS, 266, 273

Cushing, M. C., Looper, D., Burgasser, A. J., Kirkpatrick, J. D., Faherty, J., Cruz, K. L., Sweet, A., & Sanderson, R. E. 2009, ApJ, 696, 986

Cushing, M. C., Rayner, J. T., & Vacca, W. D. 2005, ApJ, 623, 1115

Cushing, M. C., Saumon, D., & Marley, M. S. 2010, AJ, 140, 1428

Cushing, M. C., Vacca, W. D., & Rayner, J. T. 2004, PASP, 116, 362

Cushing, M. C., et al. 2006, ApJ, 648, 614

—. 2011, ApJ, 743, 50

Cutri, R. M., et al. 2003, 2MASS All Sky Catalog of point sources., ed. Cutri, R. M., Skrutskie, M. F., van Dyk, S., Beichman, C. A., Carpenter, J. M., Chester, T., Cambresy, L., Evans, T., Fowler, J., Gizis, J., Howard, E., Huchra, J., Jarrett, T., Kopan, E. L., Kirkpatrick, J. D., Light, R. M., Marsh, K. A., McCallon, H., Schneider, S., Stiening, R., Sykes, M., Weinberg, M., Wheaton, W. A., Wheelock, S., & Zacarias, N.

Dahn, C. C., et al. 2002, AJ, 124, 1170

Davenport, J. R. A. 2012, in prep.

Davenport, J. R. A., Becker, A. C., Kowalski, A. F., Hawley, S. L., Schmidt, S. J., Hilton, E. J., Sesar, B., & Cutri, R. 2012, ApJ, 748, 58

Dawson, P. C. 1981, AJ, 86, 1200

Dehnen, W., & Binney, J. J. 1998, MNRAS, 298, 387

Delfosse, X., et al. 1997, A&A, 327, L25

Donati, G. B. 1863, MNRAS, 23, 100

Donati, J.-F., Forveille, T., Collier Cameron, A., Barnes, J. R., Delfosse, X., Jardine, M. M., & Valenti, J. A. 2006, Science, 311, 633

Donati, J.-F., & Landstreet, J. D. 2009, ARA&A, 47, 333

Donati, J.-F., et al. 2008, MNRAS, 390, 545

Efron, B. 1982, The Jackknife, the Bootstrap and other resampling plans

Eggen, O. J., Lynden-Bell, D., & Sandage, A. R. 1962, ApJ, 136, 748

Eisenstein, D. J., et al. 2011, AJ, 142, 72

Epchtein, N., et al. 1994, Ap&SS, 217, 3

Faherty, J. K., Burgasser, A. J., Cruz, K. L., Shara, M. M., Walter, F. M., & Gelino, C. R. 2009, AJ, 137, 1

Faherty, J. K., Burgasser, A. J., West, A. A., Bochanski, J. J., Cruz, K. L., Shara, M. M., & Walter, F. M. 2010, AJ, 139, 176

Faherty, J. K., et al. 2012, ArXiv e-prints

Fan, X., et al. 2000, AJ, 119, 928

Fleming, T. A., Giampapa, M. S., Schmitt, J. H. M. M., & Bookbinder, J. A. 1993, ApJ, 410, 387

Folkes, S. L., Pinfield, D. J., Kendall, T. R., & Jones, H. R. A. 2007, MNRAS, 378, 901

Fraunhofer, J. 1823, The Edinburgh Philosophical Journal, 9, 288

—. 1824, The Edinburgh Philosophical Journal, 10, 26

Fuhrmeister, B., Liefke, C., Schmitt, J. H. M. M., & Reiners, A. 2008, A&A, 487, 293

Fuhrmeister, B., Schmitt, J. H. M. M., & Hauschildt, P. H. 2005, A&A, 439, 1137

—. 2010, A&A, 511, A83+

Fukugita, M., Ichikawa, T., Gunn, J. E., Doi, M., Shimasaku, K., & Schneider, D. P. 1996, AJ, 111, 1748

Geballe, T. R., et al. 2002, ApJ, 564, 466

Gilmore, G., & Reid, N. 1983, MNRAS, 202, 1025

Gizis, J. E. 2002, ApJ, 575, 484

Gizis, J. E., Monet, D. G., Reid, I. N., Kirkpatrick, J. D., Liebert, J., & Williams, R. J. 2000, AJ, 120, 1085

Gizis, J. E., Reid, I. N., & Hawley, S. L. 2002, AJ, 123, 3356

Gliese, W. 1958, ZAp, 45, 293

Gliese, W., & Jahreiß, H. 1991, Preliminary Version of the Third Catalogue of Nearby Stars, Tech. rep.

Golimowski, D. A., et al. 2004, AJ, 127, 3516

Gordon, K. C., & Kron, G. E. 1949, PASP, 61, 210

Gunn, J. E., et al. 1998, AJ, 116, 3040

Hale, G. E. 1908, ApJ, 28, 315

—. 1909, PASP, 21, 205

Hall, P. B. 2002, ApJ, 564, L89

Hallinan, G., Antonova, A., Doyle, J. G., Bourke, S., Lane, C., & Golden, A. 2008, ApJ, 684, 644

Hauschildt, P. H., Allard, F., & Baron, E. 1999, ApJ, 512, 377

Hawley, S. L., & Fisher, G. H. 1992, ApJS, 78, 565

Hawley, S. L., Gizis, J. E., & Reid, I. N. 1996, AJ, 112, 2799

Hawley, S. L., & Pettersen, B. R. 1991, ApJ, 378, 725

Hawley, S. L., Walkowicz, L. M., Allred, J. C., & Valenti, J. A. 2007, PASP, 119, 67

Hawley, S. L., et al. 1995, ApJ, 453, 464

—. 2002, AJ, 123, 3409

—. 2003, ApJ, 597, 535

Helling, C., Dehn, M., Woitke, P., & Hauschildt, P. H. 2008, ApJ, 675, L105

Helling, C., Jardine, M., & Mokler, F. 2011a, ApJ, 737, 38

Helling, C., Jardine, M., Witte, S., & Diver, D. A. 2011b, ApJ, 727, 4

Henry, T. J., Jao, W.-C., Subasavage, J. P., Beaulieu, T. D., Ianna, P. A., Costa, E., & Méndez, R. A. 2006, AJ, 132, 2360

Hertzsprung, E. 1907, Astronomische Nachrichten, 176, 49

Hilton, E. J. 2011, PhD thesis, University of Washington

Hogg, D. W., Finkbeiner, D. P., Schlegel, D. J., & Gunn, J. E. 2001, AJ, 122, 2129

Holtzman, J. A., Harrison, T. E., & Coughlin, J. L. 2010, Advances in Astronomy, 2010

Houdebine, E. R. 2003, A&A, 397, 1019

Houdebine, E. R., Junghans, K., Heanue, M. C., & Andrews, A. D. 2009, A&A, 503, 929

Houdebine, E. R., & Stempels, H. C. 1997, A&A, 326, 1143

Ishida, K., Ichimura, K., Shimizu, Y., & Mahasenaputra. 1991, Ap&SS, 182, 227

Ivezić, Ž., et al. 2004, Astronomische Nachrichten, 325, 583

Jameson, R. F., Casewell, S. L., Bannister, N. P., Lodieu, N., Keresztes, K., Dobbie, P. D., & Hodgkin, S. T. 2008a, MNRAS, 384, 1399

Jameson, R. F., Lodieu, N., Casewell, S. L., Bannister, N. P., & Dobbie, P. D. 2008b, MNRAS, 385, 1771

Johns-Krull, C. M., & Valenti, J. A. 1996, ApJ, 459, L95

Johnson, D. R. H., & Soderblom, D. R. 1987, AJ, 93, 864

Johnson, H. M. 1983, ApJ, 273, 702

Jones, D. O., West, A. A., & Foster, J. B. 2011, AJ, 142, 44

Kalberla, P. M. W., & Kerp, J. 2009, ARA&A, 47, 27

Kelson, D. D. 2003, PASP, 115, 688

Kendall, T. R., Delfosse, X., Martín, E. L., & Forveille, T. 2004, A&A, 416, L17

Kendall, T. R., et al. 2007, A&A, 466, 1059

Kiraga, M., & Stepien, K. 2007, Acta Astron., 57, 149

Kirkpatrick, J. D., Henry, T. J., & Irwin, M. J. 1997, AJ, 113, 1421

Kirkpatrick, J. D., Henry, T. J., & McCarthy, Jr., D. W. 1991, ApJS, 77, 417

Kirkpatrick, J. D., et al. 1999, ApJ, 519, 802

—. 2000, AJ, 120, 447

—. 2008, ApJ, 689, 1295

—. 2010, ApJS, 190, 100

—. 2011, ArXiv e-prints

Knapp, G. R., et al. 2004, AJ, 127, 3553

Kowalski, A. F., Hawley, S. L., Hilton, E. J., Becker, A. C., West, A. A., Bochanski, J. J., & Sesar, B. 2009, AJ, 138, 633

Kowalski, A. F., Hawley, S. L., Holtzman, J. A., Wisniewski, J. P., & Hilton, E. J. 2010, ApJ, 714, L98

Kraus, A. L., & Hillenbrand, L. A. 2007, AJ, 134, 2340

Kraus, A. L., Tucker, R. A., Thompson, M. I., Craine, E. R., & Hillenbrand, L. A. 2011, ApJ, 728, 48

Kron, G. E. 1950, Leaflet of the Astronomical Society of the Pacific, 6, 52

Küker, M., & Rüdiger, G. 1999, A&A, 346, 922

Lacy, C. H., Moffett, T. J., & Evans, D. S. 1976, ApJS, 30, 85

Leggett, S. K. 1992, ApJS, 82, 351

Leggett, S. K., Allard, F., Geballe, T. R., Hauschildt, P. H., & Schweitzer, A. 2001, ApJ, 548, 908

Lépine, S., Rich, R. M., & Shara, M. M. 2007, ApJ, 669, 1235

Levenberg, K. 1944, The Quarterly Applied Mathematics, 2, 164

Liebert, J., & Burgasser, A. J. 2007, ApJ, 655, 522

Liebert, J., Kirkpatrick, J. D., Cruz, K. L., Reid, I. N., Burgasser, A., Tinney, C. G., & Gizis, J. E. 2003, AJ, 125, 343

Liebert, J., Kirkpatrick, J. D., Reid, I. N., & Fisher, M. D. 1999, ApJ, 519, 345

Lin, R. P., & Hudson, H. S. 1976, Sol. Phys., 50, 153

Lindblad, B. 1925, ApJ, 62, 191

Lippincott, S. L. 1952, ApJ, 115, 582

Lodders, K., & Fegley, Jr., B. 2006, Chemistry of Low Mass Substellar Objects, ed. J. W. Mason (Springer Verlag), 1

Lodge, O. 1909, Nature, 81, 425

Loebman, S. R., Roškar, R., Debattista, V. P., Ivezić, Ž., Quinn, T. R., & Wadsley, J. 2011, ApJ, 737, 8

Looper, D. L., Kirkpatrick, J. D., & Burgasser, A. J. 2007, AJ, 134, 1162

Looper, D. L., et al. 2008, ApJ, 686, 528

López-Morales, M. 2007, ApJ, 660, 732

Lutz, T. E., & Upgren, A. R. 1980, AJ, 85, 1390

Luyten, W. J. 1949, PASP, 61, 179

Marley, M. S., Saumon, D., & Goldblatt, C. 2010, ApJ, 723, L117

Marley, M. S., Seager, S., Saumon, D., Lodders, K., Ackerman, A. S., Freedman, R. S., & Fan, X. 2002, ApJ, 568, 335

Marquardt, D. 1963, SIAM Journal on Applied Mathematics, 11, 431

Martín, E. L., Delfosse, X., Basri, G., Goldman, B., Forveille, T., & Zapatero Osorio, M. R. 1999, AJ, 118, 2466

Mauas, P. J. D., Andretta, V., Falchi, A., Falciani, R., Teriaca, L., & Cauzzi, G. 2005, ApJ, 619, 604

Mauas, P. J. D., & Falchi, A. 1994, A&A, 281, 129

Mavridis, L. N., & Avgoloupis, S. 1987, A&A, 188, 95

McLean, I. S., Prato, L., McGovern, M. R., Burgasser, A. J., Kirkpatrick, J. D., Rice, E. L., & Kim, S. S. 2007, ApJ, 658, 1217

McLean, I. S., et al. 1998, in Society of Photo-Optical Instrumentation Engineers (SPIE) Conference Series, Vol. 3354, Society of Photo-Optical Instrumentation Engineers (SPIE) Conference Series, ed. A. M. Fowler, 566–578

McLean, M., Berger, E., & Reiners, A. 2012, ApJ, 746, 23

Mestel, L. 1968, MNRAS, 138, 359

Metchev, S. A., Kirkpatrick, J. D., Berriman, G. B., & Looper, D. 2008, ApJ, 676, 1281

Mohanty, S., & Basri, G. 2003, ApJ, 583, 451

Mohanty, S., Basri, G., Shu, F., Allard, F., & Chabrier, G. 2002, ApJ, 571, 469

Monet, D. G., Dahn, C. C., Vrba, F. J., Harris, H. C., Pier, J. R., Luginbuhl, C. B., & Ables, H. D. 1992, AJ, 103, 638

Morgan, W. W., Keenan, P. C., & Kellman, E. 1943, An atlas of stellar spectra, with an outline of spectral classification, ed. Morgan, W. W., Keenan, P. C., & Kellman, E.

Morin, J., Donati, J.-F., Petit, P., Delfosse, X., Forveille, T., & Jardine, M. M. 2010, MNRAS, 407, 2269

Morin, J., et al. 2008, MNRAS, 390, 567

Mukai, K. 1990, PASP, 102, 183

Munn, J. A., et al. 2004, AJ, 127, 3034

Nakajima, T., Oppenheimer, B. R., Kulkarni, S. R., Golimowski, D. A., Matthews, K., & Durrance, S. T. 1995, Nature, 378, 463

Newton, I. 1672, Philosophical Transactions of the Royal Society, 3075

Oppenheimer, B. R., Kulkarni, S. R., Matthews, K., & Nakajima, T. 1995, Science, 270, 1478

Osten, R. A., & Bastian, T. S. 2008, ApJ, 674, 1078

Osten, R. A., Hawley, S. L., Allred, J. C., Johns-Krull, C. M., & Roark, C. 2005, ApJ, 621, 398

Osten, R. A., et al. 2010, ApJ, 721, 785

Paletou, F. 1995, A&A, 302, 587

Parker, E. N. 1955, ApJ, 122, 293

Pesch, P. 1972, ApJ, 177, 519

Petit, M. 1961, Journal des Observateurs, 44, 11

Pier, J. R., Munn, J. A., Hindsley, R. B., Hennessy, G. S., Kent, S. M., Lupton, R. H., & Ivezić, Ž. 2003, AJ, 125, 1559

Pineda, J. S. 2012, in prep.

Probst, R. G., & Liebert, J. 1984, Scientific American, 251, 68

Ratnatunga, K. U., & Upgren, A. R. 1997, ApJ, 476, 811

Rayner, J. T., Toomey, D. W., Onaka, P. M., Denault, A. J., Stahlberger, W. E., Vacca, W. D., Cushing, M. C., & Wang, S. 2003, PASP, 115, 362

Rebassa-Mansergas, A., Gänsicke, B. T., Schreiber, M. R., Koester, D., & Rodríguez-Gil, P. 2010, MNRAS, 402, 620

Reid, I. N., Cruz, K. L., Kirkpatrick, J. D., Allen, P. R., Mungall, F., Liebert, J., Lowrance, P., & Sweet, A. 2008, AJ, 136, 1290

Reid, I. N., Gizis, J. E., & Hawley, S. L. 2002, AJ, 124, 2721

Reid, I. N., Hawley, S. L., & Gizis, J. E. 1995, AJ, 110, 1838

Reid, I. N., Kirkpatrick, J. D., Gizis, J. E., Dahn, C. C., Monet, D. G., Williams, R. J., Liebert, J., & Burgasser, A. J. 2000, AJ, 119, 369

Reiners, A., & Basri, G. 2006, AJ, 131, 1806

—. 2007, ApJ, 656, 1121

—. 2008, ApJ, 684, 1390

—. 2010, ApJ, 710, 924

Reiners, A., Joshi, N., & Goldman, B. 2012, AJ, 143, 93

Reiners, A., Seifahrt, A., Käufl, H. U., Siebenmorgen, R., & Smette, A. 2007, A&A, 471, L5

Robin, A. C., Reylé, C., Derrière, S., & Picaud, S. 2003, A&A, 409, 523

Robinson, R. D., Cram, L. E., & Giampapa, M. S. 1990, ApJS, 74, 891

Robinson, R. D., et al. 2005, ApJ, 633, 447

Robinson, Jr., R. D. 1980, ApJ, 239, 961

Ross, N. P., et al. 2011, ArXiv e-prints

Ruiz, M. T., Leggett, S. K., & Allard, F. 1997, ApJ, 491, L107

Russell, H. N. 1913, The Observatory, 36, 324

Rutherfurd, L. M. 1863, The American Journal of Science and Arts, 35, 71

Rybicki, G. B., & Hummer, D. G. 1991, A&A, 245, 171

Saar, S. H. 1988, ApJ, 324, 441

Saar, S. H., & Linsky, J. L. 1985, ApJ, 299, L47

Sanz-Forcada, J., & Dupree, A. K. 2008, A&A, 488, 715

Scalo, J., et al. 2007, Astrobiology, 7, 85

Schlegel, D. J., Finkbeiner, D. P., & Davis, M. 1998, ApJ, 500, 525

Schmidt, S. J. 2012, in prep.

Schmidt, S. J., Cruz, K. L., Bongiorno, B. J., Liebert, J., & Reid, I. N. 2007, AJ, 133, 2258

Schmidt, S. J., Kowalski, A. F., Hawley, S. L., Hilton, E. J., Wisniewski, J. P., & Tofflemire, B. M. 2011, ArXiv e-prints

Schmidt, S. J., West, A. A., Burgasser, A. J., Bochanski, J. J., & Hawley, S. L. 2010a, AJ, 139, 1045

Schmidt, S. J., West, A. A., Hawley, S. L., & Pineda, J. S. 2010b, AJ, 139, 1808

Schneider, D. P., et al. 2002, AJ, 123, 458

—. 2010, AJ, 139, 2360

Scholz, R.-D., Storm, J., Knapp, G. R., & Zinnecker, H. 2009, A&A, 494, 949

Secchi, A. 1867, Catalogo delle stelle DI cui SI E determinato lo spettro luminoso all' Osservatorio del Collegio romano

Seifahrt, A., Guenther, E., & Neuhäuser, R. 2005, A&A, 440, 967

Seifahrt, A., Reiners, A., Almaghrbi, K. A. M., & Basri, G. 2010, A&A, 512, A37

Sellwood, J. A., & Binney, J. J. 2002, MNRAS, 336, 785

Shapley, H. 1954, AJ, 59, 118

Sheppard, S. S., & Cushing, M. C. 2009, AJ, 137, 304

Short, C. I., & Doyle, J. G. 1998a, A&A, 336, 613

—. 1998b, A&A, 331, L5

Silvestri, N. M., et al. 2007, AJ, 134, 741

Simcoe, R. A., et al. 2010, in Society of Photo-Optical Instrumentation Engineers (SPIE) Conference Series, Vol. 7735, Society of Photo-Optical Instrumentation Engineers (SPIE) Conference Series

Sivarani, T., Lépine, S., Kembhavi, A. K., & Gupchup, J. 2009, ApJ, 694, L140

Skrutskie, M. F., et al. 2006, AJ, 131, 1163

Skumanich, A. 1972, ApJ, 171, 565

Smith, J. A., et al. 2002, AJ, 123, 2121

Smolčić, V., et al. 2004, ApJ, 615, L141

Spitzer, Jr., L., & Schwarzschild, M. 1951, ApJ, 114, 385

Staller, R. F. A. 1975, A&A, 42, 155

Stauffer, J. R., & Hartmann, L. W. 1986, ApJS, 61, 531

Stelzer, B., Schmitt, J. H. M. M., Micela, G., & Liefke, C. 2006, A&A, 460, L35

Stepanov, A. V., Kliem, B., Zaitsev, V. V., Fürst, E., Jessner, A., Krüger, A., Hildebrandt, J., & Schmitt, J. H. M. M. 2001, A&A, 374, 1072

Stephens, D. C., et al. 2009, ApJ, 702, 154

Stoughton, C., et al. 2002, AJ, 123, 485

Strömberg, G. 1922, ApJ, 56, 265

Tarter, J. C., et al. 2007, Astrobiology, 7, 30

Tinney, C. G., Delfosse, X., & Forveille, T. 1997, ApJ, 490, L95

Tinney, C. G., Reid, I. N., Gizis, J., & Mould, J. R. 1995, AJ, 110, 3014

Tofflemire, B. M., Wisniewski, J. P., Kowalski, A. F., Schmidt, S. J., Kundurthy, P., Hilton, E. J., Holtzman, J. A., & Hawley, S. L. 2012, AJ, 143, 12

Tsuji, T., Ohnaka, K., & Aoki, W. 1996a, A&A, 305, L1

Tsuji, T., Ohnaka, K., Aoki, W., & Nakajima, T. 1996b, A&A, 308, L29

Tucker, D. L., et al. 2006, Astronomische Nachrichten, 327, 821

Uitenbroek, H. 2001, ApJ, 557, 389

Upgren, A. R. 1978, AJ, 83, 626

Vacca, W. D., Cushing, M. C., & Rayner, J. T. 2003, PASP, 115, 389

Vacca, W. D., & Sandell, G. 2011, ApJ, 732, 8

Valenti, J. A., & Johns-Krull, C. 2001, in Astronomical Society of the Pacific Conference Series, Vol. 248, Magnetic Fields Across the Hertzsprung-Russell Diagram, ed. G. Mathys, S. K. Solanki, & D. T. Wickramasinghe, 179

van Dokkum, P. G. 2001, PASP, 113, 1420

Vernazza, J. E., Avrett, E. H., & Loeser, R. 1981, ApJS, 45, 635

Vernet, J., et al. 2011, A&A, 536, A105

Vrba, F. J., et al. 2004, AJ, 127, 2948

Walkowicz, L. M. 2008, PhD thesis, University of Washington

Walkowicz, L. M., & Hawley, S. L. 2009, AJ, 137, 3297

Walkowicz, L. M., Hawley, S. L., & West, A. A. 2004, PASP, 116, 1105

Walkowicz, L. M., Johns-Krull, C. M., & Hawley, S. L. 2008, ApJ, 677, 593

Walkowicz, L. M., et al. 2011, AJ, 141, 50

Weistrop, D. 1975, AJ, 80, 303

West, A. A., & Basri, G. 2009, ApJ, 693, 1283

West, A. A., Bochanski, J. J., Hawley, S. L., Cruz, K. L., Covey, K. R., Silvestri, N. M., Reid, I. N., & Liebert, J. 2006, AJ, 132, 2507

West, A. A., & Hawley, S. L. 2008, PASP, 120, 1161

West, A. A., Hawley, S. L., Bochanski, J. J., Covey, K. R., Reid, I. N., Dhital, S., Hilton, E. J., & Masuda, M. 2008, AJ, 135, 785

West, A. A., et al. 2004, AJ, 128, 426

—. 2011, AJ, 141, 97

Wielen, R. 1977, A&A, 60, 263

Wilsing, J., & Scheiner, J. 1909, Publikationen des Astrophysikalischen Observatoriums zu Potsdam, 56

Wilson, J. C., Miller, N. A., Gizis, J. E., Skrutskie, M. F., Houck, J. R., Kirkpatrick, J. D., Burgasser, A. J., & Monet, D. G. 2003, in IAU Symposium, Vol. 211, Brown Dwarfs, ed. E. Martín, 197–+

Wilson, J. C., et al. 2004, in Society of Photo-Optical Instrumentation Engineers (SPIE) Conference, Vol. 5492, SPIE Conference Series, ed. A. F. M. Moorwood & M. Iye, 1295–1305

Wing, R. F. 1973, in IAU Symposium, Vol. 50, Spectral Classification and Multicolour Photometry, ed. C. Fehrenbach & B. E. Westerlund, 209

Wollaston, W. H. 1802, Philosophical Transactions of the Royal Society of London, 92, 365

Wright, E. L., et al. 2010, AJ, 140, 1868

York, D. G., et al. 2000, AJ, 120, 1579

Young, T. 1802, Philosophical Transactions of the Royal Society of London, 92, 12

Zapatero Osorio, M. R., Caballero, J. A., & Béjar, V. J. S. 2005, ApJ, 621, 445

Zapatero Osorio, M. R., Martín, E. L., Béjar, V. J. S., Bouy, H., Deshpande, R., & Wainscoat, R. J. 2007, ApJ, 666, 1205

Zeeman, P. 1897, ApJ, 5, 332

Zhang, Z. H., et al. 2009, A&A, 497, 619

—. 2010, MNRAS, 404, 1817

VITA

Sarah Schmidt was born on September 17, 1984 in Riverside, a small suburb outside Chicago, to Joseph and Laurel Schmidt, a civil engineer and a political activist. Mostly due to the influence of her parents and her older brother, Jeffery, she spent her childhood dancing (ballet and tap), playing sports (basketball, softball, track, volleyball, and swim team), and learning to play piano, french horn, violin and guitar. During her senior year of high school, Sarah earned the Girl Scout Gold Award, participated in All-State Choir, and earned the title of MVP in track & field.

Sarah first became interested in astronomy at Barnard College during an Introduction to Astronomy course she took in Fall 2002. In addition to taking the required coursework, she also began research with Dr. Kelle Cruz at the American Museum of Natural History. As part of her work with Dr. Cruz, Sarah developed an interest in low mass stars and brown dwarfs which (as this dissertation may suggest) she retains today.

As a graduate student at the University of Washington, Sarah has strengthened her interest in increasing diversity in STEM fields through to her work with Pre-MAP and honed her teaching skills as instructor for the Pre-MAP Seminar, Astronomy 101, and Astronomy 190. Outside of graduate school, she has run five half marathons and been a part of the championship winning Infrared Sox for six years.

In the fall of 2012, Sarah will begin her postdoctoral position as the Columbus Prize Fellow at *The* Ohio State University.